M.J. van der Bend

Assessment and analysis of hook mounted compensation methods for offshore wind turbine blade installation

Master Thesis

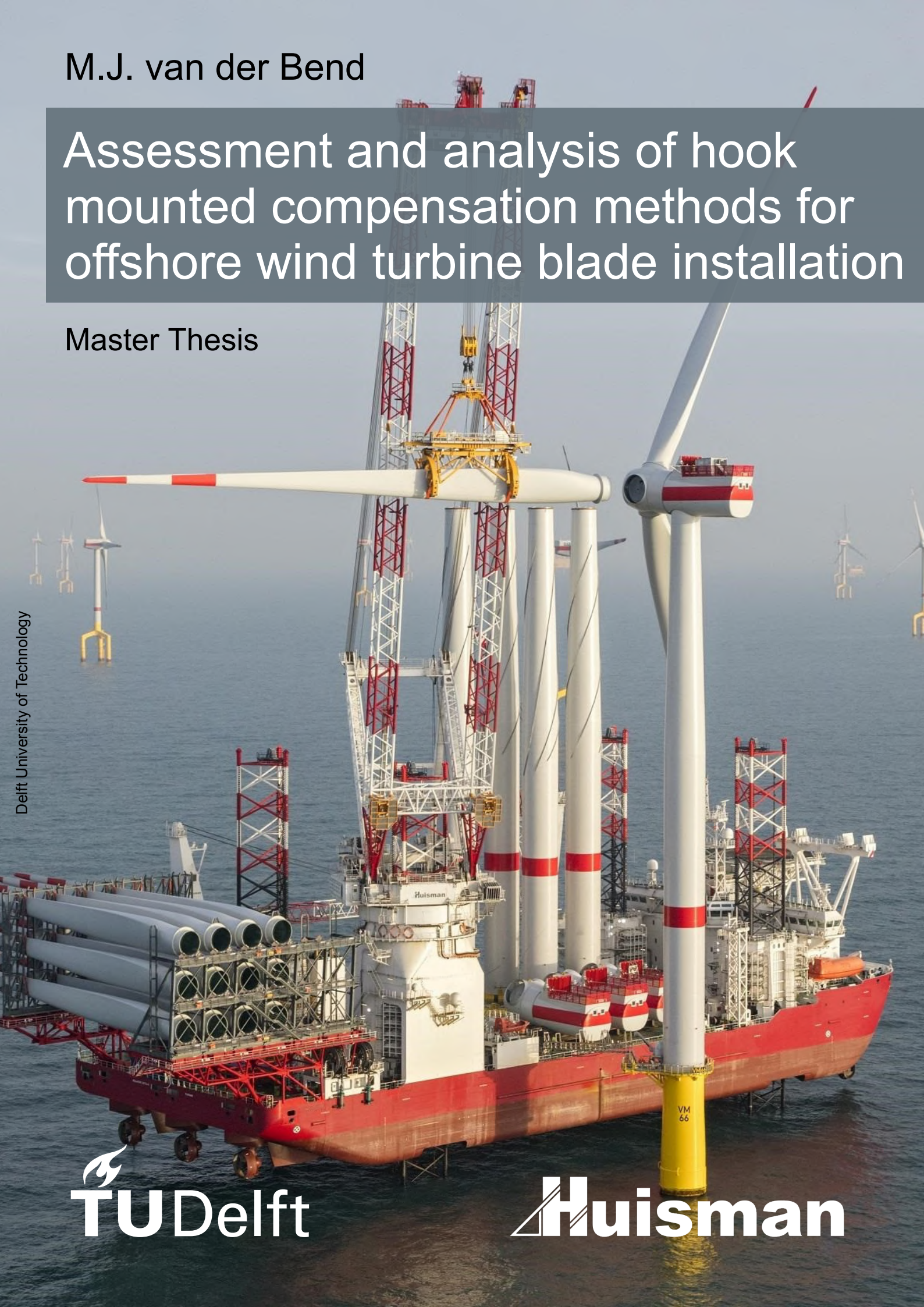

Delft University of Technology

TU Delft

Huisman

Assessment and analysis of hook mounted compensation methods for offshore wind turbine blade installation

by

M.J. van der Bend

Master Thesis

In partial fulfilment of the requirements for the degree of

Master of Science
in Mechanical Engineering

at the Department Maritime and Transport Technology of Faculty Mechanical, Maritime and Materials Engineering of Delft University of Technology

to be defended publicly on August 30, 2023 at 10:00 AM

Student number:	4688627		
MSc track:	Multi-Machine Engineering		
Report number:	2023.MME.8806		
Thesis Committee:	Dr. V. Reppa	Supervisor, Committee Chair	TU Delft
	Dr. J. Jovanova	Committee member	TU Delft
	Dr.ing. S. Schreier	Committee member	TU Delft
	Dr. G. Lavidas	Committee member	TU Delft
	Ir. R. Feith	Daily supervisor	Huisman Equipment B.V.
	Ir. M. Stofregen	Supervisor	Huisman Equipment B.V.
Date:	Wednesday 9th August, 2023		
Cover image:	[1] (modified)		

This thesis is confidential and cannot be made public until August 30, 2025.

An electronic version of this thesis is available at http://repository.tudelft.nl/.

TU Delft Huisman

Preface

This thesis is submitted in partial fulfilment of the requirements for the degree of Master of Science in Mechanical Engineering at the Delft University of Technology. The research presented in this document reflects the outcome of the work carried out over the past seven months, during which I had the opportunity to explore this fascinating and complex subject.

First and foremost, I would like to express my gratitude for the guidance provided by the university supervisor Vasso Reppa, whose support and insights were invaluable throughout this project. Particularly in the initial few months, I found it challenging to let go of certain aspects closely related to the subject. In addition to the guidance and feedback, I would like to extend special thanks for the help with crucial decisions and crossroads in the project. There were moments when I tended to take on too much, and you helped to clearly define the boundaries of what was, and what was not, feasible to explore during the project.

Furthermore, I am extremely grateful for the opportunity to conduct this project in collaboration with Huisman, who provided me with access to all the resources and knowledge necessary during the research. In particular, my daily supervisor, Rick Feith, played an integral role in supporting my work by always assisting me, and helping to quickly overcome any obstacles I encountered. I also greatly enjoyed the conversations and discussions we had during our weekly progress meetings.

At last, I would like to thank the people around me for all their support and understanding throughout the project. First and foremost, my girlfriend Kiki, whose endless patience and support greatly helped me during the busy months this project entailed. Furthermore, my parents, brother, and sister, who always have my best interests at heart. Finally, my roommates and friends, who provided the necessary distractions that were more than welcome from time to time.

I feel happy and honoured to present this thesis and look forward to my future endeavours and work within this branch of the offshore industry.

M.J. van der Bend
Rotterdam, Wednesday 9th August, 2023

Abstract

During single-blade offshore wind turbine (OWT) installation, wind disturbance results in blade root motion. The sensitivity to this wind disturbance is more significant for larger blades, reducing the allowable installation weather limit. A potential solution is a Hook Mounted Compensator (HMC) between the crane and the load that can provide high-precision compensation across multiple degree of freedom (DOF), and compensate for the influence of wind on the OWT blade. Several actuation methods (AM) have been identified that can be used in a HMC. However, these AMs have not been modelled dynamically and their effectiveness for the desired application is unknown.

The aim of this study is to analyse and assess the compensation effectiveness of these AMs in a HMC. For this purpose, the AMs are simulated and analysed in various levels of complexity and DOFs. Initially, the system is considered in a 1DOF. A linear representation is formulated, based on which a Proportional-Integral-Derivative (PID) controller for each AM is formulated. This enables simulation of the Single-Blade Installation System (SBIS) in the time domain. Assessment criteria are used to quantify the compensation effectiveness and actuation input of the AMs. To simulate the SBIS for each AM, 3DOF numerical models are developed that describe the operation of the AMs in their respective operational planes. Six actuation methods are included in the assessment.

Based on the assessment results, three AMs are combined in a HMC concept. A XY table is used to control blade root position in the x- and y-directions, gyroscopes for the z-direction, and COG shifting with counterweight to prevent gyroscope saturation. The PID controllers based on the linear 1DOF representation are used, operating in parallel, to control the blade root position in all DOF. The blade root motion is reduced by 96% along the blade axis and 86% radially. The blade root motion is sensitive to the mean wind speed, turbulence intensity, and angle of the incoming wind. The HMC shows robustness to variations in tugger line angle and pretension. The static blade pitch angle affects the magnitude and distribution of the wind-induced moment on the blade. For a pitch angle of -180, the moment around the z-axis is minimal, providing optimal HMC performance. The HMC concept can not directly actuate the blade around the z-axis. Instead, the XY table translates the blade at the COG, resulting in increased cylinder stroke and high power consumption for other pitch angles.

Two AMs were assessed to actuate the blade around the z-axis, both showing poor performance. Further exploration of AMs that can directly control the blade rotation around the z-axis could lead to improvement of the HMC concept. Additional improvement can be made in optimization of counterweight and gyroscopes sizes, potentially reducing weight and improving system performance. Further suggestions for future work include; exploring the compensating for the now neglected hub motion using the HMC, examining the stability of the HMC once the blade is mated to the hub, and the impact of sensor noise and delay on the HMC's performance.

Contents

Acronyms

3D	Three-Dimensional
BW	Bandwidth
COG	Center Of Gravity
COP	Center Of Pressure
DNV	Det Norske Veritas (classification Society)
DOF	Degree Of Freedom
DP	Dynamic Positioning
EOM	Equations Of Motion
FEA	Finite Element Analysis
GM	Gain Margin
HMC	Hook Mounted Compensator
IEA	International Energy Agency
IEC	International Electrotechnical Commission
KPI	Key Performance Indicator
LB	Lower Block
LCOE	Levelized Cost Of Electricity
LEC	Leg Encircling Cranes
MCC	Motion Compensation Crane
MSL	Mean Sea Level
NREL	National Renewable Energy Laboratory
NTM	Normal Turbulence Model
OWF	Offshore Wind Farms
OWT	Offshore Wind Turbine
PID	Proportional-Integral-Derivative
PM	Phase Margin
RMSE	Root-Mean-Square Error
SBIS	Single-Blade Installation System
SWL	Safe Working Load
TI	Turbulance Intensity
UQC	Universal Quick Connector

Nomenclature

Greek Symbols

α	Roll	rad
β	Pitch	rad
γ	Yaw	rad
μ	Frictional constant	–
ω	Rotational velocity	$\mathrm{rad\,s^{-1}}$
ρ	Density	$\mathrm{kg\,m^{-3}}$
τ	time constant	s
θ	Angle (general)	rad
ζ	Damping ratio	–

Roman Symbols

A	Area	$\mathrm{m^2}$
B	Bulk modulus	Pa
c	Damping	$\mathrm{N\,s\,m^{-1}}$
d	Distance/Stroke	m
E	Modulus of elasticity	Pa
F	Force	N
f	Frequency	Hz
G	Modulus of rigidity	Pa
g	Gravitational acceleration	$\mathrm{m\,s^{-2}}$
H	Height	m
I	Mass moment of inertia	$\mathrm{m\,kg^2}$
J	Polar mass moment of inertia	$\mathrm{m\,kg^2}$
k	Stiffness	$\mathrm{N\,m^{-1}}$
L	Length	m
M	Mass	kg
m	Moment	N m
n	Number of vanes/gyro's	–
P	Power	W
r	Radius	m
T	Thickness	m
W	Width	m

Subscripts

b	Blade	–
b^*	Combined blade and blade yoke	–
bh	Boom hoist	–

bm	Boom	–
bmh	Boomhead	–
c	Crane	–
cw	Counterweight	–
g	Gravity	–
gb	Gearbox	–
gy	Gyroscope	–
h	Hydraulic cylinder	–
l	Pendulum	–
lb	Lower block	–
m	Motor	–
mh	Main hoist	–
p	Cylinder piston	–
t	Tugger	–
tot	Total suspended load	–
v	Vane	–
w	Wind	–
xy	XY table	–
y	Blade yoke	–

Coordinate systems

$\boldsymbol{\omega}$	Rotational velocity vector	$\mathrm{rad\,s^{-1}}$
$\boldsymbol{\theta}$	Orientation vector	rad
$\boldsymbol{p}$	Position vector	m
$\boldsymbol{R}$	Rotation matrix	–
$\boldsymbol{v}$	Translational velocity vector	$\mathrm{m\,s^{-1}}$
$\mathcal{B}$	Blade-fixed coordinate system	–
$\mathcal{C}$	Crane-fixed coordinate system	–
$\mathcal{G}$	Global coordinate system	–
$\mathcal{H}$	Hook-fixed coordinate system	–
$\mathcal{W}$	Counterweight-fixed coordinate system	–

Other Symbols

$\beta_\circ$	Static blade pitch	°
$\boldsymbol{\tau}$	Load vector	N(m)
$\boldsymbol{D}$	Damping matrix	$\mathrm{N\,s\,m^{-1}}$
$\boldsymbol{f}$	Force vector	N
$\boldsymbol{K}$	Stiffness matrix	$\mathrm{N\,m^{-1}}$
$\boldsymbol{m}$	Moment vector	N m
$\boldsymbol{p}_{cog}$	Blade COG position vector (in $\mathcal{N}$)	m
$\boldsymbol{p}_{hub}$	Turbine hub position vector (in $\mathcal{N}$)	m
$\boldsymbol{p}_{root}$	Blade root position vector (in $\mathcal{N}$)	m

ω_n	Natural frequency	rad s^{-1}
ω_s	Gyroscope spin speed	rpm
ϕ_t	Tugger attachment ratio	–
σ_u	NTM standard deviation	m s^{-1}
C_D	Drag coefficient	–
C_L	Lift coefficient	–
C_M	Pitching moment coefficient	–
F_d	Damping loads	N
F_s	Spring loads	N
F_w	Wind induced loads	N
f_{fill}	Wire rope fill ratio	–
F_{pre}	Tugger pretension	N
H_{deck}	Deck height (above MSL)	m
H_{hub}	Hub height (above MSL)	m
H_{pd}	Crane pedestal height (above deck)	m
H_{qc}	Offset between UQC flange from bottom of the LB	m
I_{eq}	Equivalent crane inertia	m kg^2
I_{hinge}	Boom inertia around hinge	m kg^2
k_{ax}	Wire rope axial stiffness	N m^{-1}
k_{hydr}	Hydraulic fluid stiffness	N m^{-1}
L_1	Lower boom length	m
L_2	Upper boom length	m
L_p	Piston length	m
L_u	NTM length scale	m
L_{cog}	Offset in z between LB and blade (yoke) COG	m
M_{eq}	Equivalent crane mass	kg
m_{slip}	Slip moment for UQC friction coupling	N m
N_{falls}	Number of falls	–
r_v	Distance from vane rotational axis to LB COG	m
T/C	Airfoil thinkness ratio	–
U_w	Mean wind speed	m s^{-1}
V_p	Internal cylinder volume	m^3
X_{tip}	Crane tip x offset from hinge (in $\mathcal{N}$)	m
Z_{tip}	Crane tip z offset from hinge (in $\mathcal{N}$)	m

1

Introduction

In this chapter, an introduction to the research is provided. The first section presents general background information on offshore wind and the offshore wind turbine (OWT) installation process. In section 1.2, the problem statement is given. Based on the problem statement, the research objective is further discussed in section 1.3. In this section, the scope of the research is defined, and the main research question is derived based on the background and problem statement. The main research question is supported by sub-questions that divide the work into manageable parts that are addressed in the subsequent chapters. The approach and report outline are presented in sections 1.5 and 1.6.

1.1. Background

Driven by the global push for green energy to combat climate change, offshore wind energy capacity has significantly increased in recent years. Currently, around 16 GW of offshore wind capacity is installed within the European Union. The EU has set ambitious goals to further increase the capacity to 60 GW by 2030, and 300 GW in 2050 [2]. On top of the installation of new OWTs, the overall number of OWT that require maintenance is increasing at the same time. Blade failures make up a high proportion of all OWT failures, requiring frequent replacement [3]. The increase in the number of new OWTs to be installed, and the growing maintenance requirements, results in an increased demand for specialized lift vessels capable of OWT blade installation. To effectively compete with other energy sources, a lower levelized cost of electricity (LCOE) of offshore wind energy is pursued through economy of scale [4]. Because of this, the average individual capacity of installed OWTs has increased from 3 to 8.2 MW per turbine in 10 years time [5]. As turbine capacity scales with rotor size, the OWT installation vessels are tasked with increasingly demanding requirements, resulting in lengthier installation times and higher costs. Safe and more efficient methods for blade installation are thus crucial to the further development of offshore wind energy.

Installing the OWT blades is a complex and challenging task. The blades are lifted more than 100 meters above sea level. At such height, the flexibility of the crane and OWT tower also play a part in the installation accuracy [6]. The required accuracy for installation is in the range of 6 to 8 centimetres, while the vessel, crane, blades, and OWT assembly are all under the influence of environmental disturbances [7, 8]. Waves excite the natural frequency of the tower, causing the hub, onto which the blade needs to be installed, to move back and forth periodically [6]. Just like the turbine tower, the jack-up vessel can also sway as a result of the wave motion. However, for single-blade installation using a jack-up installation vessel, the influence of wind during installation is more significant than the movement of the vessel as a result of the waves [9, 10]. Aerodynamic forces on a turbine blade scale quadratically with wind speed. When conditions become too harsh, the installation procedure needs to be paused or stopped. The typical allowable weather limit for OWT installation is a 1.5 m significant wave height, with a mean wind speed below 10 m/s [8]. The time required for the installation of a blade takes up to 8 hours [11], where conditions must remain below the allowable weather limits.

The installation of OWTs is currently performed using jack-up vessels. An example of such a specialized lift vessel installing an OWT blade is shown in figure 1.1. The vessels are equipped with large legs used to lift the vessel out of the water, stabilizing the crane vessel. This reduces the influence of currents and waves on the installation operation, but does have significant downsides. The locations where new offshore wind farms (OWF) can be placed with jack-ups are limited, due to the limited water depth at which the vessels can operate. Also, the time lost during the jacking operation is often mentioned as a

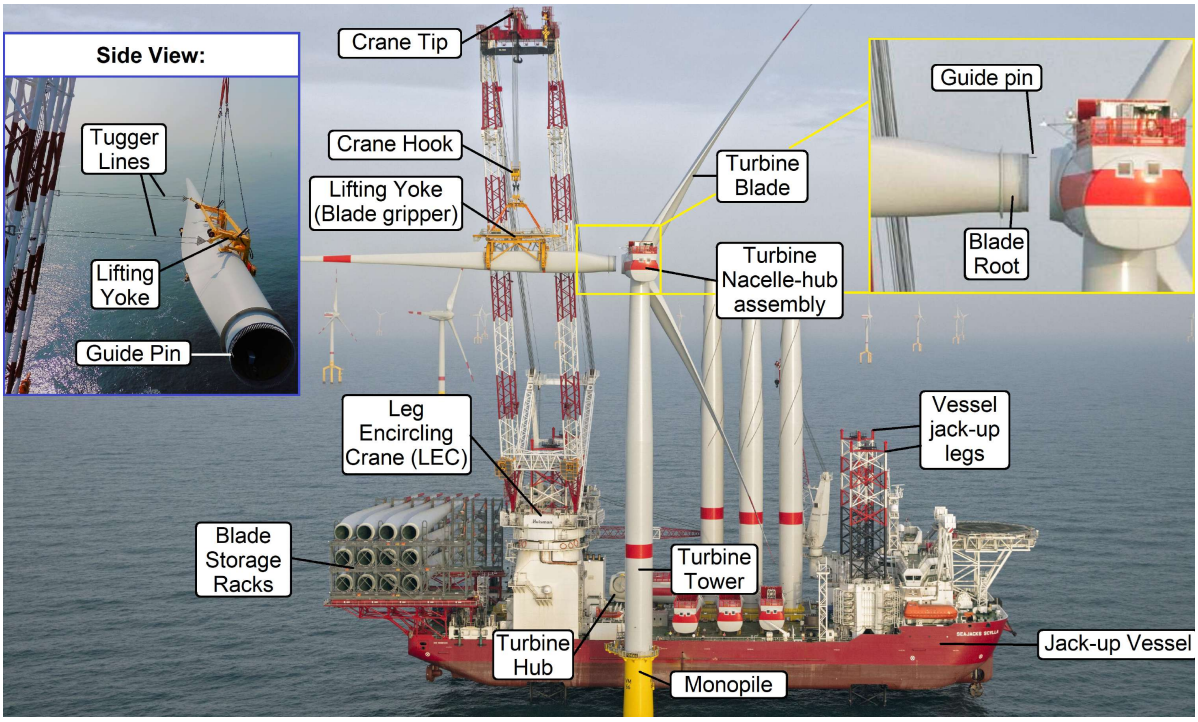

Figure 1.1: Overview of typical OWT and jack-up components during single-blade installation [1] (modified).

major disadvantage of the jack-up vessels [11, 12]. Like the blade installation, this process is weather dependent, and depending on the depth and soil condition, can take as long as the installation of a OWT blade itself [13, 14]. During installation of a turbine blade, tugger lines are used to reduce the influence of wind disturbances. The tugger lines are a set of cables that run along the length of the crane boom and are attached to the suspended blade yoke. The tugger lines are visible in the side view shown in figure 1.1. The blade is pulled towards the crane using tugger lines, resulting in a pretension in the tugger cables. The movement of the blade is somewhat reduced this way. However, due to the limited stiffness of the tugger lines, significant residual motions remain at the blade root.

1.2. Problem statement

Installation of OWTs is a challenging feat. The process requires precise coordination and high accuracy to ensure the safe installation of the blade onto the turbine hub. The combination of the blade's size, weight, and the dynamic nature of the installation environment introduces significant challenges. Deviations, misalignment, and sudden unexpected blade motion during the mating process has significant consequences, as impact with the hub can result in permanent damage to the blade root laminate [8]. The installation is strongly dependent on the wind speed. Additionally, the magnitude of the wind disturbance depends on turbulence intensity, the orientation of the blade relative to the incoming wind, and the size of the turbine blade. The latter is especially problematic due to the trend towards larger blade sizes.

For these larger turbine blades, the blade's Center of Gravity (COG), the point where the sum of gravity acts on the blade and where the blade is lifted, and the Center of Pressure (COP), the point where the sum of all the wind forces acts on the blade, are further apart. The increase in offset between these two point is all shown in figure 1.2. The offset between the COG and the COP results in a wind-induced moment on the blade. For larger blades, this effect is intensified as the offset between the two points increases, thus increasing sensitivity to wind disturbances. The significance of this effect has also been demonstrated in a study by de Leeuw [15], where simulations of blade root motion during single-blade installation for an 8.4 MW OWT blade and a 12 MW OWT blade were conducted. The study showed that the average blade root displacement increased by 280% for a 12 MW blade compared to an 8.4 MW blade under the same environmental conditions. This resulted in a 57% decrease in workability

Table 1.1: National Renewable Energy Laboratory (NREL) reference turbine blade data

Turbine capacity	5 MW	10 MW	15 MW
Blade length	61.5 m	96 m	117 m
Blade mass	17.7 t	47.7 t	63 t
Blade COG pos	20.5 m	24.2 m	26.8 m

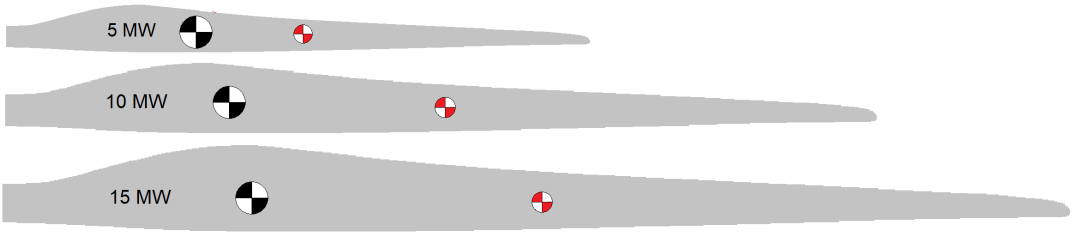

Figure 1.2: Blade COG (black-white) and approximate blade COP (red-white) for the NREL reference turbine blades

for the expected conditions at the Dogger Bank wind farm, due to the increased wind-induced blade root motion. It is anticipated that the workability will further decrease for even larger blades.

1.3. Research objective

Larger turbines are expected to enter the market in the near future. However, there are still insufficient solutions for the increased influence of wind on the blade installation. Motion compensating systems are being explored as a potential solution. These systems aim to isolate the motion of the lifted load from external disturbances such as wind. One such solution to mitigate residual blade root motion is local load stabilization, achieved by compensating for the blade motion at the hook. This approach involves the use of a Hook Mounted Compensator (HMC) between the crane and the load. The HMC can provide high-precision compensation for OWT installation across multiple degree of freedom (DOF) to compensate for the influence of wind on the turbine blade. This can benefit installation processes using jack-up vessels by expanding the range of operating conditions in which they can safely operate. The location at the hook offers the added potential of compensating for motions of both the vessel and the crane at the same time. However, this report focusing solely on compensating for the motion of the OWT blade due to wind disturbance.

Several actuation methods have been identified in collaboration with Huisman, which can be used for hook mounted compensation. An actuation method refers to a method that allows for the OWT blade to be rotated or translated relative to the global reference frame, in order to influence the position and orientation of the blade root. However, these actuation methods have not been modelled dynamically and their effectiveness for the desired application is unknown. The actuation methods have varying operating principles, and differ in the DOF in which they operate. It is expected that a single actuation method is not sufficient to control the position of the blade root in all desired DOF. However, it is unclear for which DOF compensation is required and which actuation method is most suitable for this.

The aim of this study is therefore to analyse and assess the effectiveness of the actuation methods in compensating for the blade motion as a result of the stochastic wind disturbances acting on the blade. From this analysis, a well-founded choice is made on which actuation methods can best be applied in a HMC concept. The assessment is based on a set of predetermined assessment criteria that include, among other things, the residual blade root motion after compensation and the required actuator input. The assessment process is supported by an extensive dynamic analysis.

The operational scope of the HMC is to compensate for wind induced blade motion as a result of turbulent airflow. This study considers the Single-Blade Installation System (SBIS) during the alignment phase, where the blade is suspended from a 3200 Mt Leg Encircling Cranes (LEC) crane on a jack-up vessel and aligned, but not connected to, the pre-installed turbine hub. The focus of this study is on the evaluation of the performance of different actuation methods intended for single-blade installation using a jack-up installation vessel. Other steps of the installation process and alternative installation methods

or equipment are not considered. The influences of waves on the vessel and the resulting effects on blade movement are not taken into account. The vessel is assumed to be a fixed, rigid structure with a constant position. It is assumed that there is no feedback of the blade or crane movement on the ship itself. This assumption is made because the mass and inertia of the blade is significantly smaller than that of the ship [9].

During the alignment of the blade with the hub, the hub undergoes a periodic swaying motion as well. This is the result of the excitation of the fore-aft natural frequency by wave loading. The motion is significant when the wavelength corresponds to this natural frequency [8]. However, this movement has a fixed predictable period and can possibly be compensated with less sophisticated passive motion compensators, such as tuned mass dampers [16]. Movement of the hub is therefore not taken into account. The turbine foundation and tower are modelled as a rigid structure, and the hub reference position, to which the blade is aligned, is therefore at a fixed position.

As part of the analysis, Proportional-Integral-Derivative (PID) controllers are designed for implementation of the actuation methods in a time simulation. In practice, feedback from the system states used in the feedback controller are often processed after measurement using a sensor by an observer module that filters the measurements and reconstructs non-measured states. Since the focus of this study is on the evaluation of the performance of different actuation methods and not on the sensors and observer design, this is not considered.

1.4. Research questions

The main research question for the project, based on the previously defined research objective, reads: How can the highest compensation effectiveness be achieved using hook mounted actuation methods for offshore single-blade installation?

The main research question is supported by the following sub-questions:

SQ1: What is the state of the art of motion compensation for single-blade OWT installation?

SQ2: What are the operational requirements, environmental conditions and disturbances encountered during single-blade installation using the HMC actuation methods?

SQ3: How can KPI's be defined to characterize the effectiveness of the HMC actuation methods?

SQ4: How can the single-blade installation systems for the actuation methods be described linearly?

SQ5: How can the actuated single-blade installation systems be controlled?

SQ6: How to model the HMC actuation methods for the application of single-blade OWT installation?

SQ7: How can the HMC actuation methods best be combined into a HMC concept to achieve the best performance for the set KPI's?

SQ8: How to verify the control performance and validate operation of the chosen HMC concept?

1.5. Approach

The actuation methods considered in this study have different working principles, limited to specific mechanical DOF. Therefore, each actuation method is expected to be effective on in this DOF. As a result, it is likely not possible to control the blade root position in all DOF using a single actuation method. Nevertheless, it is desired to directly compare the actuation methods within the DOF where they provide a solution. To allow for this comparison, the SBIS is described within the plane in which the actuation method operates during the assessment of the individual actuation methods, abstracted from the other DOF. This plane is called the operational plane. The orientation of the operational plane depends on the working principle of the actuation method, and considers two translation DOF and a single rotational DOF.

To study the behaviour of the actuation methods, simulations are conducted in the time domain. However, each actuation method requires its own controller. To formulate these controllers, a linear time-invariant description of the system is desired, as this allows simplified analysis in the frequency domain. For this purpose, the system is first reduced to a single mechanical DOF. A linear 1DOF mass-spring-damper representation of the SBIS is formulated for each actuation method. The mass-spring-damper

system is translated into a state-space representation. This linear analytical model is used for the analysis in the frequency domain. The same models are used to design controllers, which are later applied in the higher DOF numerical models. A PID controller is formulated for each actuation methods. To ensure a fair comparison, each controller has the same control objective, uses the same system output and reference, and is developed towards the same gain and phase margin. The resulting bandwidth depends on the working principle, dynamics, and system parameters for the actuation method used.

The individual actuation methods, described within their respective operational planes, are simulated in the time domain. Non-linear 3DOF (single plane & rotation) numerical models are constructed for each actuation methods for the application of 15 MW OWT single-blade installation. The PID controllers developed using the analytical models are implemented in the 3DOF models. The modelling and simulation is performed in a Matlab/Simulink environment. All numerical models use the MarIn toolbox wind model to calculate the aerodynamic loads acting on the blade [9].

The resulting simulated behaviour of the SBIS for each actuation method is evaluated based on assessment criteria. These criteria are used to quantify the performance of the actuation methods and allow for direct comparison between them. The assessment results are used to make an informed decision on the actuation methods to be used in a HMC concept.

The proposed HMC concept, utilizing one or more of the assessed actuation methods, is further tested in a 6DOF single-blade installation simulator model. This simulator model is again constructed within Matlab/Simulink and uses the MarIn toolbox. The simulator model is used to evaluate the effectiveness of the HMC by applying the concept in a 6DOF environment. Additionally, the sensitivity of the HMC to changes in the assumed operational and environmental conditions are examined using this simulator model.

1.6. Report outline

It is not always possible or desirable to consider all DOF in the analysis. Initially, a schematic overview is presented within the operational plane for each actuation method. Based on this, the system is reduced to a linear description in just a single mechanical DOF. The complexity and the number of DOF are gradually expanded over the successive chapters, from the initial single DOF, to the 3DOF numerical models used for assessment, and finally the full 6DOF simulator model. This progression is also illustrated in the report outline overview in figure 1.3. Below, an overview of the content of the 5 chapters is given, together with the distribution of the sub-question across the chapters.

2 **HMC Development Framework** answers sub-questions 1, 2 and 3: The development framework serves as an extension on the background provided earlier in this introduction, and provides further information to support the modelling, analysis and assessment within the main body of the report in chapter 3, 4 and 5.

section 2.1 focuses on SQ1. An overview of the state of the art in motion compensating solutions for the offshore industry is provided. The limitations of the current motion compensation solutions for the application considered in this study are highlighted, and an outlook on future development is given.

The analyses in the following chapters are based on models of the SBIS for each actuation methods. SQ2 forms the basis for these models. This sub-question is addressed through an introduction to the single-blade installation procedure, the operational conditions and associated representative load cases in section 2.2. Additionally, the properties of the interfacing systems, such as the ship, crane, and turbine, are presented.

The primary coordinate systems and conventions used throughout the report are presented in section 2.3. The various actuation methods, their working principles, and operational plane are introduced in section 2.4. The actuation methods mainly consist of untested product concepts developed internally at Huisman.

Finally, to address SQ3, assessment criteria are defined in section 2.5 based on the development framework, operational scope and objective of the HMC described previously.

3 **Linear Modelling** answers sub-questions 4 and 5: The linear analysis of the SBIS for the actuation methods is described in this chapter. In accordance with SQ4, a linear single DOF model is constructed. The process consist of reducing the system to a single mechanical DOF, and translating it into mass-spring-damper, and state-space representation, for each actuation method. Section 3.5 presents the frequency domain analysis in which PID controllers are formulated for each actuation method to answer SQ5, based on the linear 1DOF model.

4 **Non-Linear Modelling** answers sub-question 6: This chapter addresses the structure and description of the numerical models used to simulate the individual actuation methods in the time domain, and later, the proposed HMC. Section 4.4 provides the simulation results for each actuation method based on the assessment criteria defined in the second chapter.

5 **Hook Mounted Compensator** answers sub-questions 7 and 8: The result of the assessment provided in chapter 4 is used to decide on which actuation methods to use in a HMC concept to answer SQ7. The result of the 6DOF HMC simulation are presented in section 5.4, and a sensitivity analysis is performed in section 5.5 to provide an answer to SQ8.

6 **Conclusions & Future research:** In the final chapter, the conclusions of the report are discussed, and the main research question is answered. The limitation of the study are discussed and recommendations for further research are provided.

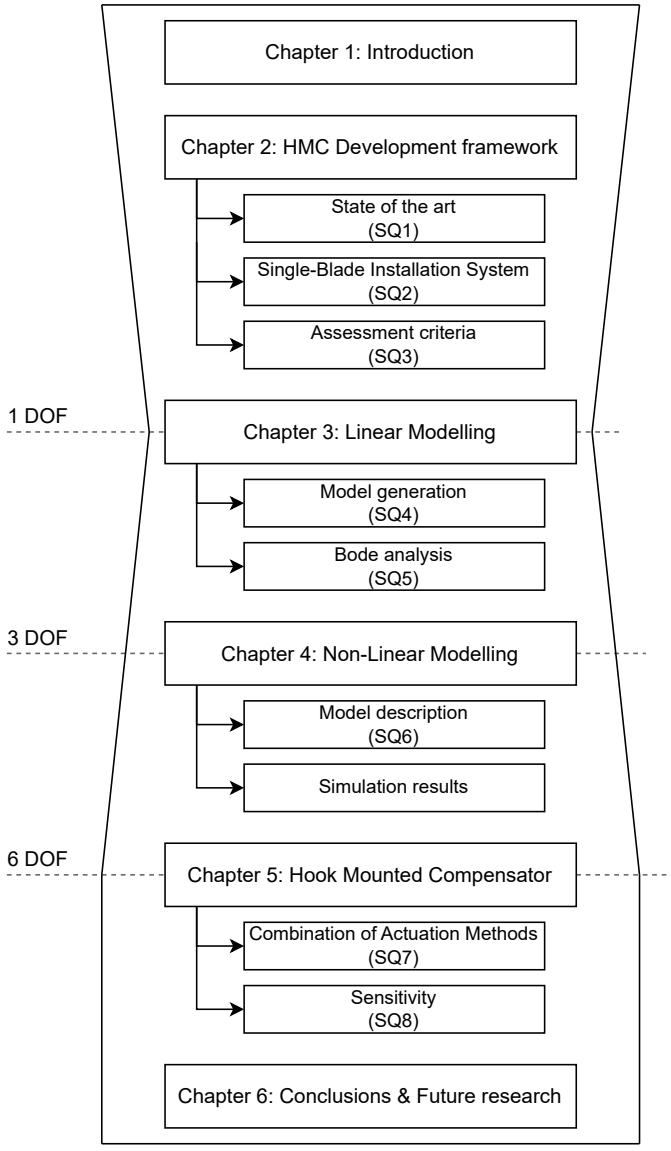

Figure 1.3: Outline of the thesis report

2

HMC Development Framework

The development framework for the hook mounted compensator is defined in this chapter. The state of the art regarding offshore motion compensation is first presented in section 2.1. The single-blade installation procedure is described and the operational conditions and representative load cases are introduced in section 2.2. Additionally, this section provides information about the properties of the interfacing systems such as the vessel, crane, and turbine. This information is required later for modelling the installation system with the actuation methods. In section 2.3 another overview of the SBIS is provided. The main coordinate systems, used in the description of the actuation methods, are defined in this section. The actuation methods, and their working principles, are introduced in section 2.4. These actuation methods operate based on different principles and are expected to only be effective in specific DOFs. The actuation methods primarily consist of internally developed, untested product concepts at Huisman. Finally, in section 2.5, the assessment criteria are defined, used in the successive chapters to directly compare the actuation methods.

This chapter addresses the following sub-question:

SQ1: What is the state of the art of motion compensation for single-blade OWT installation?

SQ2: What are the operational requirements, environmental conditions and disturbances encountered during single-blade installation using the HMC actuation methods?

SQ3: How can KPI's be defined to characterize the effectiveness of the HMC actuation methods?

2.1. State of the art

Motion compensation sees wide application within the offshore industry. Motion compensation is used to compensate for the wind and wave disturbances encountered at sea. These systems are implemented at various locations. Below, four classifications of offshore motion compensation are defined, based on the location where the motion compensation is applied. The state of the art for each classification is discussed. Figure 2.1 provides an overview of the locations where these four classes of motion compensation are incorporated within the SBIS using a jack-up.

2.1.1. Vessel motion and positioning control:

The first class of motion compensation aims to minimize the movement of the vessel itself. This class is applied within the vessel itself, as shown in figure 2.1. An example of such as system for floating vessels is dynamic positioning (DP). DP systems use the vessel's own propellers or thrusters to maintain vessel position and heading [4]. DP is effective at low frequencies, for which it can reduce vessel movement in surge, sway, and yaw by 70% [17]. Jack-ups are typically equipped with DP to maintain vessel position during the jacking operation.

2.1.2. Motion compensation platforms:

The second class of systems aims to separate vessel motion from the load, particularly in walk-to-work gangway applications. The compensation is applied at a platform on top of the vessel's deck. These platforms are designed to compensate for vessel motion in all mechanical DOF. In recent developments, predictive algorithms are being employed to enhance system effectiveness and prevent actuator limits from being exceeded [18, 19]. Systems where a crane is placed on such a platform to

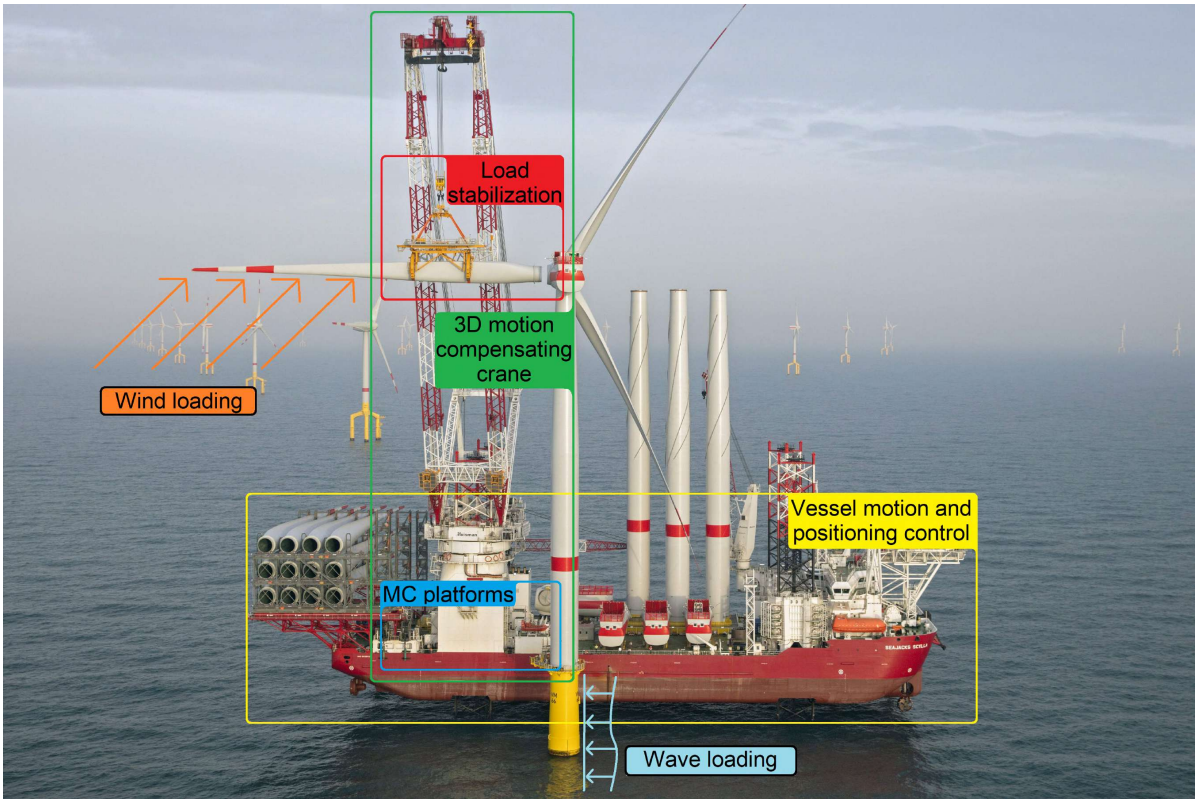

Figure 2.1: The locations where the four classes of motion compensation system are incorporated. [1] (modified).

decouple the vessel motion from the crane base exist as well [20, 21]. For a jack-up with LEC, the platform would be located in the blue marked area in figure 2.1. A problem with implementing the system in combination with the large cranes used during installation of OWT blades, is the limited capacity of the platform. The LEC used on jack-ups are used for lifting heavy loads from a stationary position and have a maximum lifting capacity of up to several thousand tonnes. This high capacity is required as the same crane vessels are also used for installation of the monopile foundations, which weigh up to 2000 tonnes each [22, 23]. Due to the massive crane weight and inertia, and the limited stiffness of the tall cranes, implementing such a solution for OWT installation is unrealistic.

2.1.3. 3D Motion compensation cranes:

The application of motion compensation within cranes themselves, known as 3D tip compensation or a 3D motion compensation crane (MCC), aims to decoupling vessel motion from the crane tip by using the crane's actuators to move the tip in the opposite direction. Most research in this area focuses on smaller offshore cranes, particularly knuckle boom cranes, which are versatile, but limited in size and capacity [24–26]. Limited research exists on 3D MCCs suitable for the installation of OWT components. Mechanical feasibility studies have identified challenges related to the stiffness and weight of 3D MCCs Buijs [27]. 3D MCCs need to be much stiffer than conventional LEC cranes, making them heavier and more expensive. Controller robustness is also identified as a challenge for the chosen actuators in the 3D MCC concepts studied by Driessen [28]. For certain actuator types, the stability of the system was compromised. Due to the lack of rigidity and stiffness of tall cranes, the precision required for single-blade installation is difficult to achieve. Another study uses simulation results of a 3D MCC similar to the crane analysed by Driessen [28], where the residual motion of the hook after compensation has an amplitude of 0.2 meters in the x-direction, and up to 1.0 meters in the y-direction [29].

2.1.4. Load stabilization:

The final class of motion compensation systems aim to reduce the movement of the load relative to the seabed or another vessel, and are often applied between the crane (tip) and the load itself, indicated by the red marked area in figure 2.1. The HMC, which is the focus of this study, is an example of a load stabilization tool. The advantage of this location, is that the load has a relatively low inertia with respect to the vessel and crane, resulting in lower required actuator input power. Another example of load stabilization are heave compensation systems, which aims to decouple the vertical DOF from vessel motion. Most existing systems combine passive and active cylinders to reduce actuation effort and are implemented around the crane winch system, as a tension control system [30]. Seaqualize [31] is a Dutch tech scale-up that develops an active inline hook mounted heave compensator. The system is intended for cranes vessels that are not equipped with high-performance active heave compensation systems themselves, increasing workability without the need for crane upgrades. A prototype version was successfully tested and DNV certified. The system uses passive cylinders in combination with an electrically driven rack and pinion system.

As described in section 2.2, it is common to use tugger lines during blade installation. A numerical model study by Leeuw [15] shows that even with these tuggers, significant blade motion remains. Ren *et al.* [32] proposes an active tugger systems, where the tugger tension is controlled to minimize the effect of wind on the blade. For this case, a significant reduction of the blade motion parallel to the tugger direction is observed. However, there is still little compensation in other directions.

Various tools have also been developed that aim to improve the installation of a turbine blade. An example is the blade dragon, which allows for the installation of a blade in more angles by rotating the blade (yoke), increasing installation flexibility. However, this product is developed for onshore installation and does not reduce the impact of the environmental disturbances [33]. Verton is a company that specializes in gyroscopic load stabilization, and introduced a new concept using adjustable wind vanes, in combination with their gyroscopic load-management system to control turbine blades. However, the concept is intended for onshore projects and has not yet been implemented successfully [34]. Finally, Burggraaf [29] devised multiple load stabilization concepts and a mechanical design for one of these concepts. This design isolates the hook's translational motion in x- and y-direction from the load. Although the effectiveness of the concept could not be proven, it does show potential for compensation in the horizontal planar DOFs. For vertical motion, an additional heave compensation system is required.

2.1.5. Future development

Of the four locations where motion compensation can be implemented, the greatest potential for development is in the 3D MCCs, and new innovative load stabilization systems. Current 3D MCCs have limited crane height and capacity. The studies from Buijs [27] and Driessen [28] into 3D MCCs that are suitable for OWT installation, show major challenges. From these studies, it is concluded that due to the height and limited stiffness of the crane, it is unlikely that the required accuracy for OWT blade installation can be achieved with a 3D MCC alone. Therefore, the development of suitable load stabilization systems remains integral for further development in OWT installation.

2.2. Single-blade installation system

During the construction of offshore wind farms, the foundations are often installed first. Later, the turbine tower, nacelle-hub assembly, and blades are installed in sequence on the already placed foundation. The OWT components are loaded onto the jack-up vessel, after which the vessel sails to the installation location. The number of components that can be transported on the installation vessels depends on the OWT size and the available deck space. Alternatively, the components are delivered at sea by a supply vessel. Due to the high sensitivity to wind conditions, the installation of the three OWT blades is often the most critical and time-consuming step. The installation time for a blade depends on the size of the OWT, taking approximately 5 to 8 hours for a 3 MW and 7 MW OWT, respectively [11].

The exact procedure for blade installation may vary between projects, as it depends on the specific guidelines provided by the turbine manufacturer for each particular turbine. The blade yoke is specifically designed for the turbine blade. The procedure described in this section offers a generalized description of the single-blade installation method. This method represents a split installation approach, where the OWT blades are delivered separately and installed onto the hub-nacelle assembly at sea.

(a) Crane lifting a blade from the storage racks used for sea fastening

(b) Lifting phase: Blade lifted from deck and moved towards the hub

(c) Alignment phase: Blade aligned with the hub

(d) Mating phase: The blade is slowly moved towards the hub

Figure 2.2: The single-blade installation stages for an OWT [35] (video stills)

Below, the steps for the single-blade installation process are given. Figure 2.2 provides an overview of the various process steps.

- **Lifting phase:** During this lifting phase, the blade is first fitted to the blade yoke, and then lifted out of the blade racks. The blade is lifted at its COG. The crane is moved to the reference position while the blade is brought close to the hub. When the weather conditions are suitable, installation continues. If there is too much blade motion due to the environmental conditions, the blade is returned to the deck while waiting for weather conditions to improve.
- **Alignment phase:** : In this phase, the blade root is aligned with the hub before mating can commence. The blade root itself is offset from the pick-up location at the blade COG along the blade axis. The alignment of the blade root with the mounting location on the hub is assisted by tugger lines, used to position the blade and reduce the effect of wind on the blade. This study focuses on the phase of the installation. One or more of the bolts on the blade are longer, referred to as the guide pin. These guides are used during the final mating process. During alignment, the guide pin on the blade root is aligned with the mounting hole on the hub, and should then be kept in this position.
- **Mating phase:** The mating phase is the final stage in the installation process. The blade is still guided by tugger lines during this phase. the aligned blade is gradually moved towards the hub. The mating itself begins as soon as the guide pin makes contact with the hub. The guide is mated to the corresponding hole on the hub. During the final approach, blades are sometimes assisted manually by a worker inside the hub. For successful mating, the guide pin must be placed in the correct hole on the hub, which requires an accuracy of about 6 to 8 centimetres [6–8].

Table 2.1: Turbulance Intensity (TI) for various wind speeds and the three turbulence classes

Class	I_{ref}	6 [m/s]	9 [m/s]	12 [m/s]	15 [m/s]	18 [m/s]
A	0.16	0.27	0.22	0.19	0.18	0.17
B	0.14	0.24	0.19	0.17	0.16	0.15
C	0.12	0.20	0.16	0.15	0.13	0.13

2.2.1. Operational conditions

The typical allowable weather limit for OWT installation using jack-ups is a significant wave height of 1.5 m and a mean wind speed of 10 m/s. However, specific allowable weather limits may vary depending on the exact equipment and OWT size. In this study, the focus is on the installation of the OWT blades, in which wind disturbance plays a major role. Wave and current disturbances are not considered.

Before OWT installation, the jack-up vessel lifts itself out of the water by lowering its legs. The legs are lowered to the sea floor. The loads on the legs are slowly increased until the vessel is safely lifted from the water. The placement of the legs may be limited by existing infrastructure on the seabed. The legs leave an imprint on the seabed when the vessel is lowered down again, changing the properties of the soil. This can result in unpredictable behaviour during leg preloading. For this reason, lowering the legs in the same location is avoided. These impressions may be present due to the earlier installation of the OWT foundation with a jack-up vessel. Consequently, the orientation of the installation vessel cannot be freely chosen based on the most favourable wind direction. In this study, a wind direction from directly behind the crane, perpendicular to the blade orientation, is assumed. This wind direction perpendicular to the blade results in the highest blade loading and is considered a critical position.

The wind conditions themselves are based on the International Electrotechnical Commission (IEC) 61400-1 standard [36]. This standard provides guidelines and specifications for the design, operation, and maintenance of OWTs, including guidelines for the modelling of wind disturbance. The reference wind speed, specific to the installation location, represents the mean wind speed over a 10-minute time period.

The standard also defines methods to model wind turbulence. Turbulence is the chaotic change and fluctuation within the mean wind speed. The NTM described in the IEC standard is used to describe this turbulent airflow. NTM is defined as per equation (2.1) [36], and provides a standard deviation of the wind turbulence. A metric that is often used to categorize turbulence, is the turbulence intensity. The standard defines three categories of expected turbulence intensities (A, B, and C) for different mean wind speeds, where A results in the highest Turbulance Intensity (TI). An overview of the turbulence intensities for the three turbulence classes and the wind speeds considered in this study is shown in table 2.1. The table is filled in with the turbulence intensity associated with the wind speed at the top of the column, and the turbulence class in the first column.

$$\sigma_u = I_{ref}(0.75U_w + 5.6) \tag{2.1}$$

$$TI = \frac{\sigma_u}{U_w} \tag{2.2}$$

As per the IEC standard, the spectral decompensation of the turbulent airflow is described by the Kaimal spectral model [37]. The spectral decompensation is given by equation (2.3), where σ_u is the standard deviation from the NTM, U_w is the mean wind speed and L_u the length scale defined in IEC 61400-1. A spectral decomposition plot is found in figure F.2.

$$S(f) = \sigma_u^2 \frac{4L_u/U_w}{(1 + 6fL_u/U_w)^{\frac{5}{3}}} \tag{2.3}$$

Table 2.2: System parameters for the 3200 mt LEC crane and tugger lines

Symbol	Value	Unit	Description
L_{bm}	140	m	Boom length (measured along boom)
M_{bm}	591e3	kg	Boom weight
M_{bmh}	147e3	kg	Boom head weight
θ_{bm}	76	deg	Boom angle (to horizontal)
θ_{bh}	57	deg	Boom angle (to horizontal)
$k_{ax,bh/mh}$	2.73e8	N	Axial hoist wire rope stiffness
L_{bh}	100	m	Boom hoist length
$N_{falls,bh}$	22	-	Number of boom hoist falls
$k_{ax,t}$	7.43e7	N	Axial tugger line wire rope stiffness
L_t	157.5	m	Tugger line length
r_t	26e3	m	Tugger line radius

2.2.2. Installation equipment

The reference crane used in the study is a Huisman 3200 mt SWL LEC, specifically developed for a jack-up installation vessel. The crane is designed for the installation of future OWTs and meets the required crane capacity and height for the installation of the 15 MW reference turbine considered in this study (see section 2.2.3). The crane parameter values are based on the crane reference position, which is the position used during OWT blade installation. This reference position, shown in figure 2.3, corresponds to a boom angle of 76 degrees. The crane is equipped with a splittable block, which means that bundles of hoist cables can be detached from the lower block when the extra capacity is not required. As the blades are relatively lightweight, it is assumed that the block is used in split configuration. The split configuration is visible in the close-up of the block in figure 2.3.

Universal quick connector

The crane is equipped with the Huisman UQC system integrated into the lower block. During OWT installation, many tools are required to be suspended from the crane. The UQC allows for quick transition between these tools. The UQC also eliminates the need for rigging, as the UQC enables a rigid connection between the lower block and the tool.

The Huisman UQC includes a drive mechanism, called the power swivel. The power swivel is used to rotate the hook or lifting tool relative to the lower block. The rotation mechanism can also be locked in place during lifting operations. To enable quick exchange of tools, the moment around the z^h-axis is transferred through a slip coupling. The maximum moment that can be transferred through friction is a function of the mass suspended from the UQC pin and is given by equation (2.4), where r_{slip} is the radius of the friction contact surface, and μ the frictional constant, assumed to be 0.1.

A system overview of the UQC with power swivel is shown in figure 2.4. The UQC pin (grey) is connected to the tool and installed in the housing (purple). The pin is held in position by the red friction coupling. The entire housing can rotate inside the UQC frame (dark blue). The two yellow motors drive the housing through as gearbox (green). Finally, the UQC frame is connected to the block by the main pin (light blue).

$$m_{slip} = r_{slip}\mu M_{tot} g\sqrt{2} \tag{2.4}$$

Tugger lines

The 3200 mt LEC is equipped with a tugger line system, which is used during installation. A tugger winch is located at the bottom of the boom, responsible for winding and unwinding the tugger line. The winch is used to generate a pretension in the line, which can be chosen by the operator. In the reference case, a static tugger line pretension of 40 kN is used. The winch is set to a maximum line tension. If the tension increases beyond the set maximum, the tugger line is allowed to slip. This is done to prevent sudden wind gusts from creating high tensions in the rigging. The tugger line runs along the entire length of the boom. The line loops through a snatch block, which travels up and down the boom along with the hoisted load. This system is used to ensure that the tugger line is always oriented horizontally. The tugger line is highlighted in orange in figure 2.3

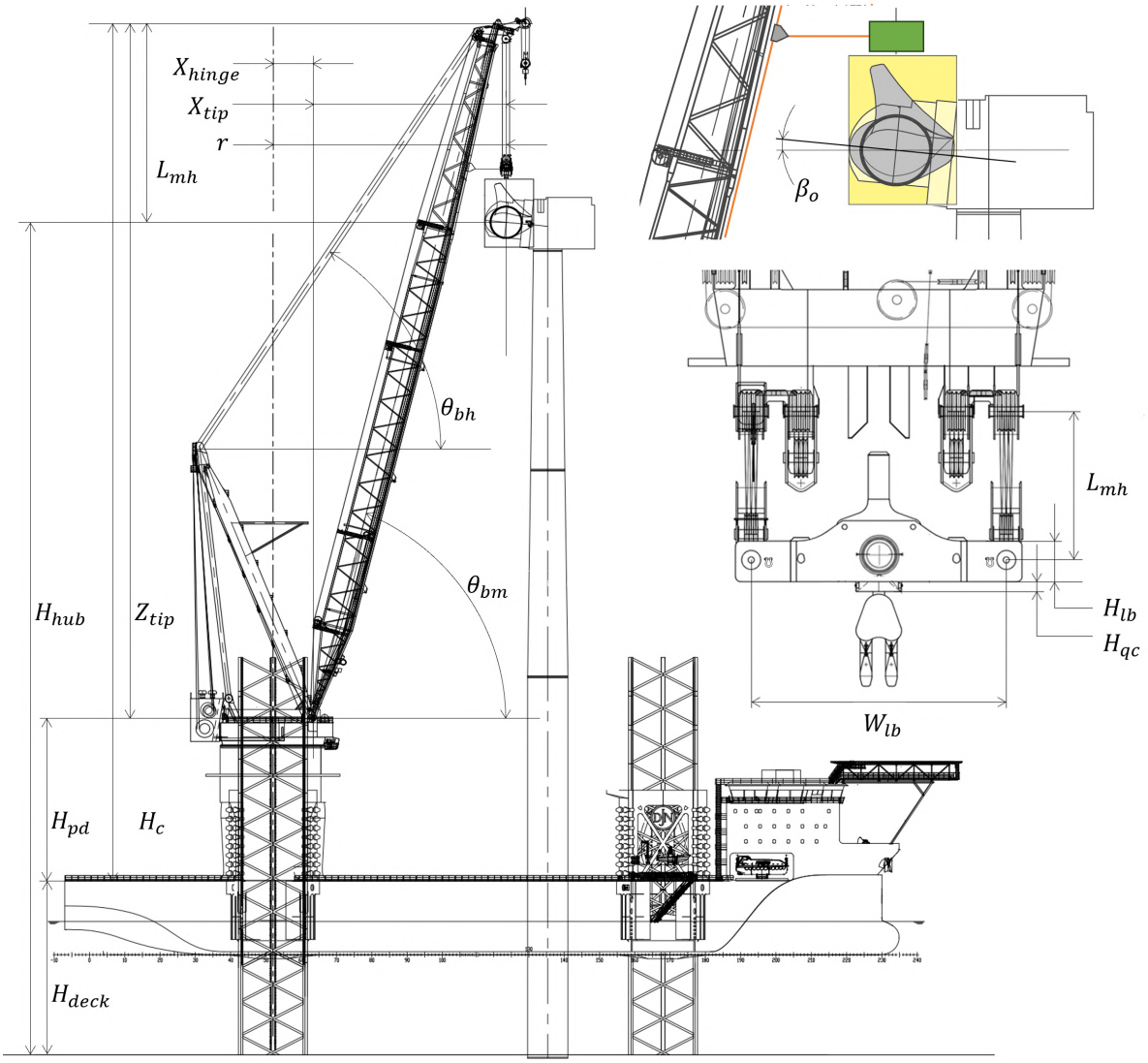

Figure 2.3: Crane in its reference position

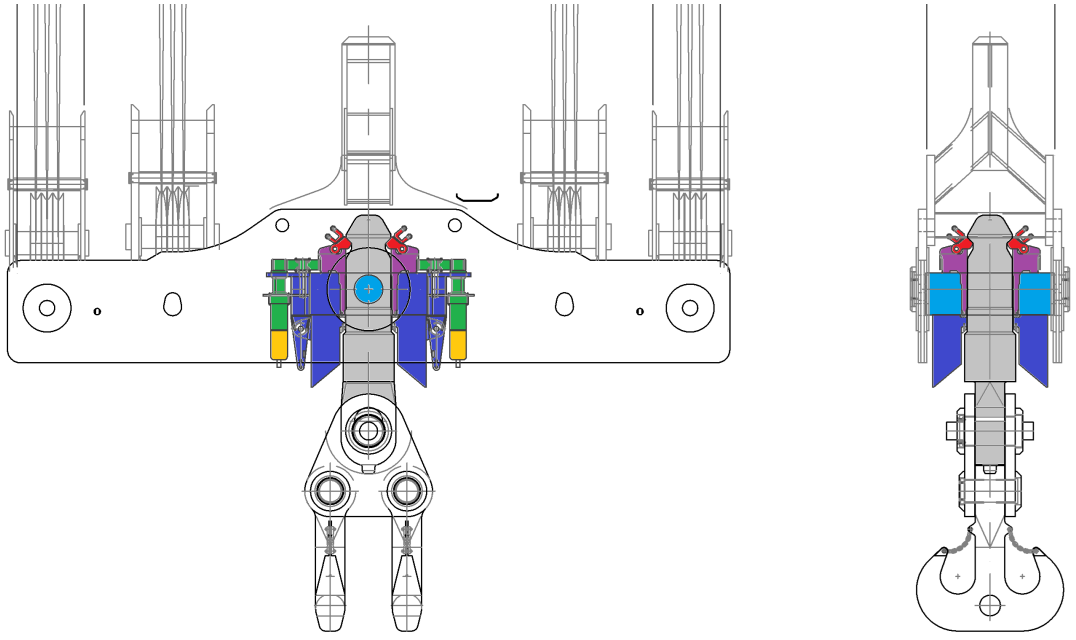

Figure 2.4: Universal Quick Connector with power swivel

Table 2.3: Main blade and blade yoke parameters

Symbol	Value	Unit	Description
L_b	117	[m]	Blade length
D_{root}	5.2	[m]	Root diameter
M_b	64e3	[kg]	Blade mass
$I_{b_{x/z}}$	46.8e6	[kg.m^2]	Blade inertia (about COG)
W_y	18	[m]	Yoke width
H_y	6.5	[m]	Yoke height
M_y	50e3	[kg]	Yoke mass

The axial stiffness of the tugger wire is given by equation (2.5), where $E \cdot f_{fill}$ has an approximate value of 35 GPa for the fibre core wire ropes used. For the 3200 mt crane in the reference position, the total tugger length is 157.5 meters. Table 2.2 provides an overview of the crane and tugger line parameters.

$$k_t = \frac{E \cdot f_{fill} \cdot \pi \cdot r_t^2}{L_t} \tag{2.5}$$

Blade yoke

A specialized blade yoke is used for lifting the blade, sometimes referred to as a blade installation tool or blade gripper. This blade yoke is also visible as the yellow frame around the blade in figures 1.1 and 2.2a. The yoke is often developed for the specific turbine blade being installed and generally provided by the turbine manufacturer. However, the yoke can also be supplied by an external party. For the 15 MW reference turbine blade, there is no existing design for a blade yoke. The assumed values for the size and weight of the yoke are based on a blade yoke for a 12 MW turbine blade [15].

An important parameter that influences the behaviour of the suspended blade, is the static blade pitch angle. This refers to the blade pitch angle of the blade in the yoke, indicated as $\beta_\circ$ in figure 2.3. The specific pitch angle of the blade varies depending on factors such as the design of the turbine, the wind conditions at the site, and the desired operational parameters. In studies with smaller turbine blades (up to 5 MW), a static pitch angle of -90 degrees is often used, as the results in more predictable behaviour [32, 38]. However, this position results in higher blade loading, making it impractical for large turbine blades. Pitch angles used during installation of large OWT blades generally range between 0 and 15 degrees. In this study, a static blade pitch angle of 7 degrees, taken from the reference blade yoke, is assumed. The influence of this static blade pitch angle is further investigated in section 5.5.

2.2.3. Reference turbine

As the wind energy industry continues to advance, larger and more powerful turbines are being developed to harness higher energy yields. The OWT used in the study is the International Energy Agency (IEA) 15-MW reference turbine, developed by the National Renewable Energy Laboratory (NREL). This turbine represents the future trend in wind turbine technology. The NREL reference turbine is specifically designed for research purposes. Various turbine sizes have been developed by NREL, which are widely used in literature. This also makes it a suitable choice for comparison and benchmarking. The OWT is installed on a monopile foundation and has a hub height of 150 meters above MSL. Blade yokes are specifically designed for the turbine blade, and are often designed and supplied by the turbine manufacturer. As no blade yoke is provided for the 15MW reference turbine, values for the yoke height, width, and weight are approximate values based on existing blade yokes for smaller turbines. The main turbine and blade yoke parameters used in subsequent analytical models, and numerical models. are summarized in table 2.3.

2.3. Coordinate systems

Three coordinate systems are defined, a global coordinate system, a hook-fixed coordinate system and a blade-fixed coordinate system. All coordinate systems follow the right-hand rule. The three coordinate systems used in the models are shown in figure 2.5.

- The origin of the global axis system, denoted by $\mathbf{o}_g$, is positioned at the intersection between the mean sea level (MSL) surface and the rotational axis of the crane (slewing axis). The three global

axes are denoted x, y and z. The z-axis point upwards and the y-axis is aligned with the jack-up vessel's heading. The x-axis is oriented according to the right-hand rule. It is assumed that the crane is oriented such that the projection of the boom on the XY plane aligns with the x-axis. The orientations about the x-, y- and z-axes are roll (α), pitch (β), and yaw (γ), respectively.

- The origin of the hook-fixed coordinate system $\mathbf{o}_h$ is located at the lower block COG, which is assumed to be located in the centre of the lower block. At $t = 0$, the axis orientation align with the global axis system. The Translational velocities in x^h-,y^h- and z^h-direction are given by u^h, v^h and w^h, while the angular velocities about the x^h-, y^h-, and z^h-axes are p^h, q^h, and r^h,
- The blade and blade yoke are modelled as a single body. The origin of the blade-fixed coordinate system $\mathbf{o}_b$ is located at the blade COG. The blade (and yoke) COG is located at the centre of the yoke, positioned directly under the lower block along the z_h-axis at $t = 0$. At $t = 0$, the z^b -axis is pointed upwards parallel to the global z-axis, regardless of the blade rotation around the y^b -axis (blade pitch) within the blade yoke. The y^b-axis runs along the length of the blade along the blade centreline. The centreline of the blade aligns with the blade yoke and intersects the yoke COG (the centreline of the blade yoke and the blade are coincident). The Translational velocities in x^b-,y^b- and z^b-direction are given by u, v and w, while the angular velocities about the x^b-, y^b-, and z^b-axes are p, q, and r,

As an example of how the actuation methods operate within the defined coordinate systems, the UQC allows for rotation of the blade (yoke) relative to the hook-fixed coordinate system along the z^b-axis, while the XY-table allows for translate of the blade (yoke) along the x^b- and y^b-axis, as indicated in figure 2.7b and figure 2.7a respectively.

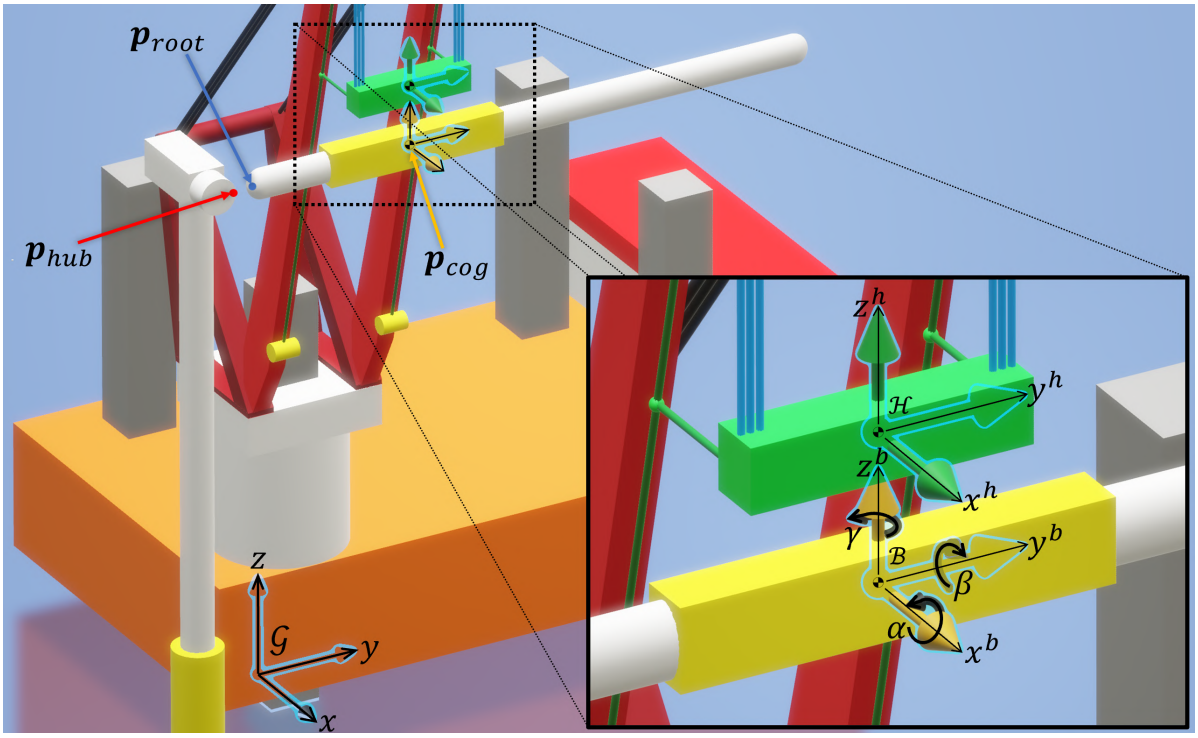

Figure 2.5: Overview of the SBIS, showing the orientation of the global, hook-fixed and blade-fixed coordinate system

Table 2.4: Denotation of the positions and velocities in their corresponding frames

Frame	Origin	Position[1]	Orientation $\mathcal{N}$	Translational vel.	Rotational velocity
$\mathcal{G}$	$\mathbf{o}_g$	$\boldsymbol{p} = [x, y, z]^\intercal$	–	$\boldsymbol{v} = [\dot{x}, \dot{y}, \dot{z}]^\intercal$	–
$\mathcal{H}$	$\mathbf{o}_h$	$\boldsymbol{p}^h = [x^h, y^h, z^h]^\intercal$	$\boldsymbol{\theta}_h = [\alpha_h, \beta_h, \gamma_h]^\intercal$	$\boldsymbol{v}_h = [u_h, v_h, w_h]^\intercal$	$\boldsymbol{\omega}_h = [p_h, q_h, r_h]^\intercal$
$\mathcal{B}$	$\mathbf{o}_b$	$\boldsymbol{p}^b = [x^b, y^b, z^b]^\intercal$	$\boldsymbol{\theta}_b = [\alpha, \beta, \gamma]^\intercal$	$\boldsymbol{v}_b = [u, v, w]^\intercal$	$\boldsymbol{\omega}_b = [p, q, r]$

[1] in corresponding frame

Table 2.5: Actuation method (AM) overview

AM	2D plane[1]	Actuated DOF	Actuator type
XY table	XY	T_x^b, T_y^b	Hydraulic Cylinder
UQC	XY	R_z^b	Motor-Gearbox
Vanes	XY	R_z^b	Motor-Gearbox
Gyroscopes	YZ	R_x^b	Motor-Gearbox
COG shifting	YZ	R_x^b	Hydraulic Cylinder

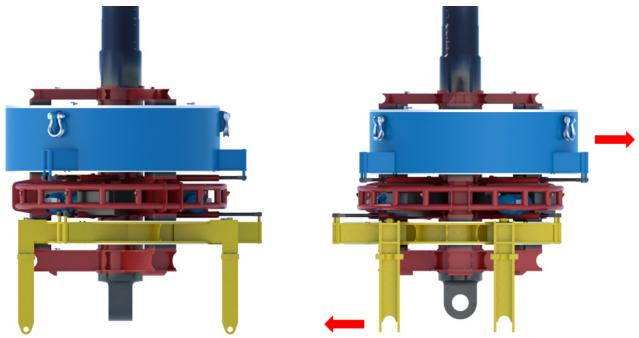

Figure 2.6: Side view of the XY table, showing the working principle behind the XY table actuation method

2.4. Actuation methods

This section introduces the actuation methods along with their working principle. The purpose of the actuation methods is to achieve control over the position of the blade root. Each actuation method utilizes a different approach to achieve this, and operates within a specific DOF. As explained in section 1.5, to allow for comparison of the individual concepts, the actuation methods are first modelled within their respective operational plane. Table 2.5 summarizes the operational plane, the actuated DOF, and the type of actuator used within each of the actuation methods. Here T_n^b stand for translation, and R_n^b for rotation in direction n within the blade-fixed coordinate system.

2.4.1. XY table

The XY table is actually a combination of two XY tables. The system itself is directly connected to the lower block using the Huisman UQC system. The first table is situated between the XY system frame, which is rigidly connected to the lower block, and the blade yoke. This table and allows for the translation of the blade yoke, and thus the blade, relative to the lower block.

The second table is situated between the frame and the counterweight. This counterweight, with a mass equal to the combined weight of the blade and blade yoke, is translated opposite to the blade. This way, the overall centre of mass does not change, and inertial loads cancel out. This working principle is visualized in figure 2.6. The integration of the XY table actuation method inside the SBIS is shown in figure 2.7a. Hydraulic cylinders are used to actuate the two XY tables. The cylinder positions are controlled to translate the blade relative to the lower block.

[1] Operational 2D plane in which actuation method is modelled (see chapter 4)

Table 2.6: XY table parameters

Symbol	Value	Unit	Description
W_{xy}	4.5	[m]	XY table width
H_{xy}	7.2	[m]	XY table total tool height (incl. pin)
M_{xy}	87e3	[kg]	Tool mass (excl. counterweight)
M_{cw}	125e3	[kg]	Counterweight mass
F_{max}	100	[kN]	Maximum actuation force
D_{max}	0.5	[m]	Cylinder stroke length

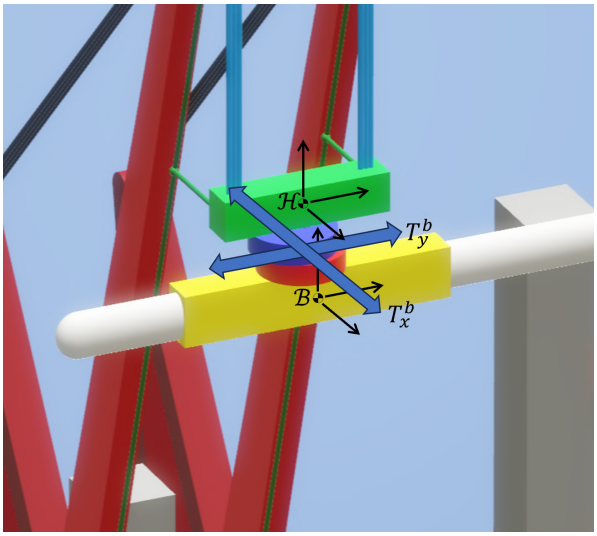

(a) AM1: XY table with counterweight

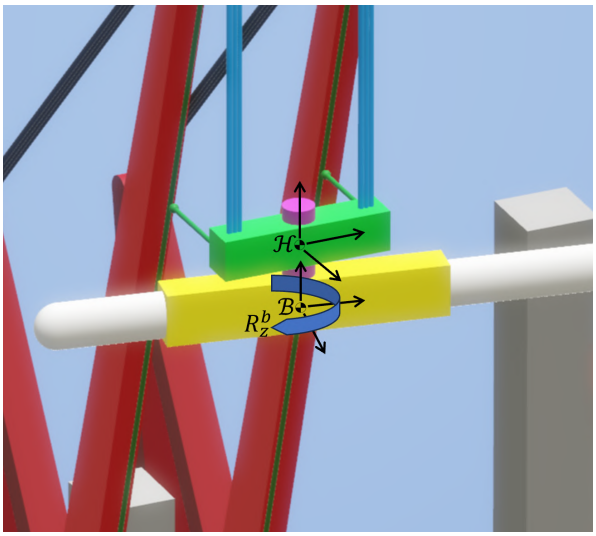

(b) AM2: UQC power swivel

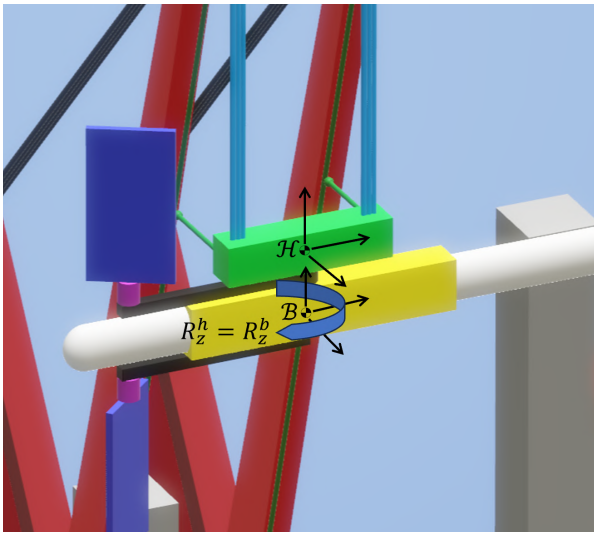

(c) AM3: Wind vanes

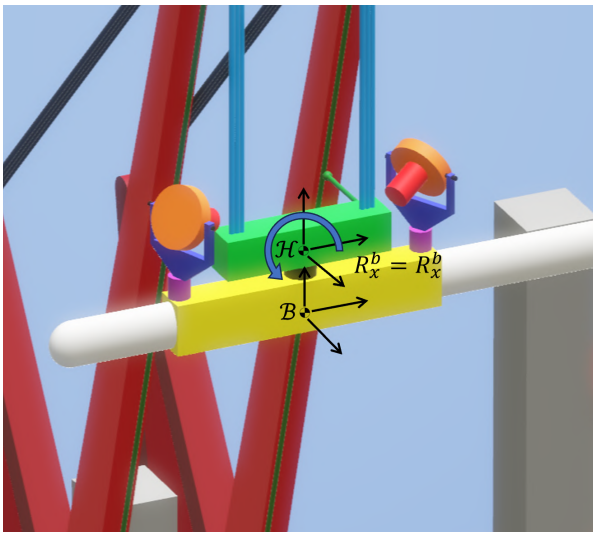

(d) AM4: Gyroscopes

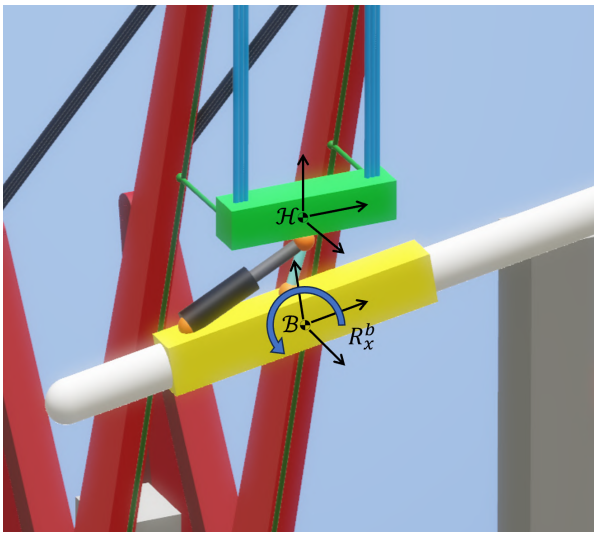

(e) AM5: COG shifting

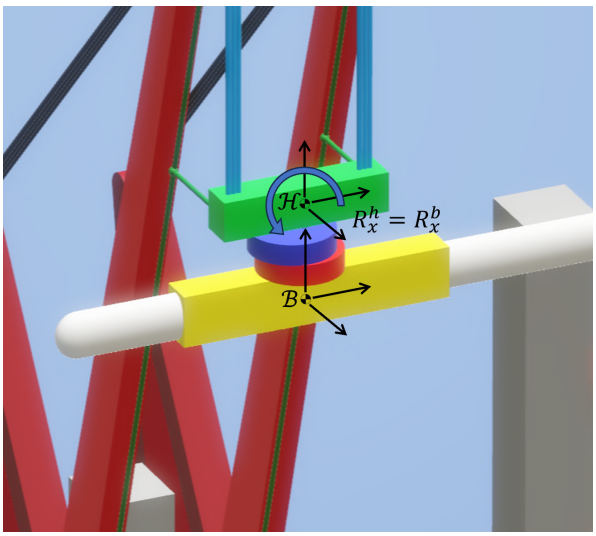

(f) AM5B: COG shifting with counterweight

Figure 2.7: Schematic models of the actuation methods considered in the study (not to scale)

Table 2.7: Wind vanes and gyroscope main parameters

Symbol	Value	Unit	Description
W_v	7	[m]	Vane width
H_v	6	[m]	Vane height
r_v	20	[m]	Vane offset (from blade COG)
R_{gy}	1	[m]	Gyroscope radius
T_{gy}	1.2	[m]	Gyroscope thickness
ω_s	400	[rmp]	Gyroscope spin speed
M_{gy}	29.6e3	[kg]	Gyroscope mass

2.4.2. Power swivel

The power swivel rotates the load about the z-axis, as shown in figure 2.7b. The moment exerted by the power swivel on the load results in an equal and opposite moment on the lower block. This moment is transferred to the crane by the hoist cables. This twisting action on the main hoist cables is an inherent side effect of a power swivel. The maximum moment that can be generated by the power swivel is limited either by the moment required to twist the main hoist wires, the maximum moment that can be transferred through the friction coupling or the available motor power. The technical specification of the power swivel drive system are summarized in table 3.2. The moment that can be transferred through the slip coupling is given by equation (2.4). For a maximum allowable lower block rotation of $45°$, the required moment is given by equation (2.6), where W_{lb} is the lower block width, L_{mh} the hoist wire length and M_{tot} the suspended mass.

$$m_{all} = \frac{M_{tot} g W_{lb}^2}{4 L_{mh}} \cdot 45° \tag{2.6}$$

2.4.3. Wind vanes

When lifting the blade, the COG serves as the lifting point, while the wind acts on the COP. Since the COG and COP are not located at the same point, a moment around the z-axis is always present. To counteract this moment, a vane is attached to the blade yoke. The yoke itself is rigidly attached to the lower block using the locked UQC. An overview of the resulting system is shown in figure 2.7c. The vane is a flat plate and is rotated by a servo motor. By adjusting the angle of the vane, the drag it generates changes, enabling control over the resulting moment on the blade yoke. The objective is to match the wind-induced moment on the blade. To maximize the moment generated by the vane drag, it is positioned far from the blade (yoke) COG. The offset between the vane mounting point and the blade COG is given by r_v. The main parameters for the wind vanes are summarized in table 2.7. In addition to drag, the vanes also generate lift and a turning moment. To minimize undesired loads on the blade yoke, two vanes are used. Both vanes are rotated the same amount but in opposite directions to balance the forces and moments, reducing unwanted loads on the blade yoke.

2.4.4. Gyroscopes

Gyroscopes are attached to the blade yoke as shown in figure 2.7d. The yoke remains rigidly attached to the lower block using the UQC. The gyroscopes are spun up around their spin axis, aligned with the y^h-axis. The gyroscope is rotated perpendicular to the spin axis, around the precession axis. The precession axis is aligned with the z^h-axis. Rotation around the precession axis, denoted by θ_{gy}, results in a moment about the axis perpendicular to the spin and precession axes. This is utilized to accelerate the yoke around the x^h-axis. As seen in equation (2.7), the moment generated by the gyroscope is a function of the precession velocity, the gyroscope's angular momentum (H_s) and the precession angle. As the precession angle increases, the moment generated around the desired axis decreases. This means that beyond a certain point, further precession will not provide the desired acceleration. Gyroscopes cannot sustain a constant moment, due to this limitation [39]. Two gyroscopes with opposing spin direction are used to minimize undesired loads. These gyroscopes are rotated by the same amount but in opposite directions. In this configuration, the gyroscopes solely generate a moment around the desired axis, while other contributions cancel out [39].

$$M_{gy} = \dot{\theta}_{gy} H_s \cos\theta_{gy} \tag{2.7}$$

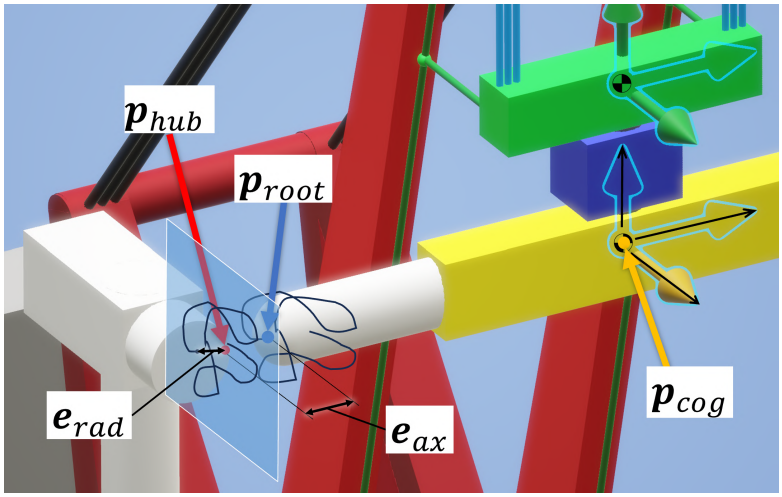

Figure 2.8: Projection of blade root motion on the XZ-plane

2.4.5. COG shifting

The COG shifting actuation method shares similarities with the first actuation method, as it works by translating the blade yoke relative to the lower block. However, in the case of COG shifting, there is no movement of a counterweight in the opposite direction. Therefore, the centre of gravity shifts, resulting in a moment. This causes the load to rotate until the COG is again located directly under the main hoist pickup point. Two variants of the COG shifting actuation method are considered, the first is shown in figure 2.7e. Here, a hydraulic cylinder is attached to the blade yoke, which is used to shift the pickup point of the blade yoke to the lower block.

Alternatively, a counterweight can be used to shift the COG. This has the advantage that the blade itself does not need to be shifted, as the counterweight provides the offset COG. However, the added weight from the counterweight can be considered a downside of this variant. Due to the rigid connection between the blade yoke and the lower block provided by the UQC, shifting the COG will result in a combined rotation of the blade yoke and the lower block. This is possible due to the finite stiffness of the main hoist cables. This variant on the COG shifting actuation method is shown in figure 2.7f. As with the XY table, actuation is achieved by hydraulic cylinders.

2.5. Assessment criteria

In this section, the assessment criteria used for comparison of the actuation methods are introduced. These focus on different aspects related to the installation process and the system performance of the hook mounted actuation methods. Collectively, the criteria provide an assessment of the accuracy, efficiency, and performance of the actuation methods during single-blade installation.

2.5.1. Blade root motion

For successful mating, the guide pin must be mated to the correct hole on the hub. Traditionally, up to 160 T-bolts are used to mount the blades to the hub. The longer the blades, the more T-bolts are required. However, as the blades increase in length, no more T-bolts can be used due to space limitations at the root. Therefore, a transition to bushing type bolts is expected. This type allows for 35% more bolts, but also requires higher accuracy during installation, as the bolt and holes are closer together. The use of bushings reduces the distance between the bolt studs from around 8 cm to 6 cm [7]. During alignment, the guide pin, at $\boldsymbol{p}_{root}$, should be as close to the centre of the mating hole, located at $\boldsymbol{p}_{hub}$. The offset between the two point projected on a plane in global XZ is called the radial root position error, and is formulated by equation (2.8). The XZ projection plane is shown in figure 2.8.

In addition to the radial position, the position of the blade root towards the hub is important. When the blade root suddenly moves towards the hub, it can lead to a collision between the root and the hub. The second assessment criterion defines this axial error between the guide pin at blade root ($\boldsymbol{p}_{root}$) and the mating hole at the hub, $\boldsymbol{p}_{hub}$, in the global y-direction, quantified by equation (2.9).

Verma *et al.* [8] simulated the dynamic response of an OWT blade and tower during single-blade installation for various environmental conditions. The resulting relative velocity between the blade root and hub were used to determine the impact damage for a collision between the blade root and hub. It is found that for a collision with a relative velocity above 0.63 m/s, damage is done to the blade root laminate, which could develop delamination cracks. This second criterion is the relative velocity between the blade root and hub, defined by equation (2.10). As the hub is assumed to be stationary, the expression simplifies to the magnitude of the root velocity.

The final criterion is defined as the blade's angle relative to the global y-axis, given by equation (2.11).

$$\boldsymbol{e}_{rad} = \left\| \boldsymbol{p}_{root,xz} - \boldsymbol{p}_{hub,xz} \right\| \tag{2.8}$$

$$\boldsymbol{e}_{ax} = \left\| \boldsymbol{p}_{root,y} - \boldsymbol{p}_{hub,y} \right\| \tag{2.9}$$

$$\boldsymbol{e}_{v} = \left\| \dot{\boldsymbol{p}}_{root} - \dot{\boldsymbol{p}}_{hub} \right\| = \left\| \dot{\boldsymbol{p}}_{root} \right\| \tag{2.10}$$

$$\boldsymbol{e}_{\angle} = \arccos \frac{\boldsymbol{a} \cdot \boldsymbol{b}}{|\boldsymbol{a}|\,|\boldsymbol{b}|} \tag{2.11}$$

$$\boldsymbol{a} = \frac{\boldsymbol{p}_{root} - \boldsymbol{p}_{cog}}{\left\| \boldsymbol{p}_{root} - \boldsymbol{p}_{cog} \right\|} \qquad \boldsymbol{b} = [0, -1, 0] \tag{2.12}$$

2.5.2. Actuator effort

The average actuator power consumption impacts the lifetime of the battery pack. Maximizing the time between battery swaps is desirable, which means minimizing the average actuator power consumption is important to extend the operation time. The actuator power consumption is calculated using equation (2.13), where the force F and torque T are the actuator effort applied by the actuator, while v and ω are the actuator translational or rotational velocity, respectively. The actuator effort provides an indication of the required size and capacity of the actuators within the system. Larger actuators tend to be heavier, more expensive, and draw more power. By analysing the maximum actuator effort, appropriate sizing and specifications of the actuators can be determined.

$$P = Fv = T\omega \tag{2.13}$$

2.6. Summary

This chapter provides further information to support the modelling in the following chapters. The focus is on SQ1 to SQ3. Furthermore, the basic coordinate systems and conventions are introduced, together with the actuation methods and their working principle. Based on the information provided in this chapter, SQ1 to SQ3 can be answered as follows.

SQ1: What is the state of the art of motion compensation for single-blade offshore wind turbine installation? Motion compensation can be applied in four different locations, with 3D MCC and load stabilization being particularly important for single-blade installation using a jack-up vessel. 3D MCCs can play a significant role in advancements in installation techniques. However, the achievable accuracy of the 3D MCC alone is not sufficient for installing turbine blades without additional load stabilization solutions such as an HMC.

SQ2: What are the operational requirements, environmental conditions, and disturbances encountered during single-blade installation using the HMC actuation methods? This study considers the alignment phase, where the blade is suspended and aligned with the hub but not yet connected to it. The blade must eventually be placed with an accuracy of 6 to 8 centimetres. The turbine considered is the IEA 15 MW reference turbine, installed with a 3200 mt LEC crane equipped with the Huisman UQC and tugger lines on a jack-up vessel. The wind disturbance is described by the NTM as specified in the IEC 61400-1 standard. Wind boxes for various wind speeds and TIs are generated in TurbSim.

SQ3: How can KPIs be defined to characterize the effectiveness of the HMC actuation methods? Two criteria categories are defined. The first and most important one is compensation effectiveness, which includes the radial and axial positional error of the blade root, the blade root velocity, and the blade angle. Additionally, the actuator input power and effort are considered, which indicates how long the system can operate on a battery, and provide an estimate on the required actuator size.

3

Linear modelling

The actuation methods require a form of control for later simulation in the time domain in chapter 4. This chapter describes the development of a simplified single DOF linear analytical model for each actuation method. Here, DOF refers to the mechanical DOF. The models enable initial analysis of the system in the frequency domain and is used to design linear controllers.

Each actuation method is implemented within the same crane, lower block and blade (yoke), introduced in the previous chapter. However, each actuation method has its own working principle, which effects the behaviour of the overall SBIS. The SBIS is the combination of the crane, lower block, blade (yoke) and actuation method. As the actuation methods significantly affect the behaviour of the SBIS, each actuation method requires a separate linear controller. The controller for each actuation method however uses the same system output, namely the blade root position. Moreover, all controllers use the same reference position, which is the mounting location on the hub. A generalized control diagram is provided in figure 3.1. Here, $[\boldsymbol{r}]$ is the reference root position, given by $\boldsymbol{p}_{hub}$. $[\boldsymbol{y}]$ is system output, in this case the blade root position, $\boldsymbol{p}_{root}$. $[\boldsymbol{e}]$ is the error between the reference and actual root position. Finally, $[\boldsymbol{u}]$ is the control input to the SBIS, and $[\boldsymbol{d}]$ is the wind disturbance, acting on the blade.

To ensure a fair comparison, the controllers are developed using a standardized process. PID controllers are formulated for each of the actuation methods based on the linear analytical model, and are all designed towards the same gain and phase margin. The resulting Bandwidth (BW) depends on the working principle, dynamics, and system parameters for the actuation method used. An overview of the methodology used to develop the linear models and controllers is provided below.

1. **Model generation:** In the first part of this chapter, linear models are first generated for the actuation methods according to the following three steps:

   (a) **Decomposition:** The first step is to decompose the continuous structure present in the SBIS (including the actuation method) into separate rigid bodies. This involves dividing the system into various representative masses, springs, and dampers that describe the SBIS. As only one mechanical DOF is considered, each rigid body i with mass M_i has a single generalized coordinate x_i, which represent the displacement from its equilibrium position. The number of generalized coordinates per model is equal to the number of separate bodies required to describe the system, and varies from 3 to 5, depending on the actuation method.

   (b) **Obtaining Equations of motion:** In the next step, the Euler-Lagrange method is used to convert the mass-spring-damper system into a set of Equations of Motion (EOM). Euler-lagrange is a mathematical technique used to derive the EOM from the system Lagrangian, Rayleigh's dissipation function and the generalized external forces (Q_i). The Lagrangian is given by equation (3.1), and is a function of all the body kinetic energy terms (T) and spring potential energy terms (V), expressed within the generalized coordinates x_i. Here $\dot{x}_i$ is the derivative of the generalized coordinate for body i with mass M_i with respect to time, and d_j is the displacement of a spring or damper j, expressed in the generalized coordinates of the body/bodies between which it is located. For instance, the displacement of a spring positioned between the two bodies 1 and 2 is given by $d = x_1 - x_2$. Rayleigh's dissipation function is given by equation (3.2), which accounts for the dissipation of energy through damping. The equations of motion are found separately for each generalized coordinate by evaluating the Euler-Lagrance equation provided in equation (3.3).

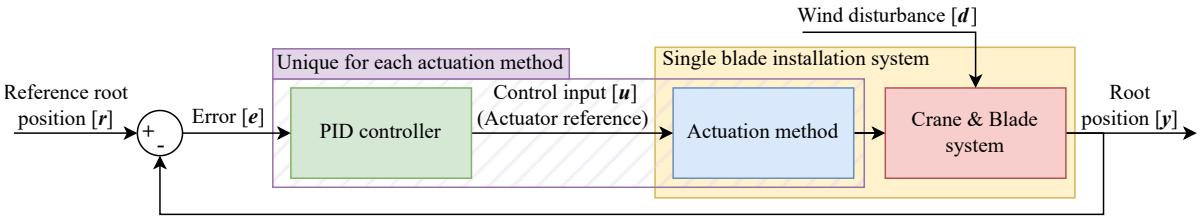

Figure 3.1: General control diagram for the SBIS with actuation method and linear controller.

$$L(x_i, \dot{x}_i, t) = T - V = \sum_{i=1}^{n} \frac{1}{2} M_i \dot{x}_i^2 - \sum_{j=1}^{m} \frac{1}{2} k_j d_j^2 \tag{3.1}$$

$$D(\dot{x}_i, t) = D = \sum_{j=1}^{m} \frac{1}{2} c_j \dot{d}_j^2 \tag{3.2}$$

$$\frac{d}{dt}\left(\frac{\delta L}{\delta \dot{x}_i}\right) - \frac{\delta L}{\delta x_i} + \frac{\delta D}{\delta \dot{x}_i} = Q_i \tag{3.3}$$

(c) **State space representation:** From the equations of motion, a state-space model is derived. Having the model in state space form allows for the further analysis of the system. The state space system is given by equation (3.4). Here $\boldsymbol{x}(t)$ is the state-vector, which contains the state and derivate of all the system's generalized coordinates. $\boldsymbol{u}(t)$ is the input vector containing all the system inputs. In the full model, the input vector contains both the control input [$\boldsymbol{u}$] and wind disturbance [$\boldsymbol{d}$] from the control diagram presented in figure 3.1. However, during the analysis and control design, the main interest is the behaviour of the system as a result of the control input, the so-called reference tracking performance. During the bode analysis, the disturbance is omitted from the input vector and $\boldsymbol{u}(t)$=[$\boldsymbol{u}$]. $\boldsymbol{y}(t)$ is the output vector containing the outputs of the system. The output vector contains the generalized coordinate corresponding with the blade root position, donated by x_b. $\boldsymbol{A}, \boldsymbol{B}, \boldsymbol{C}, \boldsymbol{D}$ are the state matrix, input matrix, output matrix and feed-through matrix, respectively.

$$\dot{\boldsymbol{x}}(t) = \boldsymbol{A}\boldsymbol{x}(t) + \boldsymbol{B}\boldsymbol{u}(t) \tag{3.4}$$

$$\boldsymbol{y}(t) = \boldsymbol{C}\boldsymbol{x}(t) + \boldsymbol{D}\boldsymbol{u}(t) \tag{3.5}$$

2. **Bode analysis:** In the second part of this chapter, the linear actuation methods models are analysed in the frequency domain and a PID controller is proposed for each actuation method.

   (a) **Hautus Lemma Test:** The Hautus Lemma Test is first used to assess the observability, stabilisability, and controllability of the states of interest in the system. In this case, the states of interest are the blade position (x_b) and velocity ($\dot{x}_b$). The Hautus Lemma Test is used to determine whether these states can be effectively controlled within the system. The location of the system poles are assessed to ensure all system poles lie in the left-half plane, which allows for further analysis of the system using Bode plots.

   (b) **Controller design:** A PID controller is proposed based on the open-loop system response to achieve a minimal gain margin of 6 dB and a phase margin of 60 degrees. The allowable controller phase and gain margin are based on a Huisman rule of thumb. The Bode analysis is used to assess the stability and performance of the system for the proposed PID controller.

The sub-question addressed in this chapter are:

SQ4: How can the single-blade installation systems for the actuation methods be described linearly?

SQ5: How can the actuated single-blade installation systems be controlled?

3.1. Assumptions & Simplifications

As no physical product exist for the considered actuation methods, this study relies on modelling and simulation of the systems for analysis and assessment. To simplify the analysis, several assumptions are made concerning the disturbances, modelling, and environmental conditions. The assumptions allow for simplified modelling and analysis, but may not fully capture all the complexities and real-world conditions. The main modelling assumptions and limitations are listed below:

1. **Neglecting Wave and Current Loading:** This study focuses solely on wind disturbances and does not consider the effects of wave and current loading. As discussed in section 1.3, wave and currents introduce additional dynamic forces and moments on the various parts of the system. These effects are however neglected.
2. **Neglecting Payload Dynamics:** The payload is relatively lightweight in comparison to the crane's weight and the ship's weight, so the dynamics of the payload do not significantly affect the ship's dynamics. Therefore, the effects of the suspended load and crane motions on the ship are neglected.
3. **Fixed Vessel:** Based on the previous two simplifications, the ship is approximated as a rigid structure, fixed to the seafloor.
4. **Simplified Modelling of Boom:** The crane boom dynamics are simplified as a rigid body at the crane tip. The effective mass and stiffness are calculated in section 3.2. For determining the effective mass and stiffness, the crane boom is simplified as a thin rigid rod that can rotate about the boom hinge along the y-axis. Only the first flexible modes of the boom in the transverse (y) direction is considered, and small angles are assumed.
5. **Linear Deformations:** The crane and wire ropes are assumed to deform linearly. The main hoist bundles are modelled as a single linear tensile springs with damping. The tugger lines are also modelled as linear tensile springs with viscous damping. The own weight of all wire ropes and wire rope bending stiffness is neglected.
6. **Constant and Viscous Friction:** Friction is assumed to be viscous and constant.
7. **Mechanical Feasibility:** The systems are assumed to be mechanically feasible, meaning they are physically realizable without violating any mechanical constraints.
8. **Full State Feedback and No Sensor Delay:** In reality, the system states need to be measured. The measured signals are often processed by an observer to reduce the effect of sensor noise, estimate unmeasured states based on the measurement, or even predict the system state shortly into the future. The sensors and observer design fall outside the scope of this study. All states are assumed to be measurable without any sensor noise or delay.
9. **Ideal Hydraulics:** The hydraulic systems are assumed to use ideal fluids with constant density and matched inlet and output port and valve sizes. Cavitation of the hydraulic fluid is also not considered.
10. **Simplified Gear Box:** The gear box is assumed to consist of a single stage. The inertia of the motor and gearbox is assumed to be dominated by the motor inertia felt at the output shaft. The stiffness of the gearbox results in a 0.01 rad rotation on the output shaft under nominal loading.
11. **Neglecting Tower Dynamics:** The turbine tower is not modelled. The motion of the nacelle-hub assembly due to wind and wave disturbances is neglected. The hub is treated as a fixed point within the global reference frame denoted by $\boldsymbol{p}_{hub}$.
12. **Simplified Blade Modelling** The blade and blade yoke are simplified as a single rigid body with a combined centre of gravity located at the blade's CoG. Blade deformations are neglected, and the blade is modelled as a rigid straight blade without prebend.
13. **Cross-Flow Principle for Aerodynamic Loads:** The cross-flow principle is used to calculate the aerodynamic loads on the blade sections. Only the wind velocity perpendicular to the blade section is used for calculating the aerodynamic loading on the blade.

3.2. Crane dynamics

The actuation methods are part of the overall SBIS. The system consists of various components, including the crane, the lower block, the suspended blade and actuators. The wind induced loads and inertial loads from the mass suspended by the crane result in reaction forces on the crane. For the analysis of the actuation methods, the crane dynamics can not be neglected. However, to reduce model complexity, the dynamics of the crane are simplified.

3.2.1. Crane boom stiffness and equivalent mass

The crane boom is modelled as a rigid body point with equivalent mass and stiffness. The stiffness of the crane in the x- and z-direction is assumed to be dominated by the stiffness of the boom hoists. The crane stiffness for the other directions is dominated by the stiffness of the crane boom itself. The crane boom stiffnesses in all 6DOF are known from a Finite Element Analysis (FEA).

Translation *x* and *z* direction

For calculation of the equivalent mass, inertia, and stiffness in the x- and z-direction, the crane boom is approximated as a rigid thin rod with a constant mass density, total mass M_{bm} and a length of L_{bm}. The boom head is modelled as a point mass at the end of the boom. A schematic of the simplified crane boom is provided in figure 3.2a. The simplification of the boom to a rigid thin rod allows for a simplified implementation of the tugger lines in the models, without neglecting the feedback from the tugger on the crane itself.

The inertia of the boom around the crane hinge is the sum of the inertia of the rigid thin rod, and the inertia of the boom head. The total inertia felt around the boom hinge is given by equation (3.6). The equivalent mass felt at distance d_{eq} as a result of the boom inertia around the hinge is given by equation (3.7). This is used to determine the equivalent mass for the crane in both the x- and z-direction.

$$I_{hinge} = \frac{1}{3} M_{bm} L_{bm}^2 + M_{bmh} L_{bm}^2 \tag{3.6}$$

$$M_{eq} = \frac{I}{d_{eq}^2} \tag{3.7}$$

The stiffness in x- and z-direction is calculated from the boom hoist stiffness. The total boom hoist stiffness is the sum of all boom hoist wire ropes stiffnesses. For the reference crane, the total number of boom hoist wire ropes is 22. The length of the boom hoist in the reference position is given by L_{bh}. The boom hoist stiffness is calculated using equation (3.8). For small displacements, the crane stiffnesses in x- and z-direction is approximated by equations (3.9) and (3.10).

$$k_{bh} = \frac{N_{falls} k_{ax,bh}}{L_{bh}} \tag{3.8}$$

$$k_{c,x} = k_{bh} \sin(\theta_{bm} - \theta_{bh}) \tag{3.9}$$

$$k_{c,z} = k_{bh} \cos(\theta_{bm} - \theta_{bh}) \tag{3.10}$$

Translation *y* direction

For the transverse direction, the boom hinge acts as a fixed constraint, as shown in figure 3.2b. For this configuration, the equivalent mass is given as

$$M_{eq} = \frac{33}{140} M_{bm} + M_{bmh}. \tag{3.11}$$

Rotation around *z*

From the FEA analysis, it is learned that the rotational stiffness of the boom at the tip along the polar axis of the boom is much lower than the stiffness in the other directions. It is assumed that a moment around the global z-axis at the crane tip acts only along the polar axis of the boom, as the deformation of the boom is dominated by the twisting of the boom around its polar axis. Due to the offset angle of the boom relative to the global z-axis, part of a moment around the global z would instead be transferred

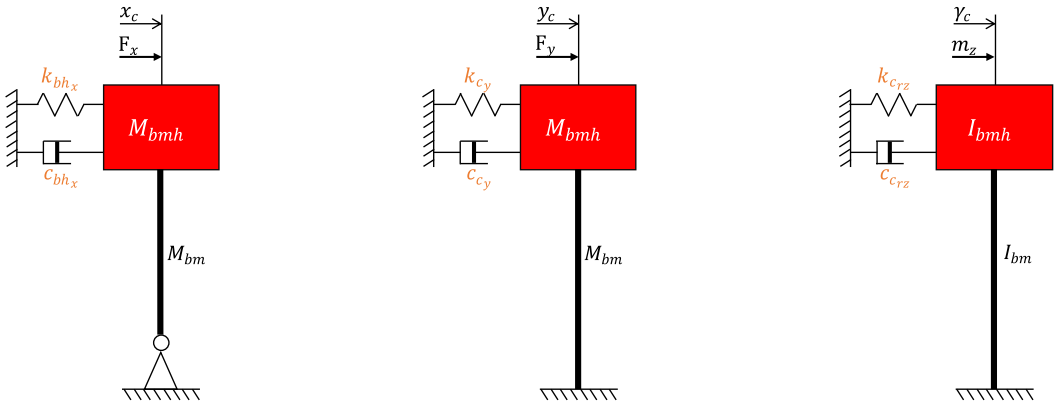

(a) x direction **(b)** y direction **(c)** Around polar axis

Figure 3.2: Schematics of simplified boom dynamics in x, y and rotation around the polar axis (about z-axis)

to a contribution around the global x-axis. This contribution is however neglected in this approximation. The equivalent polar mass moment of inertia of the clamped boom with tip mass M_{bmh} is given as

$$J_{eq} = \frac{1}{3} J_{bm} + J_{bmh}, \tag{3.12}$$

where J_{bm} and J_{bmh} are the polar mass moment of inertia of the boom and boom head, calculated as

$$J_{bm} = \frac{M_{bm}}{12} \left(W_{bm}^2 + H_{bm}^2 \right), \tag{3.13}$$

$$J_{bmh} = \frac{M_{bmh}}{12} \left(W_{bmh}^2 + H_{bmh}^2 \right). \tag{3.14}$$

Rotation around *x* and *y*

The equivalent inertia at the tip around the global x- and y-axis is approximated from the first natural frequency ω_n of the boom in the corresponding degree of freedom using equation (3.15).

$$\omega_n = \sqrt{\frac{k}{I_{eq}}} \rightarrow I_{eq} = \frac{k}{\omega_n^2} \tag{3.15}$$

Pendulum restoring force

Finally, the pendulum restoring force is represented as a spring with spring constant given by equation (3.16), where g is the gravitational acceleration, M_{tot} is the total mass of the suspended load at the end of the main hoist cable with length L_{mh}.

$$k_l = \frac{M_{tot} g}{L_{mh}} \tag{3.16}$$

3.3. Actuator dynamics

The actuation methods utilize hydraulic cylinders and hydraulic or electric motors to actuate the blade in their associated actuated DOF. The behaviour of these actuators is complex and can exhibit strong non-linear behaviour. However, these actuator dynamics are not the focus of this study; rather, it is the behaviour of the SBIS as a result of the implementation of the actuation methods in which the actuators are used. Nevertheless, the actuators cannot be fully ignored, because the performance of the system is also dependent on the behaviour of the actuators. Therefore, simplified actuator dynamics are included in the model.

The XY table (AM1) and COG shifting (AM5) actuation methods use hydraulic cylinders for actuation, while the other actuation methods utilize an electric motor with gearbox. In the following subsections, linearized sub-models for the actuators are presented, and the internal actuation dynamics are simplified. These sub-models are applied within the linear models of the actuation methods.

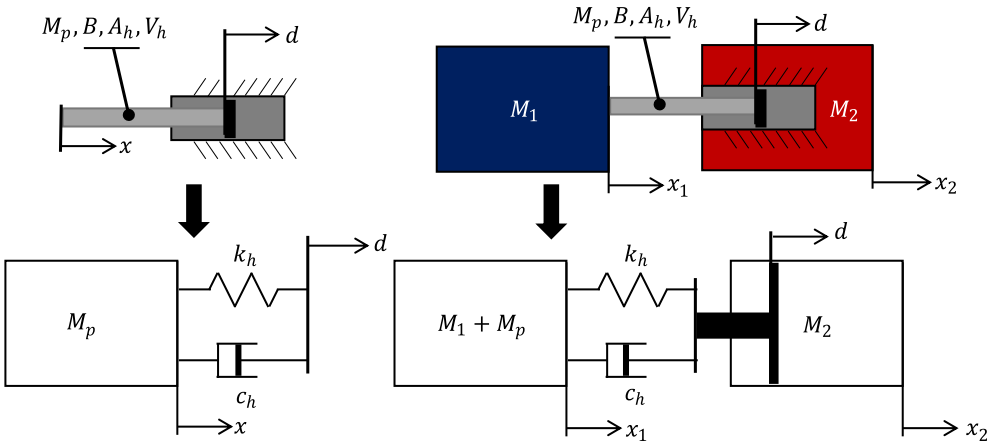

Figure 3.3: sub-models of a single hydraulic actuator, and a hydraulic actuator placed between two masses

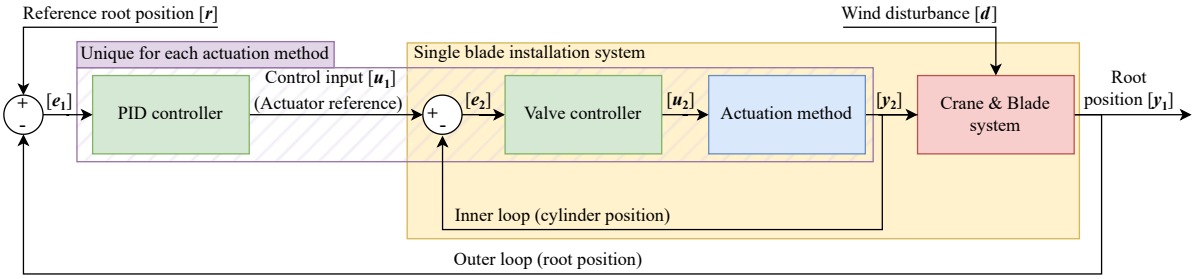

Figure 3.4: Control diagram for the SBIS with servo valve controller

3.3.1. Hydraulic cylinder

A block diagram of the simplified hydraulic actuator used in the subsequent model is given in figure 3.3. The piston has a mass M_p and an internal stiffness and damping, denoted by k_h and c_h. The stroke of the cylinder is given by d and is used as input for the model.

Dynamic response

The outer controller in figure 3.1 provides a control input [$\boldsymbol{u}_1$] to the single blade installation system. In the case of the XY table (AM1) and COG shifting (AM5), this input is a reference cylinder position, d^{ref}. This reference does however not directly correspond with the actual cylinder position, d.

Movement of a hydraulic piston is the result of a differential pressure between the two sides of the cylinder piston. This pressure differential is created using a servo valve. This servo valve typically has its own internal controller, which uses the reference cylinder position [$\boldsymbol{u}_1$] and the actual cylinder position [y2] to control the valve position. This valve position is controlled to generate the desired differential pressure, and thus eventually move the cylinder to the desired reference position. A control diagram of the system is provided in figure 3.4.

The internal dynamics of the servo valve and valve control loop are not modelled. Instead, it is assumed that the servo valve with applied internal controller behaves as an over damped system, simplified as a first order linear low pass filter with a bandwidth of 5Hz. This is the bandwidth for a typical hydraulic servo valve [40]. The transfer function that describes the assumed behaviour is given in equation (3.17).

$$\frac{d\,(s)}{d^{ref}\,(s)} = \frac{1}{\tau s + 1} \tag{3.17}$$

Actuator stiffness

An expression for the hydraulic fluid stiffness of a hydraulic actuator, k_{hydr}, is found in equation (3.18), where B is the oil bulk modulus, A_1 and A_2 are the equivalent area of the head chamber and the rod chamber, V_1 and V_2 are the volume of the head chamber and the rod chamber, and V_{L1} and V_{L2} are the fluid line volume on the head chamber and on the rod chamber, respectively [41].

Table 3.1: Hydraulic cylinder parameters

Symbol	Value	Unit	Description
B	1.38e9	Pa	Fluid bulk modulus
E	210e9	Pa	Elastic modulus
A_h	5.0e-3	m^2	Cylinder internal cross-sectional area
V_h	4.5e-3	m^3	Total cylinder volume
A_p	2.8e-3	m^2	Effective piston area
L_p	0.9	m	Piston length

$$k_{hydr} = B \cdot \left(\frac{A_1^2}{V_1 + V_{L2}} + \frac{A_2^2}{V_2 + V_{L2}} \right) \tag{3.18}$$

The fluid stiffness of a hydraulic cylinder exhibits nonlinear behaviour, as the stiffness changes with piston position due to the changing volumes on both sides. The stiffness of a hydraulic actuator is minimum at its central position. To approximate the dynamics of the hydraulic cylinders used in the actuation methods, the stiffness of the cylinders is linearized around the central position, where the hydraulic stiffness is at its lowest. For a hydraulic cylinder with an equal fluid volume on both sides, and with equal piston area on both sides, the equation simplifies to

$$k_{hydr} = \frac{2BA_h^2}{V_h}. \tag{3.19}$$

Apart from the hydraulic fluid stiffness, the overall stiffness depends on the piston rod axial stiffness k_p. Furthermore, the cylinder barrel expansion, expansion of the fluid lines and deformation of the sealing ring affect the overall stiffness of the cylinder. However, in this model, only the hydraulic fluid stiffness and the piston axial stiffness are taken into account. The stiffness of the piston is given by equation (3.20). An expression for the overall hydraulic actuator stiffness is found in equation (3.21). The damping of the hydraulic actuator is given by equation (3.22).

$$k_p = \frac{EA_p}{L_p} \tag{3.20}$$

$$k_h = \frac{1}{\frac{1}{k_{hydr}} + \frac{1}{k_p}} \tag{3.21}$$

$$c_h = 2\zeta_h \sqrt{Mk_h} \tag{3.22}$$

The cylinder parameters are based on a conceptual XY table design developed internally at Huisman. The preliminary design specifies cylinders with a 0.5-meter stroke length, with a maximum actuation force of 100 kN. The parameters used in the models are summarized in table 3.1.

3.3.2. Motor drive with gearbox

A block diagram of the motor-gearbox system used in subsequent models is provided in figure 3.5. The gearbox has an inertia J_{gb}. The internal stiffness and damping of the gearbox are denoted by k_{gb} and c_{gb}. The rotational position of the gearbox, given as θ, is used as an input of the models.

Dynamic response

As was the case with the hydraulic cylinders, the actual motor position or velocity is controlled by an internal control loop. In the case of the UQC power swivel (AM2) and wind vanes (AM3), the outer controller in figure 3.6 provides a reference position, θ^{ref}, as a control input [$\boldsymbol{u}_1$]. In the case of the gyroscopes (AM4), the control input is a reference velocity, $\dot{\theta}^{ref}$.

As with the servo valve controller, the dynamics of the inner control loop are not directly included in the model. Instead, the behaviour is again simplified. Again, the controlled motor-gearbox system is assumed to behave as an over damped linear system, described using a first-order low-pass transfer function with time constant τ. The transfer function that describes the assumed behaviour is given by equation (3.23).

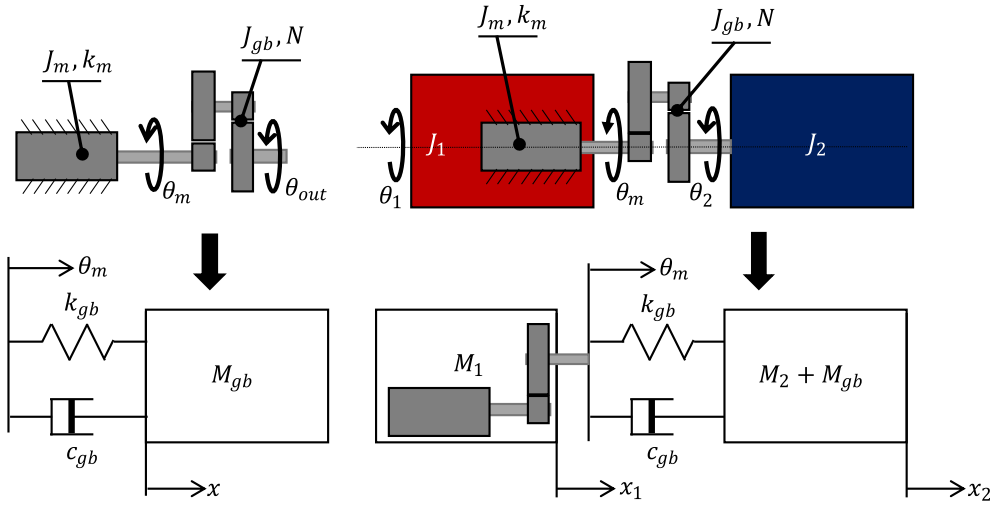

Figure 3.5: sub-models of a motor-gearbox system, and a motor-gearbox placed between two masses

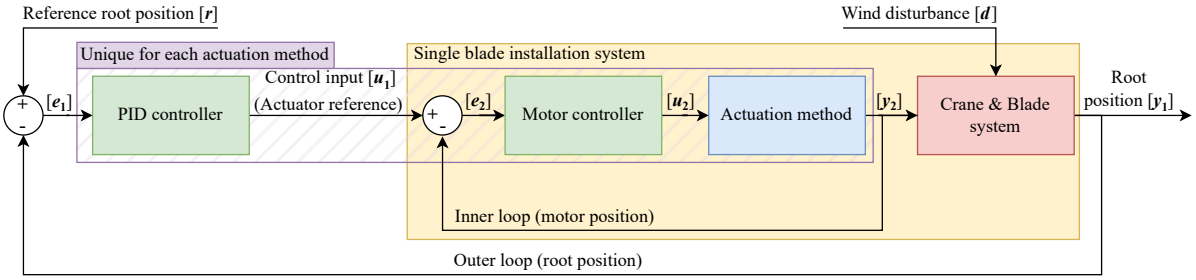

Figure 3.6: Control diagram for the SBIS with motor position controller

$$\frac{\theta_m(s)}{\theta_m^{ref}(s)} = \frac{1}{\tau s + 1} \tag{3.23}$$

The time constant that described the behaviour of the internal control loop depends on system properties, such as the motor size and inertia of the load. A suitable time constant thus needs to be determined for each actuation method that uses a motor-gearbox combination for actuation. An estimate for the response time is determined based on the control diagram provided in figure 3.6 for the vane, gyroscope, and power swivel actuation method in appendix B.

Actuator stiffness

The gearbox stiffness is estimated using the rule of thumb provided by equation (3.24), where the nominal output torque goes in hand with a 0.01 rad rotational deflection on the outgoing axis. The overall stiffness of the gearbox-motor assembly is given by equation (3.25). It is assumed that the inertia felt at the output shaft is the inertia of the motor at the input shaft, translated to the gearbox output shaft. For a single stage gearbox, this inertia at the output shaft is calculated using equation (3.26).

Table 3.2: UQC power swivel drive system parameters

Symbol	Value	Unit	Description
k_m	144e3	Nm/rad	Motor torsional stiffness
J_m	0.178	kg·m^2	Motor rotational inertia
N	123.5	-	Gear ratio
T_{nom}	150e3	Nm	Nominal output torque

$$k_{gb,nom} = \frac{T_{nom}\ [Nm]}{0.01\ [rad]} \tag{3.24}$$

$$k_{gb} = \frac{1}{\frac{1}{k_{gb,nom}} + \frac{1}{2k_m N}} \tag{3.25}$$

$$J_{gb} = 2J_m N^2. \tag{3.26}$$

The damping of the gearbox is given by equation (3.27). The damping ratio of the gearbox is assumed to be 5%. The gearbox and motor parameters used for calculating the gearbox stiffness are given in table 3.2. These are based on available Huisman UQC system information. As there is no system information available for the gyroscopes and vanes actuation methods, the same parameters are used here, as it is the expectation that actuators similar in size are required for these actuation methods.

$$c_{gb} = 2\zeta_{gb}\sqrt{Mk_{gb}} \tag{3.27}$$

3.4. Model generation

In this section, the linear, single DOF models are constructed. Each subsection presents a schematic of the SBIS with actuation method within the defined operational plane. Based on this, the three steps described earlier are followed for each actuation method, decomposition, obtaining Equations of motion and translating to the state space representation.

3.4.1. Suspended blade

A system overview of the SBIS without any actuation method is given in figure 3.7. The model could also be represented in the XY plane, however for visual aid during the construction of the model, and especially the tugger connection, the XZ plane is used for visualization. The system is discretized into three bodies, one representing the crane with mass M_c, one representing the lower block with mass M_{lb}, and finally the blade and blade yoke with representative mass M_{b^*}. The connection between the blade yoke and the lower block is provided by the quick connector in its locked position. This connection is assumed to have an infinite stiffness. The two bodies of the lower block and blade yoke can therefore be combined into a single body. The resulting mass-spring-damper system is shown in figure 3.8.

Tugger lines

Tugger lines run along the crane boom and provide a connection between the lower block and the crane boom. The tugger lines are placed under pretension by pulling the load towards the crane boom. The stiffness of the tugger lines is denoted by k_t, and is calculated using equation (3.28), where L_t is the total length of the tugger line, running along the boom.

$$k_t = k_{ax,t}/L_t \tag{3.28}$$

The tugger lines forces do not only act on the block, but also on the crane boom. The boom is modelled as a lever. For small displacements, equation (3.29) relates the displacement of the crane boom tip, and the tugger mounting locations. In all models, the tugger winches are kept at speed set point zero, which means that the rope feed rate is zero, and the tugger line ropes remain at constant length. The tension in the tugger line is not constant, as the tension can increase or decrease due to external loads.

$$x_t = \frac{L_1}{L_1 + L_2} x_c = \phi_t x_c \tag{3.29}$$

$$L_1 = H_c - H_{pd} - L_{mh} \tag{3.30}$$

$$L_2 = L_{mh} \tag{3.31}$$

The pendulum and crane stiffnesses k_l and k_c are calculated as described in section 3.2

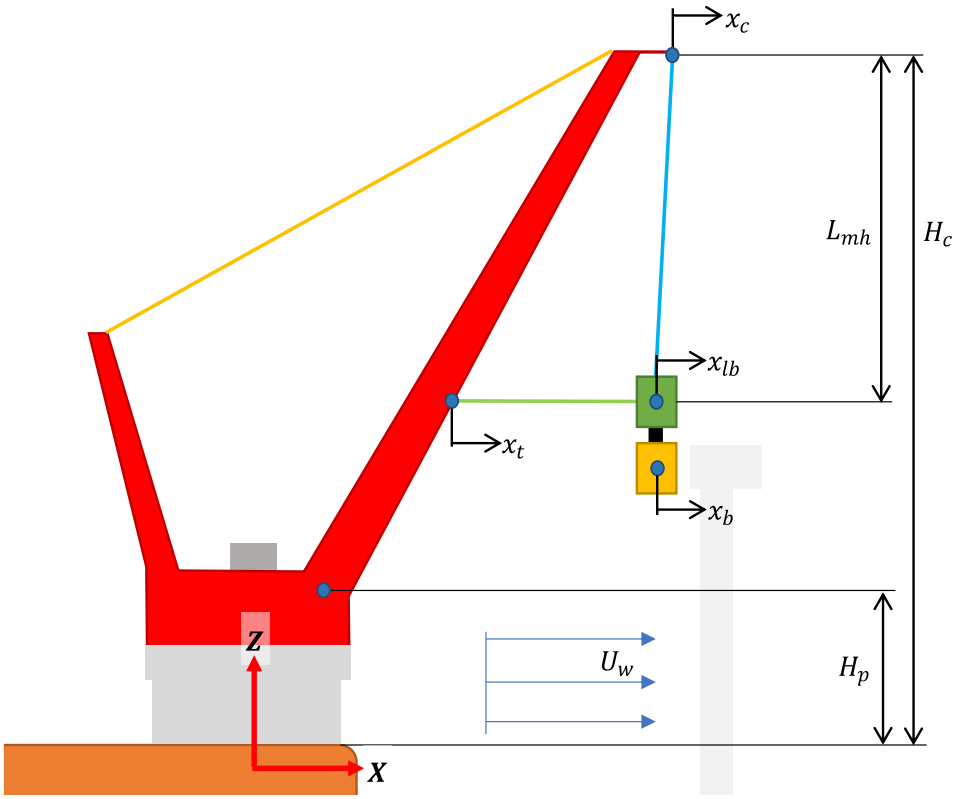

Figure 3.7: System overview of the OWT blade suspended from the main hoist wires (not to scale)

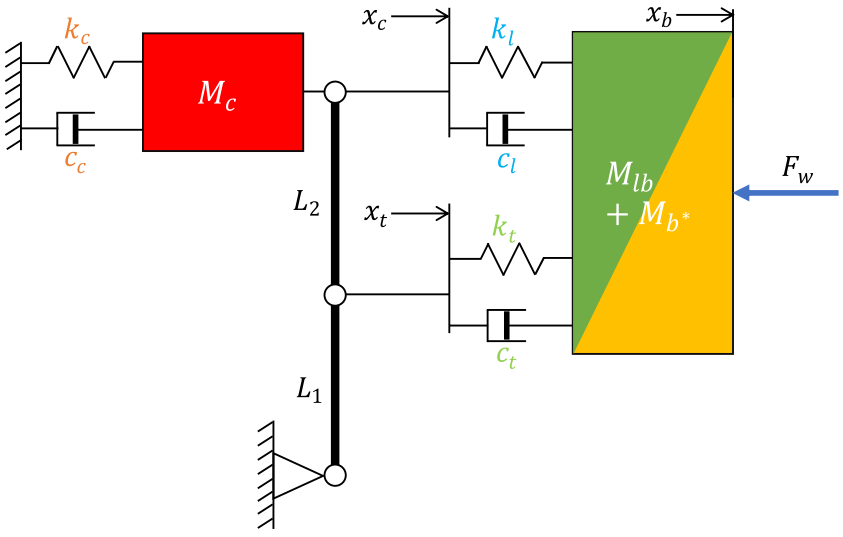

Figure 3.8: Single DOF discretized mass-spring-damper representation of the OWT blade suspended from the crane

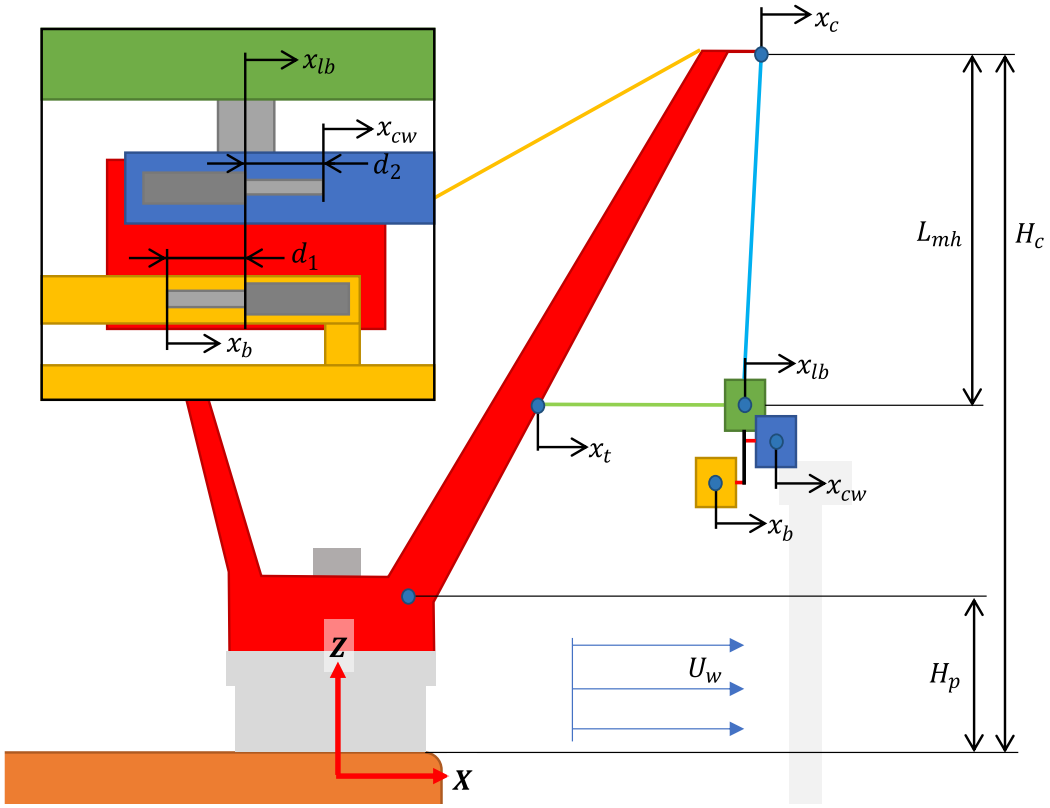

Figure 3.9: Schematic overview of the SBIS with XY table (not to scale)

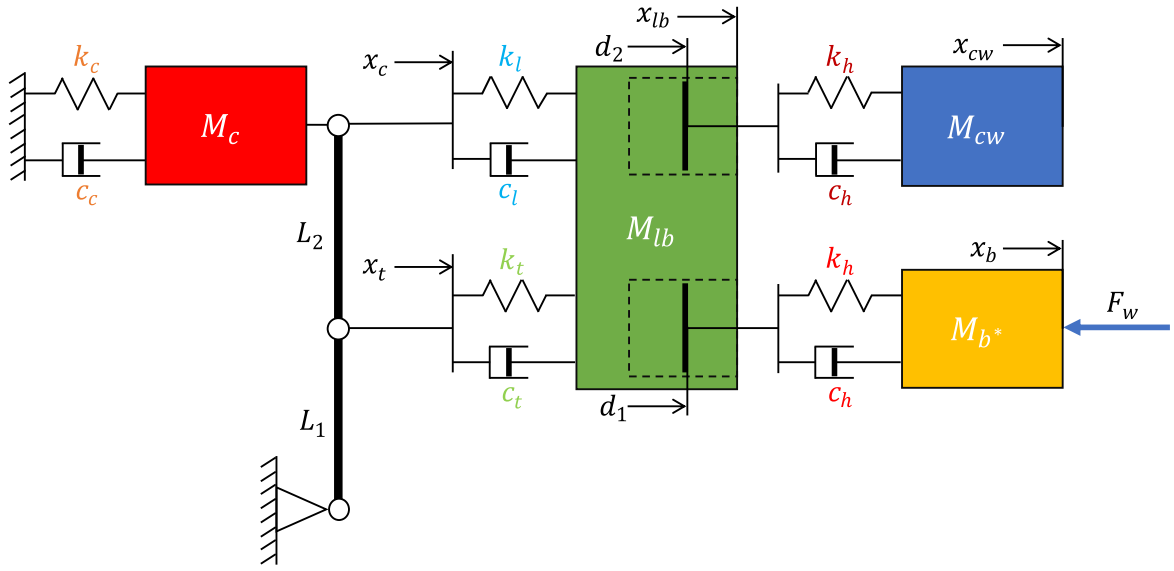

Figure 3.10: Single DOF discretized mass-spring-damper representation for the XY table actuation method

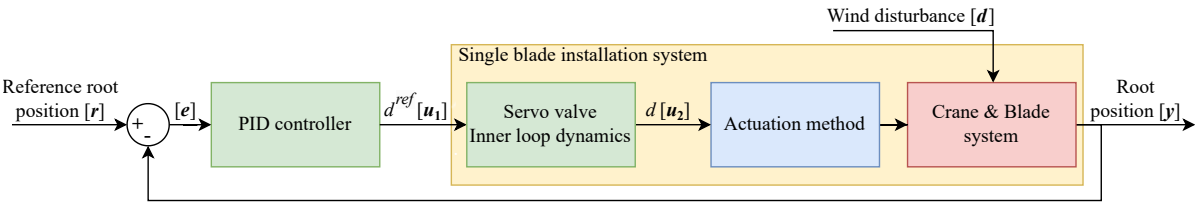

Figure 3.11: Control diagram for the XY SBIS including the simplified inner loop dynamics from section 3.3.1.

3.4.2. XY table

Figure 3.9 provides an overview of the SBIS with XY table. To illustrate the expansion of the model in relation to the model of the suspended blade from the previous section, an exception has been made here by showing the system in the XZ plane, instead of its operational plane. A schematic of the XY SBIS in its operational XY plane is also provided in figure F.1. A single DOF-dimensional mass-spring-damper representation of the XY table actuation method is shown in figure 3.10. A new body is added to the diagram, representing the counterweight with mass M_{cw}. The stiffnesses k_c, k_l and k_t are calculated as in section 3.4.1. The values change slightly compared to the suspended blade due to the increased weight of the total suspended load, M_{tot}.

Hydraulic cylinders

As described in section 2.4.1, the connection between the lower block, counterweight, and blade (yoke) is realized by hydraulic cylinders. The input to the mass-spring-damper system presented in figure 3.10 is the hydraulic cylinder stroke, denoted by d. This stroke is an output of the inner control loop. Figure 3.11 provides a control diagram of the system, showing this inner loop dynamic. The dynamic behaviour of the hydraulic actuator inner loop and the calculation of the cylinder stiffness and damping are described in section 3.3.1. As the cylinders have a finite stiffness, the two masses for the blade and lower block can no longer be combined, as was the case with the suspended blade in figure 3.8.

Equations of motions

The output of the model, [$\boldsymbol{y}$], is the blade root position. The error between the reference root position and the measured blade root position from the plant is the input for the controller. The control input [$\boldsymbol{u}_1$] to the plant is a reference cylinder position for the XY tables. The servo valve inner loop dynamics provide the cylinder positions d_1 and d_2, which are the inputs for the block diagram presented in figure 3.10. The mass-spring-damper system is represented by the following set of equation of motion. A state-space representation describing the dynamics of the SBIS with XY table is provided in appendix C.

$$\begin{bmatrix} \ddot{x}_c \\ \ddot{x}_{lb} \\ \ddot{x}_{cw} \\ \ddot{x}_b \end{bmatrix} = \begin{bmatrix} -F_{s,c} - F_{d,c} + F_{s,l} + F_{d,l} + F_{s,t} + F_{d,t} \\ F_{s,h1} + F_{d,h1} + F_{s,h2} + F_{d,h2} - F_{s,t} - F_{d,t} - F_{s,l} - F_{d,l} \\ -F_{s,h1} - F_{d,h1} \\ -F_w - F_{s,h2} - F_{d,h2} \end{bmatrix} \begin{bmatrix} M_c & & & \\ & M_{lb} & & \\ & & M_{cw} & \\ & & & M_{b^*} \end{bmatrix}^{-1} \tag{3.32}$$

Where:

$$F_{s,c} = k_c x_c \qquad F_{d,c} = c_c \dot{x}_c \tag{3.33}$$
$$F_{s,l} = k_l \left(x_{lb} - x_c\right) \qquad F_{d,l} = c_l \left(\dot{x}_{lb} - \dot{x}_c\right) \tag{3.34}$$
$$F_{s,t} = k_t \left(x_{lb} - \phi_t x_c\right) \qquad F_{d,t} = c_t \left(\dot{x}_{lb} - \phi_t \dot{x}_c\right) \tag{3.35}$$
$$F_{s,h1} = k_h \left(x_{cw} - x_{lb} + d_2\right) \qquad F_{d,h1} = c_h \left(\dot{x}_{cw} - \dot{x}_{lb}\right) \tag{3.36}$$
$$F_{s,h2} = k_h \left(x_b - x_{lb} + d_1\right) \qquad F_{d,h2} = c_h \left(\dot{x}_b - \dot{x}_{lb}\right) \tag{3.37}$$

3.4.3. Power swivel

A system overview of the SBIS with UQC power swivel within the corresponding operational plane is shown in figure 3.12. The blade suspended from the main hoist is shown from above in the XY plane. The DOF in this model is rotation instead of translation. Therefore, forces are translated to moments and rotational stiffnesses and inertias are used in the mass-spring-damper representation. In the following sections, the various system stiffnesses are derived. The blade (yoke) and lower block are simplified as uniform solids with constant density. The rotational inertias are estimated by

$$I = \frac{M(D^2 + W^2)}{12}. \tag{3.38}$$

Quick connector stiffness

The connection between the blade yoke and the lower block is provided by the UQC. The rotational stiffness is finite due to the stiffness of the drive assembly that allows for the rotation around the z^h-axis when the UQC is not in its locked position. This stiffness is assumed to be exclusively the result of the combined gearbox and motor stiffness. The damping inside the drive system and gearbox is assumed to be 5%. Section 3.3.2 describes calculation of the gearbox stiffness and inertia.

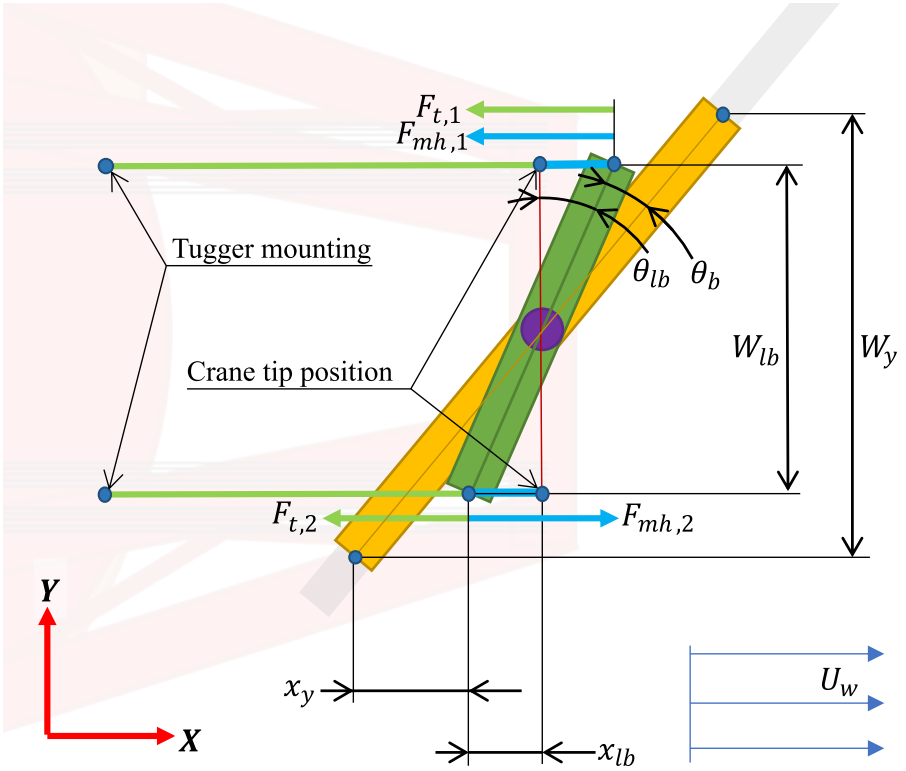

Figure 3.12: Schematic overview of the SBIS with UQC power swivel (not to scale)

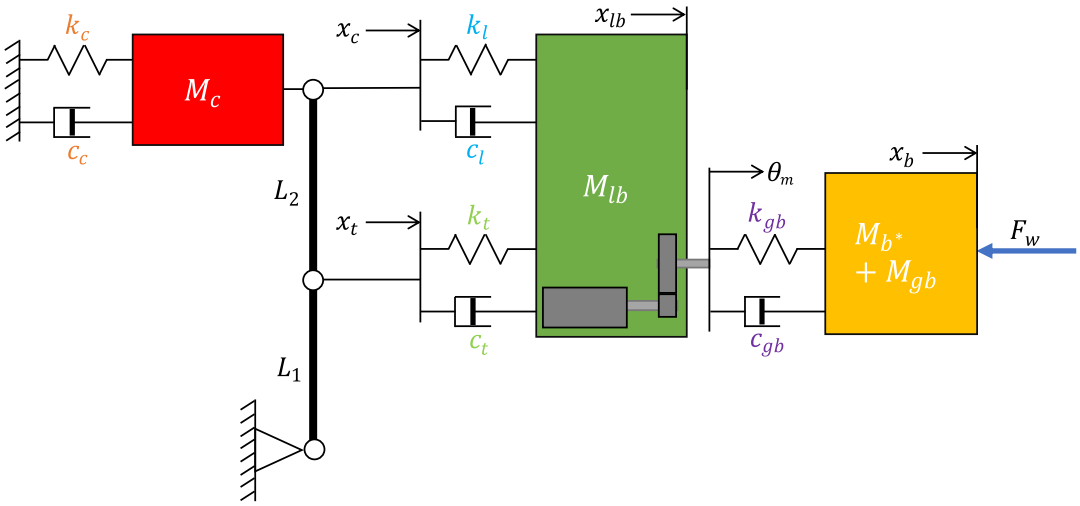

Figure 3.13: Single DOF discretized mass-spring-damper representation for the UQC power swivel actuation method

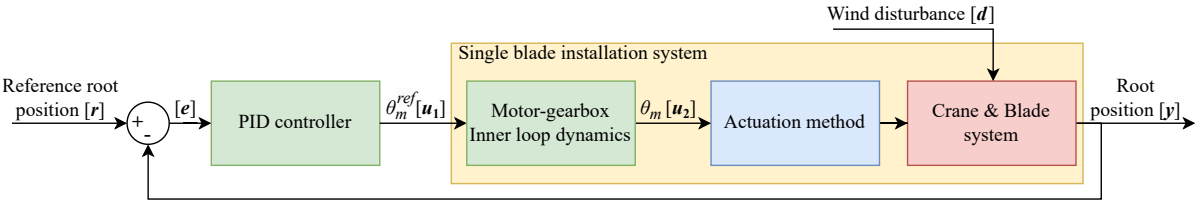

Figure 3.14: Control diagram for the power swivel SBIS including the simplified inner loop dynamics from section 3.3.2.

Hoist cable stiffness

For the calculation of the rotational stiffness provided by the hoist cables, the two bundles of hoist cables shown in figure 2.3 are modelled as two single cables with a stiffness equivalent to the 6 fall bundle. When the lower block rotates around the z^h-axis, the rotation results in a displacement of the hoist cable attachment point, denoted by x_{lb}. For small angles, this displacement is given by equation (3.39), where θ_{lb} is the relative angle between the crane tip and the lower block. This displacement relative to the crane tip results in a pendulum restoring force from the hoist cables. For a pendulum stiffness k_l, the pendulum restoring force as a function of the lower block rotation is approximated using the expression provided in equation (3.40). This results in a rotational stiffness $k_{l,rot}$. The main hoist damping is calculated using $c_l = 2\zeta\sqrt{I_{eff}k_l}$, where a damping ratio of 2% is assumed.

$$x_{lb} = \frac{\theta_{lb}W_{lb}}{2} \tag{3.39}$$

$$m_l = \frac{\theta_{lb}W_{lb}}{L_{mh}}\frac{M_{tot}g}{4} \tag{3.40}$$

$$k_{l,rot} = \frac{m_l}{\theta_{lb}} = \frac{W_{lb}^2}{L_{mh}}\frac{M_{tot}g}{4} \tag{3.41}$$

Tugger line stiffness

As with the hoist cables, the tugger line forces are translated into a torsional stiffness. The force exerted on the lower block by each tugger line is given by equations (3.42) and (3.43). The total tension is the sum of the static tugger pretension F_{pre} and the added contribution from the tugger elongation due to lower block rotation x_{lb}. Unlike with the hoist wires, pretension can be lost in one of the tugger lines during operation, as the tugger lines are tension only springs and thus can't exert any negative tension loads to the lower block. In the equations below, it is observed that in the calculation of the tugger lines' equivalent rotational stiffness, the pretension cancels out. However, the equations do not hold in cases where pretension is lost in one of the two cables. In reality, the scenario where pretension is lost result is very significant blade swing and is a dangerous situation that can't be allowed to happen. The assumption that pretension is always available is therefore acceptable.

$$F_{t,1} = F_{pre} + x_{lb}k_t \tag{3.42}$$

$$F_{t,2} = F_{pre} - x_{lb}k_t \tag{3.43}$$

$$m_t = \frac{W_{lb}}{2}F_{t,2} - \frac{W_{lb}}{2}F_{t,1} = -W_{lb}x_{lb}k_t \tag{3.44}$$

$$k_{t,rot} = \frac{m_t}{\theta_{lb}} = \frac{W_{lb}^2 k_t}{2} \tag{3.45}$$

Equations of motion

As with the XY table, the blade root position is the output of the system, given by $[y]$. The control input to the plant is a reference position for the UQC power swivel motor, θ_m^{ref}. The power swivel motor position, θ_m, follows from the motor-gearbox inner loop dynamics as shown in figure 3.14. The behaviour of the inner loop is described by equation (3.23). The block diagram presented in figure 3.13 results in the following set of equation of motion. The state space representation is provided in appendix C.

$$\begin{bmatrix}\ddot{x}_c\\ \ddot{x}_{lb}\\ \ddot{x}_b\end{bmatrix} = \begin{bmatrix}-F_{s,c} - F_{d,c} + F_{s,l} + F_{d,l} + F_{s,t} + F_{d,t}\\ F_{s,gb} + F_{d,gb} - F_{s,l} - F_{d,l} - F_{s,t} - F_{d,t}\\ -F_w - F_{s,gb} - F_{d,gb}\end{bmatrix} \begin{bmatrix}M_c & & \\ & M_{lb} & \\ & & (M_{b^*} + M_{gb})\end{bmatrix}^{-1} \tag{3.46}$$

Where:

$$F_{s,c} = k_c x_c \qquad F_{d,c} = c_c \dot{x}_c \tag{3.47}$$

$$F_{s,l} = k_l\left(x_{lb} - x_c\right) \qquad F_{d,l} = c_l\left(\dot{x}_{lb} - \dot{x}_c\right) \tag{3.48}$$

$$F_{s,t} = k_t\left(x_{lb} - \phi_t x_c\right) \qquad F_{d,t} = c_t\left(\dot{x}_{lb} - \phi_t \dot{x}_c\right) \tag{3.49}$$

$$F_{s,gb} = k_{gb}\left(x_b - x_{lb} - \theta_m\right) \qquad F_{d,gb} = c_{gb}\left(\dot{x}_b - \dot{x}_{lb}\right) \tag{3.50}$$

3.4.4. Wind vanes

A system overview of the single-blade installation with wind vanes in its operational plane is given in figure 3.15. The overview shows only one of the two vanes to reduce clutter. The quick connector is in its locked position, and the vane is used to control the rotation of the blade (yoke) around the z^h-axis. It is assumed that in the locked position, the connection between the yoke and lower block has an infinite stiffness, as was previously the case for the base case in section 3.4.1. The lower block and blade (yoke) are again combined and modelled as a single rigid mass.

Aerodynamic loads

The wind vanes rely on the aerodynamic loading on the vane to actuate the blade (yoke). The wind disturbance therefore also acts on the actuation method, as is shown in the control diagram in figure 3.17. The drag force on the flat plate is given by equation (3.51), where ρ_{air} is the air density, A_v is the cross-sectional area of the vane, U_m is the mean airspeed and C_D is the drag coefficient. The drag coefficient is a function of the angle of attack. For small values of θ_{lb}, the angle of attack is approximately θ_v. The relation between angle of attack and drag coefficient is not linear, however in this model the drag coefficient is assumed to increases linearly with increasing angle of attack up to its maximum value at an angle of attack of $\pi/2$ (90 degrees). The drag coefficient, at this maximum angle of attack, is assumed to be 2. The resulting relation between angle of attack and the drag coefficient is provided in equation (3.53).

The drag loads on the vane eventually results in a moment on the blade yoke around the z-axis. The distance between the vane rotation axis and the yoke centre is given by r_v. The moment on the blade yoke is given by equation (3.54), where n is the number of vanes, H_v is the height of the vane, and W_v the width of the vane. As the wind loading depends on the wind speed, the controller might have to be tuned to various wind speeds.

$$F_D = \frac{1}{2}\rho_{air} U_m^2 C_D A_v \tag{3.51}$$

$$A_v = H_v W_v \tag{3.52}$$

$$C_D = \frac{4(\theta_v + \theta_b)}{\pi} \quad \rightarrow \quad C_D = \frac{4\theta_v}{\pi} \tag{3.53}$$

$$m_v = r_v \cdot F_D = \frac{2n\rho_{air} U_w^2 H_v W_v r_v}{\pi}\theta_v \tag{3.54}$$

Vane servo motor

The vane itself is actuated by a servo motor that controls the angle of the vane. Due to the size of the vane required to generate the aerodynamic loading required to counteract the expected wind induced moment on the blade, a gearbox is likely to be required to actuate the vane. The motor-gearbox subsystem presented in section 3.3.2 is used to model the servo motor.

As two vanes are used, which are rotated equally, but in opposite direction, reaction moment from the motor-gearbox on the blade yoke cancel out. The servo motor and vane system are therefore included as a separate mass-spring-damper system, as shown in figure 3.16. The resulting loading on the main model is a function of the vane orientation θ_v. The equation used to couple the two mass-spring-damper systems is given by equation (3.60).

Equations of motion

The error between the blade root position [$\boldsymbol{y}$], and the reference root position [$\boldsymbol{r}$] is used as input for the controller. A control diagram for the system is provided in figure 3.17. The control input [$\boldsymbol{u}_1$] to the plant is again the reference motor position θ_m^{ref}. The servo motor internal dynamics are modelled using the 1^{st} order transfer function equation (3.23), with time constant τ_v. The servo angle is limited to $\theta_v \in \left\{\theta_v \;\middle|\; 0 \leq \theta_v \leq \frac{\pi}{2}\right\}$. The set of equations below describe the behaviour of the mass-spring-damper system in figure 3.16. The state space representation for the SBIS with power swivel is provided in appendix C.

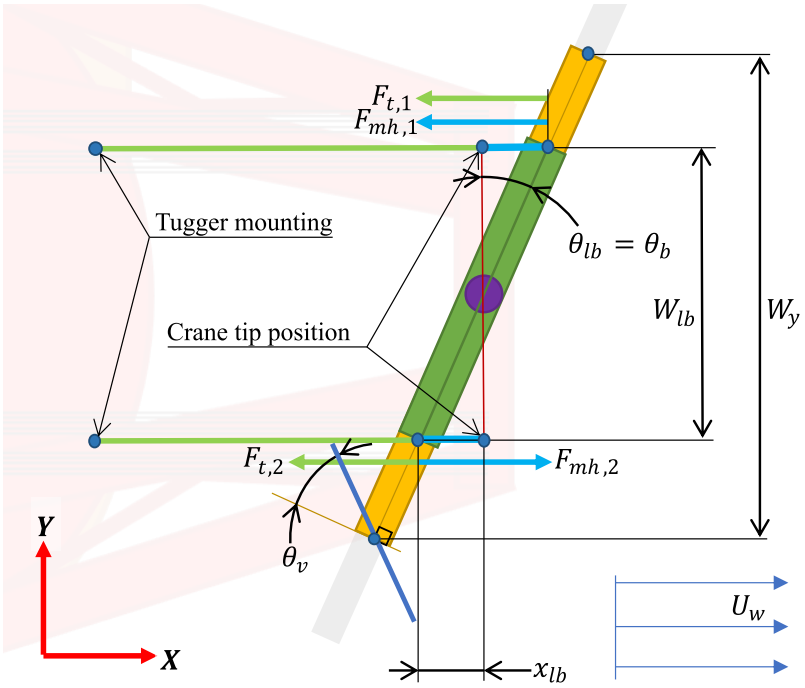

Figure 3.15: Schematic overview of the SBIS with wind vanes (not to scale)

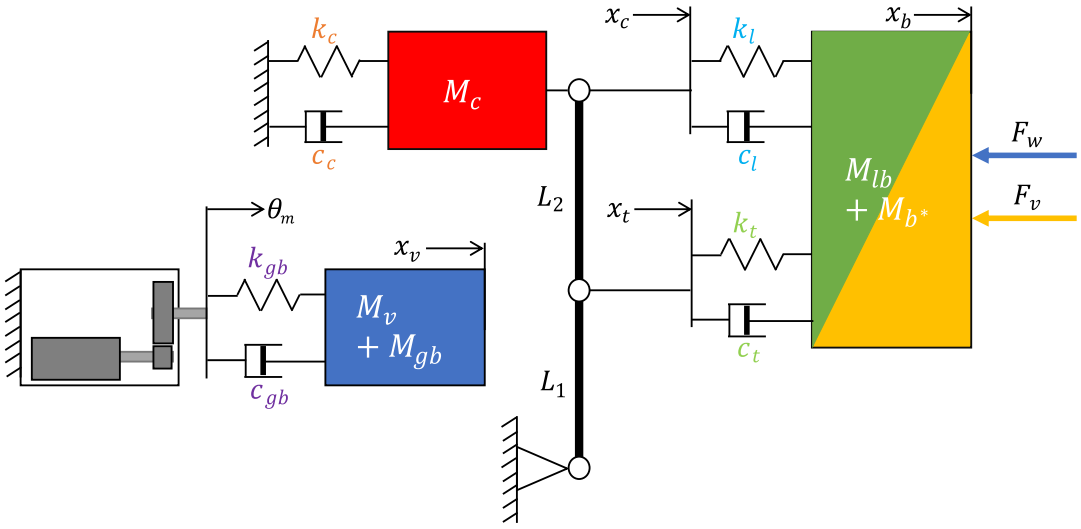

Figure 3.16: Single DOF discretized mass-spring-damper representation for the wind vanes actuation method

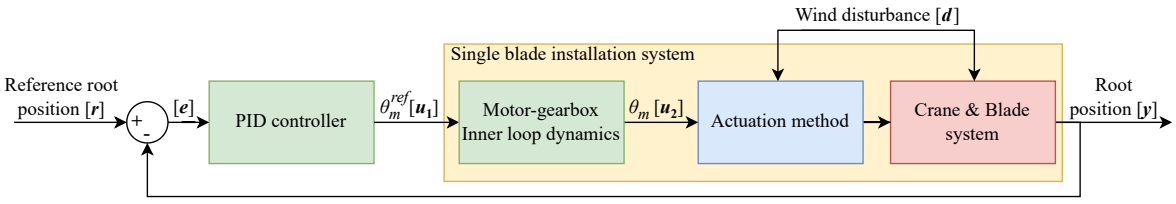

Figure 3.17: Control diagram for the wind vane SBIS including the simplified inner loop dynamics from section 3.3.2.

$$\begin{bmatrix} \ddot{x}_b \\ \ddot{x}_c \\ \ddot{x}_v \end{bmatrix} = \begin{bmatrix} -F_w - F_v - F_{s,l} - F_{d,l} - F_{s,t} - F_{d,t} \\ -F_{s,c} - F_{d,c} + F_{s,l} + F_{d,l} + F_{s,t} + F_{d,t} \\ -F_{s,gb} - F_{d,gb} \end{bmatrix} \begin{bmatrix} (M_{b^*} + M_{lb}) & & \\ & M_c & \\ & & (M_{gb} + M_v) \end{bmatrix}^{-1} \tag{3.55}$$

Where:

$$F_{s,c} = k_c x_c \qquad F_{d,c} = c_c \dot{x}_c \tag{3.56}$$
$$F_{s,l} = k_l (x_b - x_c) \qquad F_{d,l} = c_l (\dot{x}_b - \dot{x}_c) \tag{3.57}$$
$$F_{s,t} = k_t (x_b - \phi_t x_c) \qquad F_{d,t} = c_t (\dot{x}_b - \phi_t \dot{x}_c) \tag{3.58}$$
$$F_{s,gb} = k_{gb} (x_v - \theta_m) \qquad F_{d,gb} = c_{gb} \dot{x}_v \tag{3.59}$$

$$F_v = \frac{2n\rho_{air} U_w^2 H_v W_v r_v}{\pi} \theta_v = K_v \cdot x_v \tag{3.60}$$

3.4.5. Gyroscopes

figure 3.18 provides an overview of the SBIS in the YZ plane. The degree of freedom is again rotation instead of translation. However, in this model, rotation around the x-axis is considered. Therefore, the masses and linear spring stiffnesses are again converted into moments, rotational stiffnesses and inertias. The yoke and lower block remain simplified as uniform solid with constant density. The inertias are approximated by the expression provided in equation (3.61).

$$I = \frac{M(H^2 + L^2)}{12} \tag{3.61}$$

Hoist cable stiffness

The two separate hoist cable bundles are again modelled as two single cables. Due to the block width, a moment can be transferred from the cables to the block. Due to the relatively low mass of the suspended load, the block is assumed to be operated in the split configuration. For this configuration, each bundle consists out of 6 falls. The stiffness for each separate bundle is given by equation equation (3.62). The tension in the two hoist cables is a sum of the transient tension due to the suspended mass, and the added elongation due to the lower block rotation, indicated by z_{lb} in figure 3.18. The tension in the two cables is found using the expressions in equations (3.64) and (3.65) The rotational stiffness is derived from these expressions for the hoist cable tension in equations (3.66) and (3.67).

$$k_{mh} = \frac{N_{falls,mh} k_{ax,mh}}{L_{mh}} \tag{3.62}$$
$$z_{lb,1} = z_{lb,2} = \frac{\theta_{lb} W_{lb}}{2} \tag{3.63}$$
$$F_{lb,1} = \frac{M_{tot} g}{2} - z_{lb,1} k_{mh} = \frac{M_{tot} g - \theta_{lb} W_{lb} k_{mh}}{2} \tag{3.64}$$
$$F_{lb,2} = \frac{M_{tot} g}{2} + z_{lb,2} k_{mh} = \frac{M_{tot} g + \theta_{lb} W_{lb} k_{mh}}{2} \tag{3.65}$$
$$m_l = F_{lb,1} \frac{W_{lb}}{2} - F_{lb,2} \frac{W_{lb}}{2} = \frac{-\theta_{lb} W_{lb}^2 k_{mh}}{2} \tag{3.66}$$
$$k_l = \frac{m_l}{\theta_{lb}} = \frac{W_{lb}^2 k_{mh}}{2} \tag{3.67}$$

Main hoist vertical damping

As opposed to the other cases with wire ropes, a damping ratio of 2% is likely not a realistic value for the damping in the system. In a study on the hook load dynamics for a heavy lift vessel, the damping was found to be about 260 times as high as expected [42]. The higher damping is likely a result of the large number of falls, larger than expected internal friction in the wires, and the added damping from the sheaves and wire rope bending (around the sheaves). The study found a damping close to the critical damping for a crane with 80 falls (4x20 falls per bundle). As the reference crane has 6 falls per bundle for a total of 12 falls, the expected damping is somewhere between 2% and 100%, likely closer to 2%. A conservative damping value of 5% is used for the main hoist wire damping.

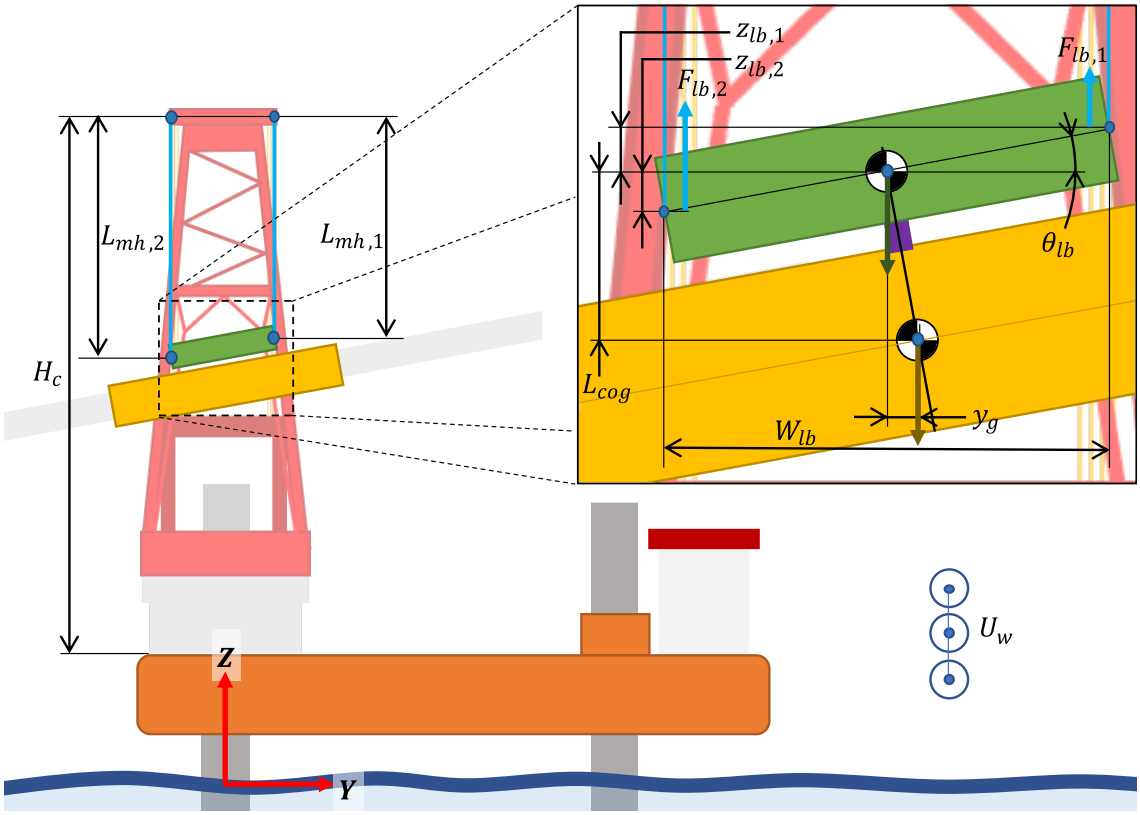

Figure 3.18: Schematic overview of the SBIS with gyroscopes (not to scale)

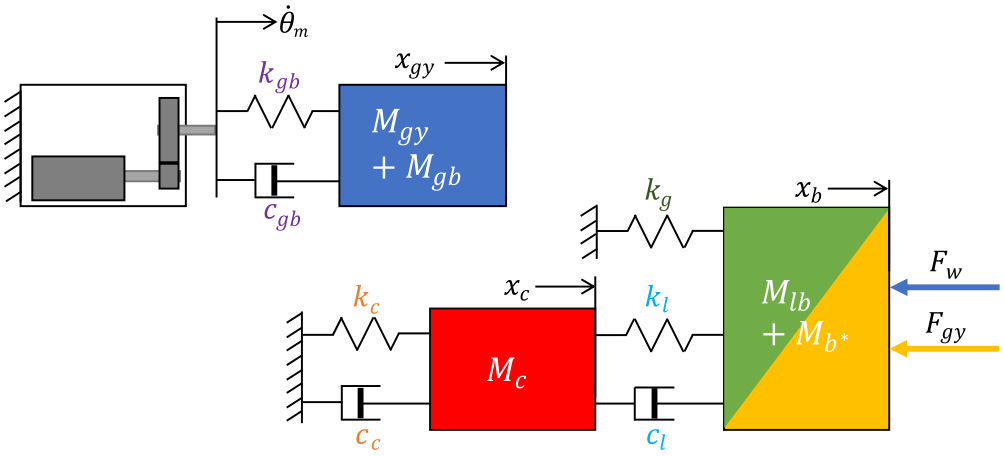

Figure 3.19: Single DOF discretized mass-spring-damper representation for the gyroscope actuation method

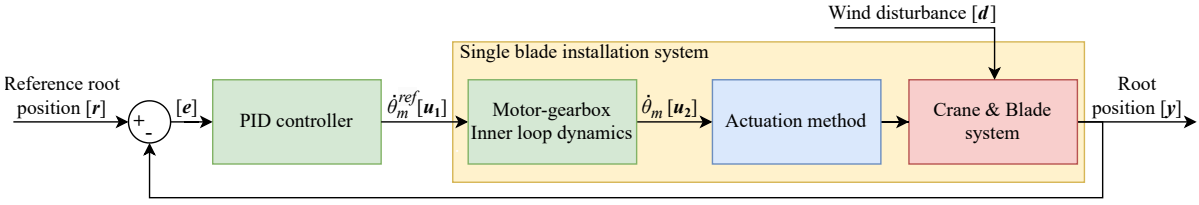

Figure 3.20: Control diagram for the SBIS with gyroscopes, including the simplified inner loop dynamics from section 3.3.2.

Gravitational loading
When the lower block rotates around the x-axis, the rotation results in a displacement of the blade centre of gravity relative to that of the lower block. For small angles, the displacement is given by $y_g = \theta_{lb} L_{cog}$. This results in a restoring moment due to the offset gravitational loads. The resulting moment is translated to a rotational stiffness k_g. This gravitational component is added to the mass-spring-damper model in figure 3.19 as a spring without damping.

$$m_g = \theta_{lb} L_{cog} \cdot M_b \cdot g \tag{3.68}$$

$$k_g = \frac{m_g}{\theta_{lb}} = L_{cog} \cdot M_b \cdot g \tag{3.69}$$

Tugger lines
The contribution of the tugger lines to the stiffness of the system around the x-axis is neglected.

Gyroscopes
The gyroscope is simplified as a solid steel disk. The mass of the disk is given by equation (3.70), where r_{gy} is the radius of the gyro disk, T_{gy} is the thickness of the disk, and ρ_{steel} is the density of steel. The inertia about the spin axis is found using the expression in equation (3.71). The resulting angular momentum of the gyroscope about the spin axis is a function of the inertia about its spin axis, I_s, and the angular spin velocity, ω_s.

$$M_{gy} = \pi r_{gy}^2 \cdot T_{gy} \cdot \rho_{steel} \tag{3.70}$$

$$I_s = \frac{M_{gy} \cdot r_{gy}^2}{2} \tag{3.71}$$

$$H_s = I_s \omega_s \tag{3.72}$$

Gyroscope servo motor
Again, a servo motor with gearbox is used to actuate the gyroscope around its precession axis. The precession axis is aligned with the z^b-axis. This servo-gearbox is again modelled using the sub-model presented in section 3.3.2. The torque from the motor-gearbox results in a reaction moment on the blade (yoke) around the z^b-axis. For this reason, two gyroscopes are used, which a rotated in opposite direction. For two gyroscopes that are rotated in equal bot opposite direction and are also precessed in the opposite direction, only the moment around the single axis of interest remains [43]. The servo motor system is included as a separate mass-spring-damper system in figure 3.19. The resulting loading on the main model is a function of the precession velocity, as the moment about the x-axis, perpendicular to the spin and precession axes, is given by equation (3.73).

$$m_{gy} = n H_s \dot{\theta}_{gy} \tag{3.73}$$

Equations of motion
A control diagram for the system is provided in figure 3.20. The blade root error is again used as input for the controller. The control input [$\boldsymbol{u}_1$] to the plant is a reference rotational velocity $\dot{\theta}_m^{ref}$. The servo motor inner loop dynamics are modelled using the 1^{st} order transfer function equation (3.23), with time constant τ_{gy}. The equations of motion for the single DOF mass-spring-damper system in figure 3.19 are given below. The state space representation is provided in appendix C.

$$\begin{bmatrix} \ddot{x}_b \\ \ddot{x}_c \\ \ddot{x}_{gy} \end{bmatrix} = \begin{bmatrix} -F_w - F_{gy} - F_{s,l} - F_{d,l} - F_{s,g} \\ -F_{s,c} - F_{d,c} + F_{s,l} + F_{d,l} \\ -F_{s,gb} - F_{d,gb} \end{bmatrix} \begin{bmatrix} (M_{b^*} + M_{lb}) & & \\ & M_c & \\ & & (M_{gb} + M_{gy}) \end{bmatrix}^{-1} \tag{3.74}$$

Where:

$$F_{s,c} = k_c x_c \qquad F_{d,c} = c_c \dot{x}_c \tag{3.75}$$

$$F_{s,l} = k_l (x_b - x_c) \qquad F_{d,l} = c_l (\dot{x}_b - \dot{x}_c) \tag{3.76}$$

$$F_{s,gb} = k_{gb}(x_{gy} - \theta_m) \qquad F_{d,gb} = c_{gb}(\dot{x}_{gy} - \dot{\theta}_m) \tag{3.77}$$

$$F_{s,g} = k_g x_b \tag{3.78}$$

$$F_{gy} = n I_s \omega_s \dot{\theta}_{gy} = K_{gy} \cdot \dot{x}_{gy} \tag{3.79}$$

3.4.6. COG shifting

An overview of the SBIS for the COG shifting actuation method is given in figure 3.21. For the wind vanes (AM3) and the gyroscopes (AM4), the reaction forces from the actuator did not influence the main system, as the reaction forces cancel out. In the case of the COG shifting actuation method, this is not the case. The COG shifting actuation method generates a moment around the x^b-axis by shifting the COG of the blade (yoke) relative to the lower block. A hydraulic cylinder actuates the shifting. The reaction forces from moving the blade (yoke) relative to the lower block result in reaction forces on the lower block.

To include all dynamics, two separate mass-spring-damper systems are presented in figure 3.22. The first described the dynamics of the system along the y-axis as a result of the reaction force from the changing cylinder position d. The second describes the system behaviour around the x^b-axis. This second system is effected by the wind disturbance and the effects of the shifted blade (yoke) COG relative to the lower block.

Translational sub-model

The translational sub-model consist of discrete masses M_{bm}, M_{lb} and M_{b^*}, representing the equivalent crane boom, lower block and blade (yoke) mass in y-direction. k_{bm} and c_{bm} are the boom stiffness in y-direction. The pendulum stiffness k_p is calculated using equation (3.16). As with the previous models, 2% damping is assumed for the crane boom and pendulum swing.

Rotational sub-model

The degree of freedom for the rotational model is rotation around the x-axis. The connection between the lower block and blade (yoke) in this DOF is provided by the locked UQC. The discrete mass of the lower block and blade (yoke) are therefore again combined into a single discrete mass. The inertia for the lower block and blade (yoke) is determined using equation (3.61). The expressions used to convert the linear spring stiffnesses to rotational stiffnesses are given in equations (3.10) and (3.67) for the crane and main hoist, respectively. The effect of gravity is again added to the model using a spring without damping, with a stiffness given by equation (3.69).

Coupling equations

The two models are coupled using two coupling equations. These equations describe the simplified relation between the translational and rotational dynamic systems. The coupling equations do not capture the full dynamics of the system. Influence of pendulation and horizontal crane deflection on the rotation of the load are for instance neglected in this approach.

The most important coupling between the two models is the moment created by the COG offset between the lower block and blade (yoke) along the y-axis, as this is the working principle behind the actuation method. The moment generated by the COG shift is given by equation (3.80).

Due to the vertical offset between the lower block COG and blade (yoke) COG, the cylinder reaction force $F_{h,b}$ results in a moment on the suspended load. This contribution is added to the moment generated by the COG shift, resulting in the coupling equation given by equation (3.81) acting on the combined discrete mass of the lower block and blade (yoke) in the rotational sub-model.

The second coupling equation converts the moments acting on the lower block and blade (yoke) to an equivalent force action on the blade (yoke). The relation between the sum of moments acting on the suspended load around the x-axis and the feedback on the blade (yoke) in the translational model is given by equation (3.82)

$$m_g = F_{g,b^*} y_g = F_{g,b^*}(x_h - x_{lb}) \tag{3.80}$$

$$m_{cog} = m_g + L_{cog} M_{b^*} \ddot{x}_h \tag{3.81}$$

$$F_{cog} = \frac{(I_{b^*} + I_{lb})\,\ddot{x}_b}{L_{cog}} \tag{3.82}$$

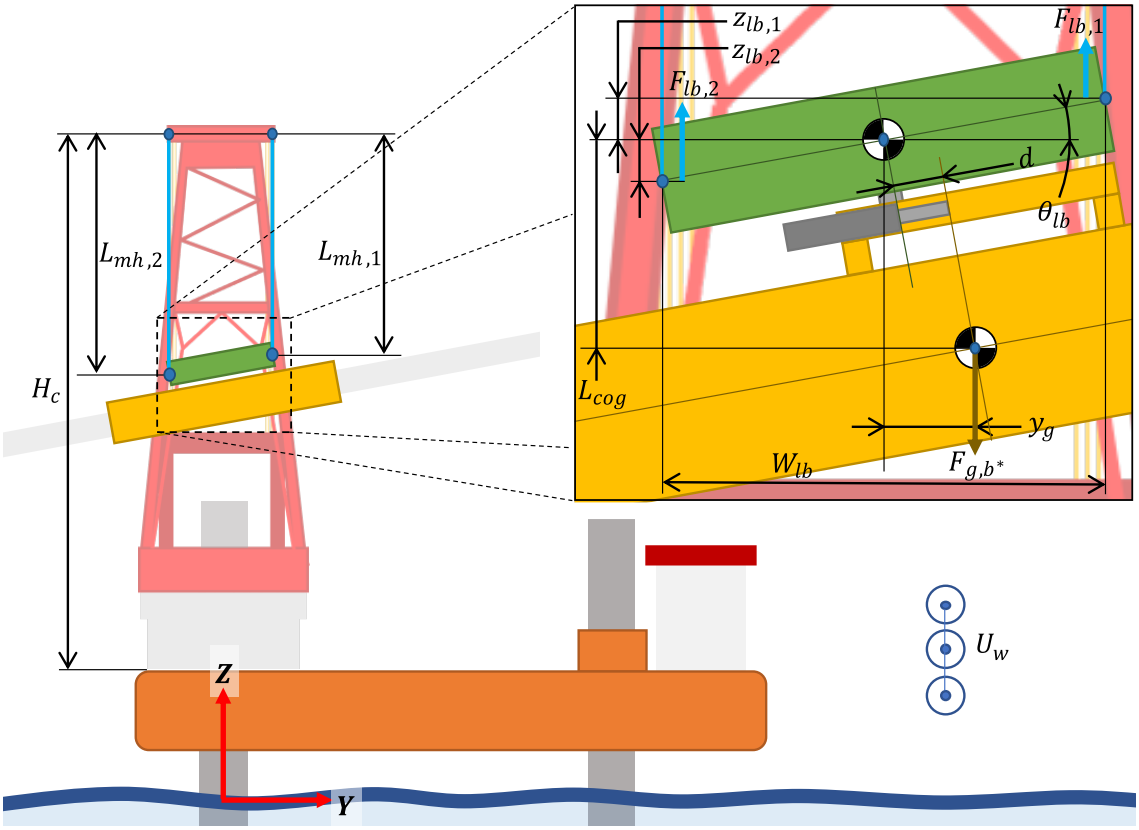

Figure 3.21: Schematic overview of the SBIS with COG shifting (not to scale)

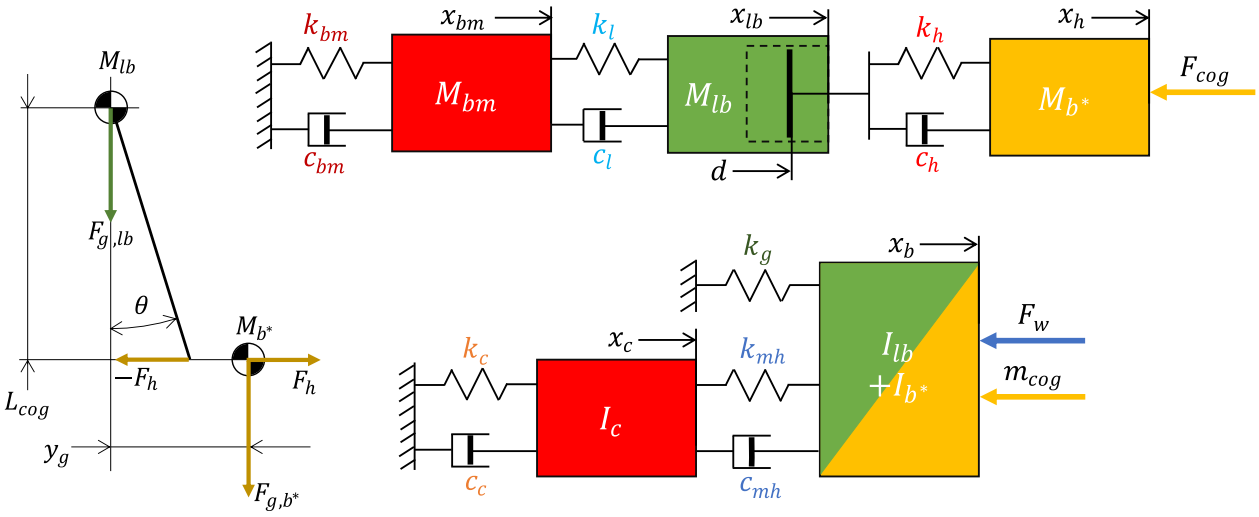

Figure 3.22: Single DOF discretized mass-spring-damper representation for the COG shifting actuation method

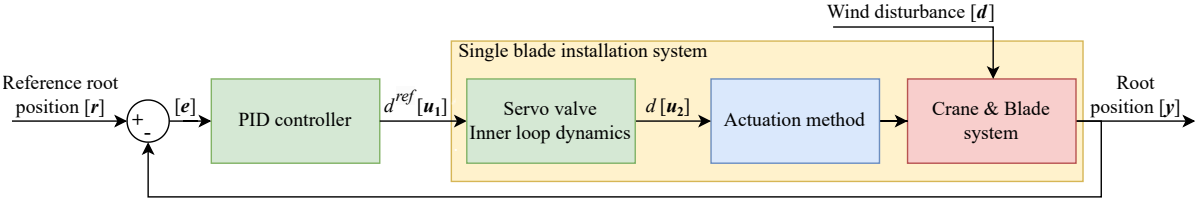

Figure 3.23: Control diagram for the cog shifting SBIS including the simplified inner loop dynamics from section 3.3.1.

Cylinder dynamics
The connection between the lower block and blade (yoke) is realized by a hydraulic actuator. This actuation method is realized using the same XY tables from AM1 (section 2.4.1), however in this case the counterweight is not shifted, resulting in a shift of the COG. The dynamics of the cylinder and the system along the y-axis is included as a separate mass-spring-damper system. The hydraulic cylinder position is an output of the inner control loop. Figure 3.23 provides a control diagram of the overall system, showing the location of the inner loop dynamics. Again, the behaviour of the inner loop is described in section 3.3.1.

Equations of motion
A control diagram for the system is provided in figure 3.20. The error between the blade root position and reference root position is again used as input for the controller. The control input [$\boldsymbol{u}_1$] to the plant is a reference cylinder position. The cylinder position d, which is the input of the block diagram presented in figure 3.22, follows from the servo valve inner loop dynamics. The inner loop dynamics are described by equation (3.17). The set of equations below describe the dynamic behaviour of the system. The corresponding state-space system is found in appendix C.

$$\begin{bmatrix} \ddot{x}_b \\ \ddot{x}_c \\ \ddot{x}_h \\ \ddot{x}_{lb} \\ \ddot{x}_{bm} \end{bmatrix} = \begin{bmatrix} -F_w - M_{cog} - F_{s,l} - F_{d,l} - F_{s,g} \\ -F_{s,c} - F_{d,c} + F_{s,l} + F_{d,l} \\ -F_{s,h} - F_{d,h} - F_{cog} \\ -F_{s,p} - F_{d,p} + F_{s,h} + F_{d,h} \\ -F_{s,bm} - F_{d,bm} + F_{s,p} + F_{d,p} \end{bmatrix} \begin{bmatrix} (I_{b^*} + I_{lb}) & & & & \\ & I_c & & & \\ & & M_{b^*} & & \\ & & & M_{lb} & \\ & & & & M_{bm} \end{bmatrix}^{-1} \tag{3.83}$$

Where:

$$F_{s,bm} = k_{bm} x_{bm} \qquad F_{d,c} = c_{bm} \dot{x}_{bm} \tag{3.84}$$
$$F_{s,p} = k_p (x_{lb} - x_{bm}) \qquad F_{d,h} = c_h \left(\dot{x}_{lb} - \dot{x}_{bm}\right) \tag{3.85}$$
$$F_{s,h} = k_h (x_h - x_{lb} - d) \qquad F_{d,h} = c_h \left(\dot{x}_h - \dot{x}_{lb}\right) \tag{3.86}$$
$$F_{s,c} = k_c x_c \qquad F_{d,c} = c_c \dot{x}_c \tag{3.87}$$
$$F_{s,l} = k_l \left(x_b - x_c\right) \qquad F_{d,l} = c_l \left(\dot{x}_b - \dot{x}_c\right) \tag{3.88}$$
$$F_{s,g} = k_g x_b \tag{3.89}$$

3.5. Bode analysis

In this second part of the chapter, the linear models are analysed in the frequency domain and a PID controller is proposed for each actuation method. The state space systems are first tested for controllability and stabilisability using the Hautus tests provided in theorem 1 [44]. These tests are a set of conditions used to determine the controllability, stabilisability, and observability properties of a linear time-invariant (LTI) system. The concepts of controllability, stabilisability, and observability are briefly explained below.

1. **Controllability:** The controllability of a state refers to its ability to be steered from any initial value to any desired value using the system's control inputs. For all the actuation methods, it is important to verify that the actuation method is able to control the states x_b and $\dot{x}_b$, which are the blade position and velocity, using the control inputs. For the XY table, these inputs are the reference cylinder positions.
2. **stabilisability:** For all other states apart from x_b and $\dot{x}_b$, the controllability is not immediately relevant, as no specific position or velocity requirements are set for these states. However, for all states in the system, it must be verified that they are stabilisable. Stabilisability refers to the ability to stabilise an unstable system using feedback control. When one of the states is not stabilisable (real part of pole > 0), it means that the overall system can not be stabilized using feedback control, meaning that the system is inherently unstable.
3. **Observability:** Observability refers to the ability to reconstruct the state of a system based on its outputs. The Hautus test for observability ensures that the system's output contains enough information to uniquely determine the state for which the Eigenvalue is tested. This test is not relevant for this study, as full state feedback is assumed, as is stated in section 3.1.

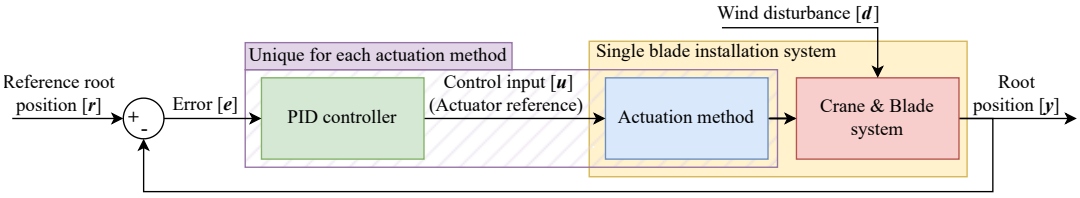

Figure 3.24: Simplified control diagram for the SBIS

Theorem 1 (Hautus test) *For a state space system in the form* $\dot{\boldsymbol{x}}(t) = \boldsymbol{A}\boldsymbol{x}(t) + \boldsymbol{B}\boldsymbol{u}(t)$, $\boldsymbol{y} = \boldsymbol{C}\boldsymbol{x}(t)$ *with* $\boldsymbol{A} \in M_n(\Re)$, $\boldsymbol{B} \in M_{n\times m}(\Re)$ *and* $\boldsymbol{C} \in M_{m\times n}(\Re)$*:*

- $(\boldsymbol{A}, \boldsymbol{B})$ *is controllable if and only if the matrix* $(\boldsymbol{A} - \lambda\boldsymbol{I}, \boldsymbol{B})$ *has rank* n *for every Eigenvalue* λ *of* $\boldsymbol{A}$*.*
- $(\boldsymbol{A}, \boldsymbol{B})$ *is stabilisable if and only if* $(\boldsymbol{A} - \lambda\boldsymbol{I}, \boldsymbol{B})$ *has rank* n *for every Eigenvalue* λ *of* $\boldsymbol{A}$ *with* $\mathrm{Re}(\lambda) \geq 0$*.*
- $(\boldsymbol{A}, \boldsymbol{C})$ *is observable if and only if* $(\boldsymbol{A} - \lambda\boldsymbol{I}, \boldsymbol{C})$ *has rank* n *for every Eigenvalue* λ *of* $\boldsymbol{A}$*.*

From the state space representation, the Eigenmodes of the system can also be determined. The Eigenmodes of a system change as the system stiffnesses and damping values change. Based on the modal analysis, it is determined which system stiffness has the main influence on the different Eigenmodes of the system. This provides insight into which system properties are limiting for the performance of the different actuation methods. The system's Eigenmodes are also represented in the open-loop Bode response $[\boldsymbol{u}] \rightarrow [\boldsymbol{y}]$.

$$C_{pid} = K_p(1 + \frac{1}{T_i}\frac{1}{s} + T_d s) \tag{3.90}$$

A Bode plot is a graphical representation of the frequency response of a system. The Bode plots provide insight in the system behaviour and are used in the following sections to design a PID control for each actuation method. A PID controller consists of three parallel controllers that work together to determine the control input based on the error signal. Equation (3.90) shows the standard PID form. K_p, T_i and T_p are the proportional gain, the integration time constant and the derivative time constant. The three control contributions are briefly explained below.

1. The P controller generates an output proportional to the error signal. It scales the error by a proportional gain constant (K_p) to produce the control effort. A higher value of K_p results in a more aggressive response, but it can also lead to overshoot and instability.
2. The I controller integrates the error over time and adds it to the control input. This to eliminate steady-state errors by continuously increasing the control output as long as there is an error present, ensuring that any long-term accumulated error is corrected. The integrator does however introduce phase lag in the system response. The integral action is governed by the integral gain constant ($K_i = 1/T_i$).
3. The D controller considers the rate of change of the error and generates a control effort based on this derivative. It provides anticipatory control by estimating the future trend of the error. The control effort is proportional to the rate of change of the error multiplied by the derivative gain constant (K_d). The derivative action helps dampen the system's response to reduce overshoot and oscillations.

The control objective for each controller is to align the blade root, $\boldsymbol{p}_{root}$, with the hub ,$\boldsymbol{p}_{hub}$. As turbine tower dynamics are not included, the reference position is a stationary point in the global reference frame. The locations of these point within the SBIS are visualized in figure 2.5.

The controllers are designed towards the same design criteria, expressed as a minimum Phase Margin (PM) and Gain Margin (GM). The PM and GM are both measures of the stability of the closed-loop control system. The PM is the amount of phase lag a system can tolerate before becoming unstable. Gain margin represents the amount of gain that can be added to the system before it becomes unstable. The design requirements for the PID controllers are based on a Huisman rule of thumb, and are a minimum GM of 6 dB and a minimum PM of 60 degrees.

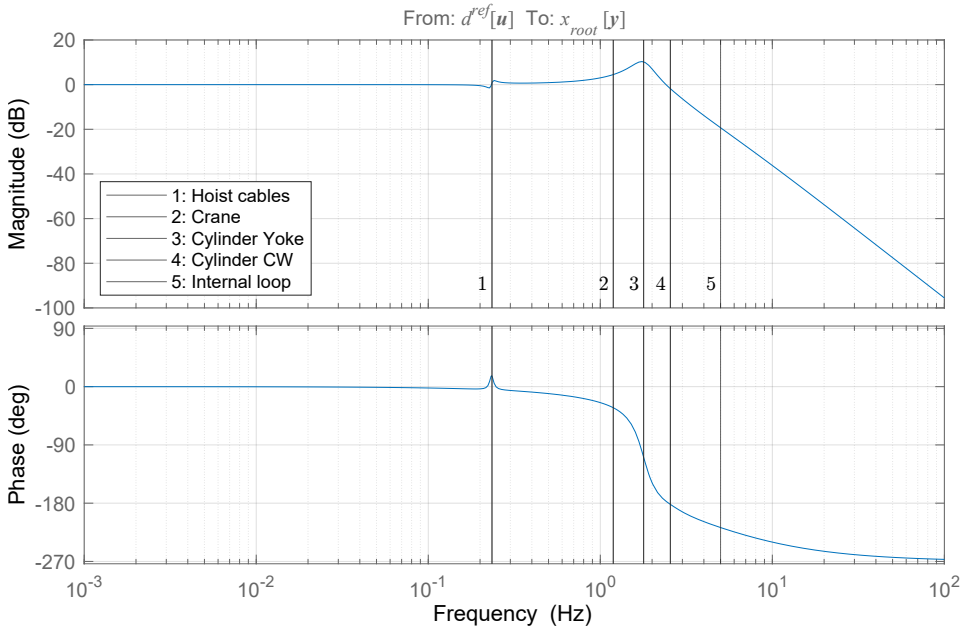

Figure 3.25: Open-loop response of SBIS with XY table.

Table 3.3: Natural period (T_n) and relation between amplitudes for the system's Eigenmodes

Mode	1	2	3	4	5
x_b	1	0.04	1	1	1
x_{cw}	1	0.05	1	0.83	0.91
x_{lb}	0.98	0.02	0.05	0.95	0
x_c	0.05	1	0	0 .02	0
Valve[1]	0	0	0	0	0.97
T_n (s)	4.26	0.84	0.56	0.39	0.20

Table 3.4: XY table pole locations

Pole	ζ	f [Hz]
-0.05 ± 1.47i	0.031	0.234
-0.42 ± 7.46i	0.056	1.190
-1.64 ± 11.10i	0.146	1.786
-3.38 ± 15.60i	0.211	2.543
-31.4	1	5

Table 3.5: Control and performance parameters

	Value	unit
K_p	1	-
T_i	0.2	s
T_d	0.15	s
PM	60	deg
GM	∞	dB
BW	3.67	Hz

3.5.1. XY table

The pole locations for the SBIS model with XY table are given in table 3.4. An overview of the system's Eigenmodes is given in table 3.3. The Eigenmodes are plotted in the open-loop system response in figure 3.25. The system has four complex pole pairs, and three complex zero pairs. The phase peak in the system response around 0.08 Hz is the result of neighbouring complex pole and zero pairs that correspond to the natural frequency of pendulum swing. Around 1.8 Hz, there is a complex pole pair that leads to -180 degree phase jump, corresponding to the natural frequency of the hydraulic cylinder.

As described in section 3.4.2, the actuation method has a counterweight. This is moved in the opposite direction to the blade to reduce the feedback from inertial loads to the rest of the system. In practice, it will be difficult to ensure that the counterweight has the exact mass as the blade (yoke), for example due to variation in blade weight. For the remainder of this paper, a counterweight with 110% of the total blade (yoke) mass is assumed. Because the counterweight and blade (yoke) have a different mass, but are moved in equal but opposite direction, an effect from the inertial load on the rest of the system is observed. This is reflected, for example, by the first peak around 0.08 Hz. As state above, this Eigenmode corresponds to the pendulum swing of the entire load under the crane, which is excited by the residual inertial reaction loads on the lower block.

In the case that the counterweight is lighter than the blade (yoke), the pole and zero pairs will switch positions, resulting in a peak with phase loss instead of the phase gain. Phase loss is unfavourable here because it can lead to stability problems when the phase exceed -180 degrees. For this reason, it is more desirable to have a heavier rather than lighter counterweight.

[1] Servo valve inner loop dynamics section 3.3.1

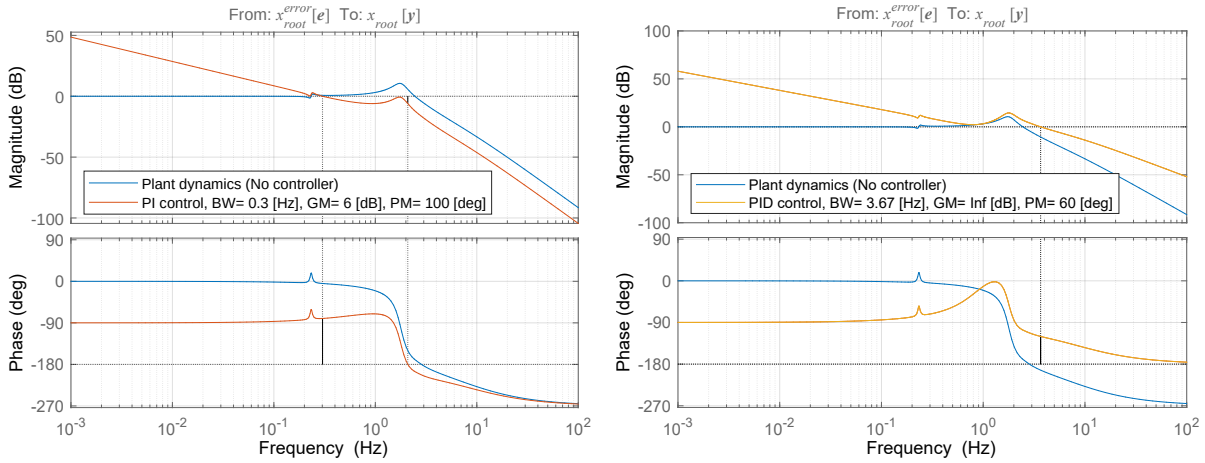

Figure 3.26: Open-loop responses for the PI and the final PID controlled SBIS with XY table

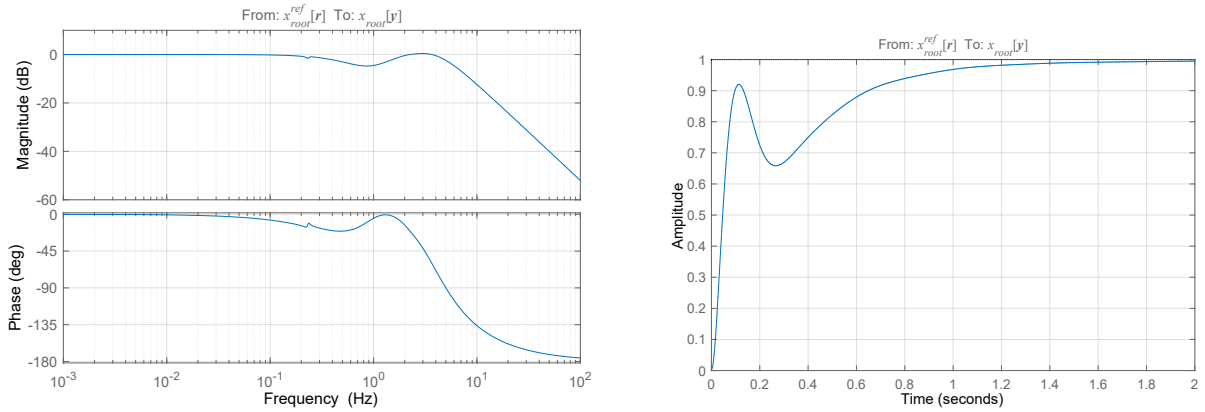

Figure 3.27: Closed-loop response (left) and step response (right) for the controlled SBIS with XY table

Open-loop

All poles are in the left half plane, which means that the system is stabilisable. For the A and B matrix given in appendix C.1, it follows from the Hautus test that the system is controllable for both x_b and $\dot{x}_b$. Based on the open-loop Bode response in figure 3.25 a PID controller is designed. The open-loop system does not contain any poles in the origin. So an integration action is needed to remove steady state error. Figure 3.26 shows the system with a PI controller with proportional gain $K_p = 0.225$ and integration time constant $T_i = 0.133$.

Using a derivative action at $T_d = 0.15$, the -180 degree phase jump due to the cylinder stiffness can be partly compensated. The gain can therefore be increased, and the bandwidth is further increased to 3.76 [Hz]. Note that by applying a derivation action for this purpose, the controlled system is sensitive to large changes in cylinder stiffness. when the cylinder stiffness changes, the frequency where the phase jump occurs shifts. If the stiffness is significantly lower than expected, the phase jump may move left in front of the derivative action. This can lead to stability problems. An open-loop Bode plot for the PID controlled system is found in figure 3.26. The controller gains and performance parameters are given in table 3.5.

Closed-loop

figure 3.27 shows the closed-loop responses of the PID controlled system. The energy in the Kaimal wind spectrum, shown in figure F.2, is focusses within the lower frequencies and decreases quickly for higher frequencies. In the spectral decompensation plot, it is observed that the energy is primarily concentrated in frequencies well below 0.1 Hz. For frequencies below 0.1 Hz, the controlled system shows good performance. However, there is a dip around 0.05 Hz. As a result, a dip is also seen in the step response.

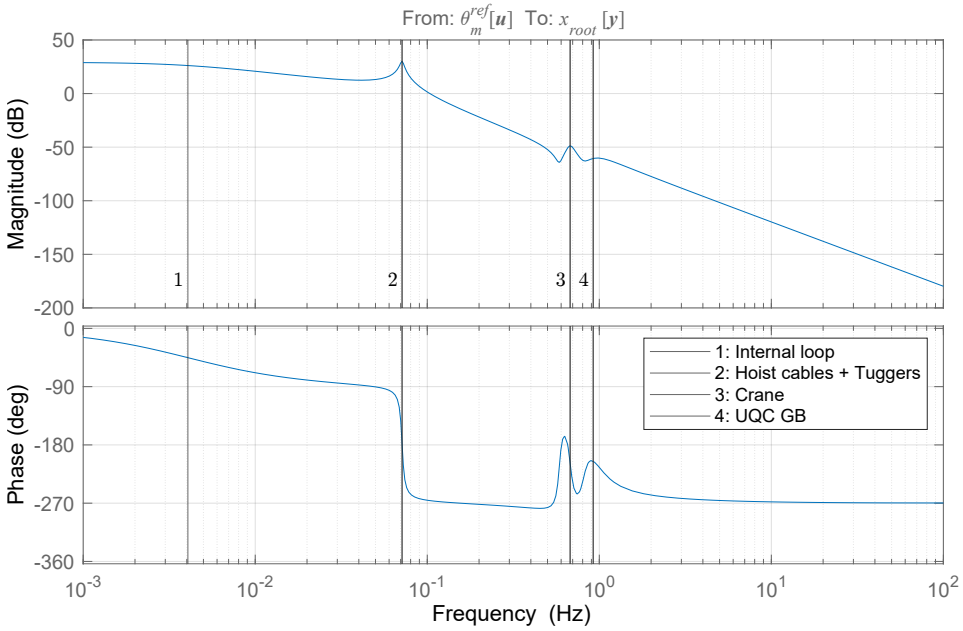

Figure 3.28: Open-loop response of SBIS with the UQC power swivel.

Table 3.6: Natural period (T_n) and relation between amplitudes for the system's Eigenmodes

Mode	1	2	3	4
x_b	0.20	1	0.02	0.01
x_{lb}	0	0.42	0.83	1
x_c	0	0.06	1	0.16
Gearbox[2]	1	0	0	0
T_n (s)	242	14.0	1.48	1.09

Table 3.7: Power swivel pole locations

Pole	ζ	f [Hz]
-0.03	1	0.004
-0.01 $\pm$ 0.45i	0.03	0.07
-0.22 $\pm$ 4.25i	0.05	0.68
-1.39 $\pm$ 5.62i	0.24	0.92

Table 3.8: Control and performance parameters

	Value	unit
K_p	0.45	-
T_i	11.8	s
T_d	2	s
PM	61	deg
GM	6.6	dB
BW	0.0043	Hz

3.5.2. Power swivel

The system poles for the SBIS model with UQC power swivel are listed in table 3.7. Table 3.6 presents an overview of the system's Eigenmodes. The Eigenmodes are plotted in the open-loop system response in figure 3.28. The system has three complex pole pairs, and two complex zero pairs. The open-loop response shows the very slow response of the motor-gearbox. This causes the first phase loss of 90 degrees at 4e-3 Hz. This is the result of the underpowered power swivel for this application. At 0.07 Hz there is a complex pole pair that leads to another 180 phase loss, due to the natural frequency of the suspended load under the main hoist and tuggers around the z-axis. At 0.7 and 0.9 Hz, two more peaks are visible in the open-loop due to complex zero-pole pairs associated with the natural frequency of the crane and gearbox.

The first Eigenmode, a result of the inner control loop's slow response, has very long natural periods of 242 seconds. The slow response of the inner loop severely limits the performance of the power swivel system for motion compensation. The second Eigenmode corresponds to the rotation of the suspended load around the z-axis under the crane. The main stiffnesses that determine the frequency for this Eigenmode are the hoist pendulum rotational stiffness and the tugger rotational stiffness. The expressions for the pendulum and tugger rotational stiffness are given by equation (3.41) and equation (3.45). The rotational stiffnesses are both highly dependent on the lower block width. Wider lower blocks are better for transferring moments around the z-axis. The increased stiffness around the z-axis is one of the reasons for the trend towards wider lower blocks used for offshore LECs.

[2]Motor-gearbox inner loop dynamics section 3.3.2

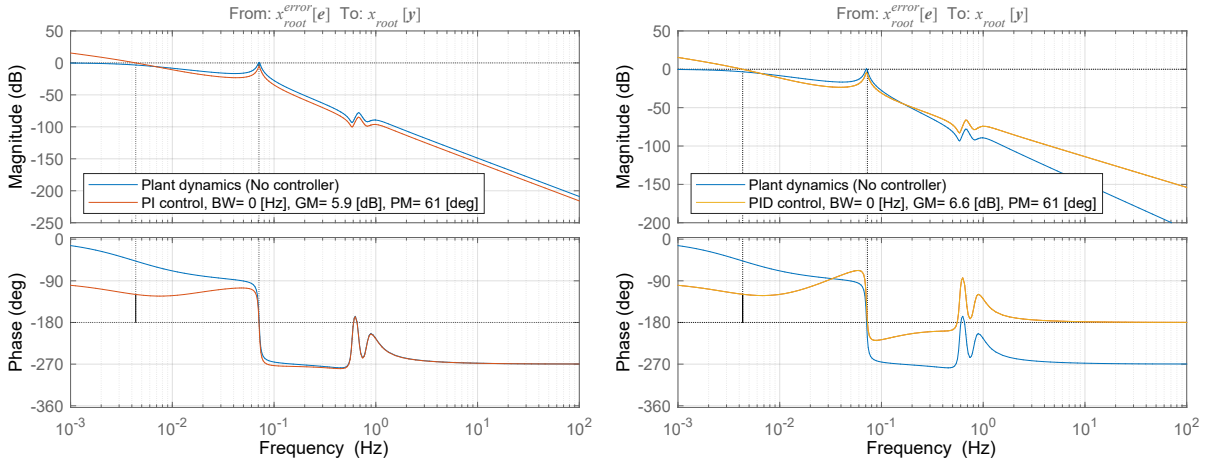

Figure 3.29: Open-loop responses for the PI and the final PID controlled SBIS with power swivel

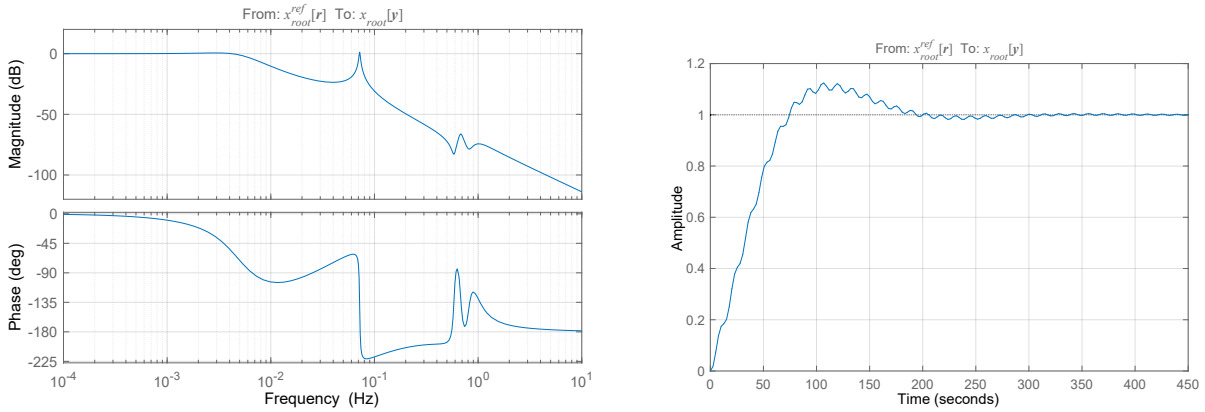

Figure 3.30: Closed-loop response (left) and step response (right) for the controlled SBIS with power swivel

Open-loop

All poles are in the left half plane, which means that the system is stabilisable. For the A and B matrix given in appendix C.2, the system is controllable for both x_b and $\dot{x}_b$. Based on the open-loop Bode response in figure 3.28, a PID controller is designed. An integration action is again needed to remove steady state error. Figure 3.29 shows the system with a PI controller with proportional gain $K_p = 0.45$ and integration time constant $T_i = 11.8$.

The slow internal dynamics limit the bandwidth of the controlled system. Due to the initial 90 degree phase loss from the inner position loop, the -180 degree phase jump due to the pendulum-tugger rotational stiffness can not be compensated with a derivative action. This is also shown in figure 3.29, where even with derivative action, the phase remains below -180 degrees. The final controller gains and performance parameters are summarized in table 3.8.

Closed-loop

figure 3.30 shows the closed-loop responses of the PID controlled system. The closed-loop response shows good tracking performance up to a frequency of 0.004 Hz. The low bandwidth of the controlled system results in a slow response. This is also clearly visible in the step response. From this initial analysis, it seems that the UQC power swivel is not well suited for the proposed application.

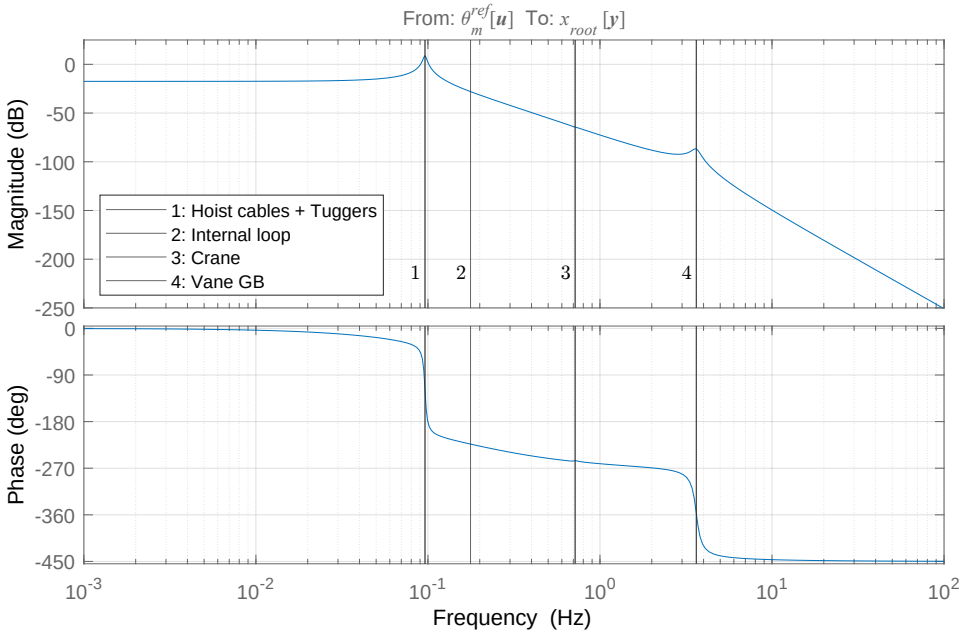

Figure 3.31: Open-loop response of SBIS with wind vanes.

Table 3.9: Natural period (T_n) and relation between amplitudes for the system's Eigenmodes

Mode	1	2	3	4
x_b	1	0	0.02	0
x_c	0.14	0	1	0
x_v	0	1	0	1
Gearbox[3]	0	0.90	0	0
T_n (s)	10.4	5.66	1.39	0.28

Table 3.10: Wind vanes pole locations

Pole	ζ	f [Hz]
-0.01 ± 0.60i	0.02	0.10
-1.11	1	0.18
-0.17 ± 4.50i	0.04	0.72
-1.14 ± 22.80i	0.05	3.63

3.5.3. Wind vanes

table 3.10 shows the pole locations for the SBIS model with wind vanes. Table 3.9 provides an overview of the system's Eigenmodes, also plotted in the open-loop response in figure 3.31. The system has three complex pole pairs, and one complex zero pair. The first -180 degree phase jump corresponds with the Eigenfrequency of the pendulum rotation around the z-axis at 0.1 Hz. The second -180 degree phase jump is the result of the servo gearbox' Eigenfrequency. The effect of the crane's Eigenfrequency and corresponding pole-zero pairs at 0.7 Hz, are barely visible in the open-loop response.

The first Eigenmode has a natural period of 10 seconds and corresponds to the suspended load rotating around the z-axis. Again, the stiffnesses that determine the frequency for this Eigenmode are the hoist pendulum rotational stiffness and the tugger rotational stiffness. As was the case with the UQC power swivel, these stiffnesses are highly dependent on the lower block width and the hoist cable length.

Open-loop

All poles are in the left half plane and the system is controllable for both x_b and $\dot{x}_b$. A PID controller is proposed based on the open-loop Bode response in figure 3.31. An integration action is first added to remove steady state error. Figure 3.32 shows the system with a PI controller with proportional gain $K_p = 0.64$ and integration time constant $T_i = 0.2$.

In the case of the wind vanes, the inner loop dynamics do not cause major problems. Using a derivative action on $T_d = 20$, the -180 degree phase jump from the natural frequency of the suspended load around the z-axis is partly compensated. This way, the bandwidth of the controller is increased to 0.11 [Hz]. Again, by applying a derivation action to compensate for the first Eigenmode, the controller is

[3]Motor-gearbox inner loop dynamics section 3.3.2

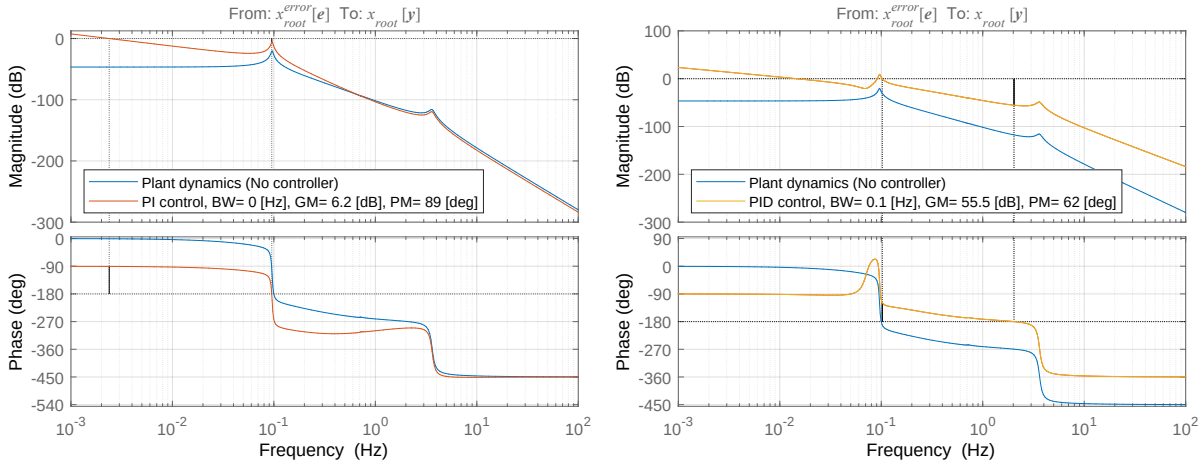

Figure 3.32: Open-loop responses for the PI and the final PID controlled SBIS with wind vanes

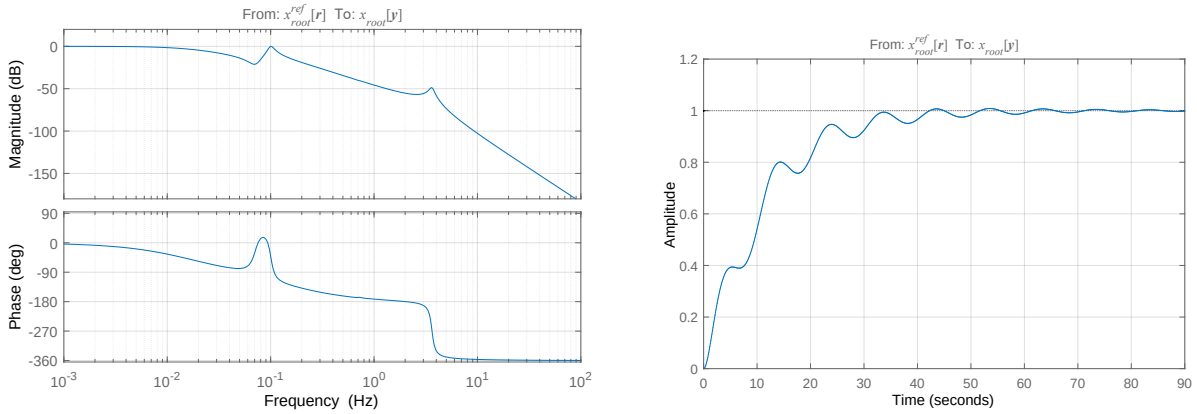

Figure 3.33: Closed-loop response (left) and step response (right) for the controlled SBIS with wind vanes

sensitive to large changes in the pendulum stiffness around the z-axis. The sensitivity to the system parameters was also the case for the XY table. However, unlike for the XY table, the stiffness of the pendulum stiffness depends on the hoist cable length, and is thus variable during hoisting operations. For a longer hoist cable, the stiffness decreases, shifting the Eigenfrequency to the left. This can lead to instability and means that the controller may need to be retuned when the hoist cable length changes significantly. However, during the alignment phase where the compensation is required, the hoist cable length is mostly constant. An open-loop Bode plot for the PID controlled system is found in figure 3.32. The controller parameters are summarized in table 3.11.

Closed-loop

figure 3.33 shows the closed-loop responses of the PID controlled system. The controlled system shows good tracking performance up to 0.01 Hz. There is a dip in the tracking performance around 0.05 Hz. The tracking performance recovers at a frequency of 0.1 Hz, before finally sloping down. As with the UQC power swivel, the bandwidth of the controlled system is low. This is mainly due to the low rotational stiffness of the pendulum and tuggers around the z-axis.

Table 3.11: Control and performance parameters for the wind vanes PID controller

Parameter	Value	unit
K_p	10	-
T_i	0.5	s
T_d	10	s
Phase Margin	62	deg
Gain Margin	55.5	dB
Bandwidth	0.102	Hz

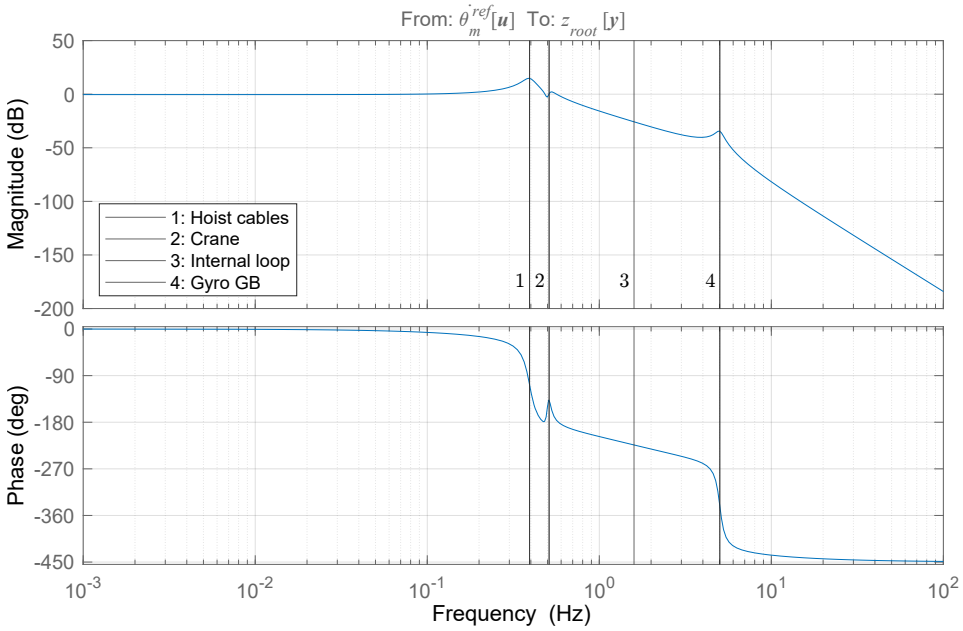

Figure 3.34: Open-loop response of SBIS with gyroscopes.

Table 3.12: Natural period (T_n) and relation between amplitudes for the system's Eigenmodes

Mode	1	2	3	4
x_b	1	1	0.01	0
x_c	0.09	0.59	0	0
x_{gy}	0	0	1	1
Gearbox[4]	0	0	0.44	0
T_n (s)	2.55	1.96	0.63	0.23

Table 3.13: Gyroscopes pole locations

Pole	ζ	f [Hz]
-0.19 ± 2.46i	0.08	0.39
-0.13 ± 3.21i	0.04	0.51
-10	1	1.59
-1.35 ± 27i	0.05	4.30

Table 3.14: Control and performance parameters

	Value	unit
K_p	9.5	-
T_i	0.465	s
T_d	0.8	s
PM	61	deg
GM	22.3	dB
BW	0.464	Hz

3.5.4. Gyroscopes

The pole locations for the linear single DOF SBIS model with gyroscopes are given in table 3.13. The system's Eigenmodes are shown in table 3.12. The Eigenmodes are again plotted in the open-loop system response in figure 3.34. The system has three complex pole pairs, and one complex zero pair. The first -180 degree phase jump at 0.4 Hz corresponds to the natural frequency of the suspended load around the x-axis. After this, around 0.5 Hz, there is a complex zero-pole pair combination that results in a phase peak. This corresponds to the natural frequency of the crane. The second -180 degree phase jump is the result of the gearbox Eigenfrequency in the gyroscope drive.

The first Eigenmode has a natural period of 2.55 seconds and corresponds to the suspended load rotating around the x-axis. The rotational stiffness of the suspended load around the x-axis is considerably higher than the stiffness around the z-axis. This is made possible by the rigid connection between the lower block and the blade (yoke) through the UQC. In the case of rotation around the x-axis, the contribution of the tuggers to the rotational stiffness is neglected. The rotational stiffness is therefore only given by equation (3.62). The stiffness is strongly dependent on the lower block width. In addition, the stiffness is higher for a stiffer hoist cable. If the block is not used in split mode, as assumed here, the stiffness will double and the frequency for this Eigenmode will thus move to the right.

[4] Motor-gearbox inner loop dynamics section 3.3.2

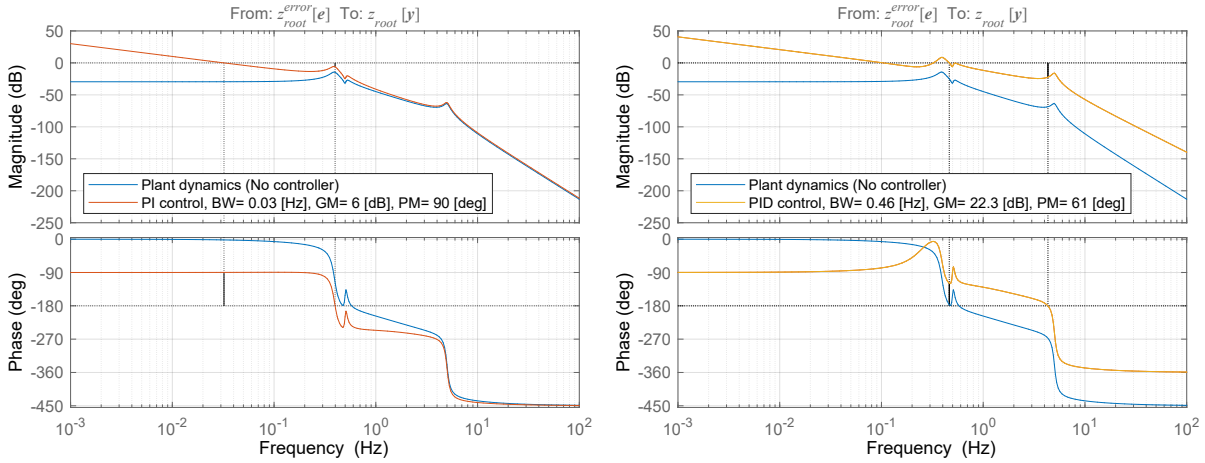

Figure 3.35: Open-loop responses for the PI and the final PID controlled SBIS with gyroscopes

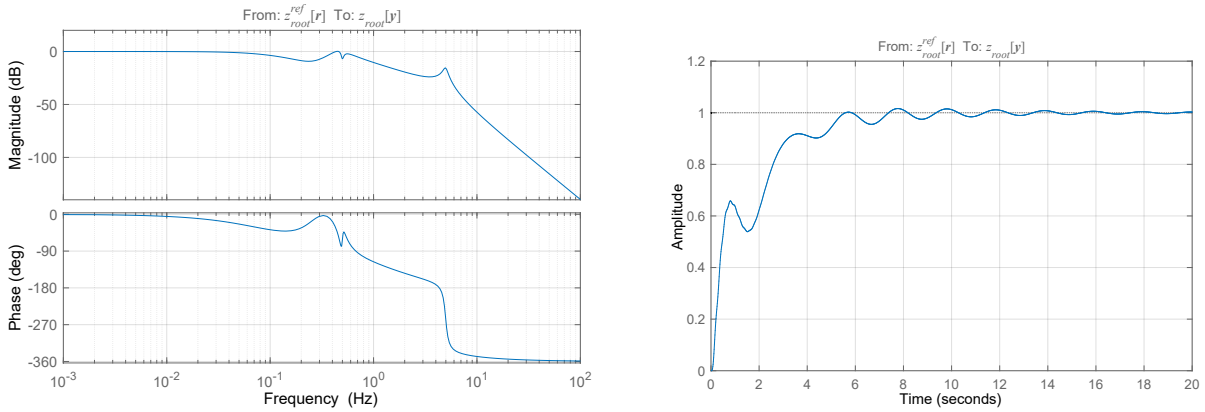

Figure 3.36: Closed-loop response (left) and step response (right) for the controlled SBIS with gyroscopes

Open-loop

All poles are in the left half plane, which means that the system is stabilisable. For the A and B matrix given in appendix C.4 it follows from the Hautus test that the system is controllable for both x_b and $\dot{x}_b$. Based on the open-loop Bode response in figure 3.34, a PID controller is designed. Figure 3.35 shows the open-loop system response with a PI controller with proportional gain $K_p = 1.2$ and integration time constant $T_i = 0.2$.

Using a derivative action at $T_d = 0.8$, the -180 degree phase jump due to the first Eigenmode is partly compensated. This way, the bandwidth of the controller is increased to 0.46 [Hz]. As was previously the case with the wind vanes, this derivative is sensitive to the rotational stiffness of the main hoist, in this case around the x-axis. If the stiffness is significantly lower than expected, the phase jump may move to the left before the derivative action, which can lead to stability problems. The rotational stiffness decreases for longer hoist cable length, a reduction in the of hoist falls, or for a reduced lower block width. An open-loop Bode plot for the PID controlled system is found in figure 3.35. The controller gains and performance parameters are summarized in table 3.14.

Closed-loop

figure 3.36 show the closed-loop response of the PID controlled system. The gyroscope show a good tracking performance up to 0.6 Hz. The energy in the Kaimal wind spectrum is focussed within the lower frequencies and is most significant below 0.1 Hz. For the frequencies below 0.1 Hz, the controlled system shows good performance. The step response shows a quick response. Small oscillations remain in the response with a frequency of 0.5 Hz, which corresponds to the Eigenfrequency of the crane.

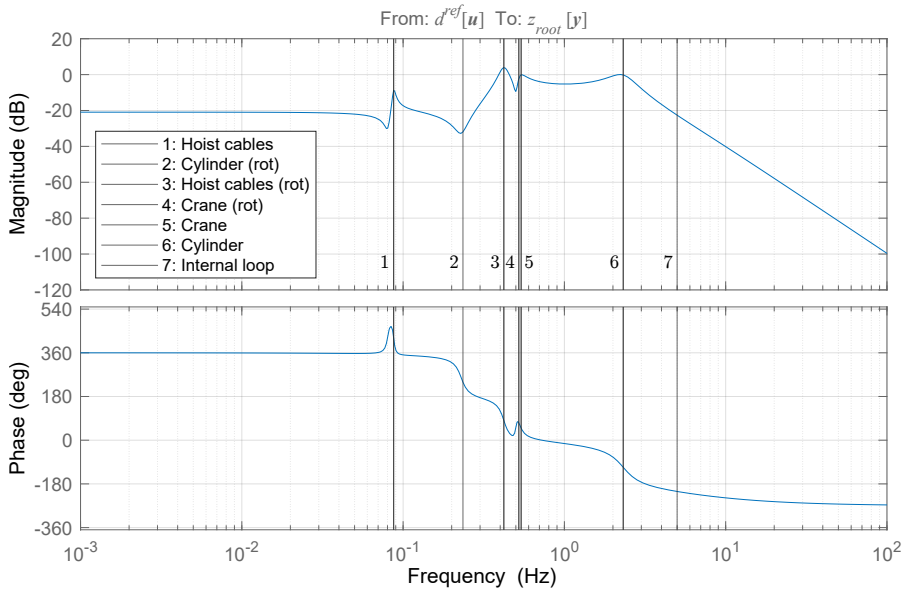

Figure 3.37: Open-loop response of SBIS with COG shifting

Table 3.15: Natural period (T_n) and relation between amplitudes for the system's Eigenmodes

Mode	1	2	3	4	5	6	7
x_b	0	1	1	1	0	0	0
x_c	0	0	0.13	0.35	0	0	0
x_h	1	0.55		0	0.04	1	1
x_{lb}	1	0.9	0	0	0.04	0.06	0.1
x_{bm}	0.24	0	0	0	1	0	0
Valve [5]	0	0	0	0	0	0	0.1
T_n (s)	10.0	4.17	2.37	1.92	1.78	0.53	0.2

Table 3.16: COG shifting pole locations

Pole	ζ	f [Hz]
-0.02 ± 0.63i	0.03	0.10
-1.51	1	0.24
-0.18 ± 2.64i	0.07	0.42
-0.18 ± 3.27i	0.06	0.52
-0.29 ± 3.52i	0.08	0.56
-1.78 ± 11.8i	0.15	1.89
-31.40	1	5

Table 3.17: Control and performance parameters

	Value	unit
K_p	3	-
T_i	0.02	s
PM	81	deg
GM	8.4	dB
BW	0.104	Hz

3.5.5. COG shifting

table 3.16 displays the pole locations for the linear Single DOF COG shifting SBIS. The system's Eigenmodes are found in table 3.15. These are again plotted in the open-loop system response in figure 3.37. The system has five complex pole pairs, and four zero pairs. The linear system consists of a translational and rotational system, coupled using the coupling equation given by equations (3.81) and (3.82). The first peak in the phase plot around 0.08 Hz is the result of neighbouring complex pole pair and zero pairs at the natural frequency of pendulum swing. This mode has a relatively long natural periods of 12 seconds. The main stiffnesses that determine the frequency associated with this Eigenmode are the hoist pendulum stiffness and the tugger stiffness. The expression for pendulum stiffness is found in equation (3.62), and is highly dependent on the hoist cable length. When the length of this hoist cable is shortened, the frequency of this mode will move to the right in the Bode plot.

The second Eigenmode at 0.24 Hz is a result of the coupling between the translational and rotational models. When the cylinder translates the blade, the reaction force also causes a rotation of the suspended load around the x-axis. This results in a phase loss of 180 degrees, and corresponds to the natural frequency of the cylinder translated to the rotational system.

The third Eigenmode corresponds with the suspended load rotating around the x-axis. As was the case with the gyroscopes, this complex pole results in another -180 degree phase jump. The frequency is slightly different from the gyroscope model, as the inertia of the suspended load is also slightly different. The same resonance peak corresponding to the crane natural frequency is also observed. Finally, around 1.9 Hz there is a complex pole pair that leads to -180 degree phase jump, corresponding to the natural frequency of the hydraulic cylinder.

[5] Servo valve inner loop dynamics section 3.3.1

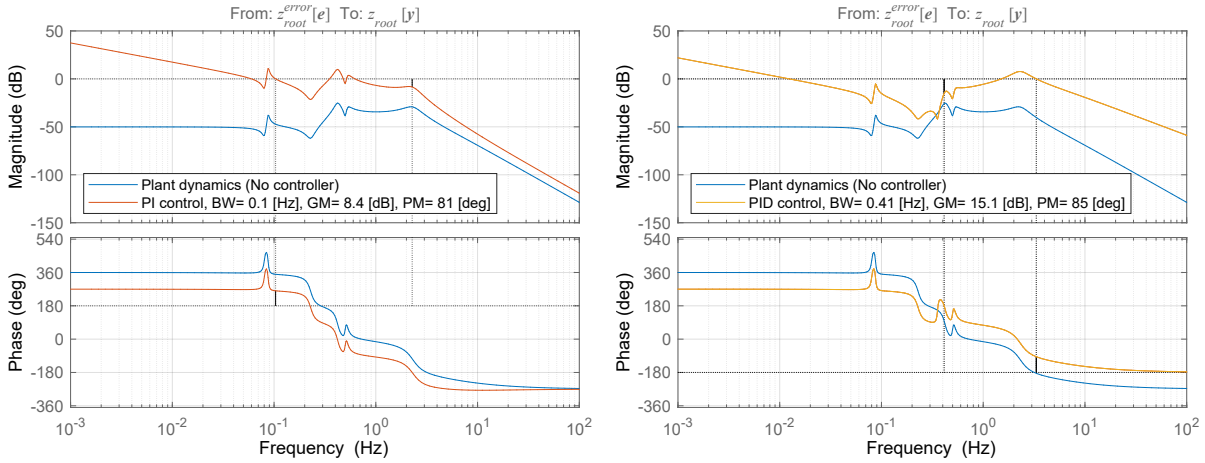

Figure 3.38: Open-loop responses for the final PI and PID controlled SBIS with COG shifting (AM5 & AM5.B)

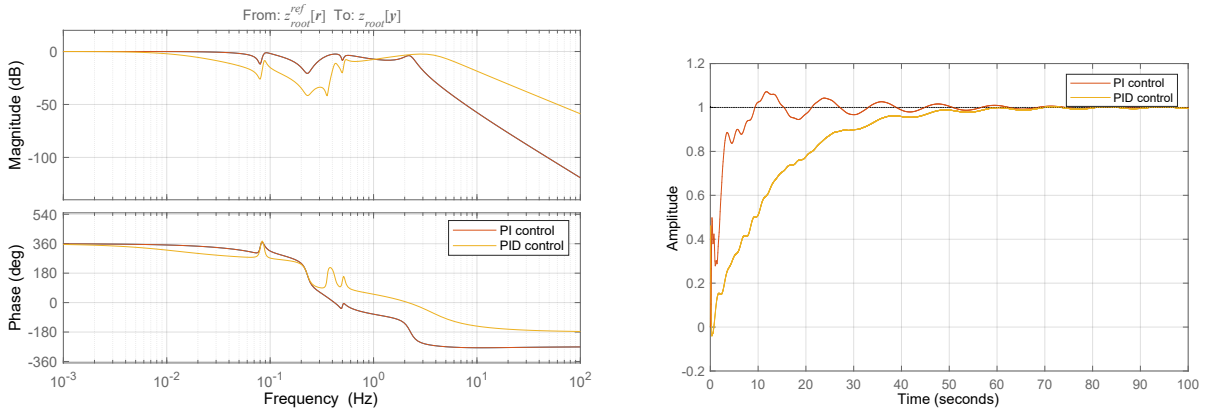

Figure 3.39: Closed-loop response (left) and step response (right) for the controlled SBIS with COG shifting

Open-loop

All poles are in the left half plane and the system is controllable for both x_b and $\dot{x}_b$. Based on the open-loop Bode response in figure 3.37 a linear controller is proposed. The same controller is used for the COG shifting method with (AM5.B) and without (AM5) counterweight. A comparison between the two is found in appendix F.3. The open-loop system does not contain any poles in the origin. So an integration action is needed to remove steady state error. The open response for with a PI controller with proportional gain $K_p = 3$ and integration time constant $T_i = 0.02$ is shown in figure 3.35.

Closed-loop

The PI controlled system has a bandwidth of 0.11 Hz, limited by the two subsequent -180 degree phase jumps. These correspond with the cylinder Eigenfrequency effecting the rotational system, and the stiffness of the hoist cables around the x-axis. Due to the quick succession of the phase jumps, a derivative action is not effective at increasing the control performance. Figure 3.38 shows the system response for a PID controlled system, with a derivative action at $T_d = 10$. Although the theoretical bandwidth is improved, this does not result in an improved performance. This is clear from the step responses for the PI and PID controlled system shown in figure 3.39.

The closed-loop response for the PI controlled system shows good tracking performance up to around 0.04 Hz. Due to the various Eigenfrequencies effecting the system after this, the performance fluctuates before first sloping down slowly from 0.5Hz, and then quickly beyond 2 Hz, due to the complex pole pair corresponding with the hydraulic cylinder's natural frequency. The step response time is approximately 9 seconds. Small oscillations with a frequency of 0.1 Hz remain, which corresponds to the Eigenfrequency of the load pendulum.

3.6. Summary

This chapter addresses the development and analysis of the 1DOF models. A key objective of creating these linear models is to formulate a PID controller. This controller enables the simulation of actuation methods in the time domain in chapters 4 and 5. Additionally, the simplified 1DOF representations are later used to verify the behaviour of numerical models in the frequency domain in appendix D. On the basis of the analysis in this chapter, subquestions four and five are answered as follows.

SQ4: How can the single-blade installation systems for the actuation methods be linearly described? Simplified models are introduced to characterize the dynamics of actuators. Hydraulic cylinders and motor-gearboxes often contain internal controllers regulating cylinder stroke and motor position or speed. In further modelling, these internal dynamics are simplified using first-order transfer functions. The time constant governing these dynamics is determined separately for each actuation method that uses a motor-gearbox for actuation in appendix B.

The model development involves reducing the 6DOF system to a single degree of freedom, corresponding to the actuated DOF for the actuation method. The system is represented using a mass-spring-damper model, which is then translated into a state-space model using the Euler-Lagrange method. This provides the linear mathematical expression of the system suitable for further analysis. It is worth noting that the linear representation significantly simplifies reality and assumes no significant coupling between the DOF. This coupling between different DOF is investigated in verification simulation runs covered in subsequent chapters. Refer to appendix D for more details.

SQ5: How can the actuated single-blade installation systems be controlled? A frequency domain analysis is performed on the linear 1DOF models. All actuation methods yield stabilisable systems where the blade root position is controllable. The open-loop responses are analysed, based on which PID controllers are proposed. Noteworthy insights from this analysis are summarized below:

- The PID controlled XY table exhibits good tracking performance with a bandwidth of 3.67 Hz, sufficient for wind disturbance, since most of the wind spectrum energy lies within frequencies below 0.1 Hz. When the counterweight mass is close enough to that of the blade (yoke), as assumed here, the hydraulic cylinder stiffness limits the bandwidth.
- When the counterweight does not exactly match the mass of the blade (yoke), compensation introduces feedback to the system. A lighter counterweights result in a phase loss peak at 0.23 Hz, while a heavier counterweight results in phase gain in the open-loop response. Therefore, a slightly heavier counterweight is more favourable for the controlled system.
- Both the UQC power swivel and wind vanes show low bandwidths of 0.004 Hz and 0.1 Hz respectively. The power swivel's limitation is its small motor handling a large rotational inertia, leading to slow response. However, it is anticipated that even with increased motor power, a high bandwidth is unlikely. The rotational stiffness of the pendulum around the z-axis is low, which also limits the performance of the wind vane. This stiffness can be increased by decreasing the hoist cable length or by using a wider lower block.
- For all actuation methods, pendulum stiffness depends on hoist cable length, which can affect controller stability during hoisting operations.
- While crane stiffness has negligible impact on the XY table, power swivel, and wind vanes, its natural frequency in the actuated DOF of the gyroscope is close to the control bandwidth of 0.46 Hz. However, the primary limiting factor remains the hoist cable stiffness. Again, the width of the lower block is important for this stiffness, as well as the stiffness and the number of cable bundles. A split-block configuration is assumed. However, using all bundles will increase stiffness, and could yield a higher bandwidth.
- The COG shifting models, feature a translational and rotational model connected through coupling equations. Both the translational and rotational pendulum stiffness are limiting. Also, a phase loss is observed that corresponds to the hydraulic cylinder's natural frequency, fed back to the rotational system. Using a PI controller instead of PID improves tracking and closed-loop performance due to closely spaced limiting modes. The hoist cable length, lower block width, and the vertical offset between the lower block and blade COG (L_{cog}), significantly impact dynamics. A shorter hoist length, wider LB, and minimizing L_{cog} are advantageous.

4

Nonlinear modelling

To evaluate the actuation input and compensation effectiveness of the actuation methods, simulations are performed in the time domain. The simulations of the individual actuation methods are performed within their respective operational planes. The linear PID controllers developed based on the 1DOF linear models are applied. The additional two DOF allows the models to capture more multidimensional dynamic behaviour and provides a more detailed and realistic insight into how the system behaves in the time domain.

The 3DOF numerical models that describe the blade installation system for the actuation methods are introduced first. The models, used to simulate the single blade installation systems, are built from several building blocks that describe different parts of the SBIS. The blocks used to construct the nonlinear 3DOF (single plane & rotation) numerical assessment models are introduced in section 4.1.

The models are specifically developed for the application of single-blade installation of a 15 MW OWT blade, with a separate model for each actuation method. To ensure the models behave as expected, two verification methods are described in section 4.2. In this section and accompanying appendix D, the coupling between the DOF is also explored.

All modelling and simulation is conducted within the Matlab/Simulink environment. For the sake of consistency, the nomenclature and conventions used to describe the model dynamics are chosen to agree with the MarIn toolbox [9]. This ensures compatibility with the MarIn wind model and facilitates future model expansion in chapter 5, using the transformation functions provided by the toolbox. The simulation results are presented in section 4.4.

This chapter further addresses the sixth sub-question:

SQ6: How to model the HMC actuation methods for the application of single-blade OWT installation?

4.1. Numerical model

For the numerical modelling of the SBIS, additional crane-fixed and weight-fixed coordinate systems are introduced on top of the originally defined coordinate system in section 2.3. The coordinate systems also follow the right-hand rule. The orientation of the original and additional coordinate systems used in the 3DOF numerical models are shown in figure 4.1 for the SBIS with XY table.

- The origin of the crane-fixed coordinate system $\mathbf{o}_c$ is located between the main hoist point at the crane tip. The axis orientation align with the global axis system at $t = 0$. The translational and angular velocities in x^c-,y^c- and z^c-direction are given by u_c, v_c, w_c and p_c, q_c, r_c, respectively.
- The origin of the weight-fixed coordinate system $\mathbf{o}_w$ is located at the COG of the counterweight. At $t = 0$, the origin is positioned directly under the lower block along the z_h -axis. The axis orientation align with the global axis system at $t = 0$. The translational and angular velocities in x^w-,y^w- and z^w-direction are given by u_w, v_w, w_w and p_w, q_w, r_w, respectively.

Six numerical models are developed, each for a SBIS with their corresponding actuation method. The SBIS with actuation method is described in three DOFs, two translational and one rotational DOF. The included DOFs depend on the actuated DOF. The XY table, Power swivel and vanes are described in yaw-plane (XY), while the gyroscopes and COG shifting are described in roll-plane (YZ). For yaw-plane and roll-plane, the position and orientation state of a body is given as per equation (4.1).

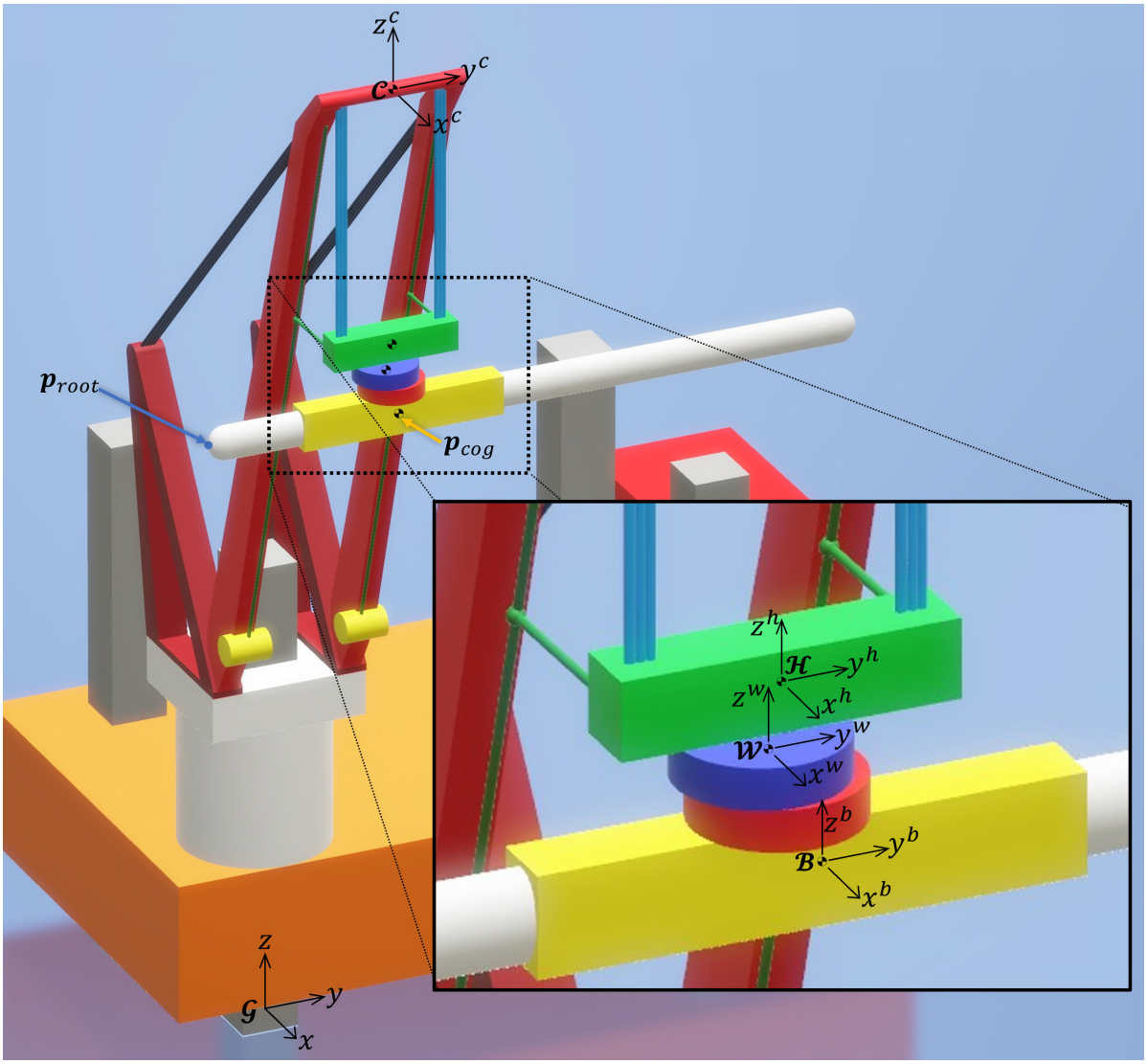

Figure 4.1: Overview of the original and additional coordinate systems for the SBIS (with XY table)

Table 4.1: Denotation of the position and velocity parameters for original and additional coordinate systems

Frame	Origin	Position[1]	Orientation $\backslash\mathcal{N}$	Translational vel.	Rotational velocity
$\mathcal{G}$	$\mathbf{o}_g$	$\boldsymbol{p} = [x, y, z]^\top$	$-$	$\boldsymbol{v} = [\dot{x}, \dot{y}, \dot{z}]^\top$	$-$
$\mathcal{H}$	$\mathbf{o}_h$	$\boldsymbol{p}^h = [x^h, y^h, z^h]^\top$	$\boldsymbol{\theta}_h = [\alpha_h, \beta_h, \gamma_h]^\top$	$\boldsymbol{v}_h = [u_h, v_h, w_h]^\top$	$\boldsymbol{\omega}_h = [p_h, q_h, r_h]^\top$
$\mathcal{B}$	$\mathbf{o}_b$	$\boldsymbol{p}^b = [x^b, y^b, z^b]^\top$	$\boldsymbol{\theta}_b = [\alpha, \beta, \gamma]^\top$	$\boldsymbol{v}_b = [u, v, w]^\top$	$\boldsymbol{\omega}_b = [p, q, r]$
$\mathcal{C}$	$\mathbf{o}_w$	$\boldsymbol{p}^c = [x^c, y^c, z^c]^\top$	$\boldsymbol{\theta}_c = [\alpha_c, \beta_c, \gamma_c]^\top$	$\boldsymbol{v}_c = [u_c, v_c, w_c]^\top$	$\boldsymbol{\omega}_c = [p_c, q_c, r_c]^\top$
$\mathcal{W}$	$\mathbf{o}_w$	$\boldsymbol{p}^w = [x^w, y^w, z^w]^\top$	$\boldsymbol{\theta}_w = [\alpha_w, \beta_w, \gamma_w]^\top$	$\boldsymbol{v}_w = [u_w, v_w, w_w]^\top$	$\boldsymbol{\omega}_w = [p_w, q_w, r_w]^\top$

$$\text{yaw-plane} \rightarrow \begin{bmatrix} \boldsymbol{p}_i \\ \boldsymbol{\theta}_i \end{bmatrix} = \begin{bmatrix} x_i \\ y_i \\ \gamma_i \end{bmatrix}, \qquad \text{roll-plane} \rightarrow \begin{bmatrix} \boldsymbol{p}_i \\ \boldsymbol{\theta}_i \end{bmatrix} = \begin{bmatrix} y_i \\ z_i \\ \alpha_i \end{bmatrix} \tag{4.1}$$

[1] in corresponding frame

The models are constructed from blocks, which describes a part of the system. For example, a block can describe the dynamics of the crane body, or the dynamics of the main hoist between the crane and lower block body. The blocks are built in a Simulink library, which means they are identical for any numerical model in which they are used. By using the same blocks in the numerical models, it is certain that all these sub-models behave identically in all numerical models. The blocks are divided into three categories, briefly described below. An overview of the different building blocks is found in table 4.2. Table 4.3 provides an overview of which blocks are used in each model.

1. **Dynamics:** This block describes the 3DOF body dynamics of the crane at the crane tip, and the lower block, blade (yoke) or counterweight around their COG. These blocks use the forces acting on the body as an input and provide the position in the global frame $\mathcal{G}$ and velocity in their corresponding local frame as output. The blocks are explained in more detail in section 4.1.2.
2. **Internal coupling:** This type of block describes the coupling between two bodies. This type of blocks uses the states from two of the body dynamics block as their input. In some cases, there is an additional control input. This control input is a reference motor speed, or reference cylinder and motor position. Blocks that fall under this category include the main hoist loads, tugger line loads, UQC loads, and hydraulic cylinder loads. The output of these blocks are the forces and moments acting on the two corresponding bodies. Section 4.1.3 further discusses the contents of the individual blocks.
3. **External loads:** This type of block describes the calculation of external load acting on the SBIS from either gyroscopic precession, gravity or aerodynamic loads. For the latter, the wind model from the MarIn toolbox [9] is used. It is assumed that there is no feedback from the system states to the gyroscope and vane. Despite being external loads and there being no direct feedback from the system states to the vane and wind box, the wind loads and vane loads blocks use the blade (yoke) body state as input. This is needed as the wind loading depend on the blade orientation. The output consists of forces and moments acting on the blade (yoke). These blocks are described in section 4.1.4

Table 4.2: Overview of blocks used to build numerical models, including block inputs and outputs

Name	Short form	Type	Input(s)	Output(s)
Crane	C	Dynamics	$\boldsymbol{\tau}_{mh}, \boldsymbol{\tau}_t$	$\boldsymbol{\eta}_c, \boldsymbol{\nu}_c$
Lower block	LB	Dynamics	$\boldsymbol{\tau}_{mh}, \boldsymbol{\tau}_t, \boldsymbol{\tau}_{qc}, \boldsymbol{\tau}_h, \boldsymbol{\tau}_{cw}$	$\boldsymbol{\eta}_h, \boldsymbol{\nu}_h$
Blade (yoke)	B	Dynamics	$\boldsymbol{\tau}_{qc}, \boldsymbol{\tau}_h, \boldsymbol{\tau}_w, \boldsymbol{\tau}_v, \boldsymbol{\tau}_{qy}$	$\boldsymbol{\eta}_b, \boldsymbol{\nu}_b$
Counterweight	CW	Dynamics	$\boldsymbol{\tau}_{cw}$	$\boldsymbol{\eta}_w, \boldsymbol{\nu}_w$
Main hoist	MH	Coupling	$\boldsymbol{\eta}_h, \boldsymbol{\eta}_c$	$\boldsymbol{\tau}_{mh}$
Tugger lines	T	Coupling	$\boldsymbol{\eta}_h, \boldsymbol{\eta}_c$	$\boldsymbol{\tau}_t$
UQC	QC	Coupling	$\boldsymbol{\eta}_h, \boldsymbol{\eta}_b$	$\boldsymbol{\tau}_{qc}$
Power swivel	PS	Coupling	$\boldsymbol{\eta}_h, \boldsymbol{\eta}_b, \ \boldsymbol{u}_{qc}$	$\boldsymbol{\tau}_{qc}$
Hydraulics	H	Coupling	$\boldsymbol{\eta}_h, \boldsymbol{\eta}_b, \ \boldsymbol{u}_h$	$\boldsymbol{\tau}_h$
CW Hydraulics	CWH	Coupling	$\boldsymbol{\eta}_h, \boldsymbol{\eta}_w, -\boldsymbol{u}_h$	$\boldsymbol{\tau}_{cw}$
Wind	W	External	$\boldsymbol{\eta}_b$	$\boldsymbol{\tau}_w$
Gravity	G	External	$\boldsymbol{\eta}_h, \boldsymbol{\eta}_b, \boldsymbol{\eta}_w$	$\boldsymbol{\tau}_g$
Vanes	V	External	$\boldsymbol{\eta}_b, \ \boldsymbol{u}_v$	$\boldsymbol{\tau}_v$
Gyroscopes	GY	External	$\boldsymbol{u}_{qy}$	$\boldsymbol{\tau}_{qy}$

Table 4.3: Blocks used to construct the SBIS for each actuation method

AM	Plane	CW	C	LB	B	MH	T	QC	PS	H	CWH	W	G	V	GY
XY table	XY	✓	✓	✓	✓	✓	✓			✓	✓	✓			
Power swivel	XY		✓	✓	✓	✓	✓		✓			✓			
Vanes	XY		✓	✓	✓	✓	✓	✓				✓		✓	
Gyroscopes	YZ		✓	✓	✓	✓		✓				✓	✓		✓
COG shifting	YZ		✓	✓	✓	✓				✓		✓	✓		
COG shifting CW	YZ	✓	✓	✓	✓	✓		✓			✓	✓	✓		

4.1.1. Coordinate rotations and translations

A rotation matrix $\boldsymbol{R}$ is introduced in equation (4.2). This matrix allows for the transformation of positions and vectors between the different defined coordinate systems. Here, $\boldsymbol{\theta}_i$ represents the orientation of frame i relative to the global coordinate system. Equation (4.2) shows the rotation matrix between the global and blade-fixed coordinate systems for both the yaw-plane and roll-plane models.

$$\text{yaw-plane} \rightarrow \boldsymbol{R}\left(\boldsymbol{\theta}_b\right) = \begin{bmatrix} \cos\gamma & -\sin\gamma \\ \sin\gamma & \cos\gamma \end{bmatrix} \tag{4.2}$$

$$\text{roll-plane} \rightarrow \boldsymbol{R}\left(\boldsymbol{\theta}_b\right) = \begin{bmatrix} \cos\alpha & -\sin\alpha \\ \sin\alpha & \cos\alpha \end{bmatrix} \tag{4.3}$$

Coordinate translations

The coordinate rotations and translations conventions used are formulated by Diebel *et al.* [45]. Using the rotation matrix $\boldsymbol{R}$, the transformation of a vector in the global frame $\mathcal{G}$ to the blade-fixed frame $\mathcal{B}$ is given by equation (4.4). The operation in the opposite direction is realized using the transform of the same rotation matrix, shown in equation (4.5).

$$\boldsymbol{z}^b = \boldsymbol{R}\left(\boldsymbol{\theta}_b\right)\boldsymbol{z} \tag{4.4}$$

$$\boldsymbol{z} = \boldsymbol{R}\left(\boldsymbol{\theta}_b\right)^\top \boldsymbol{z}^b \tag{4.5}$$

For the transformation of a point in space, the offset to the origin first needs to be subtracted. An example of the transformation of a point from global to the blade-fixed coordinates system and vice versa are shown in equation (4.6) and equation (4.7), respectively. Here $\mathbf{o}_b$ is the origin of the blade-fixed coordinate system in the $\mathcal{G}$-frame, and $\mathbf{o}_g^b$ the origin of the global coordinate system in the $\mathcal{B}$-frame.

$$\boldsymbol{p}^b = \boldsymbol{R}\left(\boldsymbol{\theta}_b\right)\boldsymbol{p} + \mathbf{o}_g^b \quad = \boldsymbol{R}\left(\boldsymbol{\theta}_b\right)\left(\boldsymbol{p} - \mathbf{o}_b\right) \tag{4.6}$$

$$\boldsymbol{p} = \boldsymbol{R}\left(\boldsymbol{\theta}_b\right)^\top \boldsymbol{p}^b + \mathbf{o}_b = \boldsymbol{R}\left(\boldsymbol{\theta}_b\right)^\top \left(\boldsymbol{p}^b - \mathbf{o}_g^b\right) \tag{4.7}$$

Motion of a Fixed Point on a Rigid Body

For a point $\boldsymbol{p}$ rigidly attached to body j at $\boldsymbol{p}_p^j$, the general expression for the velocity of $\boldsymbol{p}$ in terms of the motion of the rigid body is given by equation (4.8).

$$\boldsymbol{v}_p = \boldsymbol{v}_j + \boldsymbol{\omega}_j \times \boldsymbol{p}_{p/j} \tag{4.8}$$

Where $\boldsymbol{p}_j$ is the global position of the body, $\boldsymbol{v}_j$ the body's global velocity, and $\boldsymbol{\omega}_j$ the angular velocity. $\boldsymbol{p}_{p/j}$ is the position of point $\boldsymbol{p}$ relative to the COG of body j in the global frame. For the 3DOF planar models, the expression is rewritten to equation (4.9)

$$\boldsymbol{v}_p = \boldsymbol{v}_j + \boldsymbol{R}\left(\boldsymbol{\theta}_j\right)^\top \boldsymbol{C}\left(\boldsymbol{\omega}_j\right)\left(\boldsymbol{p}_p^j - \mathbf{o}_j^j\right). \tag{4.9}$$

$$\boldsymbol{C}(\boldsymbol{\omega}) = \begin{bmatrix} 0 & -\omega \\ \omega & 0 \end{bmatrix} \tag{4.10}$$

Euler angle rate matrix

The Euler angle rate matrix $\boldsymbol{T}$ is another transformation matrix which is used to transform the body-fixed angular velocity ω to the global angular velocity u. The two transformation matrices $\boldsymbol{R}$ and $\boldsymbol{T}$ are combined to form the transformation matrix $\boldsymbol{J}\left(\boldsymbol{\theta}\right)$, which allows for transformation of the body-fixed velocities to their global equivalent, as shown in equation (4.12). For the reduced 3DOF models, the Euler angle rate matrix simplifies to $\boldsymbol{T}(\boldsymbol{\theta}) = I_1$.

$$\boldsymbol{J}\left(\boldsymbol{\theta}\right) = \begin{bmatrix} \boldsymbol{R}\left(\boldsymbol{\theta}\right) & 0_{1\times 2} \\ 0_{2\times 1} & \boldsymbol{T}(\boldsymbol{\theta}) \end{bmatrix} \tag{4.11}$$

$$\dot{\boldsymbol{\eta}} = \boldsymbol{J}\left(\boldsymbol{\theta}\right)\boldsymbol{\nu} = \begin{bmatrix} \dot{\boldsymbol{p}} \\ \dot{\boldsymbol{\theta}} \end{bmatrix} = \boldsymbol{J}\left(\boldsymbol{\theta}\right)\begin{bmatrix} \boldsymbol{v} \\ \boldsymbol{\omega} \end{bmatrix} \tag{4.12}$$

4.1.2. Body dynamics

There are a total of 4 bodies, namely the crane, lower block, blade (yoke) and counterweight. Each body has a mass and inertia and is modelled as a rigid-body. All loads act on the COG of the body. The kinematics of the bodies are described by Newton's second law. The dynamics of the blade (yoke) and counterweight rigid bodies are described by equation (4.13), where $\boldsymbol{M} = diag\begin{bmatrix} M & M & I \end{bmatrix}$ is the mass matrix that belongs to the body. I describes the inertia of the body. For the models in the XY plane, this is the inertia around the z-axis I_z. For the models in the YZ plane, the inertia around the x-axis, I_x, is used instead. $\boldsymbol{\tau}_{cpl,i}$ and $\boldsymbol{\tau}_{ex,i}$ are the coupling and external loads acting on the body. Finally, n_{cpl} and n_{ex} are the numbers of coupling and external loads acting on the body, respectively. The output from the body dynamics block are the global position and orientation $\boldsymbol{\eta}$ and the translational and rotations velocity in the local frame $\boldsymbol{\nu}$.

$$\boldsymbol{M}\dot{\boldsymbol{\nu}} = \sum_{i=1}^{n_{cpl}} \boldsymbol{\tau}_{cpl,i} + \sum_{i=1}^{n_{ex}} \boldsymbol{\tau}_{ex,i} \tag{4.13}$$

Crane stiffness

The dynamics of the crane is described by equation (4.14), where the extra contribution $\boldsymbol{\tau}_c$ are the loads, due to the stiffness of the crane. This contribution is determined by equation (4.15), where $\boldsymbol{\eta}_{c_\circ}$ is the initial position and orientation of the crane, $\boldsymbol{K}_c$ is the stiffness matrix of the crane and $\boldsymbol{D}_c$ the damping matrix, given by equation (4.17) or equation (4.18).

$$\boldsymbol{M_c}\dot{\boldsymbol{\nu}}_c = \sum_{i=1}^{n_{cpl}} \boldsymbol{\tau}^c_{cpl,i} + \sum_{i=1}^{n_{ex}} \boldsymbol{\tau}^c_{ex,i} + \boldsymbol{\tau}^c_c \tag{4.14}$$

$$\boldsymbol{\tau}^c_c = (\boldsymbol{\eta}_c - \boldsymbol{\eta}_{c_\circ})\boldsymbol{K}_c + \boldsymbol{\nu}_c\boldsymbol{D}_c \tag{4.15}$$

$$\boldsymbol{\eta}_c = \begin{bmatrix} \boldsymbol{p}_c \\ \boldsymbol{\theta}_c \end{bmatrix}, \quad \boldsymbol{\eta}_{c_\circ} = \begin{bmatrix} \boldsymbol{p}_{c_\circ} \\ \boldsymbol{\theta}_{c_\circ} \end{bmatrix} \tag{4.16}$$

$$\text{yaw-plane} \rightarrow \boldsymbol{K}_c = \begin{bmatrix} k_{c,x} & 0 & 0 \\ 0 & k_{c,y} & 0 \\ 0 & 0 & k_{c,\gamma} \end{bmatrix}, \qquad \boldsymbol{D}_c = \begin{bmatrix} c_{c,x} & 0 & 0 \\ 0 & c_{c,y} & 0 \\ 0 & 0 & c_{c,\gamma} \end{bmatrix} \tag{4.17}$$

$$\text{roll-plane} \rightarrow \boldsymbol{K}_c = \begin{bmatrix} k_{c,y} & 0 & 0 \\ 0 & k_{c,z} & 0 \\ 0 & 0 & k_{c,\alpha} \end{bmatrix}, \qquad \boldsymbol{D}_c = \begin{bmatrix} c_{c,y} & 0 & 0 \\ 0 & c_{c,z} & 0 \\ 0 & 0 & c_{c,\alpha} \end{bmatrix} \tag{4.18}$$

4.1.3. Coupling loads

The coupling blocks describe the coupling between the rigid bodies provided by the wire ropes, hydraulic cylinders, or the Huisman UQC.

Main hoist (MH)

The wire ropes are modelled as tensile-only springs. The models utilize the "Lifting equipment/Wire rope" submodel available in the MarIn toolbox [9]. The weight of the cables themselves is neglected. The model of the wire rope in the MarIn toolbox is defined by equation (4.19). Here, $\boldsymbol{p}_A$ and $\boldsymbol{p}_B$ are the positions of the wire rope ends, $l_\circ$ is the static length of the wire rope, and k and c are the stiffness and damping of the wire rope.

$$\boldsymbol{f}_A = -\left(\kappa(\delta_{AB})k\delta_{AB} - c\dot{\delta}_{AB}\right)\frac{\boldsymbol{l}_{AB}}{|\boldsymbol{l}_{AB}|} \tag{4.19}$$

$$\boldsymbol{f}_B = -\boldsymbol{f}_A \tag{4.20}$$

$$\boldsymbol{l}_{AB} = \boldsymbol{p}_A - \boldsymbol{p}_B \tag{4.21}$$

$$\delta_{AB} = |\boldsymbol{l}_{AB}| - l_\circ \tag{4.22}$$

$$\kappa(\delta_{AB}) = \begin{cases} 1 & \delta_{AB} \geq 0 \\ 0 & \delta_{AB} < 0 \end{cases} \tag{4.23}$$

The inputs of the Main Hoist (MH) block are the positional and velocity states of the crane and lower block, denoted by $\boldsymbol{\eta}_c, \boldsymbol{\nu}_c, \boldsymbol{\eta}_h$ and $\boldsymbol{\nu}_h$. The two main hoist cables, each with 6 falls, are modelled as linear tensile springs with stiffness k_{mh}, damping c_{mh} and length l_{mh}. The mounting of the hoist cable on the crane side is given by equation (4.25). The mounting of the main hoist on the lower block side is given by equation (4.26). $\boldsymbol{p}^c_{mh_c,i}$ and $\boldsymbol{p}^h_{mh_h,i}$ represent the positions of the main hoist mounting expressed in the local coordinate system. In the local coordinate system, these positions are both given by $\begin{bmatrix}0 & \pm W_{lb}/2\end{bmatrix}^\top$ for the XY models, and $\begin{bmatrix}\pm W_{lb}/2 & 2\end{bmatrix}^\top$ for the YZ models.

$$\boldsymbol{\eta}_c = \begin{bmatrix}\boldsymbol{p}_c \\ \boldsymbol{\theta}_c\end{bmatrix}, \quad \boldsymbol{\nu}_c = \begin{bmatrix}\boldsymbol{v}_c \\ \boldsymbol{\omega}_c\end{bmatrix}, \quad \boldsymbol{\eta}_h = \begin{bmatrix}\boldsymbol{p}_h \\ \boldsymbol{\theta}_h\end{bmatrix}, \quad \boldsymbol{\nu}_h = \begin{bmatrix}\boldsymbol{v}_h \\ \boldsymbol{\omega}_h\end{bmatrix} \tag{4.24}$$

$$\boldsymbol{p}_{A,i} = \boldsymbol{p}_{mh_c,i} = \boldsymbol{p}_c + \boldsymbol{R}(\boldsymbol{\theta}_c)\boldsymbol{p}^c_{mh_c,i} \tag{4.25}$$

$$\boldsymbol{p}_{B,i} = \boldsymbol{p}_{mh_h,i} = \boldsymbol{p}_h + \boldsymbol{R}(\boldsymbol{\theta}_h)\boldsymbol{p}^h_{mh_h,i} \tag{4.26}$$

The outputs of the Main Hoist (MH) block are the loads on the crane and lower block in their respective coordinate systems, given by equation (4.27).

$$\boldsymbol{\tau}^c_{mh_c} = \sum_{i=1}^{2} \begin{bmatrix}\boldsymbol{R}(\boldsymbol{\theta}_c)^\top \boldsymbol{f}_{A,i} \\ \boldsymbol{C}\left(\boldsymbol{p}^c_{A,i}\right)\boldsymbol{R}\left(\boldsymbol{\theta}_c\right)^\top \boldsymbol{f}_{A,i}\end{bmatrix} \tag{4.27}$$

$$\boldsymbol{\tau}^h_{mh_h} = \sum_{i=1}^{2} \begin{bmatrix}\boldsymbol{R}\left(\boldsymbol{\theta}_h\right)^\top \boldsymbol{f}_{B,i} \\ \boldsymbol{C}\left(\boldsymbol{p}^h_{B,i}\right)\boldsymbol{R}(\boldsymbol{\theta}_h)^\top \boldsymbol{f}_{B,i}\end{bmatrix} \tag{4.28}$$

Tugger lines (T)

The inputs of the Tugger Lines (T) block are again the state of the crane and the lower block, denoted by $\boldsymbol{\eta}_c$, $\boldsymbol{\nu}_c$, $\boldsymbol{\eta}_h$, and $\boldsymbol{\nu}h$. Similar to the main hoist wires, the tuggers are modelled as linear tensile springs. The tugger lines have stiffness k_t, damping c_t, and length l_t.

As with the initial linear models, the crane is not fully modelled in the numerical models. Instead, the simplified representation described in section 3.2, is used to capture the dynamic behaviour of the crane. The relationship between the displacement of the crane tip and that of the tugger mounting is given by equation (4.29).

$$\phi_t = \frac{H_c - H_{pd} - L_{mh}}{H_c - H_{pd}} \tag{4.29}$$

$$\boldsymbol{p}_t = \phi_t(\boldsymbol{p}_c - \boldsymbol{p}_{hinge}) \tag{4.30}$$

$$\boldsymbol{\theta}_t = \phi_t \boldsymbol{\theta}_c \tag{4.31}$$

In reality, this simplified relationship does not hold, and the relationship between the crane tip and tugger mounting displacements will be nonlinear due to the finite stiffness of the boom. However, it is expected that the effect of this nonlinearity on the rest of the system is small, and therefore a simplified implementation of this dynamics is chosen. The mounting location of the tugger on the crane and lower block is given by equation (4.32) and equation (4.26), respectively.

$$\boldsymbol{p}_{A,i} = \boldsymbol{p}_{t_c,i} = \boldsymbol{p}_t + \boldsymbol{R}(\boldsymbol{\theta}_t)\begin{bmatrix}0 & \pm W_c/2\end{bmatrix}^\top \tag{4.32}$$

$$\boldsymbol{p}_{B,i} = \boldsymbol{p}_{t_h,i} = \boldsymbol{p}_h + \boldsymbol{R}(\boldsymbol{\theta}_h)\begin{bmatrix}0 & \pm W_{lb}/2\end{bmatrix}^\top \tag{4.33}$$

The outputs of the tugger lines block (T) are the loads on the crane and lower block in their respective coordinate systems, given by equation (4.34).

$$\boldsymbol{\tau}^c_t = \sum_{i=1}^{2} \begin{bmatrix}\boldsymbol{R}(\boldsymbol{\theta}_t)^\top \phi_t \boldsymbol{f}_{A,i} \\ \boldsymbol{C}\left(\boldsymbol{p}^c_{A,i}\right)\boldsymbol{R}(\boldsymbol{\theta}_t)^\top \phi_t \boldsymbol{f}_{A,i}\end{bmatrix} \tag{4.34}$$

$$\boldsymbol{\tau}^h_t = \sum_{i=1}^{2} \begin{bmatrix}\boldsymbol{R}(\boldsymbol{\theta}_h)^\top \boldsymbol{f}_{B,i} \\ \boldsymbol{C}\left(\boldsymbol{p}^h_{B,i}\right)\boldsymbol{R}(\boldsymbol{\theta}_h)^\top \boldsymbol{f}_{B,i}\end{bmatrix} \tag{4.35}$$

Huisman Universal Quick Connector (QC & PS)
The Huisman UQC provides a connection between the lower block and the blade (yoke) bodies. The inputs for the blocks that describe the UQC dynamics are the position and velocity states of these two bodies, denoted by $\boldsymbol{\eta}_b, \boldsymbol{\nu}_b, \boldsymbol{\eta}_h$ and $\boldsymbol{\nu}_h$.

$$\boldsymbol{\eta}_b = \begin{bmatrix} \boldsymbol{p}_b \\ \boldsymbol{\theta}_b \end{bmatrix}, \quad \boldsymbol{\nu}_b = \begin{bmatrix} \boldsymbol{v}_b \\ \boldsymbol{\omega}_b \end{bmatrix}, \quad \boldsymbol{\eta}_h = \begin{bmatrix} \boldsymbol{p}_h \\ \boldsymbol{\theta}_h \end{bmatrix}, \quad \boldsymbol{\nu}_h = \begin{bmatrix} \boldsymbol{v}_h \\ \boldsymbol{\omega}_h \end{bmatrix} \tag{4.36}$$

Two variants of the Huisman UQC are implemented. The first variant is the UQC in its locked position, denoted as QC. In this position, the drive system is locked, and the connection between the lower block and the blade is provided by the clamped pin in all mechanical DOF. The stiffness of the locked UQC is given by k_{uqc} in all directions.

For the second variant with denotation PS, the power swivel is activated. In this mode, the rotation of the blade yoke relative to the lower block is controlled using the control input $\boldsymbol{u}_{qc}^{ref} = \begin{bmatrix} 0 & 0 & \theta_{uqc}^{ref} \end{bmatrix}^\top$.The rotational stiffness and damping between the lower block and the blade are determined by the motor-gearbox assembly. The stiffness and damping for this assembly are determined as described in section 3.3.2. This results in the following stiffness and damping matrices for the QC and PS blocks.

$$\boldsymbol{K}_{qc} = \text{diag}\left\{ k_{uqc}, \quad k_{uqc}, \quad k_{uqc} \right\}, \qquad \boldsymbol{D}_{qc} = \text{diag}\left\{ c_{uqc} \quad c_{uqc} \quad c_{uqc} \right\} \tag{4.37}$$

$$\boldsymbol{K}_{ps} = \text{diag}\left\{ k_{uqc} \quad k_{uqc} \quad k_{gb} \right\}, \qquad \boldsymbol{D}_{ps} = \text{diag}\left\{ c_{uqc} \quad c_{uqc} \quad c_{gb} \right\} \tag{4.38}$$

Based on η and κ, the relative position and velocity between the lower block and blade (yoke) COG is calculated in the hook-fixed coordinate system using the expressions given in equations (4.39) and (4.40).

$$\boldsymbol{\delta}_{bh}^b = (\boldsymbol{\eta}_b - \boldsymbol{\eta}_h)^b = \boldsymbol{R}(\boldsymbol{\theta}_b)^\top (\boldsymbol{\eta}_b - \boldsymbol{\eta}_h) \tag{4.39}$$

$$\dot{\boldsymbol{\delta}}_{bh}^b = (\boldsymbol{\nu}_b - \boldsymbol{\nu}_h)^b = \boldsymbol{\nu}_b - \boldsymbol{J}\left(\boldsymbol{\theta}_b - \boldsymbol{\theta}_h\right) \boldsymbol{\nu}_h \tag{4.40}$$

In the case where the UQC is in the locked position, the loads of the UQC coupling on the blade are given by equation (4.41). Here, $\boldsymbol{\delta}_{bh_\circ}^h$ represents the static offset between the blade (yoke) and lower block COG within the hook-fixed coordinate system. For the XY models, this offset is given by, $\boldsymbol{\delta}_{bh_\circ}^h = \begin{bmatrix} 0 & 0 & 0 \end{bmatrix}^\top$. For the YZ models, the static offset is given by $\boldsymbol{\delta}_{bh_\circ}^h = \begin{bmatrix} 0 & L_{cog} & 0 \end{bmatrix}^\top$.

In the case when the power swivel is used, the dynamics are described by equation (4.42). Here, $\boldsymbol{u}_{qc} = \begin{bmatrix} 0 & 0 & \theta_m \end{bmatrix}^\top$ represents the output of the motor inner control loop dynamics, which is approximated by equation (3.23).

$$\boldsymbol{\tau}_{qc}^b = \begin{bmatrix} \boldsymbol{f}_{qc}^b \\ \boldsymbol{m}_{qc}^b \end{bmatrix} = \boldsymbol{K}_{qc}(\boldsymbol{\delta}_{bh_\circ}^b - \boldsymbol{\delta}_{bh}^b) - \boldsymbol{D}_{qc}\dot{\boldsymbol{\delta}}_{bh}^b \tag{4.41}$$

$$\boldsymbol{\tau}_{ps}^b = \begin{bmatrix} \boldsymbol{f}_{ps}^b \\ \boldsymbol{m}_{ps}^b \end{bmatrix} = \boldsymbol{K}_{ps}(\boldsymbol{u}_{qc} - \boldsymbol{\delta}_{bh}^b) + \boldsymbol{D}_{ps}(\dot{\boldsymbol{u}}_{qc} - \dot{\boldsymbol{\delta}}_{bh}^b) \tag{4.42}$$

The reaction forces on the lower block resulting from the forces on the blade are given by equation (4.43), where $\boldsymbol{\theta}_{bh} = \boldsymbol{\theta}_b - \boldsymbol{\theta}_h$, τ^b represents the corresponding forces on the blade, and $\boldsymbol{p}_{bh}^h$ is the relative distance between the COG of the lower block and the COG of the blade where the forces act, given by equation (4.44).

$$\boldsymbol{\tau}^h = \begin{bmatrix} \boldsymbol{f}^h \\ \boldsymbol{m}^h \end{bmatrix} = \begin{bmatrix} \boldsymbol{R}(\boldsymbol{\theta}_{bh})\boldsymbol{f}^b \\ \boldsymbol{R}(\boldsymbol{\theta}_{bh})\boldsymbol{m}^b + \boldsymbol{C}\left(\boldsymbol{p}_{bh}^h\right) \boldsymbol{R}(\boldsymbol{\theta}_{bh})\boldsymbol{f}^b \end{bmatrix} \tag{4.43}$$

$$\boldsymbol{p}_{bh}^h = \boldsymbol{R}(\boldsymbol{\theta}_h)^\top (\mathbf{o}_b - \mathbf{o}_h) \tag{4.44}$$

Hydraulic cylinders (H & CWH)
Like the Huisman UQC, the hydraulic cylinders provide a connection between the lower block and the blade (yoke). Therefore, the inputs for this block are once again $\boldsymbol{\eta}_b, \boldsymbol{\nu}_b, \boldsymbol{\eta}_h$ and $\boldsymbol{\nu}_h$. In addition, there is a control input $\boldsymbol{u}_h^{ref} = \begin{bmatrix} d_x^{ref} & d_y^{ref} & 0 \end{bmatrix}^\top$ that contains a reference position for the hydraulic cylinders.

The forces on the blade from the hydraulic coupling are given by equation (4.45), where $\boldsymbol{\delta}_{bh}^{b}$ and $\dot{\boldsymbol{\delta}}_{bh}^{b}$ again represent the relative position and velocity between the lower block and the blade (yoke) COG, given by equations (4.39) and (4.40). $\boldsymbol{u}_h = \begin{bmatrix} d_x & d_y & 0 \end{bmatrix}^\top$ is the output from the servo valve inner loop dynamics described by equation (3.17), providing the position of the cylinder's piston.

$$\boldsymbol{\tau}_h^b = \begin{bmatrix} \boldsymbol{f}_h^b \\ \boldsymbol{m}_h^b \end{bmatrix} = \boldsymbol{K}_h(\boldsymbol{\delta}_{bh_\circ}^b + \boldsymbol{u}_h - \boldsymbol{\delta}_{bh}^b) - \boldsymbol{D}_h \dot{\boldsymbol{\delta}}_{bh}^b \tag{4.45}$$

$\boldsymbol{K}_h$ and $\boldsymbol{D}_h$ are the stiffness and damping matrices for the hydraulic coupling. The matrices are given by equation (4.46) for models in the XY yaw-plane, and equation (4.47) for models in the YZ roll-plane.

$$\text{yaw-plane} \rightarrow \boldsymbol{K}_h = \text{diag}\left\{k_h, \quad k_h, \quad k_{uqc}\right\}, \qquad \boldsymbol{D}_h = \text{diag}\left\{c_h, \quad c_h, \quad c_{uqc}\right\} \tag{4.46}$$

$$\text{roll-plane} \rightarrow \boldsymbol{K}_h = \text{diag}\left\{k_h, \quad k_{uqc}, \quad k_{uqc}\right\}, \qquad \boldsymbol{D}_h = \text{diag}\left\{c_h, \quad c_{uqc}, \quad c_{uqc}\right\} \tag{4.47}$$

In the case of the hydraulic cylinder that provided the connection between the lower block and the counterweight bodies, the block inputs are $\boldsymbol{\eta}_w, \boldsymbol{\nu}_w, \boldsymbol{\eta}_h$ and $\boldsymbol{\nu}_h$. There is also the control input $\boldsymbol{u}_h$, which contains the reference positions for the cylinders.

$$\boldsymbol{\tau}_h^w = \begin{bmatrix} \boldsymbol{f}_h^w \\ \boldsymbol{m}_h^w \end{bmatrix} = \boldsymbol{K}_h(\boldsymbol{\delta}_{wh_\circ}^w - \boldsymbol{u}_h - \boldsymbol{\delta}_{wh}^w) - \boldsymbol{D}_h \dot{\boldsymbol{\delta}}_{wh}^w \tag{4.48}$$

$$\boldsymbol{\tau}^h = \begin{bmatrix} \boldsymbol{f}^h \\ \boldsymbol{m}^h \end{bmatrix} = \begin{bmatrix} \boldsymbol{R}(\boldsymbol{\theta}_{bh})\boldsymbol{f}^b \\ \boldsymbol{R}(\boldsymbol{\theta}_{bh})\boldsymbol{m}^b + \boldsymbol{C}\left(\boldsymbol{p}_{wh}^h\right)\boldsymbol{R}(\boldsymbol{\theta}_{bh})\boldsymbol{f}^b \end{bmatrix} \tag{4.49}$$

$$\boldsymbol{p}_{wh}^h = \boldsymbol{R}(\boldsymbol{\theta}_h)^\top(\mathbf{o}_w - \mathbf{o}_h) \tag{4.50}$$

When the counterweight and the blade are shifted outward by the XY table, this displacement results in a slight increase in the inertia of the suspended load around the z^h-axis. Due to the conservation of rotational momentum, this will lead to a slight decrease in the rotational velocity around the z^h-axis. However, this coupling dynamics are neglected in the model. The increase in inertia for a cylinder displacement d is given by equation (4.51). For a cylinder displacement of 1 meter, the extra inertia is 4% of the total suspended inertia. It is expected that the cylinder displacement in practice remains below 1 meter. In this case, the increase in inertia is relatively small and is neglected.

$$I_d = 2(M_b g d^2) \tag{4.51}$$

4.1.4. External loads

The external load blocks describe the external loads acting on the SBIS that do not form coupling between two bodies. These include the wind-induced loading on the blade and wind vanes, the moment generated by gyroscopic precession, and gravity.

Wind (W)

The numerical models utilize the wind model from the MarIn Toolbox to calculate the wind-induced loads on the blade. The aerodynamic load on the blade depends on the position, orientation, and velocity of the blade. Therefore, the inputs for the wind block are the blade position, orientation, and velocity state vectors given by $\boldsymbol{\eta}_b$ and $\boldsymbol{\nu}_b$. The working of the wind model, developed by Ren *et al.* [9], is briefly explained below. For a more comprehensive description of the toolbox and its associated functions, the reader is referred to the original publication.

The blade is divided into a group of n segments with $n+1$ nodes. The wind model utilizes the cross-flow principle to calculate the aerodynamic forces on the blade at each node. The cross-flow principle considers only the wind perpendicular to the blade's pitch axis. Therefore, in the local coordinate system, it holds that $f_{w,y}^b = 0$. The overall wind-induced load is obtained by integrating all the local two-dimensional elemental loads acting along the span around the blade COG.

The NREL 15 MW reference turbine is applied in the model [46]. Blade data for the NREL 5 MW reference OWT is included in the published toolbox. The MarIn function 'init_blade_hawc2' is used to convert the 15MW NREL blade data to the format used by the wind model. This function is validated in the original publication, and closely approximates all parameters required by the wind model at each

node i by interpolating the data from the reference turbine. The aerodynamic coefficients are a function of the local angle of attack (AOA), denoted by α_i, and the blade thickness ratio, T/C_i. The lift force, drag force, and pitching moment acting on the i^{th} node, denoted by L_i, D_i, and M_i, are given by equations (4.52) to (4.54).

$$L_i = \frac{1}{2}\rho_a C_l\left(\alpha_i, T/C_i\right) A_i V_i^2, \tag{4.52}$$

$$D_i = \frac{1}{2}\rho_a C_d\left(\alpha_i, T/C_i\right) A_i V_i^2, \tag{4.53}$$

$$M_i = \frac{1}{2}\rho_a C_m\left(\alpha_i, T/C_i\right) A_i V_i^2, \tag{4.54}$$

In these expressions, ρ_a is the air density, C_l, C_d, and C_m are the aerodynamic coefficients, A_i is the wing area and V_i is the local inflow airspeed. The wind model uses a turbulence box as a model input. The turbulence box consists of evenly distributed points in space that moves along with the mean wind speed. For each point, a wind velocity in u, v and w is stored for each time step. The local wind speed in u, v and w, denoted by $\boldsymbol{\nu}_w$ is interpolated from the turbulence box, and used to determine the inflow airspeed. The inflow air speed is the relative velocity between the local wind speed and the velocity of the aerodynamic COP $C_{1/4}$ at node i, given by $\boldsymbol{\nu}_{C_{1/4},i}$. Due to the contribution of the local blade velocity, aerodynamic damping is also included in the model. The angle of attack at node i is determined by equation (4.55), where θ_z represents the blade twist and $\beta_\circ$ represents the static blade pitch angle inside the yoke.

$$\alpha_i = \theta_z + \beta_\circ + \alpha = \theta_z + \beta_\circ + \operatorname{atan2}\left[w^b_{wi} - w^b_{C_{1/4}},\ \ u^b_{wi} - u^b_{C_{1/4}}\right] \tag{4.55}$$

The turbulence boxes are generated in the stochastic simulation tool TurbSim [37]. TurbSim generates the wind boxes based on user provided wind box dimensions, mean wind speed and turbulence intensity category according to the IEC guidelines described in section 2.2.1. Separate turbulence boxes are generated for each turbulence category and for mean wind speeds of 6, 9, 12, 15, and 18 m/s, for a total of 15 turbulence boxes. A TurbSim input file for generating the wind turbulence box for class A and a mean wind speed of 18 m/s is provided in appendix G

As previously mentioned, the cross-flow principle is assumed, which means that the force component in the y^b-axis is negligible. The force and moment vectors acting on each individual node i are then given by equation (4.56). The total wind-induced force and moment acting on the blade (yoke) COG is given by equation (4.57).

$$\boldsymbol{f}^b_{w,i} = \boldsymbol{R}(\alpha)^\top \begin{bmatrix} -D_i \\ 0 \\ L_i \end{bmatrix}, \qquad \boldsymbol{m}^b_{w,i} = \begin{bmatrix} 0 \\ M_i \\ 0 \end{bmatrix} \tag{4.56}$$

$$\boldsymbol{\tau}^b_w = \begin{bmatrix} \boldsymbol{f}^b_w \\ \boldsymbol{m}^b_w \end{bmatrix} = \begin{bmatrix} \sum_{i=0}^{n} \boldsymbol{f}^b_{w,i} \\ \sum_{i=0}^{n} \left[\boldsymbol{C}\left(\boldsymbol{p}^b_{C_{1/4,i}}\right)\boldsymbol{f}^b_{w,i} + \boldsymbol{m}^b_{w,i}\right] \end{bmatrix} \tag{4.57}$$

Vanes (V)

The wind vanes are attached to the blade yoke, which means that the aerodynamic load on the vane is not only dependent on the vane angle relative to the blade yoke, but also the state of the blade yoke itself. Therefore, the inputs for the wind vane block are the position and velocity state vectors $\boldsymbol{\eta}b$ and $\boldsymbol{\nu}b$. Additionally, there is a control input denoted by $\boldsymbol{u}_v^{ref} = \theta_v^{ref}$, which represents the reference position for the servo motor used to actuate the wind vane itself. The stiffness of the motor-gearbox assembly and the behaviour of the servo motor inner control loop are described in section 3.3.2. From the inner loop dynamics, the actual motor position θ_m, corrected for the gearbox ratio, is obtained. The dynamics of the vane are described by equation (4.58), where k_{gb_v} represents the stiffness of the gearbox, c_{gb_v} represents the damping of the vane servo gearbox, and M_w represents the pitching moment of the wind on the vane.

$$(I_{vane} + J_{gb})\ddot{\theta}_v = k_{gb_v}(\theta_m - \theta_v) + c_{gb_v}(\dot{\theta}_m - \dot{\theta}_v) + M_w \tag{4.58}$$

For the aerodynamic load calculation of the wind vane, the wind vanes are divided in 25 nodes and the MarIn wind model is used again. In the case of the wind vane, the inflow air speed is the relative velocity between the local wind speed and the velocity of the vane at node i. The angle of attack at node i is given by equation (4.59), where θ_v represents the angle of the wind vane relative to the blade yoke.

$$\alpha_i = \theta_v + \alpha = \theta_v + \text{atan}\,2\left[v^b_{wi} - v^b_{C_{1/4}},\ \ u^b_{wi} - u^b_{C_{1/4}}\right] \tag{4.59}$$

De wind vanes are modelled as a flat plate with the following simplified aerodynamics properties.

$$C_l\left(\alpha_i\right) = 2\cos\left(\alpha_i\right)\sin\left(\alpha_i\right), \tag{4.60}$$

$$C_d\left(\alpha_i\right) = 2\sin^2\left(\alpha_i\right), \tag{4.61}$$

$$C_m\left(\alpha_i\right) = -\sin\left(\alpha_i\right)/4, \tag{4.62}$$

The overall aerodynamic load of the wind vanes on the blade, presented in the blade-fixed coordinate system, is ultimately given by equation (4.63). In this equation, $\boldsymbol{f}^b_{v,i}$ and $\boldsymbol{m}^b_{v,i}$ represent the force and moment acting on each vane node i, determined by the MarIn wind model. $\boldsymbol{p}^b_{v,i}$ represents the position of node i relative to the blade COG

$$\boldsymbol{\tau}^b_v = \begin{bmatrix}\boldsymbol{f}^b_v \\ \boldsymbol{m}^b_v\end{bmatrix} = \begin{bmatrix}\sum_{i=0}^n \boldsymbol{f}^b_{v,i} \\ \sum_{i=0}^n \left[\boldsymbol{C}\left(\boldsymbol{p}^b_{v,i}\right)\boldsymbol{f}^b_{v,i} + \boldsymbol{m}^b_{v,i}\right]\end{bmatrix} \tag{4.63}$$

Gyroscope (GY)
The only input of the gyroscope block is the control input $\boldsymbol{u}_{gy}$. This is the reference velocity of the servo motor used to actuate the gyroscopic precession. The stiffness of the motor-gearbox assembly and the behaviour of the motor's inner control loop are described in section 3.3.2. From the inner loop dynamics, the actual motor velocity $\dot{\theta}_m$, corrected for the gearbox ratio, is obtained. The dynamics between the motor-gearbox assembly and the gyroscope are described by equation (4.64):

$$(I_{gy} + J_{gb})\ddot{\theta}_{gy} = (k_{gb_{gy}}(\theta_m - \theta_{gy}) + c_{gb_{gy}}(\dot{\theta}_m - \dot{\theta}_{gy}) \tag{4.64}$$

The moment exerted by the gyroscopes on the blade, expressed in the blade-fixed coordinate system, is given by equation (4.65). Here, θ_{gy} represents the precession angle of the gyroscope. At a precession angle of 0 degrees, the gyroscope is in its neutral position and generates the largest moment for a certain precession velocity. Furthermore, $\dot{\theta_{gy}}$ represents the precession velocity, H_s represents the gyroscope angular momentum, and n represents the number of gyroscopes.

$$\boldsymbol{\tau}^b_{gy} = \begin{bmatrix}0 & 0 & nH_s\dot{\theta}_{gy}\cos(\theta_{gy})\end{bmatrix}^\top \tag{4.65}$$

Gravity (G)
Finally, in the gravity block, the loading on the three suspended bodies as a result of the gravitational acceleration g is determined. The inputs of the gravity block are the positions of the lower block, blade (yoke), and, where applicable, the position of the counterweight. The output of the gravity block is the loading on these bodies, given by equation (4.66), equation (4.67), and equation (4.68), where N is 1 for the 3DOF models and 2 for the 6DOF simulator.

$$\boldsymbol{\tau}^b_{g,b} = \begin{bmatrix}\boldsymbol{f}^b_{g,b} \\ \boldsymbol{m}^b_{g,b}\end{bmatrix} = \begin{bmatrix}\boldsymbol{R}(\boldsymbol{\theta}_b)^\top[0_{N\times1}, (M_b + M_y)g]^\top \\ \top\end{bmatrix} \tag{4.66}$$

$$\boldsymbol{\tau}^h_{g,h} = \begin{bmatrix}\boldsymbol{f}^h_{g,h} \\ \boldsymbol{m}^h_{g,h}\end{bmatrix} = \begin{bmatrix}\boldsymbol{R}(\boldsymbol{\theta}_h)^\top[0_{N\times1}, M_h g]^\top \\ \boldsymbol{C}(\mathbf{o}^h_b)\boldsymbol{f}^h_{g,b} + \boldsymbol{C}(\mathbf{o}^h_{cw})\boldsymbol{f}^h_{g,cw}\end{bmatrix} \tag{4.67}$$

$$\boldsymbol{\tau}^w_{g,cw} = \begin{bmatrix}\boldsymbol{f}^w_{g,cw} \\ \boldsymbol{m}^w_{g,cw}\end{bmatrix} = \begin{bmatrix}\boldsymbol{R}(\boldsymbol{\theta}_w)^\top[0_{N\times1}, M_{cw}g]^\top \\ \top\end{bmatrix} \tag{4.68}$$

Table 4.4: Blocks used to construct the SBIS baseline models

AM	Plane	CW	C	LB	B	MH	T	QC	PS	H	CWH	W	G	V	GY
XY baseline (No AM)	XY		✓	✓	✓	✓	✓	✓				✓			
YZ baseline (No AM)	YZ		✓	✓	✓	✓		✓				✓	✓		

4.2. Model verification

To verify the behaviour of the numerical models, two different methods are employed. First, numerical simulation for simplified cases are performed, to check whether the system behaves as expected. The simulation results for the simplified cases are shown and discussed in appendix D.1.1.

Secondly, the behaviour of the numerical models for the actuation methods is analysed in the frequency domain. The numerical models are linearized in the Matlab/Simulink environment. The open-loop response of the linearized numerical models is compared to that of the linear models described in the previous chapter. The expectation is that the response closely matches the behaviour predicted by the linear models. The open-loop comparisons are presented in appendix D.1.2

4.3. Baseline

To compare the actuation methods, assessment criteria have been defined in section 2.5. In addition to directly comparing the actuation methods with each other, a comparison to a baseline without any actuation method provides further insight in the reduction of blade root motion. For this purpose, an additional numerical model is constructed of the SBIS without any actuation method. The blocks included in the baseline models are summarized in table 4.4.

Two baseline simulations are conducted, one with a model in the XY plane and one in the YZ plane. The resulting blade root error, velocity, and blade angle is shown in figure 4.2a and figure 4.2b.

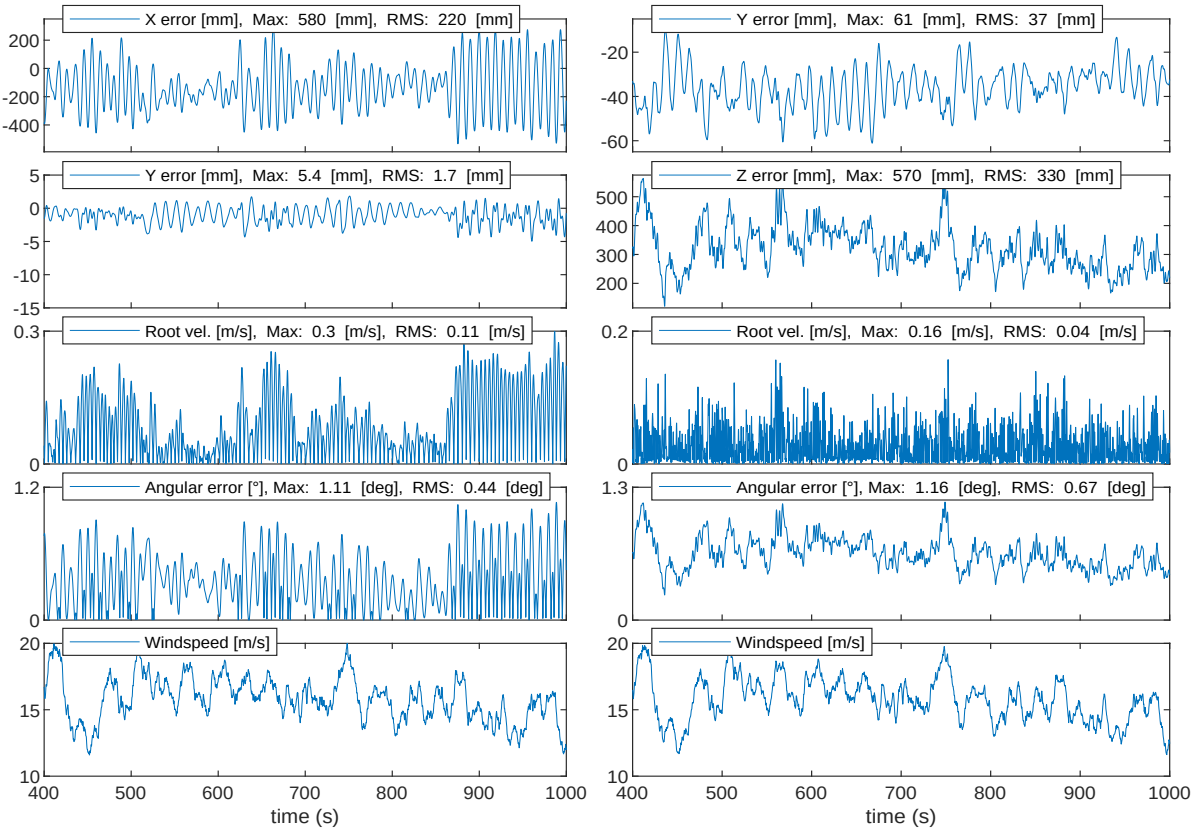

(a) Blade motion for XY baseline run

(b) Blade motion for YZ baseline run

Figure 4.2: Numerical simulation results for SBIS without actuation method (Baseline). U_w = 15, TI = 0.18.

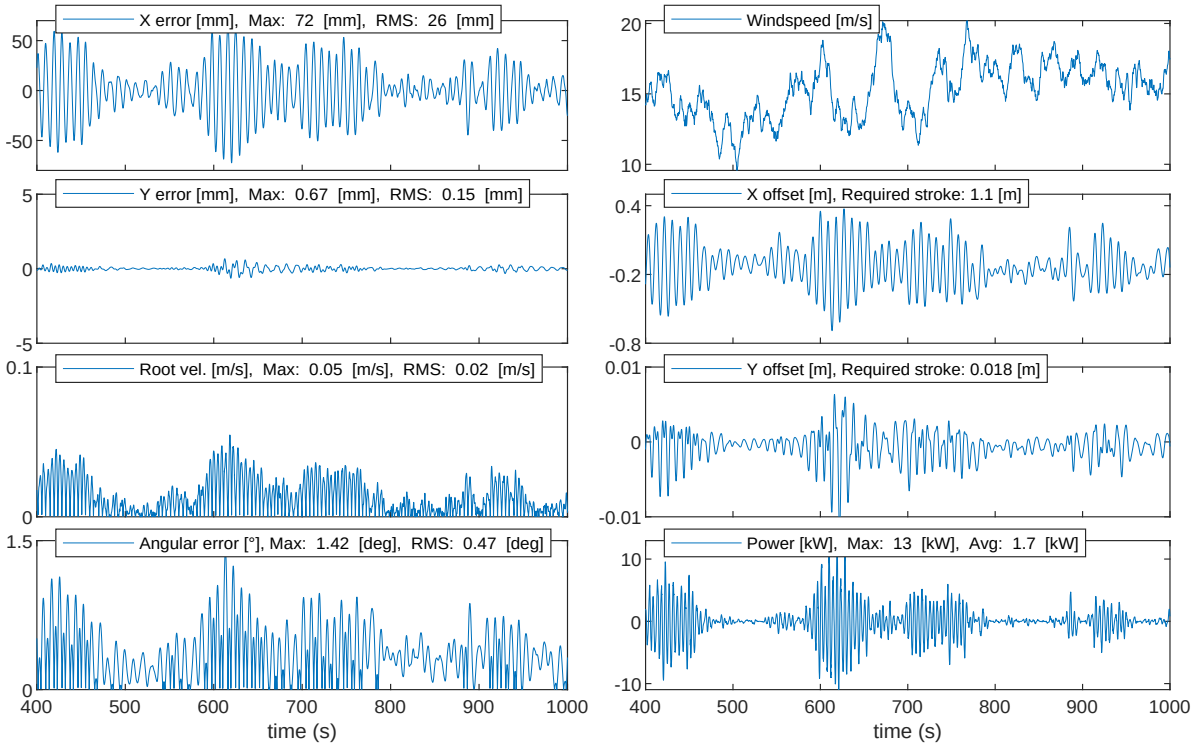

(a) Compensation effectiveness

(b) Actuator input

Figure 4.3: Numerical simulation results for SBIS with XY table. U_w = 15, TI = 0.18.

4.4. Numerical results

The simulation results for the assessment criteria introduced in section 2.5 are presented and discussed in the subsequent sections for each actuation method. An overview of the results for all actuation methods is provided in section 4.5.

4.4.1. XY table

A notable aspect of the XY table is the relatively large blade angle compared to other actuation methods. However, this was expected, since this actuation method does not have a way to compensate for the blade angle directly. Instead, the blade is translated to account for the rotation. The XY table reduces the root position error by 87% in both x- and y-direction. In the x-direction, the maximum residual error is 72 mm, with a root-mean-square error of 26 mm.

Due to the inability to directly compensate for the blade angle, the XY table compensates for rotation around the z-axis by translating the blade at the COG. Due to the large blade length, small rotations of the blade quickly results in significant displacement at the root. This is demonstrated in equation (4.69), where θ_b represents the maximum angle of 1.42 degrees in radians, and L_{cog} is the distance between the blade root and the blade COG, and d_θ the required cylinder offset at the COG to compensate for the blade rotation. The stroke length required for the x cylinder to compensate for the blade motion is 1.1 meters, where the stroke length is the required range of the cylinder, given by equation (4.70).

Due to the large actuation strokes and the substantial weight of the blade, the actuation effort and power consumption are relatively high. The average actuator power exerted is 1.7 kW. This is the power considering no losses. In reality, there will be losses in the actuation system, for instance due to friction. The actual required input power is likely considerably higher.

$$d_\theta = \theta_b L_{cog} = 0.248 \cdot 28.6 = 0.709[m] \tag{4.69}$$

$$\text{Strokelength} = \Delta d = d_{max} - d_{min} \tag{4.70}$$

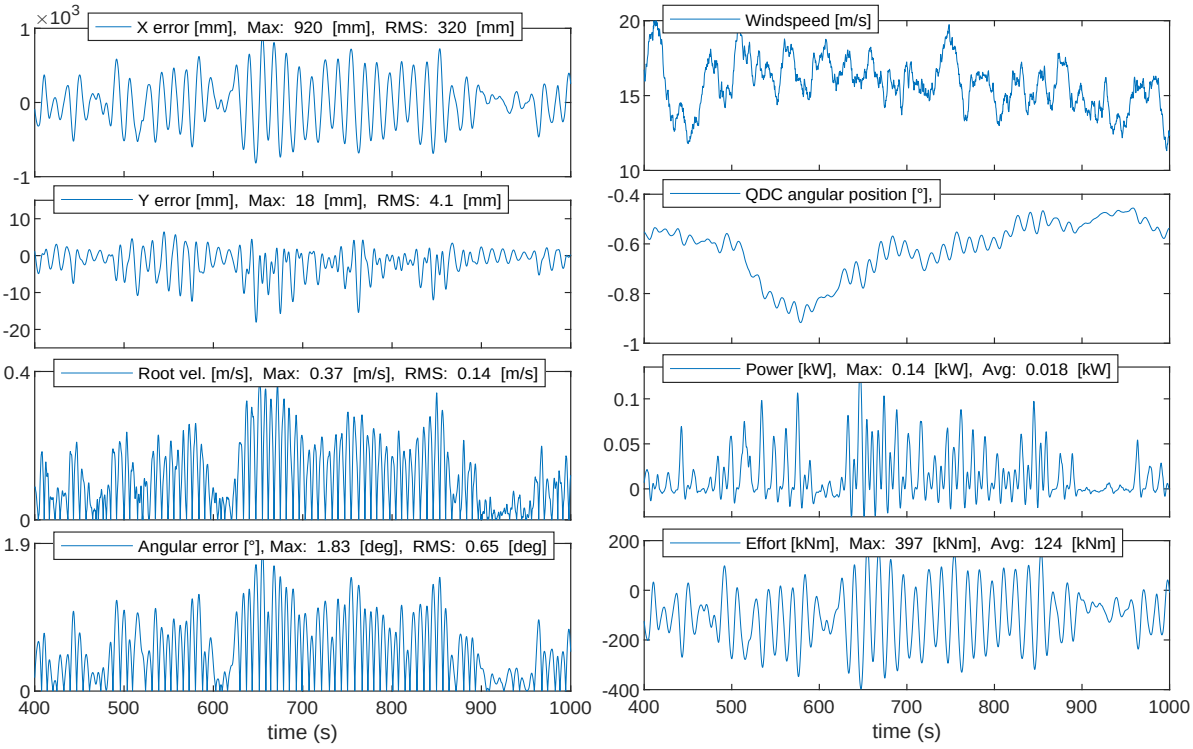

(a) Compensation effectiveness

(b) Actuator input

Figure 4.4: Numerical simulation results for SBIS with UQC power swivel. U_w = 15, TI = 0.18.

4.4.2. Power swivel

The simulation results for the SBIS with UQC power swivel are shown in figures 4.4a and 4.4b. The root position error due to the addition of the power swivel actuation method has increased compared to the reference. From the linear analysis it is already clear that the system is strongly limited by the underpowered motor-gearbox, for the chosen application. This is also reflected in these results. Due to the very slow response of the system, blade movement cannot be compensated effectively. Since the stiffness of the UQC is lower with the power swivel activated than when it is locked, the rotation of the blade is greater. As a result, a greater error and maximum speed are observed.

As stated in section 2.4.2, the torque of the UQC motor is transmitted by a slip clutch. The maximum permissible moment that can be transferred for a load mass of 261 tons is 113 kNm. This is less than the torque that must now be applied by the power swivel. In addition, the power swivel can exert a maximum torque of 300 kNm. It is clear from these results that the UQC power swivel is not suitable to compensate for blade rotation around the z-axis caused by the wind.

4.4.3. Wind vanes

Also for the wind vanes, the actuation method does not succeed in effectively compensating for the blade movement at the blade root. An improvement is seen for the wind vanes. In x-direction, blade root error has been reduced by 41%, from 580 to 340 mm. In the y-direction, an increase is seen in the blade root error. Because the vanes are at an angle to the incoming wind, they not only generate drag, but also lift. Two vanes are used that rotate in opposite directions to prevent unwanted loads on the blade in the y-direction. However, because the vanes are large, and the wind is turbulent, the local wind speed can differ between the vanes. This still creates an unwanted load on the blade.

The wind vanes have a surface area of 6×7 meters. This size is necessary to ensure that a greater moment can always be exerted with the vanes than the wind delivers on the blade. If this is not the case, control authority is lost, which can lead to major sudden blade movement. Although the required power for the vanes is not very large, it is clear from the simulation that the vanes must be able to rotate relatively quickly in order to respond to the higher-frequency turbulence. The large vanes, along with the large moment required to rotate the vane quickly, can create additional challenges.

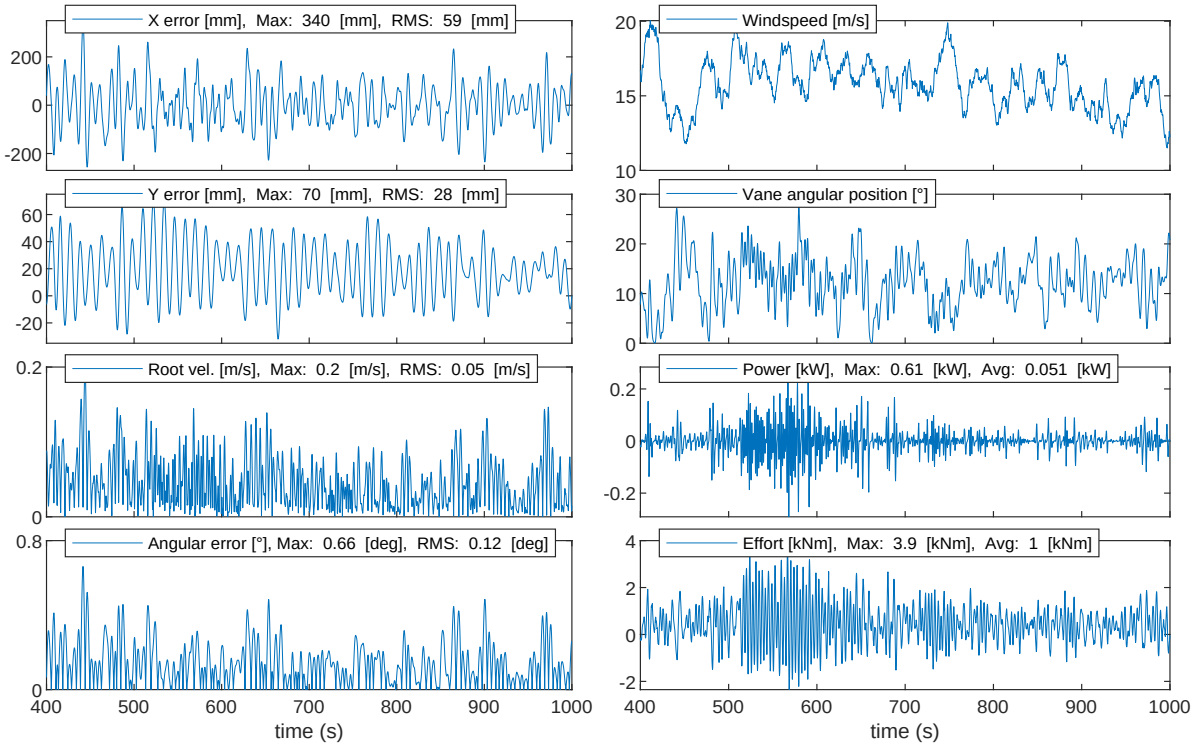

(a) Compensation effectiveness

(b) Actuator input

Figure 4.5: Numerical simulation results for SBIS with wind vanes. U_w = 15, TI = 0.18.

4.4.4. Gyroscopes

As stated in section 2.4.4, the gyroscopes are unable to compensate for a constant moment, due to saturation. This is also evident in the simulation results shown in figure 4.6. In the simulation, the saturation point is reached after less than 40 seconds. Without a solution of saturation, this actuation method is therefore unsuitable for the application.

To investigate the effectiveness of the gyroscopes in a scenario without saturation issues, the gyroscopes are simulated neglecting the saturation dynamics. This means that the gyroscopes are allowed to rotate indefinitely and the exerted moment is independent of the precession angle, as given by equation (4.72). Here $\dot{\theta}_{gy}$ is the gyroscope precession velocity, and H_s is the gyroscope angular momentum around the spin axis. In reality, the moment around the y-axis is given by equation (4.71), where the moment around the z-axis decreases for a precession angle approaching $\pi/2$, after which the sign changes.

The simulation results for the gyroscope (without saturation) are shown in figures 4.7a and 4.7b. The root position error in z-direction has been drastically reduced by 91% from 570 to 47 mm. Due to the cross flow principle, the force on the blade aligned with the blade pitch axis is zero. As the blade rotates about the x-axis, part of the blade lift produces a component in the y-direction, causing the blade to pendulate. Adding a gyroscope reduces maximum blade angle from 1.16 to 0.11. Because the gyroscope prevents rotation of the blade, the pendulation effect is also reduced, and the displacement of the blade in y-direction decreases from 61 to 47 mm.

The angular momentum of the gyroscope remains constant in magnitude, but changes direction when the gyroscope is precessed. At its neutral position, the angular momentum is aligned with the spin axis, but after the precession is induced, it develops a component in the direction of the precession axis. As part of the momentum is transferred to this direction, the gyroscope's spin speed reduces slightly. This means that most of the work done to accelerate the suspended load around the x-axis comes from the reduction in gyroscope spin, and is not supplied by the servo motors. The maximum power required by the servo motor is 60 kW, while the spin motor needs to supply a maximum of 12 kW to maintain gyro spin speed. Again, losses are not taken into account in the power calculation.

$$M_z^b = \dot{\theta}_{gy} H_s \cos\theta_{gy} \tag{4.71}$$

$$M_z^b = \dot{\theta}_{gy} H_s \tag{4.72}$$

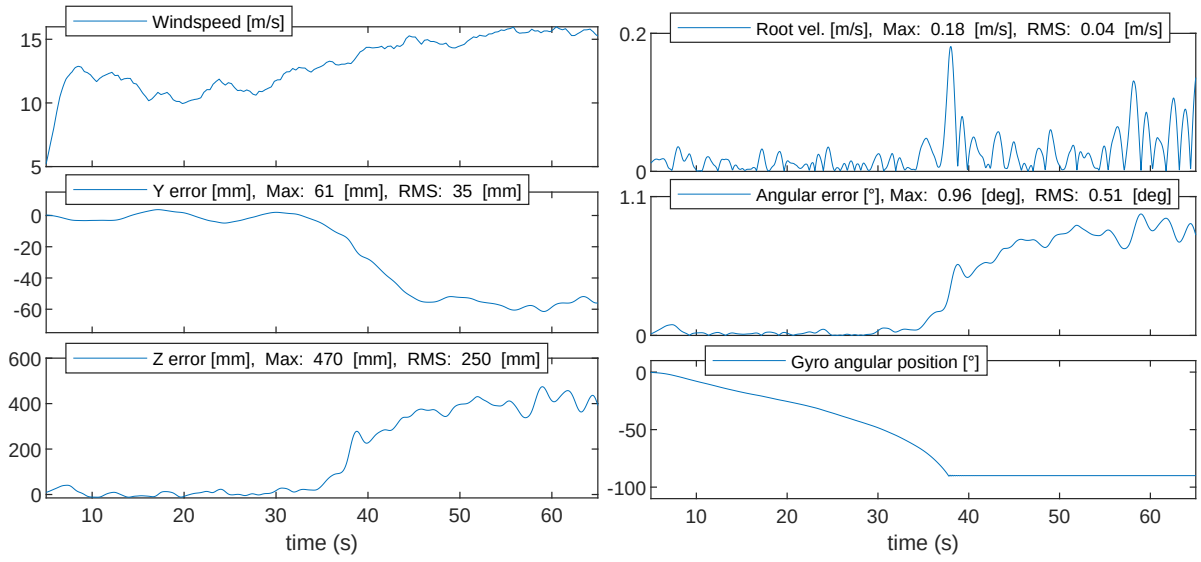

(a) Compensation effectiveness **(b)** Actuator input

Figure 4.6: Numerical simulation results for SBIS with gyroscopes. U_w = 15, TI = 0.18.

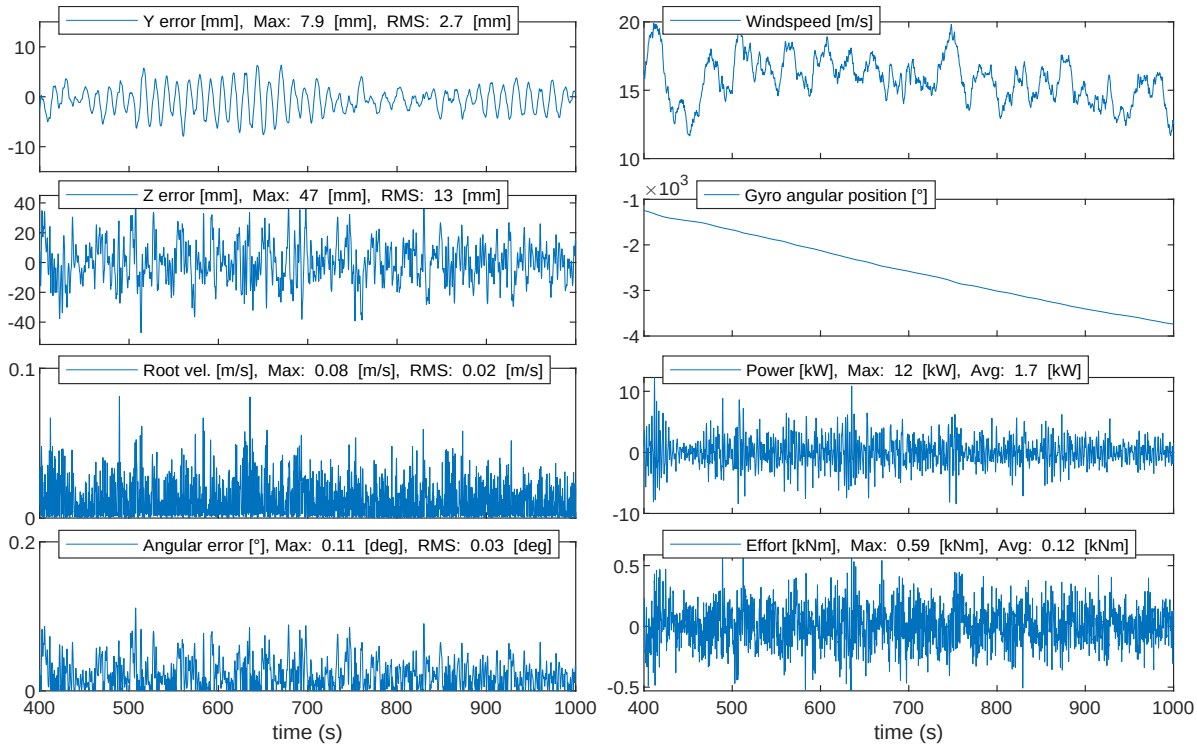

(a) Compensation effectiveness **(b)** Actuator input

Figure 4.7: Numerical simulation results for SBIS with gyroscopes without saturation. U_w = 15, TI = 0.18.

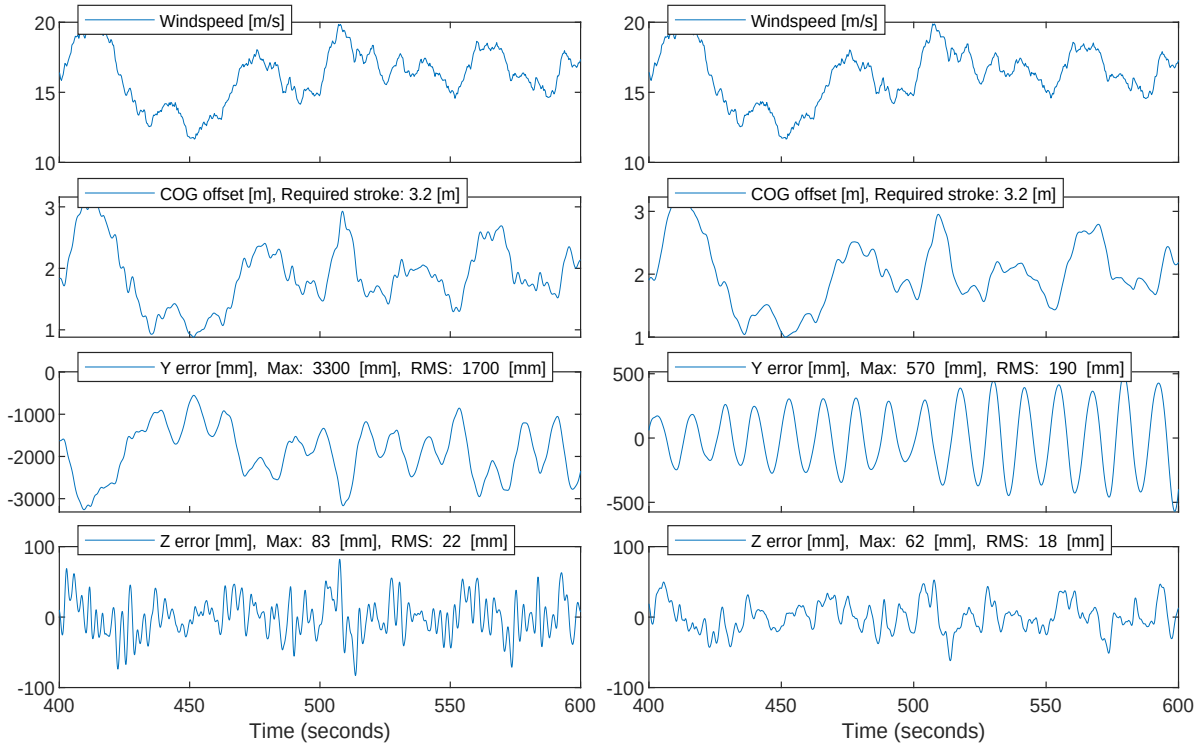

(a) COG shifting (AM5)

(b) COG shifting with counterweight (AM5B)

Figure 4.8: Blade root motion for the SBIS with the two COG shifting actuation method variants. U_w = 15, TI = 0.18.

4.4.5. COG shifting

The concept of the COG shifting actuation method, as introduced in section 2.4.5, moves the attachment point of the hoist cable relative to the blade, effectively shifting the blade's COG below the lower block. Due to the resulting COG offset, a moment is generated around the x-axis. The numerical simulation blade motion result for the SBIS with the COG shifting action method (AM5) is provided in figure 4.8a.

Compared to the baseline, the actuation method is able to reduce the z error. However, moving the blade results in a significant error in the y-direction. To compensate for the wind-induced moment, a displacement of over 3 meters is required. it is evident that the blade needs to make large movements to compensate for the fluctuating wind disturbance. Thus, it is clear that moving the blade is not a viable solution.

figure 4.8b again presents the blade motion, here for COG shifting with a counterweight (AM5B). By moving a counterweight instead of the blade, a similar motion compensation effectiveness is achieved for blade root z motion, while reducing the y error. The blade root error in y-direction however remains significant. The actuation of the counterweight results in inertial reaction loads on the suspended load in the y-direction, which excites the pendulation of load. This is evident in the constant frequency of the y-error, corresponding with the natural pendulum frequency of the load suspended from the main hoist cables.

To reduce this effect, the controller from section 3.5.5 is slowed down by reducing the gain. Figure 4.9 provides a comparison between the controller used before, and the slowed down controller, together with the resulting blade root motion in y- and z-direction. By reducing the controller gain, the pendulation of the load is reduced, at the cost of reduced motion compensation effectiveness in z-direction. Due to the way the effectiveness in y and z are linked, the error in z cannot be compensated without causing significant displacement in the y-direction.

All simulation results for the assessment criteria are given in figures 4.10a and 4.10b.

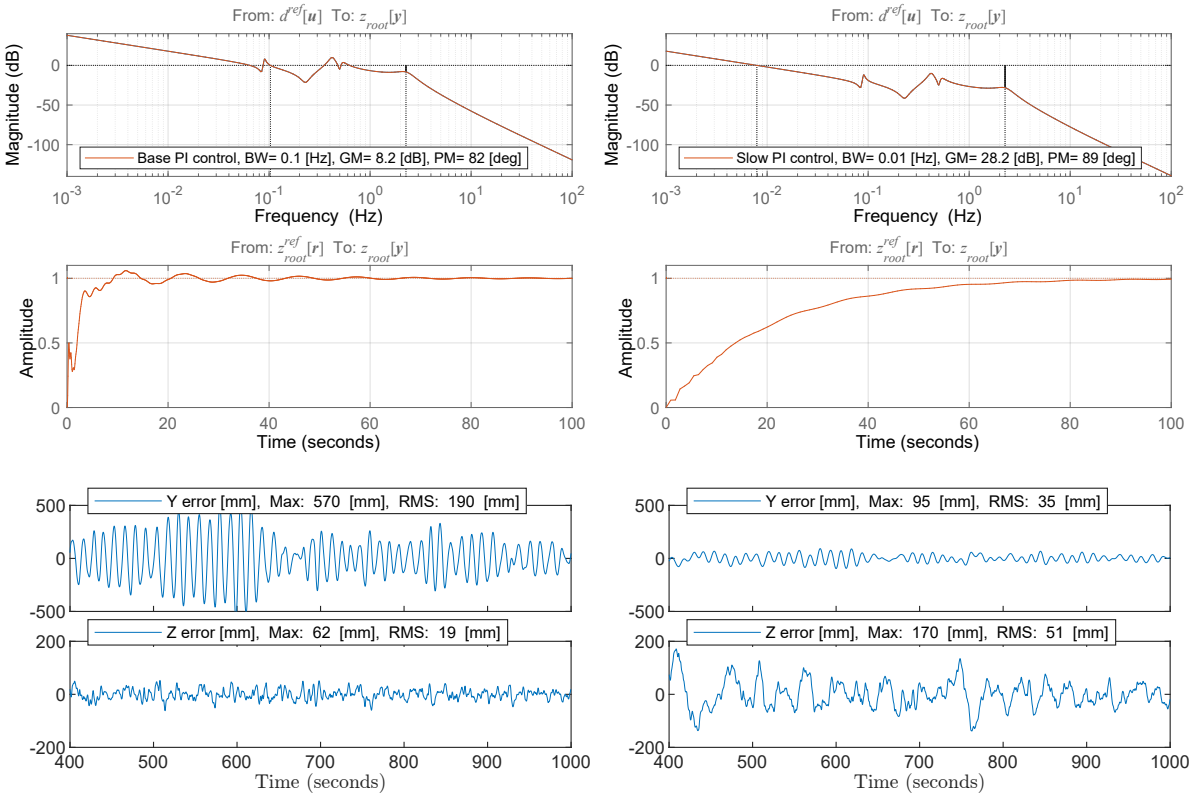

(a) Standard controller

(b) Slowed down controller

Figure 4.9: Controller response and blade root motion for standard and slowed down controller. U_w = 15, TI = 0.18.

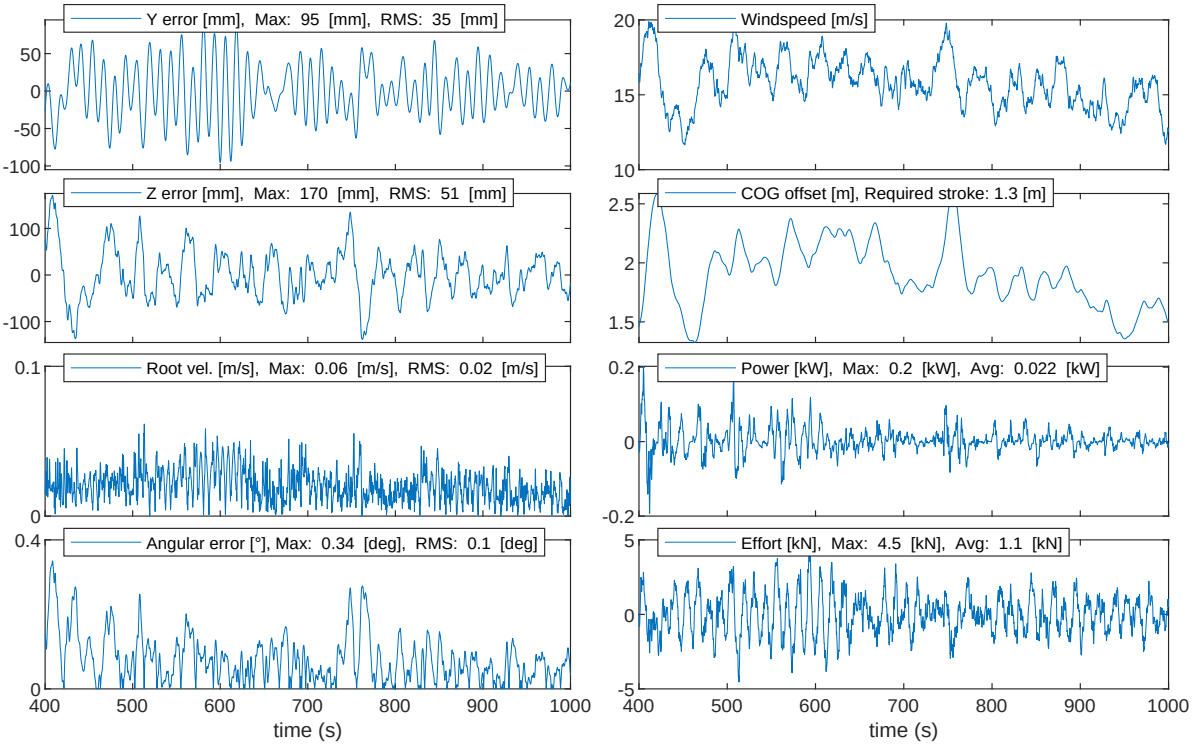

(a) Compensation effectiveness

(b) Actuator input

Figure 4.10: Simulation results for SBIS with COG shifting with counterweight and slowed down controller. U_w = 15, TI = 0.18.

Table 4.5: Overview of simulation results for the actuation methods in XY plane

	XY Baseline	XY table	UQC power swivel	Wind vanes	Unit
Max. Radial error ($\boldsymbol{e}_{rad}$)	580	72	918	342	[mm]
Max. Axial Error ($\boldsymbol{e}_{ax}$)	5.4	0.67	18	70	[mm]
Max. Blade root vel. ($\boldsymbol{e}_{v}$)	0.3	0.05	0.37	0.20	[m/s]
Max. Blade angle ($\boldsymbol{e}_{\angle}$)	1.11	1.4	1.8	0.66	[deg]
Mean Power consumption	-	1.7	0.018	0.051	[kW]
Max. Actuator Effort	-	40 [kN]	397 [kNm]	3.9 [kNm]	-
Req. Stroke length	-	1.06	-	-	[m]
Total suspended mass (M_{tot})	261	473	261	296	[t]

Table 4.6: Overview of simulation results for the actuation methods in YZ plane

	YZ Baseline	Gyroscopes	COG	COG with CW	COG with CW (Slow)	Unit
Max. Radial error ($\boldsymbol{e}_{rad}$)	570	47	83	62	171	[mm]
Max. Axial Error ($\boldsymbol{e}_{ax}$)	61	7.9	3309	570	95	[mm]
Max. Blade root vel. ($\boldsymbol{e}_{v}$)	0.16	0.080	0.52	0.31	0.060	[m/s]
Max. Blade angle ($\boldsymbol{e}_{\angle}$)	1.6	0.11	0.20	0.12	0.34	[deg]
Mean Power consumption	-	1.7	1.1	0.61	0.022	[kW]
Max. Actuator Effort	-	0.59 [kNm]	55 [kN]	33 [kN]	4.5 [kN]	-
Req. Stroke length	-	-	2.3	2.2	1.3	[m]
Total suspended mass (M_{tot})	261	355	304	448	448	[t]

4.5. Summary

This chapter focuses on addressing the sixth sub-question, *How to model the HMC actuation methods for the application of single-blade OWT installation?* The numerical models are built in Matlab/Simulink and constructed using blocks that describe a specific part of the system. There are three distinct blocks types: body dynamics, coupling loads, and external load blocks. The wind model from the MarIn toolbox is used to calculate wind loads, and uses the NREL turbine blade data and a TurbSim wind box input.

As part of the verification, the 3DOF numerical models are linearized around $t = 0$, and its frequency response compared to the linear 1DOF models from chapter 3. Verification runs are also conducted to validate the basic behaviour of the model, and map the inter-DOF coupling. A critical coupling effect on the XY table is the yaw moment arising from compensation in one transverse direction when there's an existing stroke in the perpendicular direction. However, the simulations indicate no instability occurs for the strokes encountered during operation.

The PID controllers developed in chapter 3, based on the simplified 1DOF linear models, are used during simulation. The assessment criteria results for all actuation methods are presented in tables 4.5 and 4.6. Additional outputs are presented. These are not used in the assessment, but offer more insights into operation and performance. The first is the hydraulic cylinder stroke length (via equation (4.70)). A rough weight estimates is provided as well, based on the mass of the counterweights, gyroscopes, and wind vanes. Additional mass is included for the servo drives. The gyroscope mass is estimated from disk volume. The wind vane is assumed to weigh 2500 kg, and the COG shifting counterweight 100 tonnes. Finally, the mass of the servo motor-gearbox is estimated at 15 tonnes.

- The XY table cannot directly compensate for rotation, necessitating a considerable stroke length. Nevertheless, good compensation effectiveness is observed.
- For both the power swivel and wind vanes, compensation effectiveness is notably low. This is in line with the low control bandwidth. Furthermore, the wind vanes need to rotate quickly to compensate for the turbulent wind. this in combination with the large vane area required to counteract the wind induced moment on the blade, provide challenges for this actuation method.
- The gyroscope exhibits good performance but faces a significant limitation in saturation. The gyroscope saturates within 40 seconds, losing control authority thereafter. The gyroscopes handle the fluctuating disturbances well, but struggles with constant moments, as expected.
- Due to the significant required COG displacement, a counterweight is required for COG shifting. There is a negative correlation between the achieved radial and axial error. A high effectiveness in the intended radial direction is achieved, at the cost of a large pendulum amplitude, resulting in substantial axial errors. By reducing the control gain, the pendulum swing amplitude significantly decreases, albeit at the expense of reduced radial compensation effectiveness.

5

Hook mounted compensator

In the previous chapter, the actuation methods are assessed based on the criteria defined in section 2.5. This assessment is used to select actuation methods to use in a HMC concept. The HMC, using one or more of the actuation methods, is applied in a simulator model. For the assessment of the actuation methods, 3DOF numerical models were used. These 3DOF numerical models capture the dynamics of the SBIS within the operational plane of the actuation method. The combined HMC is however intended to control the blade root position in all DOF. Therefore, the existing numerical model is expended to describe all 6 mechanical DOF. This also allows studying more of the nonlinear dynamic as a result of the coupling between the six DOF that are accommodated within the model.

In section 5.3, the coordinate rotations and translations required to expand the existing numerical model to 6DOF are given. The same verification method is used as for the 3DOF numerical models. The wind model from the MarIn toolbox [9] is again used in the simulator model. In addition, functions from the toolbox are used to realize the full DOF coordinate rotations, translations, and transformations. The 6DOF simulator is build in Matlab/Simulink to agree with the single-blade installation of the 15 MW reference turbine blade using the 3200 mt LEC.

The simulator model is used to quantify the effectiveness of the HMC, by applying the concept in a 6DOF environment. The simulation results are given in section 5.4. The result are provided for the reference case, described in chapter 2. In section 5.5 the sensitivity of these results to deviations from the reference case is investigated.

The sub-question addressed in this chapter are:

SQ7: How can the HMC actuation methods best be combined into a HMC concept to achieve the best performance for the set KPI's?

SQ8: How to verify the control performance and validate operation of the chosen HMC concept?

5.1. Actuation method combination

Based on the assessment of the actuation methods, a hook-mounted compensator concept is proposed. The two actuation methods around the z^b-axis were found to be ineffective. Therefore, it is not possible to directly compensate for rotation around this axis with the HMC based on the assessment methods included in the study. The blade root translation in the x-direction resulting from pure rotation around the z-axis is given by equation (4.69). To compensate for this error, the XY table is used. Additionally, the XY table compensates for blade motion in the y-direction.

Using the COG shifting actuation method, no high compensation effectiveness in the z-direction could be achieved without introducing significant pendulum swing in the y-direction. To control the blade root position in the z-direction, the gyroscope actuation method proves to be the most effective. However, the gyroscope experiences saturation as it cannot handle the constant wind induced moment. To solve this problem, the slowed-down COG shifting actuation method is added. The slowly operating COG shifting actuation method is well suited for compensating for the low-frequency component of the wind disturbance, which eventually leads to gyroscope saturation. The gyroscope, on the other hand, can effectively compensate for higher-frequency blade motion due to turbulent airflow.

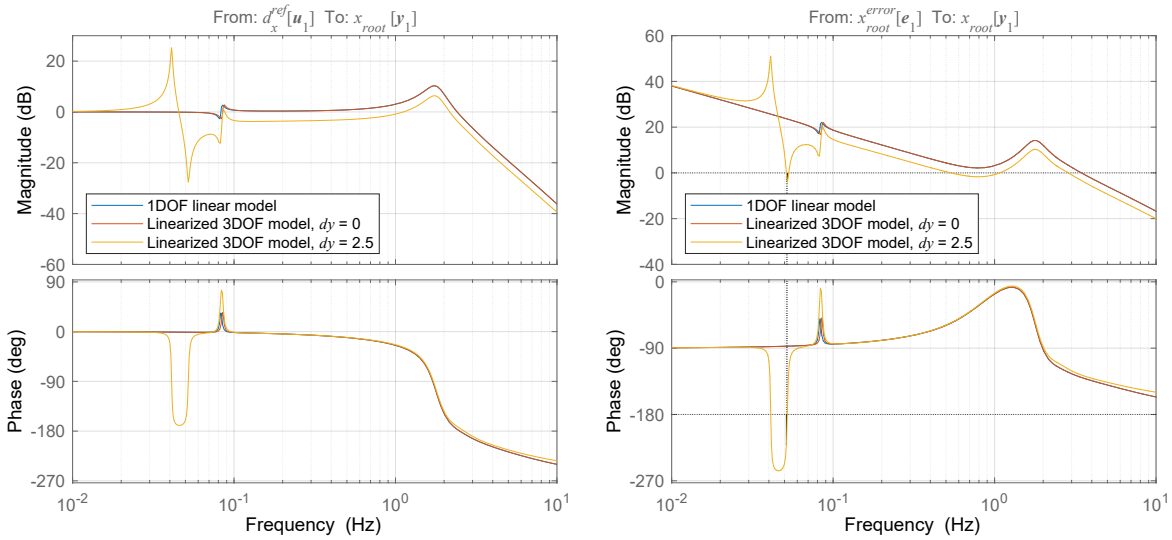

(a) Open-loop plant response

(b) Open-loop response with the linear XY table controller

Figure 5.1: Open-loop responses for the XY table in x-direction with a cylinder stroke of 0 and 2.5 meters in y-direction

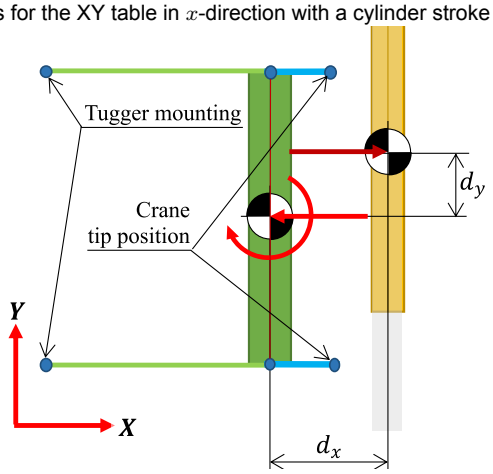

Figure 5.2: Coupling between loads in XY and yaw

During the evaluation and verification of the 3DOF yaw-plane model, it was found that there is a significant coupling between the translational and rotational DOF in the yaw-plane. When there is a misalignment between the blade-fixed and hook-fixed coordinate systems within the XY plane, and a force is exerted perpendicular to this offset, the force results in a translation acceleration and an acceleration around the yaw axis. This behaviour is shown in the schematic provided in figure 5.2. There is a displacement of the blade with respect to the lower block in the y-direction indicated by d_y. When a force is applied in the x-direction, for example, by the cylinder of the XY table, this results in a reaction force and reaction moment around the lower block's COG.

This coupling is especially significant for the implementation of the COG shifting actuation method in combination with the XY table. Both concepts use a counterweight. However, due to the coupling, it is not possible to use a single counterweight for the combined HMC concept in combination with the linear controllers. Figure 5.1a shows the open-loop response for compensation using the XY table in the x-direction for various offsets in y, denoted by d_y. For large offsets of the counterweight in y, a significant effect in the x response is observed. The yaw rotation of the suspended load due to the moment results in feedback to the tuggers, which excites the pendulum motion of the suspended load under the crane. The COG shifting method requires an offset of the counterweight in the y^h-direction of up to 2.5 meters. This displacement poses stability problems for compensation using the XY table in x the direction when the same counterweight is used. This is visible in figure 5.1b, where the XY table control is unstable in the x-direction with a cylinder stroke of 2.5 meters.

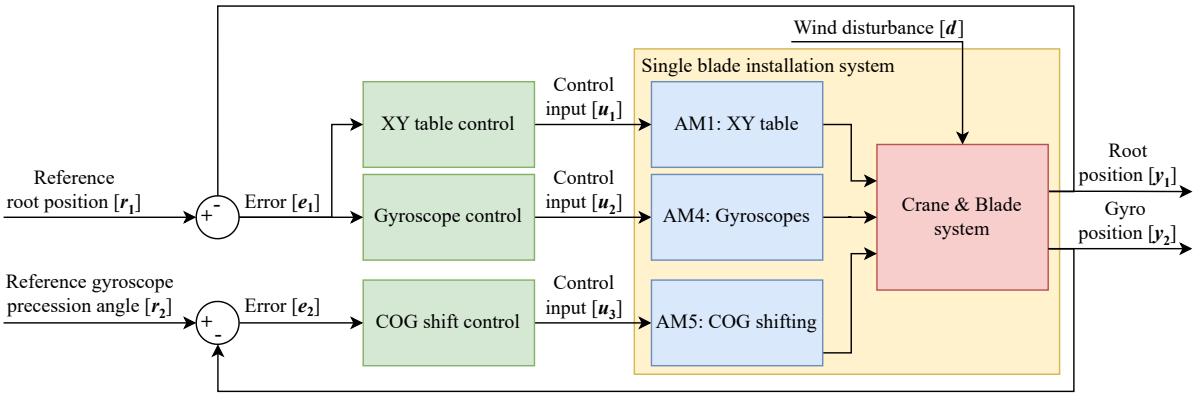

Figure 5.3: Control diagram for the combined HMC concept.

Due to the UQC connection between the yoke and the lower block, they rotate together around the x-axis. The gyroscopes can therefore be installed at any arbitrary location on the suspended load, and the applied moment will result in rotation of the blade. The XY table moves the blade and counterweight with respect to the lower block. The XY table itself consists of a frame that is attached to the lower block with the UQC pin. This frame itself does not move. The blade yoke and XY table are moved relative to this frame with hydraulic cylinders. If the gyroscopes are attached to the moving yoke, an equal mass must be added to the counterweight as well. This makes the HMC heavier and increases the potential reaction load from XY table compensation. Therefore, the gyroscopes in the HMC concept are placed on the non-moving part of the suspended load. This can be, for example, on the lower block or on the frame of the XY table. Owing to assumption 6 (section 3.1), the mechanical implementation is outside the scope of this research, and no further investigation is conducted on how the integration of the actuation methods should be realized mechanically.

5.2. Control combination

As for the individual actuation methods, the hook mounted compensator requires a controller to allow simulation in the time domain. A controller is proposed based on a combination of the linear controllers developed in chapter 3. A control diagram for the combined controller is presented in figure 5.3. In the diagram, $[\boldsymbol{y}_1]$ is the blade root position, which was the only system state used by the linear controllers introduced in chapter 3. The blade root position $\boldsymbol{p}_{root}$ is compared to the reference $[\boldsymbol{r}_1]$. This reference is the location of the mounting hole on the hub, given by $\boldsymbol{p}_{hub}$. The resulting error $[e_1]$ consists of a three-dimensional signal, given in equation (5.1).

$$\boldsymbol{e_1} = \begin{bmatrix} e_{1_x} \\ e_{1_y} \\ e_{1_z} \end{bmatrix} \tag{5.1}$$

$$\boldsymbol{u_1} = \begin{bmatrix} u_{1_x} \\ u_{1_y} \end{bmatrix} = \begin{bmatrix} d_x^{\text{ref}} \\ d_y^{\text{ref}} \end{bmatrix} \tag{5.2}$$

$$\boldsymbol{u_2} = \begin{bmatrix} \dot{\theta}_{\text{m}}^{\text{ref}} \end{bmatrix} \tag{5.3}$$

$$\boldsymbol{u_3} = \begin{bmatrix} d_{\text{cog}}^{\text{ref}} \end{bmatrix} \tag{5.4}$$

Although the XY table and gyroscope actuation methods both use the same reference position and measured output state, both actuation methods operate within different DOF. The XY table, as the name suggests, operates in the XY plane. The XY table controller uses the x and y component of the error $[e_1]$ to generate a two-dimensional control input $[\boldsymbol{u}_1]$. The control input consists of reference cylinder positions for the hydraulic cylinders inside the XY table, aligned with x^b and y^b. The gyroscope operates in the z-direction, and only considers the z component of the error, e_{1_z}. The control input from

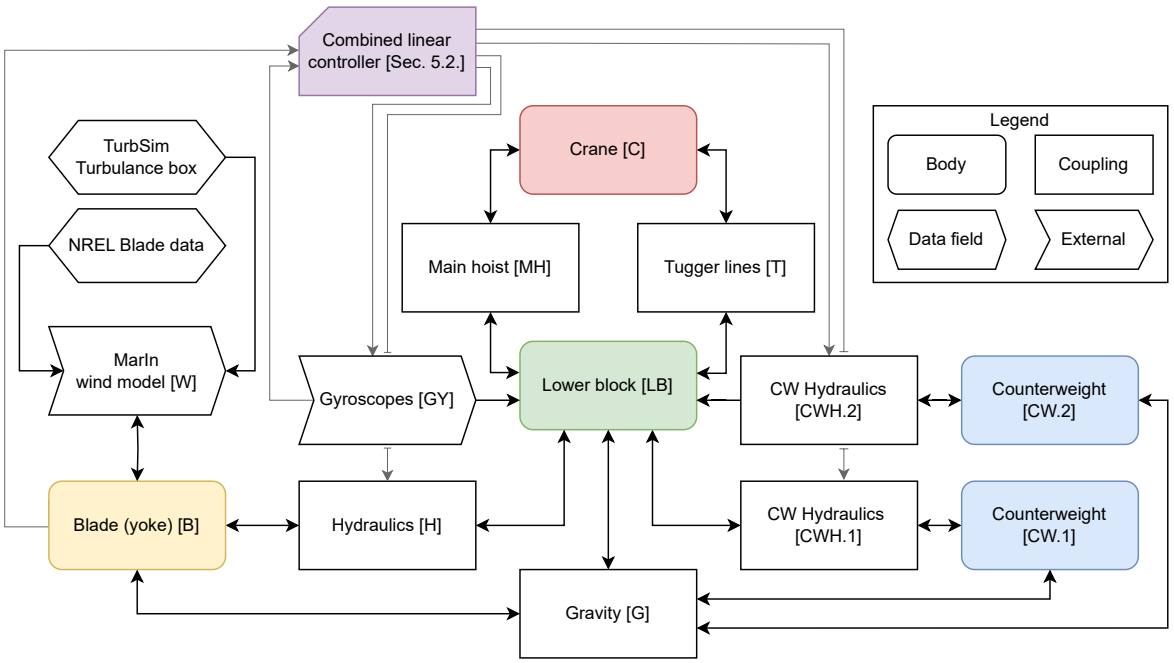

Figure 5.4: Overview of the 6DOF numerical model build from the model blocks introduced in section 4.1

Table 5.1: Blocks used to construct the 6DOF simulator models

AM	CW	C	LB	B	MH	T	QC	PS	H	CWH	W	G	V	GY
6DOF baseline		✓	✓	✓	✓	✓	✓				✓	✓		
6DOF HMC simulator	✓(2×)	✓	✓	✓	✓	✓			✓	✓(2×)	✓	✓		✓

the gyroscope controller, $[u_2]$, is one dimension signal consisting out of a reference precession speed for the gyroscopes. As long as the coupling between the three translational DOF is limited, both these controllers operate in parallel and should not significantly affect each other's operation as long as the coupling between their operational DOF is limited.

The purpose of the COG shifting actuation method is no longer to directly control the blade position, since the gyroscopes are used for this. The purpose of the COG shifting method is instead to compensate for the low frequency 'constant' component of the wind disturbance, to prevent saturation at the gyroscopes. To achieve this, an alternative control method has been proposed, in which the COG shifting controller uses the position of the gyroscope to generate a control input signal. The gyroscope angular precession position is taken as a second system output, denoted by $[y_2]$. The gyroscope position is compared to the reference position $[r_2]$, which is the gyroscope's neutral position. The error between the two, denoted by $[e_2]$, is the input to the COG shifting controller. The control input from the COG shifting controller is a reference position for the COG shifting counterweight.

5.3. Simulator model

Instead of relying on simplified 3DOF numerical models, a more comprehensive 6DOF simulator is utilized to verify the effectiveness of the proposed HMC and combined controller. The 6DOF simulator uses the same numerical description of the system as presented in section 4.1. However, to accommodate the additional DOF, different input parameters need to be used, and the mass, stiffness, and damper matrices need to be expanded to describe all 6DOF. figure 5.4 and table 5.1 provided an overview of the building blocks integrated in the simulator model.

As described in section 5.1, the gyroscope is attached to the non-moving part of the HMC. Due to the rigid connection between the XY frame and the lower block, this can be anywhere on the XY frame, or lower block. The mass of the lower block and XY frame are combined in the lower block body. A comprehensive list of all input parameters is presented in Appendix appendix E.

5.3.1. 6DOF coordinate rotations & translations

The 6DOF simulator model is constructed using the transformation and rotation matrices included in the MarIn Toolbox [9], and incorporates the same wind model and wind box data as before. Unlike the 3DOF models that operated within a single plane, the 6DOF model encompasses all six mechanical DOF, necessitating the use of the alternative coordinate transformations. The full coordinate rotations and translations follow the conventions as described in Diebel *et al.* [45]. Equation (5.5) provides an example for the rotations matrices from the blade-fixed to the global coordinate system used to rotate the blade coordinate system to the global coordinate system in Euclidean space for the Euler angel α, β, γ, about axes x, y, z respectively.

$$\begin{aligned}\boldsymbol{R}(\boldsymbol{\theta}_b) &= \boldsymbol{R}_3(\gamma) \cdot \boldsymbol{R}_1(\alpha) \cdot \boldsymbol{R}_2(\beta) \\ &= \begin{bmatrix} \cos(\gamma) & \sin(\gamma) & 0 \\ -\sin(\gamma) & \cos(\gamma) & 0 \\ 0 & 0 & 1 \end{bmatrix} \cdot \begin{bmatrix} 1 & 0 & 0 \\ 0 & \cos(\alpha) & \sin(\alpha) \\ 0 & -\sin(\alpha) & \cos(\alpha) \end{bmatrix} \cdot \begin{bmatrix} \cos(\beta) & 0 & -\sin(\beta) \\ 0 & 1 & 0 \\ \sin(\beta) & 0 & \cos(\beta) \end{bmatrix}\end{aligned} \tag{5.5}$$

The transformation of a vector in the global frame $\mathcal{G}$ to the blade-fixed frame $\mathcal{B}$, and the other way around, is done again using equation (4.4). The transformation of a position is again given by equation (4.6)

6DOF motion of a Fixed Point on a Rigid Body

For the 6DOF model, the motion of the point $\boldsymbol{p}$ attached to body j at $\boldsymbol{p}_p^j$ is given by equation (5.6), where the body has a position $\boldsymbol{p}_j$, velocity $\boldsymbol{v}_j$ and angular velocity $\boldsymbol{\omega}_j$ [45].

$$\boldsymbol{v}_p = \boldsymbol{v}_j + \boldsymbol{R}\left(\boldsymbol{\theta}_j\right)^{\mathsf{T}} \boldsymbol{C}\left(\boldsymbol{\omega}_j\right) \left(\boldsymbol{p}_p^j - \mathbf{o}_j^j\right) \tag{5.6}$$

where $\boldsymbol{C}(\omega)$ is given by:

$$\boldsymbol{C}(\boldsymbol{\omega}) = \begin{bmatrix} 0 & -\omega_3 & \omega_2 \\ \omega_3 & 0 & -\omega_1 \\ -\omega_2 & \omega_1 & 0 \end{bmatrix}. \tag{5.7}$$

6DOF Euler angle rate matrix

For the 6DOF description, the Euler angle rate matrix $\boldsymbol{T}$, used to transform the body-fixed angular velocity ω to the global angular velocity u, is given by equation (5.8). The two transformation matrices $\boldsymbol{R}$ and $\boldsymbol{T}$ are combined to form the transformation matrix $\boldsymbol{J}\left(\boldsymbol{\theta}\right)$, which allows for transformation of the body-fixed velocities to their global equivalent.

$$\boldsymbol{T}(\boldsymbol{\theta}) = \begin{bmatrix} \cos(\beta) & 0 & \sin(\beta) \\ \tan(\alpha)\sin(\beta) & 1 & -\cos(\beta)\tan(\alpha) \\ -\sin(\beta)/\cos(\alpha) & 0 & \cos(\beta)/\cos(\alpha) \end{bmatrix} \tag{5.8}$$

$$\boldsymbol{J}\left(\boldsymbol{\theta}\right) = \begin{bmatrix} \boldsymbol{R}\left(\boldsymbol{\theta}\right) & 0_{3\times3} \\ 0_{3\times3} & \boldsymbol{T}(\boldsymbol{\theta}) \end{bmatrix} \tag{5.9}$$

5.3.2. Verification

For the 6DOF model, the same verification methods are employed as for the 3DOF numerical model in chapter 4. The first method involves conducting numerical simulations for simplified cases, where the system is subjected to specific inputs or conditions to validate its expected behaviour. The simulation results for these simplified cases are presented and discussed in appendix D.2.1.

Additionally, the behaviour of the numerical models is analysed in the frequency domain. The simulator model is linearized in the Matlab/Simulink environment, and the open-loop response compared to the linear models described in chapter 3. This linearization and comparison is elaborated in appendix D.2.2.

5.4. Numerical results

5.4.1. Baseline

To provide a baseline for evaluating the effectiveness of the HMC, a simulation is performed on the SBIS without HMC. This baseline serves as a reference to quantify the compensation effectiveness of the HMC concept. A separate numerical model is again constructed for the baseline simulation, which represents the behaviour of the suspended blade during single-blade installation for the reference case.

The blade root error, velocity, and blade angle are obtained over a 10-minute simulation and presented in figures 5.5a and 5.5b. Without any compensation, the radial blade root error has a maximum of 0.69 m, while the axial error has a maximum of 0.23 m. There is significant rotation of the blade, with a maximum angular error of 1.43 degrees. The maximum velocity at the blade root is 0.24 m/s.

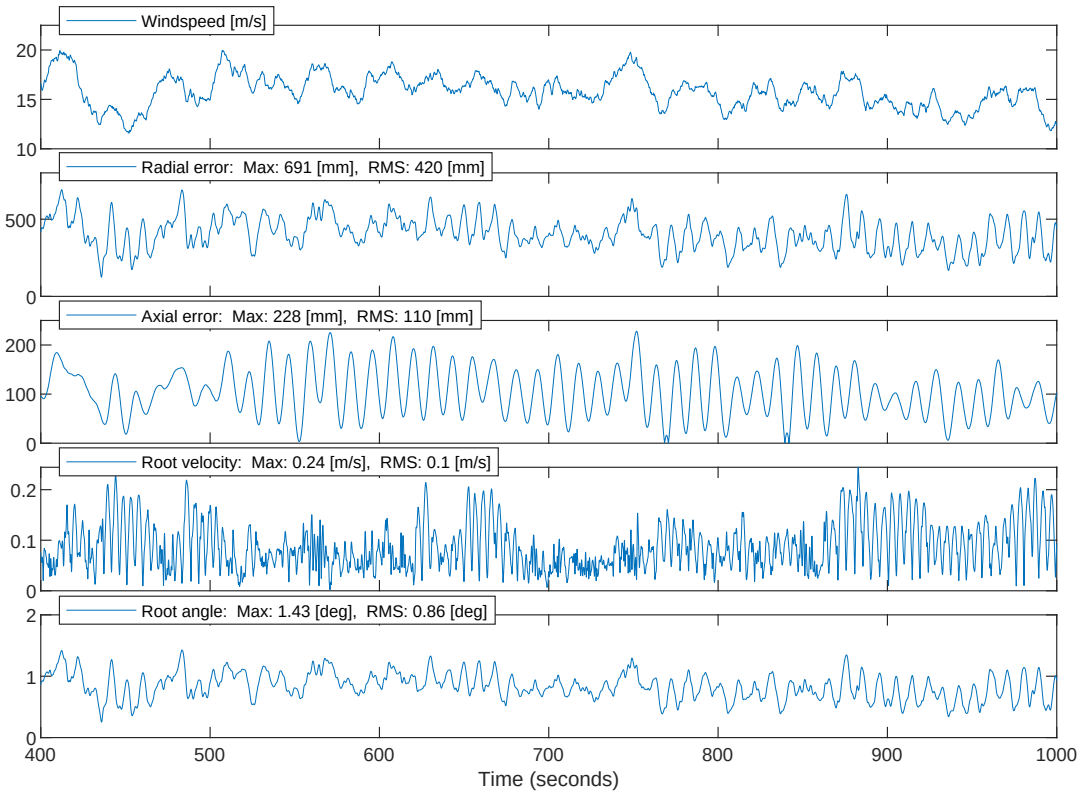

(a) Wind speed and blade (root) motion

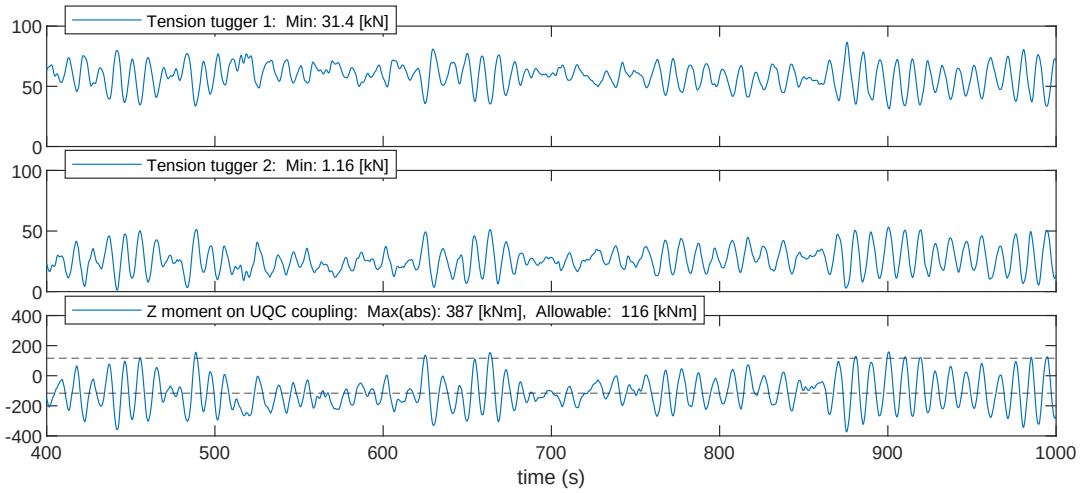

(b) Tugger tension and moment on UQC slip coupling

Figure 5.5: 6DOF simulator results for the SBIS without compensator, U_w = 15, TI = 0.18.

Table 5.2: Overview of simulation results for the baseline and SBIS with the proposed HMC.

	Baseline	HMC	Unit
Max. Radial error	691	99.9	[mm]
Max. Axial error	228	8.73	[mm]
Max. Root velocity	0.244	0.0981	[m/s]
Blade angle	1.43	0.788	[deg]
Min. Tugger tension	1.16	17.26	[kN]
Max. z Moment UQC	387	348	[kNm]
Allowable z moment UQC	116	295	[kNm]
Stroke length XY table (x)	-	0.16	[m]
Stroke length COG shifting	-	3.43	[m]
Max. angle Gyroscopes	-	77.6	[deg]
Mean Power XY table	-	3.45	[kW]
Mean Power COG shifting	-	0.202	[kW]
Mean Power Gyroscopes	-	0.445	[kW]
Max. Effort XY table	-	85.2	[kN]
Max. Effort COG shifting	-	13	[kN]
Max. Effort Gyroscopes	-	1.41	[kNm]
Total suspended mass	261	663	[t]

The moment that is transferred through the friction coupling inside the UQC is limited, as the coupling will slip if the allowable moment given by equation (2.4) is exceeded. If this is the case, the load under the UQC starts to rotate freely. This is highly undesirable, as this results in the load rotating uncontrollably during installation of the OWT blades. Since all actuation methods, including the HMC, are based around the rigid connection between the lower block and the blade yoke, the moment on the friction coupling is logged. This is not part of the assessment, but indicates whether the existing design of the UQC is suitable for this application, or whether adjustments are needed to the UQC to allow single-blade installation of 15MW OWTs. Because the load is very light without a compensator, the allowable slip moment is also low. In the case of the baseline run, the allowable moment is exceeded. As the baseline only serves as a reference for the blade movement, this is not relevant yet.

In addition to the UQC, the tugger line tensions are also tracked. During installation, losing tugger line tension results in very significant and sudden yaw motion. The tugger lines are linear tensile springs, and can therefore only prevent rotation of the blade if both lines remain under tension. When pretension is lost, the blade will rotate around the tugger attachment point still under tension, as shown in figure D.4a. This behaviour is also observed in the verification results presented in figures D.2b and D.14b. For the baseline, pretension is maintained over the entire 10-minute period. However, the margin is very small, with a minimum tugger tension of 1.16 kN.

5.4.2. Single-blade installation system with hook mounted compensator

The simulator model is used to assess the performance of the proposed HMC and combined controller. Simulations are conducted over a 10-minute interval. The initial 400 seconds of the simulation are omitted to mitigate the effects of the transient behaviour at the start of the simulation. The summarized results, including those for the baseline, are presented in table 5.2.

Figure 5.6 provides a comparison of the radial blade root motion for the baseline and the system with HMC. The HMC reduces the maximum radial blade root error by 86%, from approximately 691 mm to 99.9 mm. The compensation effectiveness is comparable to that observed for the individual XY table and gyroscope during the assessment in section 4.4. The HMC, with the combined linear controllers, remains stable for the reference case and significantly reduces the radial blade root motion. Moreover, the compensation effectiveness for axial error is even higher, with a reduction of the maximum axial error from 228 mm to 8.73 mm, resulting in a compensation effectiveness of 96%.

Despite not being directly controlled, the results demonstrate a significant reduction in both the maximum and the Root-Mean-Square Error (RMSE) of the blade root velocity and blade angle.

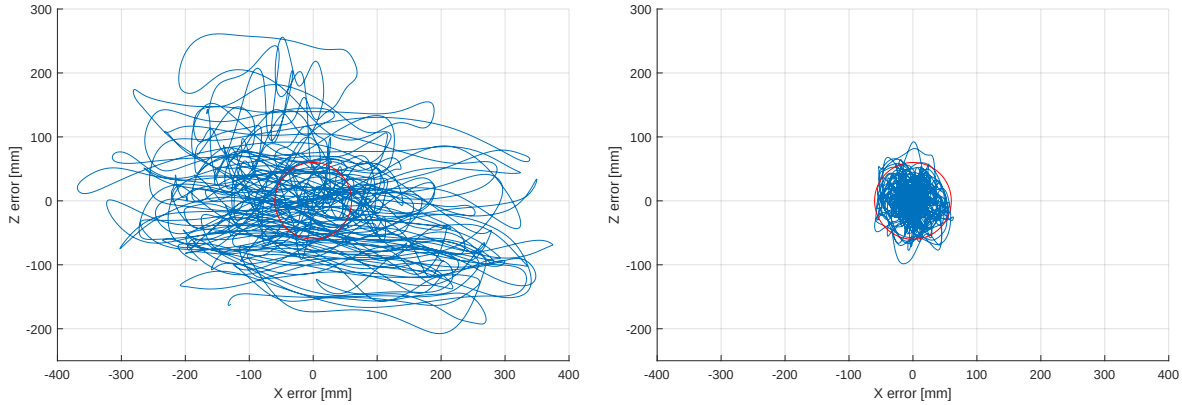

(a) Baseline

(b) SBIS with HMC

Figure 5.6: Radial blade root motion over a 10-minute period, U_w = 15, TI = 0.18.

During the 10-minute simulation, the maximum allowable moment that can be transmitted by the UQC is exceeded several times. This indicates that in its current configuration, the UQC is not a suitable solution for achieving a rigid connection between the lower block and the blade yoke. A difference in the tugger line tension compared to the baseline is also observed throughout the simulated time interval. In the baseline case, one of the tugger lines experiences high loading, while the other is close to losing pretension. Although one tugger line still bears a higher average load, the uneven distribution is reduced, and the margin in remaining tugger tension is increased from 1.16 kN to 17.3 kN.

Figure 5.8a presents the time series of actuator displacements over the 10-minute interval. The displacements of the XY table are separated into the x- and y-directions. The HMC does not directly control blade rotation around the z-axis. Instead, it compensates for blade rotation by translating the entire blade in x-direction at the COG using the XY table. As a result, a larger actuator stroke length is required for the x-direction compared to the y-direction. The required stroke length in the y-direction is 0.16 meters, The required stroke length in the x-direction is 0.67 meter, exceeding the 0.5 meters considered in the current conceptual design.

The maximum precession angle reached by the gyroscopes is 78 degrees. Throughout the 10-minute simulation, the gyroscopes do not reach saturation, indicating that the COG shifting method effectively prevents the loss of control authority for the gyroscopes with the current configuration. However, it is evident that the stroke length required for the COG shifting method is significant, measuring 3.4 meters.

Finally, the time series for actuator power and effort are depicted in figures 5.8b and 5.8c. For the XY table, the actuation effort of the most heavily loaded cylinder is shown. An overview of the required actuation effort for each individual cylinder in the XY table is found in Appendix appendix F.4. The actuation effort for the XY table remains within the design limits of the current conceptual design, where the cylinders can exert a maximum force of 100 kN. The average power consumption of the HMC without losses is 4.05 kW, with the XY table accounting for 84% of the power consumption.

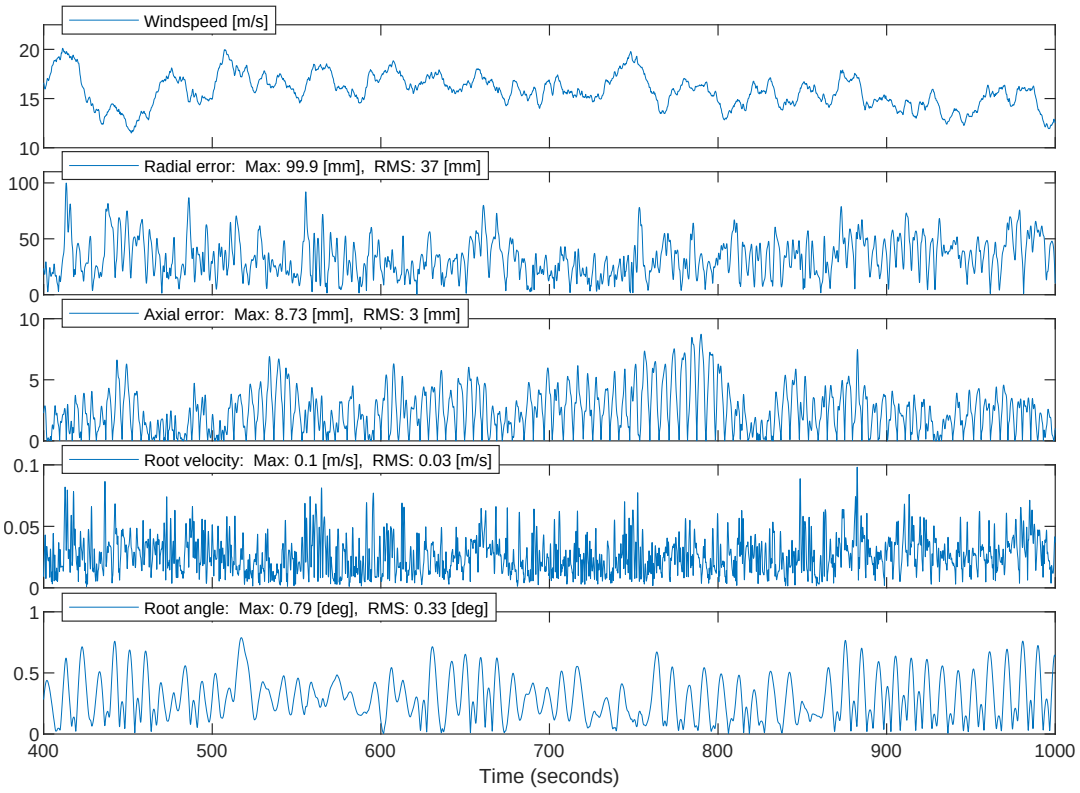

(a) Wind speed and blade (root) motion

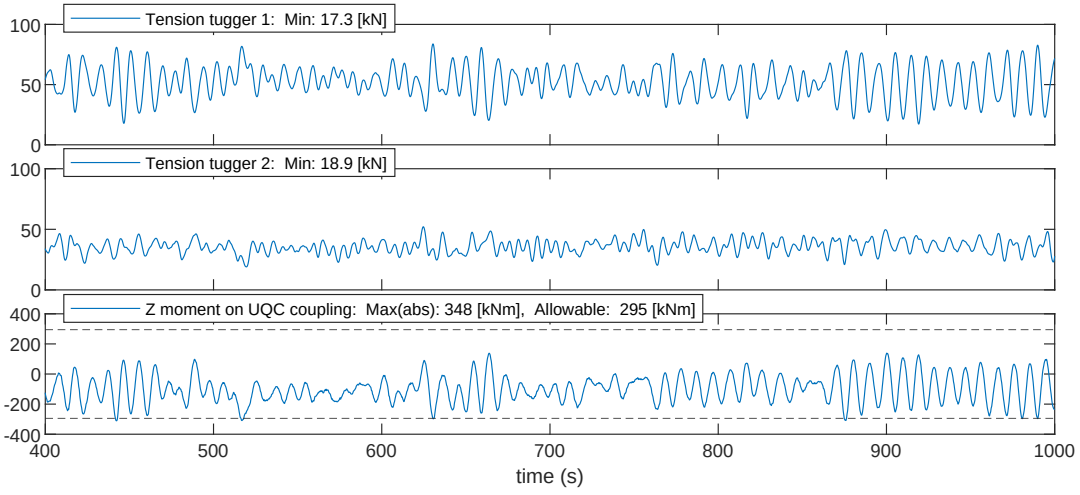

(b) Tugger tension and moment on UQC slip coupling

Figure 5.7: 6DOF simulator results for the SBIS with HMC, U_w = 15, TI = 0.18.

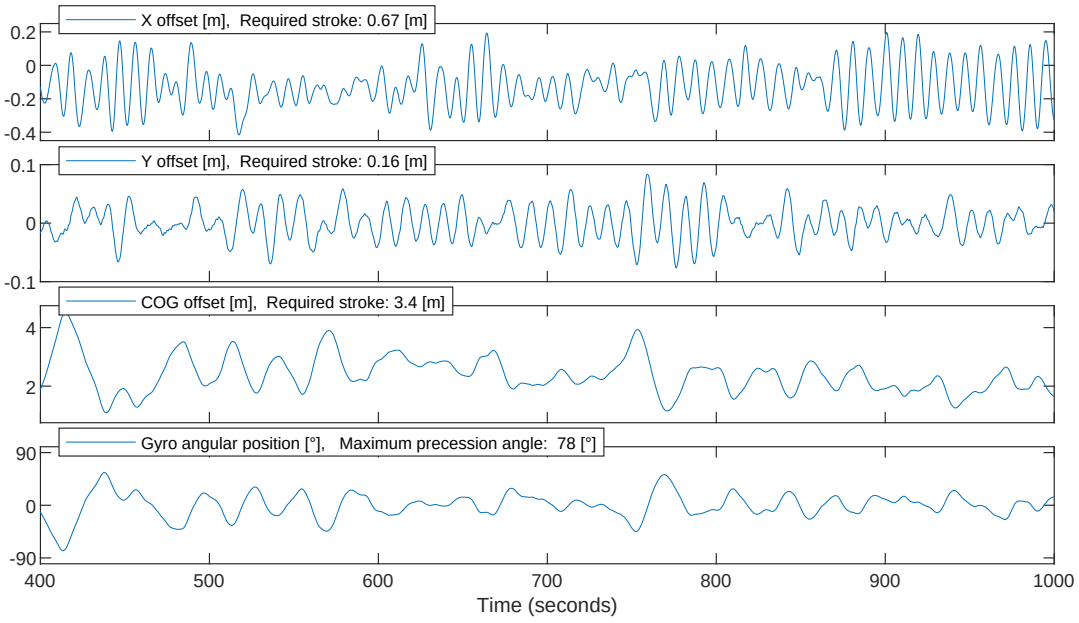

(a) Actuator stroke

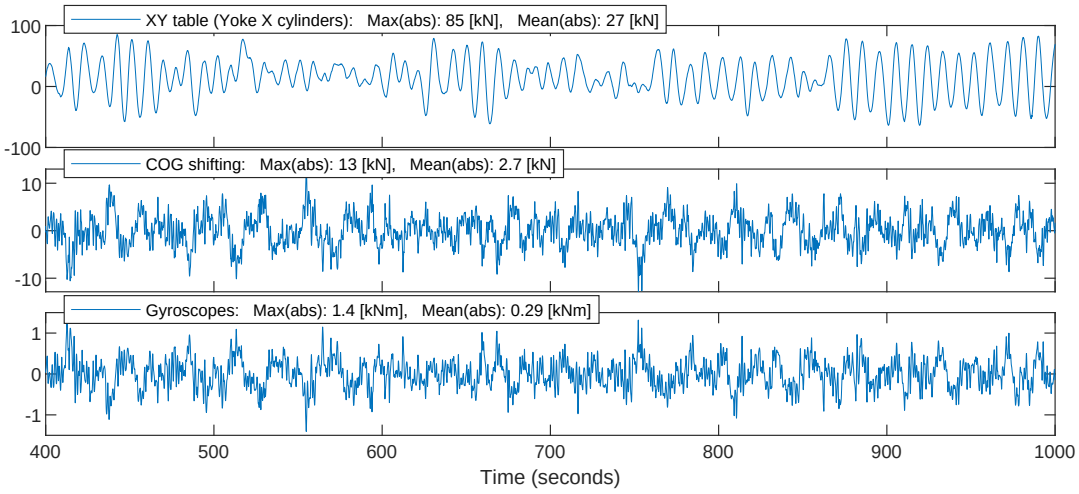

(b) Actuator power consumption

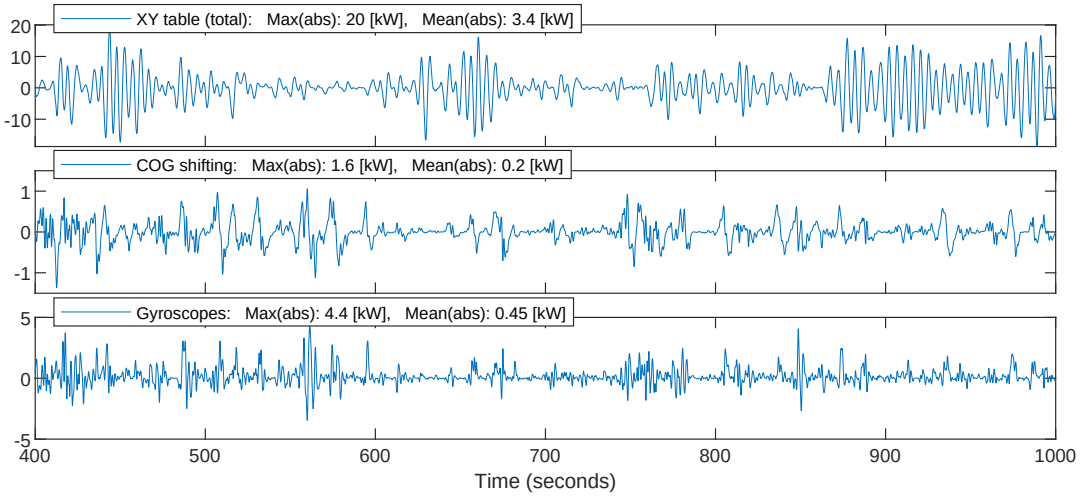

(c) Actuator effort

Figure 5.8: 6DOF simulator results for the SBIS with HMC, U_w = 15, TI = 0.18.

Table 5.3: Variable variation in the sensitivity analysis

Case	U_w [m/s]	θ_w [deg][1]	TI [-]	ζ scaling [%]	W_c [m]	T_{pre} [kN]	$\beta_\circ$ [deg]
S1	9, 12, 15, 18	0	0.18	-	10	40	7
S2	15	-120:30:90	0.18	-	10	40	7
S3	15	0	0.16, 0.13	-	10	40	7
S4	15	0	0.18	$\pm$10, $\pm$25	10	40	7
S5	15	0	0.18	-	12:2:20	40	7
S6	15	0	0.18	-	10	0,15, 20, 30, 80	7
S7	15	0	0.18	-	10	40	-190:10:-170, -15:10:25, 20
Ref.	15	0	0.18	-	10	40	7

5.5. Sensitivity

The obtained results presented in the previous section are expected to be sensitive to environmental conditions and some assumed model parameters. This section aims to investigate whether, and to what extent, the results are sensitive to variations in wind speed, wind direction, turbulence intensity, system damping, tugger line pretension and static blade pitch angle. The goal is to further evaluate the performance of the HMC and the combined controller under various conditions.

Table 5.3 provides an overview of the seven sensitivity cases that have been examined, along with the values of the varied parameters. For each scenario, the 10-minute simulation is repeated. To facilitate a clear comparison of the results, the results are summarized in bar graphs for each case. The first bar graph represents the motion compensation effectiveness, and displays the maximum and the root-mean-square for the radial and the axial blade root position error. The RMSE, around a mean of zero, can also be interpreted as the standard deviation of the root position error. To gain insight into the impact on actuator requirements, the mean power consumption of the HMC is also depicted. Additionally, the minimum tugger tension and the maximum moment on the friction coupling of theUQC are provided. These indicators provide insight into which case the implementation of the HMC may be feasible within the existing installation system.

5.5.1. Mean wind speed

An important environmental condition during the installation of an OWT blade using the single-blade installation method is the mean wind speed. As expected, blade motion increases for higher wind speeds. There is also a significant increase in the required power consumption. On the other hand, at lower wind speeds, the error decreases. The moment on the friction coupling of the UQC also decreases at lower wind speeds. This is expected since the load on the blade decreases. Theoretically, the aerodynamic load increases quadratically for an increase in wind speed. This relationship seems to be reflected in the observed maximum moment on the UQC. However, the sample size is too small to draw definitive conclusions. At a mean wind speed of 12 m/s, the moment remains well below the allowable slip moment, and the maximum radial error is reduced to around 60 mm. A radial error of 60 millimetres is the assumed accuracy required for single-blade installation. Based on these results, the installation of the 15 MW OWT blades is feasible up to a wind speed of approximately 12 m/s.

Figure 5.9 illustrates the radial blade root motion for the four tested wind speeds. It clearly shows the influence of the wind speed on the achieved accuracy. The red circle represents the target for the required accuracy of 60 mm.

[1] Angle of incoming wind relative to the global x-axis

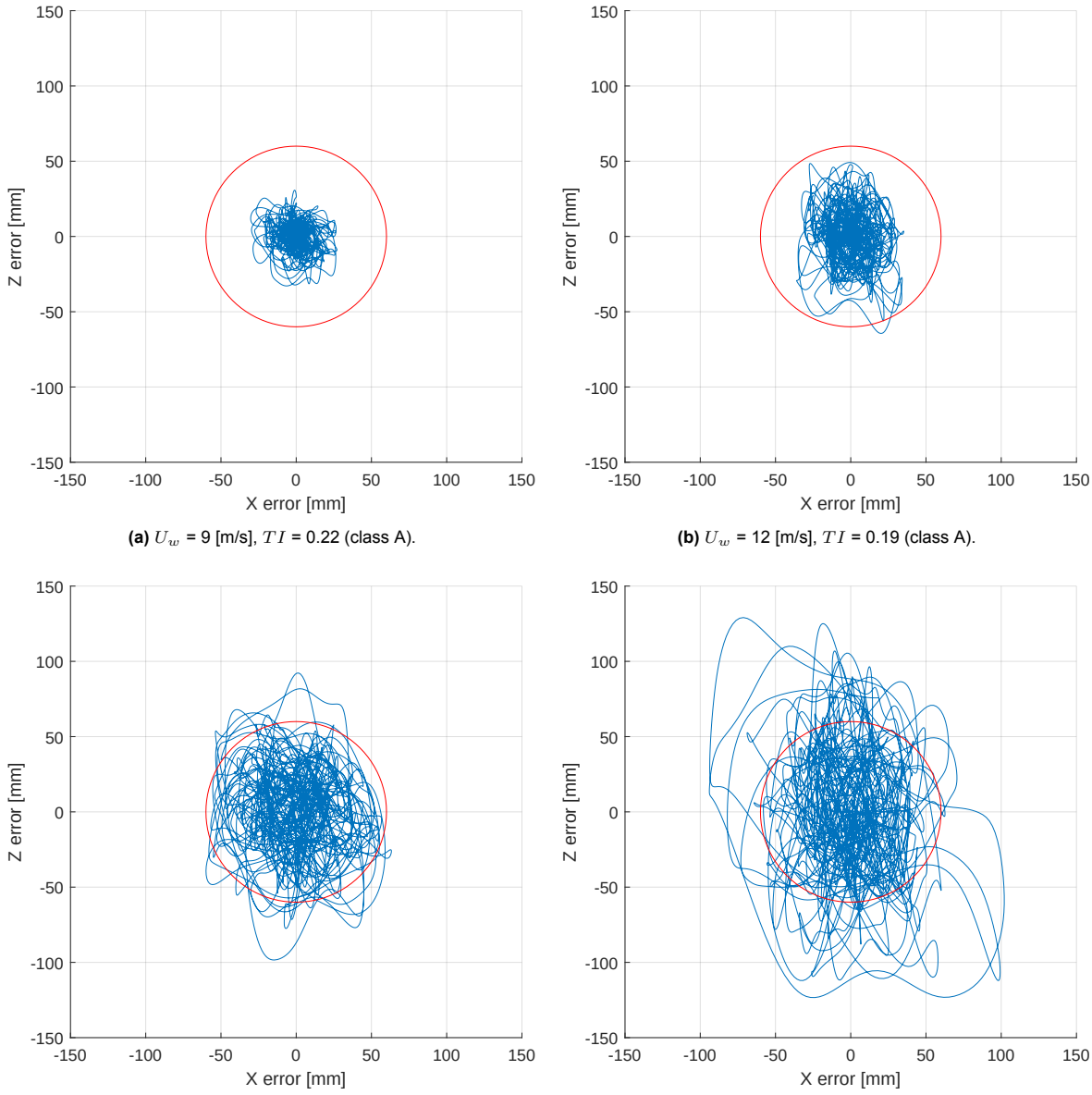

(a) U_w = 9 [m/s], TI = 0.22 (class A).

(b) U_w = 12 [m/s], TI = 0.19 (class A).

(c) U_w = 15 [m/s], TI = 0.18 (class A).

(d) U_w = 18 [m/s], TI = 0.17 (class A).

Figure 5.9: Blade root position over a 10-minute period for a mean wind speed (U_w) of 9, 12, 15 and 18 m/s, $I_{ref} = 0.16$ (Class A).

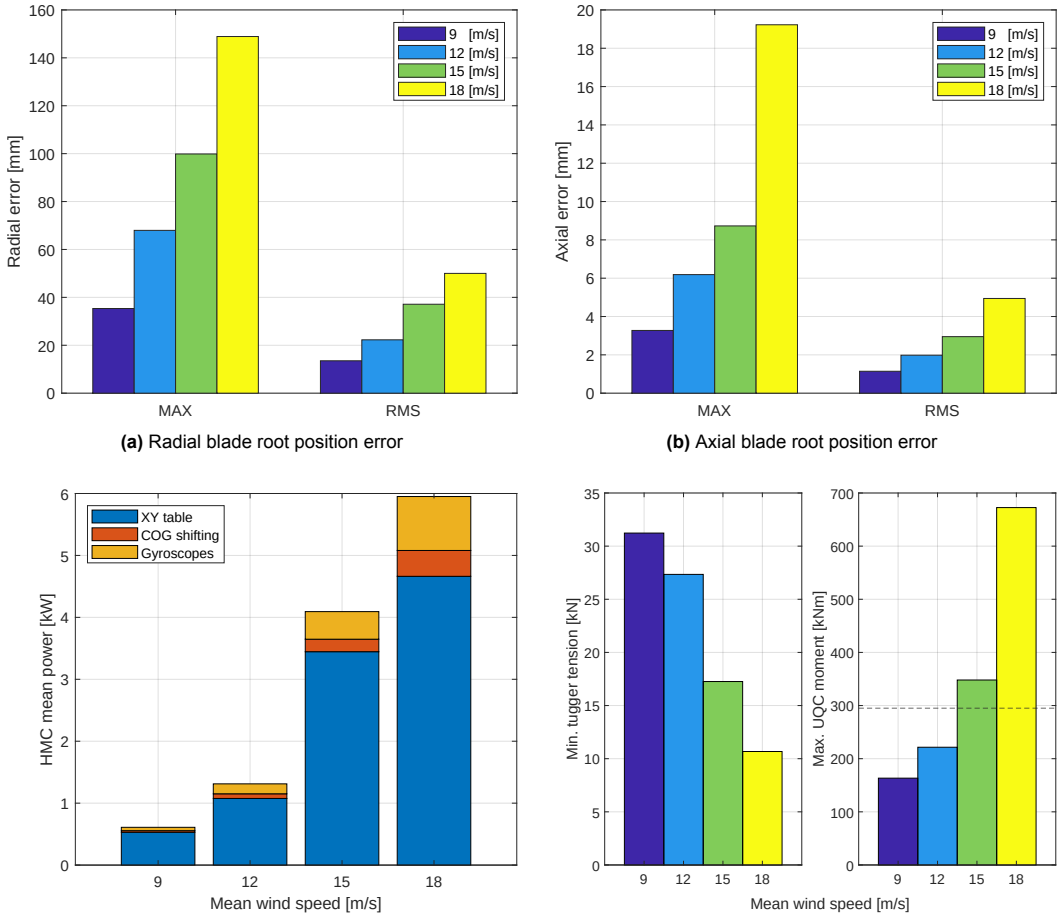

(a) Radial blade root position error

(b) Axial blade root position error

(c) HMC actuator power

(d) Tugger tension and UQC moment

Figure 5.10: Simulation results of SBIS with HMC for mean wind speed (U_w) of 9, 12, 15 and 18 m/s, $I_{ref} = 0.16$ (class A).

5.5.2. Wind direction

To assess the effect of wind direction on the results, the incoming wind direction was rotated in 30 degree intervals from -90 to 120 degrees relative to the reference case. In the case of a 90-degree angle, the wind is aligned with the y-axis instead of the x-axis. For a uniform wind without turbulence, this should result in zero aerodynamic loads on the blade for the assumed cross-flow conditions in the MarIn wind model.

The results clearly demonstrate the effect of wind direction. As expected, the wind direction aligned with the x-axis assumed in the reference case represents the most critical situation. Due to the non-uniform and turbulent nature of the wind, there is a small amount of blade motion when the wind direction is rotated by 90 degrees. The effective incoming wind speed at the blade is determined by the cosine of the relative angle between the blade and wind direction. This relationship between the angle and blade motion appears to be reflected in the results. When the wind direction is rotated beyond 90 degrees, the blade motion increases again.

The maximum angle at which the system remains stable is 120 degrees. Beyond this point, the tugger pretension is lost due to the aerodynamic loads. At angles greater than 90 degrees, the wind no longer blows from behind the crane (in the positive x-direction), but instead has a component in the negative x-direction. As a result, the drag loads result in a reduction of pretension instead of an increase in pretension when the wind blows from behind the crane. This in combination with the moment around the z-axis due to the wind loading results in a loss of pretension.

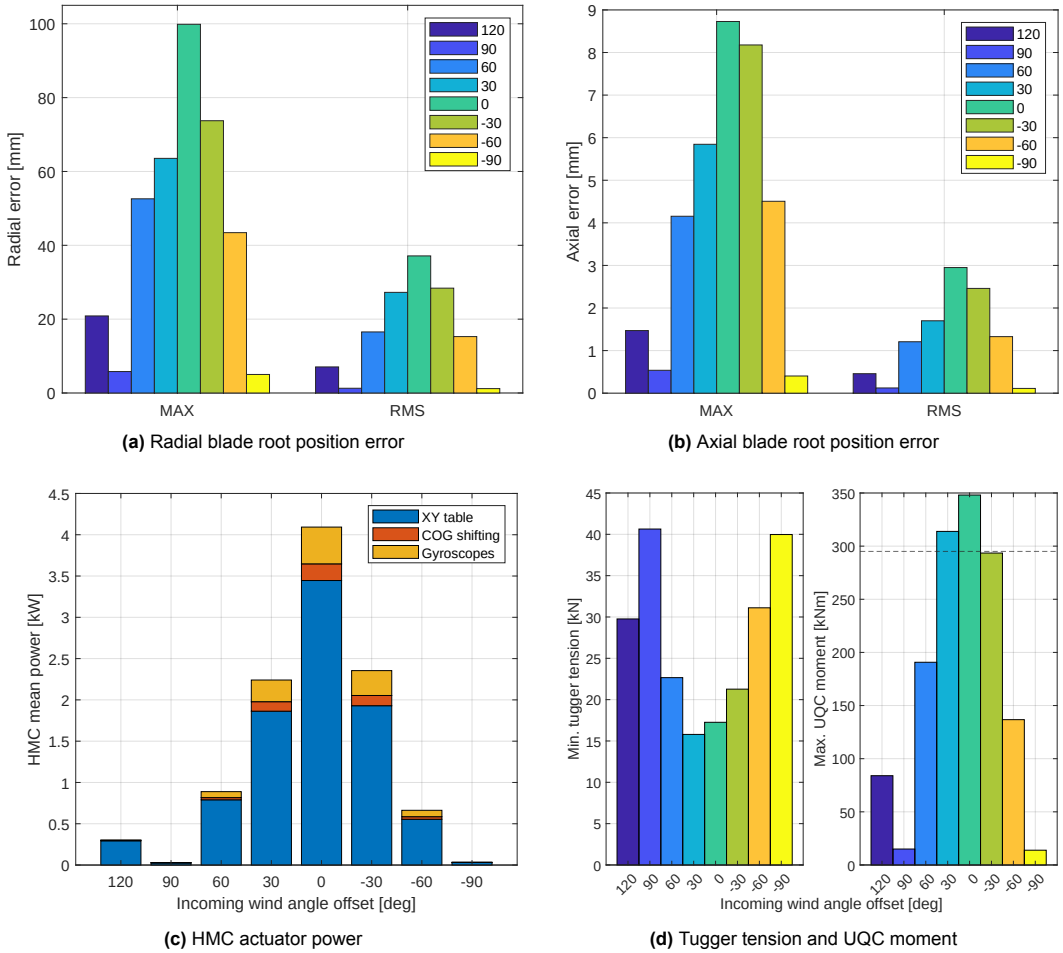

(a) Radial blade root position error

(b) Axial blade root position error

(c) HMC actuator power

(d) Tugger tension and UQC moment

Figure 5.11: Results for the SBIS with HMC for wind direction of 120[°] up to -90[°] in 30[°] intervals, U_w = 15 [m/s], TI = 0.18.

5.5.3. Turbulence intensity

The IEC standard defines three turbulence classes. All three turbulence classes were used. The results in figure 5.12 demonstrate that the system is sensitive to turbulence intensity. All measured system outputs appear equally sensitive to the intensity of turbulence. For turbulence class C, the blade motion decreases by approximately 25% compared to the reference case with turbulence class A. This also leads to a decrease in HMC power consumption. Additionally, for the lowest turbulence class, the moment on the UQC coupling remains below the allowable slip moment.

5.5.4. Damping

The assumed damping values were varied by $\pm$ 10% and $\pm$ 25% from the reference case. The results are presented in figure 5.13. An important observation is that the controller remains stable in all cases. The radial and axial errors do not show equal sensitivity to changes in damping. The radial error shown very low sensitivity to changes in damping, while the axial error decreases for higher damping values.

A possible explanation for this behaviour is that the gyroscope and XY table provide much smaller feedback to the rest of the system compared to the COG shifting method. Due to the use of two gyroscopes that rotate in equal but opposite direction, there is no reaction moment on the block. The counterweight on the XY table reduces its response to the rest of the system. On the other hand, the reaction loads from the COG shifting, which operates in the y-direction, are not cancelled out and excite pendulum swing in the y-direction. Increasing damping in the system ensures that this excitation is more effectively damped, leading to a decrease in the error in the y-direction. Since the XY table and gyroscopes have less impact on the rest of the system, additional damping in the rest of the system has less effect on the radial compensation effectiveness.

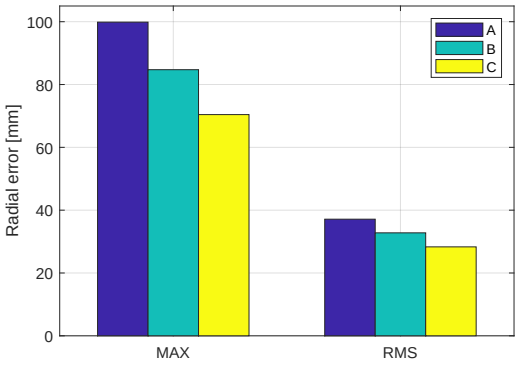

(a) Radial blade root position error

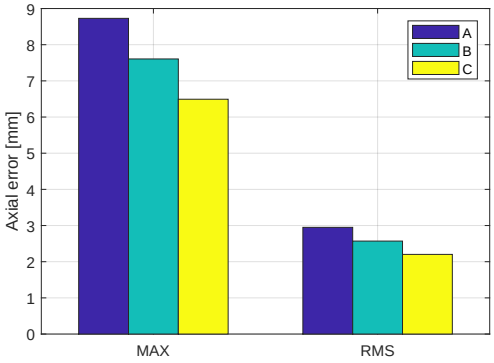

(b) Axial blade root position error

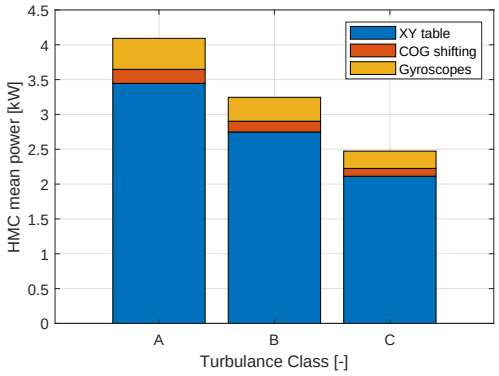

(c) HMC actuator power

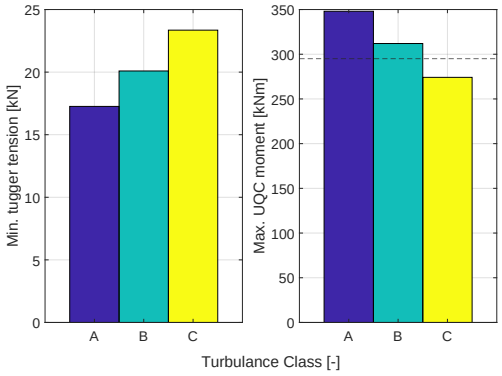

(d) Tugger tension and UQC moment

Figure 5.12: Simulation results of SBIS with HMC for U_w = 15, and TI = 0.13 (class C), 0.16 (class B) and 0.18 (class A)

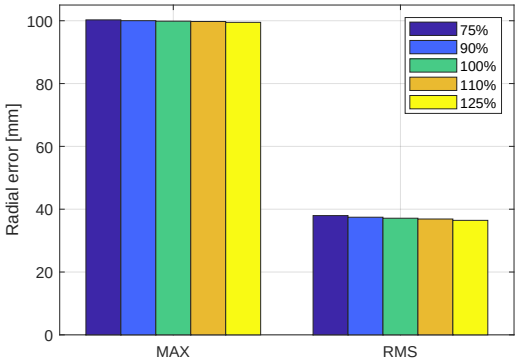

(a) Radial blade root position error

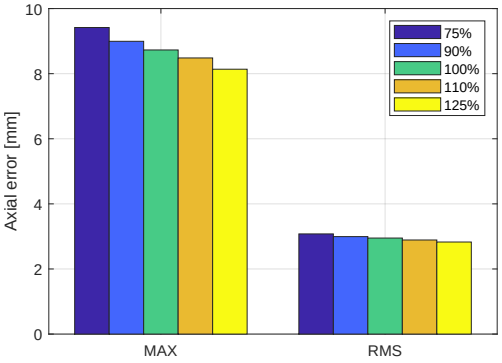

(b) Axial blade root position error

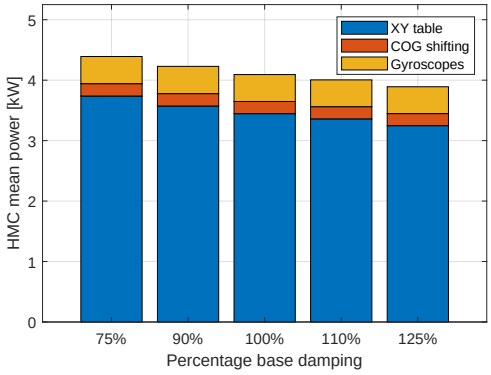

(c) HMC actuator power

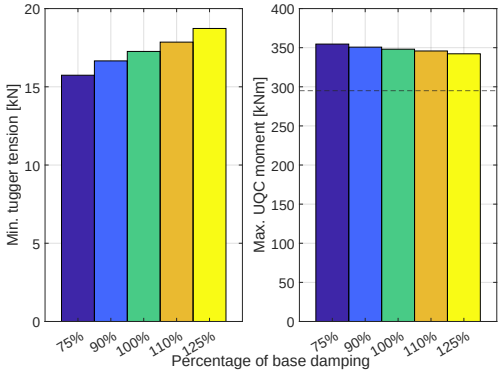

(d) Tugger tension and UQC moment

Figure 5.13: Results of the SBIS with HMC for additional damping of $\pm$10% and $\pm$25%, U_w = 15 [m/s], TI = 0.18.

5.5.5. Tugger line angle

Previously, it was assumed that tugger lines are parallel and aligned with the x-axis. Although parallel tugger lines are often desired, this is not always the case in reality. Extenders are often added to the yoke to increase the distance between the attachment points and achieve parallel tugger lines, as shown in figure 1.1. However, for the proposed HMC, the tugger lines are connected to the lower block instead of the blade yoke. The lower block has mounting eyes on the side for attaching the tugger lines. The mounting on the crane is not adjustable in width. The tugger lines run along the boom, which is typically wider than the lower block. If no extenders can be added to the lower block, the tugger lines will be at an angle, as depicted in figure 5.16.

When the tugger lines are at an angle, it introduces an additional coupling between the translational x and y DOF. To investigate the effect of this additional coupling, the width of the tugger mounting on the crane is varied between 10 and 20 meters, corresponding to tugger angles ranging from 0 to 27 degrees. The results are summarized in figure 5.14. The effect of the coupling is reflected in the y error. Due to the additional coupling between x and y, the error in the y-direction increases for larger tugger angles. Additionally, a larger tugger angle results in higher power requirements for the HMC. For smaller angles, the error, and power requirements initially appear to decrease. However, this is likely due to variance in the results caused by the complex non-linear dynamic behaviour of the system.

Furthermore, it is observed that the overall tension increases for larger tugger line angles. The tuggers need to deal with the same loading in the x-direction. However, due to the angle, an additional component in the y-direction is introduced, resulting in an overall increase in line tensions.

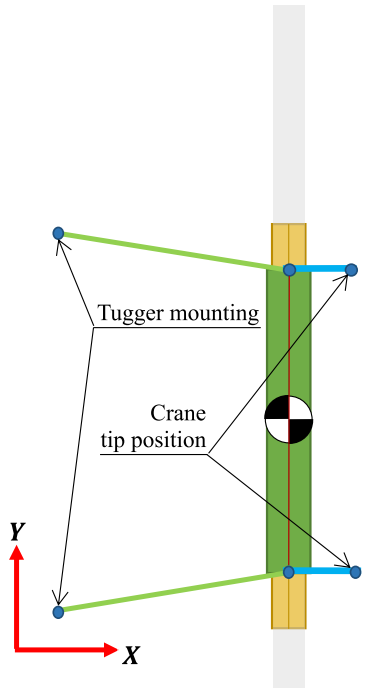

Figure 5.16: Tugger line under an angle due to the wider crane

5.5.6. Tugger line pretension

The static pretension in the tugger lines is chosen by the operator based on environmental conditions. Based on the results in figure 5.15, a relationship between the simulation output and the static tugger pretension is observed. Higher pretension creates a stiffer system in the x-direction, leading to a slightly improved compensation effectiveness in the radial direction. However, the axial error seems to slightly increase for higher pretension.

Again, it is evident from these results that the system behaviour changes significantly when pretension is lost. In cases with insufficient pretension, both HMC power consumption and blade root error increase.

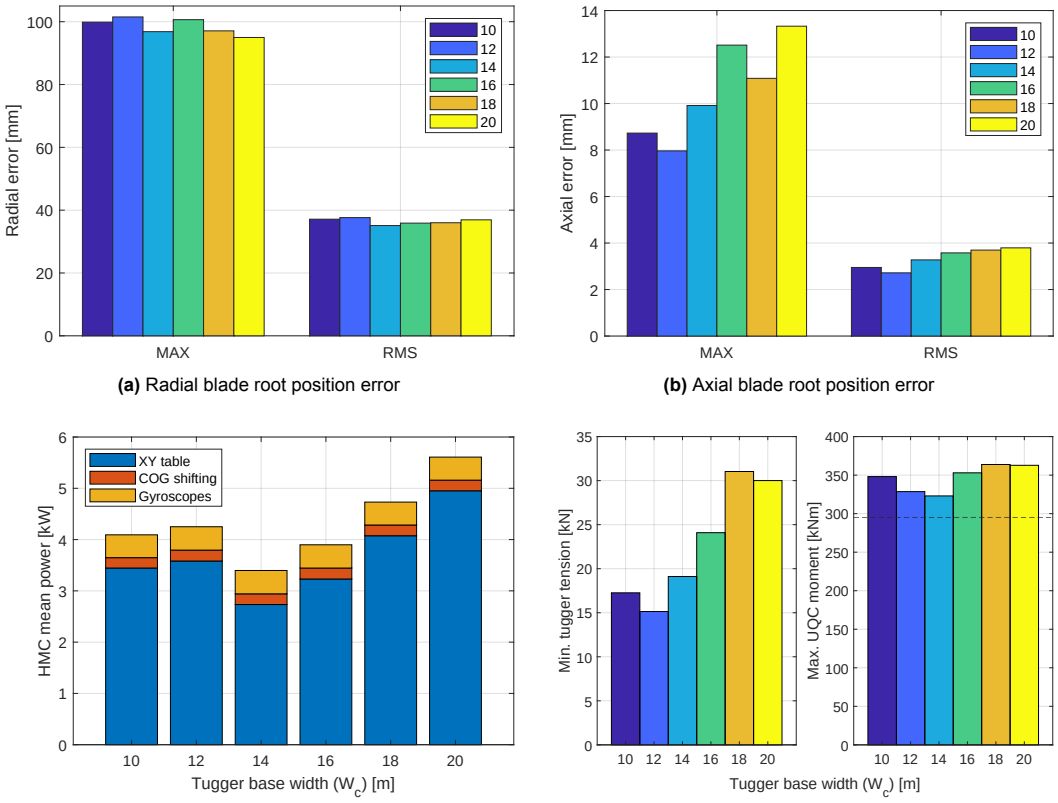

(a) Radial blade root position error

(b) Axial blade root position error

(c) HMC actuator power

(d) Tugger tension and UQC moment

Figure 5.14: Results of the SBIS with HMC for a crane width (W_c) from 10 to 20 meters, U_w = 15, and TI = 0.18 (class A)

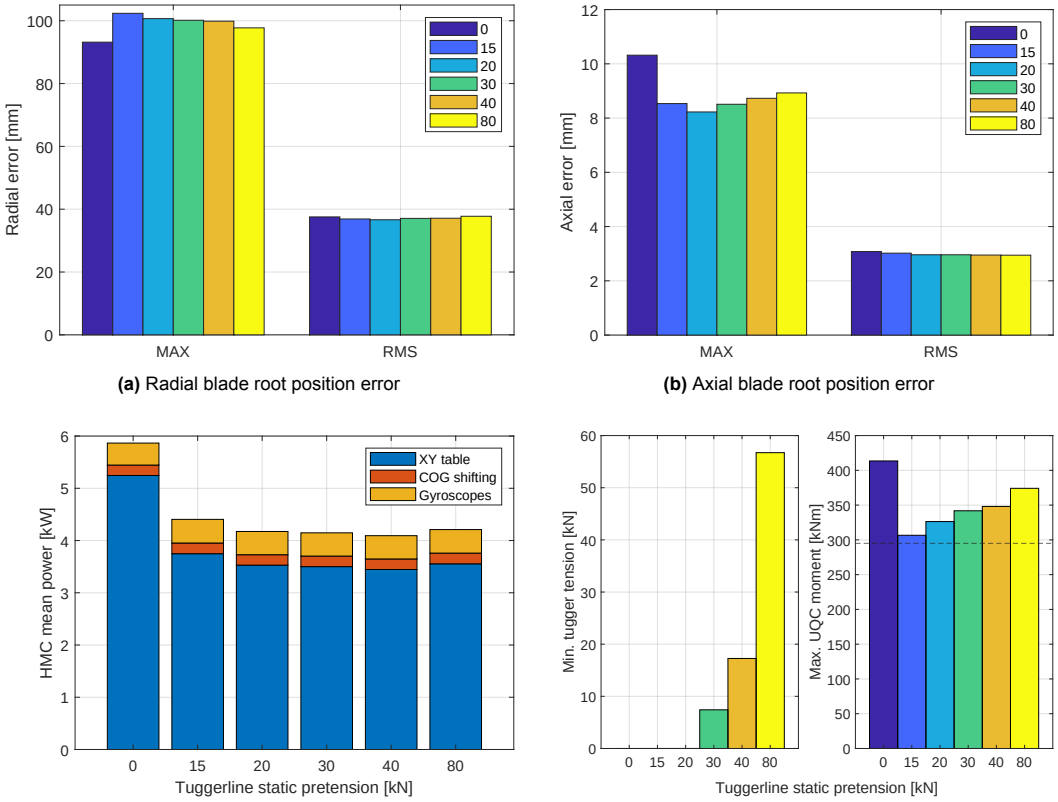

(a) Radial blade root position error

(b) Axial blade root position error

(c) HMC actuator power

(d) Tugger tension and UQC moment

Figure 5.15: Simulation results of SBIS with HMC for various static tugger pretensions, U_w = 15, and TI = 0.18 (class A)

5.5.7. Static blade pitch

For all simulations performed up to this point, a static blade pitch angle $\beta_\circ$ of 7 degrees was assumed. This angle was adopted from the reference blade yoke used. In practice, this angle can be adjusted by modifying the yoke.

The blade angle in the yoke has significant effects on the aerodynamic loading of the blade. This has been mapped in figure 5.17. A single blade is placed in the wind model from the MarIn toolbox. The blade is fixed in position and subjected to a uniform airflow with a constant velocity of 12 m/s. The resulting moments around the blade COG are shown for the full range of blade pitch angles. By adjusting the pitch angle, the type of loading on the system is adjusted. Note that the actual blade angle during the simulation is not constant, as the blade yoke (to which the blade is attached) is free to rotate about the pitch axis. The motion is ultimately constrained by the main hoist and tugger line connections to the suspended load, shown in figure 2.3.

The proposed HMC cannot compensate for rotation around the z-axis. Therefore, it is desirable to limit the load around the z-axis as much as possible. A large blade pitch region that results in a low moment around the z-axis is observed around 0 and -180 degrees. The angles of -180 and -5 degrees are particularly interesting, as the load in both x- and z-directions is low for these angles. The simulation results for blade angles of -190, -180, -170, -15, -15, -5, 5, 15, 20, and 25 degrees are shown in figure 5.18. The reference case with a pitch angle of 7 degrees is also included.

As expected, the results are highly sensitive to the static blade pitch angle. The main observation that is made, is the inability of the proposed HMC to cope with a large moment around the z-axis. For the relatively small increase in pitch angle from 20 to 25 degrees, there is a significant increase in blade root error. This is a result of the loss of tugger pretension due to the large moment around z, causing the blade to yaw significantly.

On the other hand, the performance of the system is greatly improved by adjusting the blade angle to -180 degrees. This blade orientation results in minimal aerodynamic loading. The aerodynamics loading at this blade angle can be well compensated by the HMC.

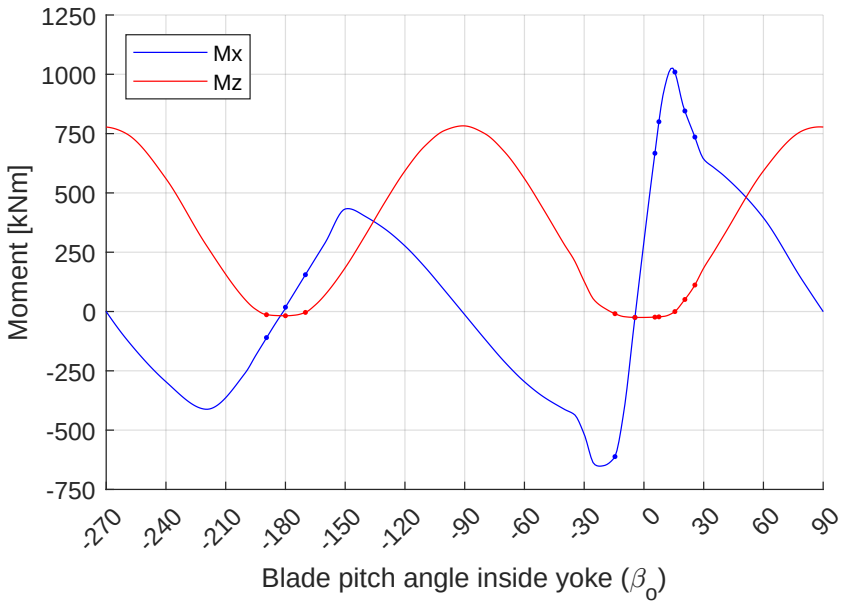

Figure 5.17: The wind induced moment on the 15MW turbine blade in uniform flow with constant velocity U_w = 12 m/s for various static blade pitch angles $\beta_\circ$

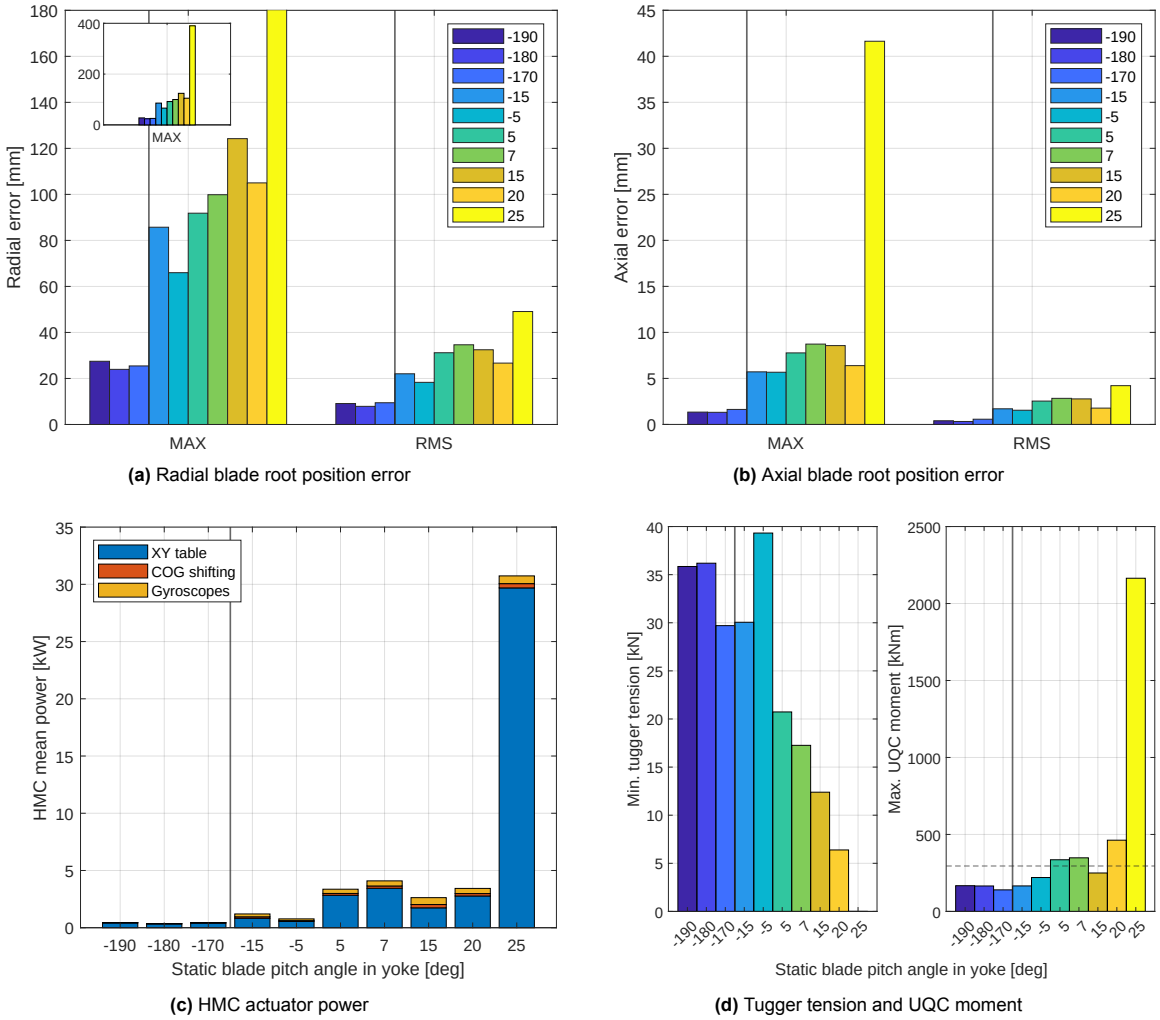

(a) Radial blade root position error

(b) Axial blade root position error

(c) HMC actuator power

(d) Tugger tension and UQC moment

Figure 5.18: Simulation results of SBIS with HMC for various static blade pitch angle ($\beta_\circ$), U_w = 15, and TI = 0.18 (class A)

5.6. Summary

This final chapter addresses the final two sub-questions, elaborated upon below.

SQ7: How can the HMC actuation methods best be combined into a HMC concept to achieve the best performance for the set KPI's? Based on simulation results of the individual actuation methods, a selection is combined into a HMC concept. The XY table is employed for compensation in the x- and y-directions, while the gyroscope handles compensation in the z-direction. To avoid gyroscope saturation, the COG shifting method with counterweight is included, capable of generating a constant moment through counterweight shifting.

Both the XY table and COG shifting utilize counterweights translating in the y-direction. An efficient approach would be merging these counterweights into one. However, the COG shifting method demands a substantial stroke. Verification runs show that significant cylinder stroke in the y-direction can lead to stability issues for compensation in the x-direction. This prevents simultaneous use of the counterweights in combination with the existing PID controllers.

The HMC controller consists out of three parallel PID controllers. The XY table and gyroscope controllers, developed using the 1DOF models, are implemented without alteration. Both utilize a separate portion of the error signal and operate in parallel. The COG shifting controller, is adjusted. Instead of blade root error, it considers the gyroscope's offset from the neutral position as input, requiring an extra system output: the gyroscope precession angle.

Table 5.4: Simulation results of proposed HMC effectiveness

	Baseline	HMC	Unit	Reduction
Max. Radial error	691	99.9	[mm]	85.5%
Max. Axial error	228	8.73	[mm]	96.2%
Max. Root velocity	0.244	0.0981	[m/s]	59.8%
Blade angle	1.43	0.788	[deg]	44.9%
Mean Power Consumption HMC	-	4.10	[kW]	-

SQ8: How to verify the control performance and validate operation of the chosen HMC concept? To verify and validate the proposed HMC's control performance and operation, the concept is applied in a full 6DOF simulator. This model is reconstructed from the same model blocks described in section 4.1.2. Two models are simulated: a baseline consisting of the SBIS without any actuation methods, and a model of the SBIS with the HMC. The main results are summarized in table 5.4.

In addition to comparing the SBIS with and without the HMC for the reference case, a sensitivity analysis was conducted by varying various system parameters. The key findings for each sensitivity case are summarized below:

- **Mean wind speed:** As anticipated, higher wind speeds lead to increased blade motion and higher power consumption. The observed relationship between aerodynamic load and wind speed aligns with theory, though the limited sample size cautions definitive conclusions. Results suggest that the installation of 15 MW OWT blades is viable up to around 12 m/s wind speed, with radial errors meeting the required accuracy of 60 mm.
- **Wind direction:** The reference case with wind aligned along the x-axis is most critical, while rotation by 90 degrees yields minimal blade motion. However, for very low angles, the results should be interpreted cautiously due to the cross-flow assumption. The blade's effective incoming wind speed is governed by the cosine of the angle, which is observed back in the blade position error. Beyond 120 degrees, tugger pretension is lost, leading to a loss of stability.
- **Turbulence intensity:** The three IEC turbulence classes were tested, revealing sensitivity to turbulence intensity; turbulence class C demonstrated a 25% reduction in blade motion and HMC power consumption compared to class A.
- **Damping:** Stable controller behaviour was observed for $\pm$25% damping. Radial and axial errors exhibited differing sensitivities to damping changes, with radial error showing low sensitivity while axial error decreased with higher damping. It is not fully understood why this is the case, but this discrepancy may stem from a more pronounced coupling between overall damping and the COG shifting actuation method, which operates in the axial direction, in contrast to the XY table and gyroscopes that provide less feedback to the system due to their operational principles.
- **Tugger line angle:** Introducing an angle to the tugger lines creates additional coupling between the translational x and y degrees of freedom. Varying the tugger line angle from 0 to 27 degrees reveals that larger angles lead to increased axial error, higher HMC power demands, and elevated overall tugger tension due to the additional y-direction tension component introduced by the angle.
- **Tugger line pretension:** Tugger pretension is varied from 0 to 80 kN. Increased pretension yields a slight improvement in radial compensation effectiveness. However, a slight increase in axial error is noted for higher pretensions. Both effect are small though. Most evident is again the result of losing pretension, which leads to a significant increase in HMC power consumption and blade root error.
- **Static blade pitch:** The proposed HMC lacks the capability to directly compensate around the z-axis, which favours blade angles where the wind-induced moment around this axis is minimal. This is the case for static pitch angle around 0 and -180 degrees. There is a strong sensitivity between the performance of the SBIS with HMC and the static blade pitch angle. Due to the HMC's inability to handle large moments about the z-axis, a slight pitch angle increase from 20 to 25 degrees results in a massive increase in blade root error, due to large yaw-motions when tugger pretension is lost. On the other hand, the performance is increased by choosing a static pitch angle of -5 or -180 degrees, effectively minimizing aerodynamic loading.

6

Conclusions and Recommendations

The research presented in this paper is focused on the analysis and assessment of actuation methods that can be applied to a hook-mounted compensation tool to reduce the impact of aerodynamic loads on a turbine blade during single-blade installation, aiming to enhance the future installation of offshore wind turbines. The research has been conducted in collaboration with Huisman Equipment BV. The objective of the study is to gain more insight into how the actuation methods behave within the SBIS, in order to make a well-founded decision regarding which actuation methods are best suited for a hook-mounted compensator. The project contributes to a more extensive knowledge and understanding of the applicability of the individual actuation methods, and the use of local stabilization in the shape of a hook-mounted compensator for single-blade installation in general.

The main research question reads: How can the highest compensation effectiveness be achieved using hook mounted actuation methods for offshore single-blade installation?

6.1. Conclusions

The main research question has been addressed through eight subquestions, through four steps in chapters 2 to 5. Below, for each chapter, the corresponding research questions are provided, a brief overview is given of the approach applied in the chapter, and the main conclusions are summarized.

2. Development framework

SQ1: What is the state of the art of motion compensation for single-blade OWT installation?

SQ2: What are the operational requirements, environmental conditions and disturbances encountered during single-blade installation using the HMC actuation methods?

SQ3: How can KPI's be defined to characterize the effectiveness of the HMC actuation methods?

This chapter forms a foundation for the main content of the report, providing an extended context for the subsequent analyses. Based on literature, the state of offshore motion compensation solutions is reviewed, and the single-blade installation process, operational conditions, and requirements are provided. Additionally, the interfacing systems like vessel, crane, and turbine are defined. This information serves as a basis for modelling the SBIS in the subsequent chapters.

- Studies focused on developing 3D MCC for OWT blade installation have identified significant challenges. Achieving the required installation accuracy for OWT blades solely through 3D MCCs is unlikely. Hence, the development of effective load stabilization systems remains important for developments in OWT installation.
- The installation method is particularly sensitive to wind disturbances. Aerodynamic loads on the suspended blade lead to blade root motion. During the final installation steps, a radial accuracy of 6 to 8 cm is required to align and mate the guide pin on the blade root with the corresponding hole on the turbine hub. The blade root velocity should be minimized to reduce damage in case of guide pin impact with the hub. Laminate damage can occur at impact velocities above 0.6 m/s.
- Two categories of KPIs are defined to assess the effectiveness of actuation methods. The first category focuses on compensation effectiveness, including radial and axial positional errors of the blade root, blade root velocity, and blade angle. The second category includes actuator input power and effort.

3. Linear modelling:

SQ4: How can the single-blade installation systems for the actuation methods be described linearly?

SQ5: How can the actuated single-blade installation systems be controlled?

The chapter addresses the linear model development. This process involves reducing the 6DOF system into a single DOF corresponding with the actuated DOF for the actuation method. Each actuation method actuates a specific DOF, and operational planes are defined in which the operation of the actuation method is described. A mass-spring-damper representation of the SBIS is constructed based on the description of the actuation method within its respective operational plane. Using the Euler-Lagrange method, a state space model for the system is derived. The open-loop response of the SBIS is examined and used to propose a PID controller for each actuation method. Below, the main conclusion and insight from this chapter are summarized.

- The XY table achieves the highest bandwidth of 3.67 Hz. Due to the use of the counterweight, there is minimal feedback to the rest of the system. The limiting factor is the stiffness of the hydraulic cylinder itself. When the counterweight does not exactly match the mass of the blade (yoke), compensation introduces feedback to the system. A slightly heavier counterweight is preferred over a lighter counterweight, as the system feedback result in phase gain, instead of phase loss, which is the case for the lighter counterweight.
- The pendulum stiffness of the load under the hoist cables is often limiting. For the wind vanes and power swivel, that both operate around the z-axis, the performance in the considered configuration is significantly constrained by this. The stiffness depends on the hoist cable length and the width of the lower block. In general, a wider lower block and shorter hoist cable lengths are favourable to hook mounted compensation methods. A wider attachment of the tugger lines also increases the hoist stiffness around the z-axis. In this study it is assumed that the distance between the tugger lines is equal to the lower block width, but in practice this could be increased with extensions on the block. As the rotational stiffness around the z-axis of the suspended load under the cables depends on the hoist cable length, it also changes during hoisting operations, which can impact control stability. However, during the alignment phase, the hoist cable length does not vary significantly.
- The gyroscope achieves the second-highest bandwidth. The primary limiting factor here again is the hoist cable stiffness. The stiffness of the suspended load around the x-axis depend on the width of the lower block, and the stiffness and the number of hoist cables. Since the load is light, a split-block configuration is assumed. However, for the gyroscope actuation method, and for hook mounted compensation in general, it is favourable to utilize all bundles, as this increases stiffness and damping in the main hoist. The bandwidth of the gyroscope in the current configuration is 0.46 Hz. Given that most of the wind spectrum energy lies within frequencies below 0.1 Hz, this bandwidth is sufficient to counteract wind disturbances.

4. Non-Linear modelling:

SQ6: How to model the HMC actuation methods for the application of single-blade OWT installation?

This chapter present the assessment of the individual actuation methods. To this effect, simulations are carried out within the designated 3DOF operational planes, using the linear PID controllers developed before. Numerical models are constructed with distinct blocks to simulate specific aspects of the system, including body dynamics, coupling loads, and external loads. The wind model from the MarIn toolbox is used to compute the wind loads. Modelling and simulation are conducted within Matlab/Simulink. Below, the insights in the performance of the actuation methods based on the simulations are listed.

- Verification runs were used to verify the fundamental behaviour of the model and to identify interactions between the DOF. A significant coupling effect is present for the XY table. When a cylinder offset exists in one direction, compensation in the perpendicular direction generates a yaw moment. This effect becomes more prominent with larger cylinder strokes. Simulations validate that the stroke remains within acceptable limits to prevent controller instability.
- As the XY table cannot directly compensate for rotation, it required considerable stroke length to compensate for rotation of the blade. Nevertheless, the compensation effectiveness of the XY

table is excellent, reducing the radial error from 580 mm for the baseline without any actuation method to 72 mm, which is an 87% reduction.

- For both the power swivel and wind vanes, compensation effectiveness is low. In fact, for the power swivel, the error increases due to a reduction in tugger line tension caused by the actuation method. The low effectiveness of these two methods aligns with the low bandwidth, stemming from the relatively low stiffness of the suspended load around the z-axis. For the power swivel, an additional problem is that the existing system is underpowered for the intended application. Increasing the motor size is expected to yield marginal improvements, since the low hoist stiffness causes the block to twist, leading to rapid loss of tugger tension.
- The gyroscope initially performs well but encounters saturation limitations after approximately 40 seconds, resulting in a loss of control. While this method shows potential in handling fluctuating disturbances, it struggles to counteract the constant wind-induced moment on the blade.
- An inverse correlation exists between achieved radial and axial errors using the COG shifting actuation method. Effective radial blade root compensation is achieved with the COG shifting actuation method, reducing the radial error by 89%. This comes at the cost of significant pendulum swinging in the y-direction, leading to substantial axial errors up to 570 mm. By reducing the control gain, the pendulum swing amplitude is reduced, but compromising radial compensation effectiveness. Due to the substantial stroke required to sufficiently shift the COG and generate the desired moment, a counterweight must be employed. Shifting the blade's position leads to axial errors of several meters.

5. Hook Mounted Compensation

SQ7: How can the HMC actuation methods best be combined into a HMC concept to achieve the best performance for the set KPI's?

SQ8: How to verify the control performance and validate operation of the chosen HMC concept?

Based on the results found for the assessment criteria for each individual actuation methods, an HMC concept is proposed in this chapter. A simulator model is used to quantify the effectiveness of the HMC, by applying the concept in a 6DOF environment. Additionally, the sensitivity of the HMC to changes in the assumed operational and environmental conditions are examined. The main conclusions of the chapter are summarized below.

- The XY table is employed for compensation in the x- and y-directions, while the gyroscope handles compensation in the z-direction. To avoid gyroscope saturation, the COG shifting method with counterweight is included, capable of producing a constant moment through shifting of the counterweight.
- Both the XY table and COG shifting utilize counterweights translating in the y-direction. An efficient approach would be merging these counterweights into one. However, the COG shifting method demands a substantial stroke. Verification runs show that significant cylinder stroke in the y-direction can lead to stability issues for compensation in the x-direction. This prevents simultaneous use of the counterweights in combination with the existing PID controllers. Combining these two counterweights might be achievable with retuned or more sophisticated control methods that can address for the strong coupling.
- In addition to a combination of the actuation methods, a combined controller is proposed, which integrates the linear controllers from the individual XY table and gyroscope actuation methods, allowing them to work in parallel. An alternative control approach is used for the COG shifting. Instead of the blade root error, it uses the gyroscope's precession offset from the neutral position as input, necessitating the gyroscope precession angle as an additional system output. The XY table and gyroscope controllers, developed using the 1DOF linear representation, remain stable in the 6DOF simulator model and are effective in controlling the HMC.
- When expanding to 6DOF, more coupling between the DOF is observed. As discussed earlier, the actuation with the XY table generates a yaw moment when an offset already existed between the blade and the lower block COG in the perpendicular direction from the cylinder stroke. As there is also a vertical offset between the blade (yoke) and the lower block's COG, denoted as L_{cog}, the same coupling effect is observed around the pitch and roll axes. This has a notable impact

on the XY table's open-loop response in the x direction. Compensation in the x-direction, due to the offset between the blade (yoke) and the lower block COG (L_{cog}), also induces a pitching moment, which in turn excites the tugger lines. In the current setup, this effect is not strong enough to destabilize the controller. However, with an L_{cog} 1.25 times the current offset, stability is compromised. The same effect is also present in the y-direction, resulting in roll motion. However, the roll motion does not result in significant strain in the tugger lines, whereby the impact is not as significant for compensation in the y-direction.

- Despite the additional coupling between the DOF described above, the PID controllers based on the 1DOF linear models remain stable, and the HMC is effective in reducing blade root motion. An 85% reduction in the maximum radial error is observed compared to the baseline. This baseline considers the same SBIS without any actuation method. Furthermore, a 96% reduction in the maximum axial blade root error is achieved. Despite not being directly controlled, a significant reduction in both blade root velocity (60%) and blade angle (45%) is observed when implementing the HMC. On top of this, the HMC also has a favourable impact on the distribution of loads on the two tugger lines.
- Both the individual actuation methods and the combined HMC concept use the Huisman UQC to achieve a rigid connection between the lower block and the yoke. In this UQC, moments around the z-axis are transmitted through a friction coupling. This dynamic is not directly included in the model, however the moment on the coupling is measured to examine whether the allowable moment on the friction coupling is not exceeded. For certain cases, the moment surpasses the allowable limit, particularly for wind speeds exceeding 12 m/s. To apply the HMC with the Huisman UQC during higher wind speeds, modifications to the UQC are necessary to increase the allowable moment on the friction coupling.
- The residual blade root motion is strongly dependent on the mean wind speed, and in a lesser degree to turbulence intensity. For a turbulence intensity of IEC class A, the maximum wind speed for which a blade root positioning accuracy of 60 mm is achieved, and for which the existing UQC system can be used, is around 12 m/s. For a reduced turbulence intensity, the same accuracy is achieved at higher wind speeds. A maximum blade root error of 68 mm is found for 15 m/s with the lowest turbulence class C.
- Placing the tugger line at an angle by increasing the width of the tugger mounting at the crane results in a small increase in the axial error. Also, higher HMC power requirements, and increased overall tugger tension is observed. However, the additional coupling between the x and y DOF does not lead to instability. An increase in static tugger pretension has only minor effect on the performance of the HMC. However, the effect of losing tugger pretension are more significant, increasing the HMC power consumption by 50%. Losing tugger pretension does however not significantly increase blade root error, indicating that the HMC is robust to the loss of tugger line tension.
- By changing the static blade pitch angle $\beta_\circ$, the wind-induced moment on the blade changes significantly, both in overall magnitude, and the distribution of the loading over the x- and z-axis. There is a strong sensitivity between the performance of the HMC and the static blade pitch angle. The proposed HMC lacks the capability to directly compensate around the z-axis. For pitch angles that result in large moments around the z-axis, a large increase in blade root error is observed, due to large wind induced yaw-motion when tugger pretension is lost, for which the HMC can not effectively compensate. On the other hand, the performance is further increased by using a static pitch angle of -5 or -180 degrees, where the wind-induced moment around the z-axis is minimal.

6.2. Recommendations for future research

This study shows that hook mounted compensation is a promising solution to wind-induced blade root motion during single-blade OWT installation. However, the subject examined in this study is extensive and complex, offering numerous possibilities for further research and improvement. Below is a list of recommendations for future research:

- None of the actuation methods considered in this study offer an effective solution for direct actuation of the blade around the z-axis. Consequently, the compensation for rotation around the z-axis is handled by the XY table, which is not specifically intended for this purpose. This leads to a large required stroke length of the x cylinder on the XY table and higher power consumption.

  The gyroscopes are currently applied in a single axis. However, it is also possible to rotate the gyroscopes around two axes. This introduces added complexity, but possibly, the existing set of gyroscopes can also be employed to actuate the blade around the z-axis. However, an alternative actuation method is still required that is able to exert a constant moment around the z-axis, as otherwise, the gyroscopes will simply saturate.

  Because the dynamics of the system around the z-axis differ significantly from that around the x-axis, the same gyroscope controller cannot be used for the additional axis. Therefore, an additional controller needs to be designed for compensation using the gyroscope about the z-axis. It is recommended to further investigate the dual application of the gyroscope to enhance the effectiveness and efficiency of the proposed HMC.
- In the initial phases, technical specifications were assumed for the size of the counterweights and gyroscope used in the actuation methods. The sizing of these component and the effect on system performance has not been considered in this study. Improvement in the sizing of these components could reduce the weight of the HMC, and possibly improve system performance. However, lower mass does reduce the moment that can be transferred through the current UQC friction coupling.

  Furthermore, the current design employs two distinct counterweights—one for the XY table and another for COG shifting. Further research into alternative control methods, capable of coping with the significant coupling that arises when a single counterweight is used, could lead to additional weight reduction.
- The dynamics of the tower were not considered. In reality, the hub undergoes a periodic sway motion. The location of the hook-mounted compensator allows for compensation of the hub's motion as well. This does introduce additional complexities. The relative position between the blade root and the hub needs to be measured, instead of just the blade position. Additionally, the hub's motion has a much higher frequency compared to blade motion due to the wind disturbance. The compensating performance for the higher-frequency hub motion is unknown and requires further investigation.
- This study solely focuses on the alignment phase of single-blade installation, where the blade is still freely suspended from the crane. Once the blade is mated, a connection is created between the blade and the hub, altering the dynamics of the system. It is recommended that the effect on the stability of the controlled HMC is investigated for the scenario where blade root is attached to the hub.
- Ideal sensors and measurable states were assumed. However, in reality, certain states might be challenging to measure accurately, and sensor data could be affected by noise and delay. To allow practical application of the proposed HMC, the impact of these factors requires further research.
- In the context of this study, the primary focus is placed on the analysis and assessment of the actuation methods, in order to directly compare them. Additionally, a fundamental understanding of how the HMC reacts to diverse environmental conditions and model parameters is developed through the constructed simulation model. However, to gain a deeper insight into how well the performance of the proposed HMC aligns with real-world scenarios, further verification of the model or a physical scale model is recommended.

Bibliography

[1] Seajacks, *Offshore wind solutions*, Apr. 2022. [Online]. Available: https://www.seajacks.com/offshore-wind-solutions/.

[2] European commission, *An eu strategy to harness the potential of offshore renewable energy for a climate neutral future*, Nov. 2020.

[3] Z. Ren, A. S. Verma, Y. Li, J. J. Teuwen, and Z. Jiang, "Offshore wind turbine operations and maintenance: A state-of-the-art review," *Renewable and Sustainable Energy Reviews*, vol. 144, p. 110 886, 2021. DOI: 10.1016/j.rser.2021.110886.

[4] Z. Jiang, "Installation of offshore wind turbines: A technical review," *Renewable and Sustainable Energy Reviews*, vol. 139, p. 110 576, 2021. DOI: 10.1016/j.rser.2020.110576.

[5] L. Ramírez, D. Fraile, G. Brindley, C. Walsh, and L. Van de Velde, *Offshore wind in europe: Key trends and statistics 2020*, Feb. 2022.

[6] Z. Jiang, Z. Gao, Z. Ren, Y. Li, and L. Duan, "A parametric study on the final blade installation process for monopile wind turbines under rough environmental conditions," *Engineering Structures*, vol. 172, pp. 1042–1056, 2018. DOI: 10.1016/j.engstruct.2018.04.078.

[7] K. Ha, "Reduction of stress concentration factor (scf) on the bolted joint connection for a large wind turbine rotor blade through various design modifications," *Applied Sciences*, vol. 10, no. 18, p. 6588, 2020.

[8] A. S. Verma, Z. Jiang, N. P. Vedvik, Z. Gao, and Z. Ren, "Impact assessment of a wind turbine blade root during an offshore mating process," *Engineering Structures*, vol. 180, pp. 205–222, 2019. DOI: 10.1016/j.engstruct.2018.11.012.

[9] Z. Ren, Z. Jiang, R. Skjetne, and Z. Gao, "Development and application of a simulator for offshore wind turbine blades installation," *Ocean Engineering*, vol. 166, pp. 380–395, 2018. DOI: 10.1016/j.oceaneng.2018.05.011.

[10] Y. Zhao, Z. Cheng, P. C. Sandvik, Z. Gao, and T. Moan, "An integrated dynamic analysis method for simulating installation of single blades for wind turbines," *Ocean Engineering*, vol. 152, pp. 72–88, 2018. DOI: 10.1016/j.oceaneng.2018.01.046.

[11] D. Ahn, S. C. Shin, S. Y. Kim, H. Kharoufi, and H. C. Kim, "Comparative evaluation of different offshore wind turbine installation vessels for korean west–south wind farm," *International Journal of Naval Architecture and Ocean Engineering*, vol. 9, no. 1, pp. 45–54, 2017. DOI: 10.1016/j.ijnaoe.2016.07.004.

[12] Y. Zhao, Z. Cheng, Z. Gao, P. C. Sandvik, and T. Moan, "Numerical study on the feasibility of offshore single blade installation by floating crane vessels," *Marine Structures*, vol. 64, pp. 442–462, 2019. DOI: 10.1016/j.marstruc.2018.12.001.

[13] W. Sonnema, "3d fe analysis of four legged jack-up vessels during preloading in cohesive soil," 2019.

[14] J. Fila, "Numerical assessment of preloading strategies for jack-up vessels in cohesive soils," 2018.

[15] K. de Leeuw, "Single lift blade alignment for large offshore wind turbines: A critical assessment of the alignment process of next generation wind turbine blades," 2019.

[16] Z. Jiang, "The impact of a passive tuned mass damper on offshore single-blade installation," *Journal of Wind Engineering and Industrial Aerodynamics*, vol. 176, pp. 65–77, 2018. DOI: 10.1016/j.jweia.2018.03.008.

[17] SINTEF Ocean, *Simo 4.10.3 user guide*, Sep. 2017.

[18] B. Li, "Operability study of walk-to-work for floating wind turbine and service operation vessel in the time domain," *Ocean Engineering*, vol. 220, p. 108 397, 2021. DOI: 10.1016/j.oceaneng.2020.108397.

[19] P. Van der Steen, "Ship motion prediction for the ampelmann system," 2016.

[20] S. Wang, Y. Sun, H. Chen, and J. Du, "Dynamic modelling and analysis of 3-axis motion compensated offshore cranes," *Ships and Offshore Structures*, vol. 13, no. 3, pp. 265–272, 2018. DOI: 10.1080/17445302.2017.1360981.

[21] M. Sun, S. Wang, G. Han, L. An, H. Chen, and Y. Sun, "Modeling and dynamic analysis of a triple-tagline anti-swing system for marine cranes in an offshore environment," *Journal of Marine Science and Engineering*, vol. 10, no. 8, p. 1146, 2022. DOI: 10.3390/jmse10081146.

[22] K. Hermans and J. Peeringa, *Future XL monopile foundation design for a 10 MW wind turbine in deep water*. ECN, 2016.

[23] J. Velarde and E. E. Bachynski, "Design and fatigue analysis of monopile foundations to support the dtu 10 mw offshore wind turbine," *Energy Procedia*, vol. 137, pp. 3–13, 2017. DOI: 10.1016/j.egypro.2017.10.330.

[24] Internetbureau Antum, *Motion compensated crane - bm-t40*, 2015. [Online]. Available: https://www.barge-master.com/products/bm-t40/.

[25] SMST equipment, *3d motion compensated cranes*, 2022. [Online]. Available: https://www.smstequipment.com/offshore-cranes/3d-motion-compensated-cranes/.

[26] MacGregor, *3-axis motion compensation cranes*, 2018. [Online]. Available: https://www.macgregor.com/Products/products/offshore-and-subsea-load-handling/3-axis-motion-compensation-cranes/.

[27] R. Buijs, "3d motion compensation for an offshore crane," Nov. 2017.

[28] M. Driessen, "Feasibility assessment of motion compensated cranes at an early design stage," 2021.

[29] D. J. G. Burggraaf, "Design of a motion compensating tool to improve the installation of offshore wind turbines," Jul. 2022.

[30] J. Woodacre, R. Bauer, and R. Irani, "A review of vertical motion heave compensation systems," *Ocean Engineering*, vol. 104, pp. 140–154, 2015. DOI: 10.1016/j.oceaneng.2015.05.004.

[31] Seaqualize, *News*, 2021. [Online]. Available: https://www.seaqualize.com/news.

[32] Z. Ren, Z. Jiang, Z. Gao, and R. Skjetne, "Active tugger line force control for single blade installation," *Wind Energy*, vol. 21, no. 12, pp. 1344–1358, 2018. DOI: 10.1002/we.2258.

[33] Liftra, *Lt975 - blade dragon*, 2018. [Online]. Available: https://liftra.com/products/lt975-blade-dragon.html.

[34] M. Wheeler, *New technology provides a steady hand when installing wind turbines*, Mar. 2022. [Online]. Available: https://createdigital.org.au/new-technology-provides-steady-hand-installing-wind-turbines/.

[35] S. Gamesa, *How it all comes together at sea: Installing an offshore wind farm*, Jun. 2020. [Online]. Available: https://www.youtube.com/watch?v=mDvS7tizetg&t=169s.

[36] I. E. Commission *et al.*, "Iec61400-1: 2005 wind turbines–part 1: Design requirements," *International Electrotechnical Commission, https://webstore. iec. ch/publication/5426, Accessed June*, vol. 24, p. 2020, 2005.

[37] B. Jonkman, "Turbsim user's guide v2. 00.00," *Natl. Renew. Energy Lab*, 2014.

[38] L. Kuijken, "Single blade installation for large wind turbines in extreme wind conditions: A quasi-steady aeroelastic study in high wind speeds under different inflow angles," 2015.

[39] D. Brown and M. Peck, "Energetics of control moment gyroscopes as joint actuators," *Journal of guidance, control, and dynamics*, vol. 32, no. 6, pp. 1871–1883, 2009.

[40] 2018. [Online]. Available: https://www.moog.com/literature/ICD/Moog-ServoValves-78Series-Catalog-en.pdf.

[41] H. Feng, Q. Du, Y. Huang, and Y. Chi, "Modelling study on stiffness characteristics of hydraulic cylinder under multi-factors.," *Strojniski Vestnik/Journal of Mechanical Engineering*, vol. 63, 2017.

[42] T. Hartmans, "Hook load fluctuations during offshore heavy lifting," 2016.

[43] H. Jin, T. Wang, F. Yu, Y. Zhu, J. Zhao, and J. Lee, "Unicycle robot stabilized by the effect of gyroscopic precession and its control realization based on centrifugal force compensation," *IEEE/ASME Transactions on Mechatronics*, vol. 21, no. 6, pp. 2737–2745, 2016. DOI: 10.1109/TMECH.2016.2590020.

[44] M. L. Hautus, "Controllability and observability conditions of linear autonomous systems," *Ned. Akad. Wetenschappen*, vol. 72, pp. 443–448, 1969.

[45] J. Diebel *et al.*, "Representing attitude: Euler angles, unit quaternions, and rotation vectors," *Matrix*, vol. 58, no. 15-16, pp. 1–35, 2006.

[46] E. Gaertner *et al.*, "Definition of the IEA 15-megawatt offshore reference wind turbine," International Energy Agency, Tech. Rep., 2020. [Online]. Available: https://www.nrel.gov/docs/fy20osti/75698.pdf.

Appendices

A

Scientific Research Paper

Assessment and analysis of hook mounted compensation methods for offshore wind turbine blade installation

M.J. van der Bend[a], Dr. V. Reppa[a], Ir. R Feith[b]

[a] *Dept. of Maritime and Transport Technology, Faculty Mechanical, Maritime and Materials Engineering, Delft University of Technology, Delft, NL*

[b] *Huisman Equipment B.V., Admiraal Trompstraat 2, 3115 HH, Schiedam, The Netherlands (NL)*

Abstract

During single-blade offshore wind turbine (OWT) installation, wind disturbance results in blade root motion. The sensitivity to this wind disturbance is more significant for larger blades, reducing the allowable weather limit for which installation is possible. A potential solution is a Hook Mounted Compensator (HMC) between the crane and the load that can provide high-precision compensation for OWT installation across multiple degrees of freedom (DOF), and compensate for the influence of wind on the turbine blade. Several Actuation Methods (AM)s have been identified that can be used in a HMC. However, these AMs have not been modelled dynamically and their effectiveness for the desired application is unknown. The aim of this study is therefore to analyse and assess the compensation effectiveness of these AMs. For this purpose, the AMs are simulated and analysed in various levels of complexity and DOFs. Initially, the system is considered in a single mechanical DOF. A linear representation is formulated, based on which a Proportional-Integral-Derivative (PID) controller for the AM is designed. This enables simulation of the Single-Blade Installation System (SBIS) in the time domain. Assessment criteria are established to evaluate the performance of the AMs. These criteria assess both the compensation effectiveness and the actuation input required. To simulate and assess the AMs, 3DOF numerical models are developed that describe the operation of the AMs in their respective operational plane. Based on the assessment results, three AMs are selected for application in a combined HMC concept. The chosen AMs are an XY table, employed to control blade root position in the x- and y-directions, gyroscopes used for controlling blade root position in the z-direction, and a COG shifting weight to prevent gyroscope saturation. The HMC utilizes the same PID controllers developed using the linear single DOF representation, working in parallel to control the blade root position. The behaviour of the installation system with the HMC is compared to a baseline without compensator in a 6DOF simulator model to verify the performance of the HMC and its controller. The motion of the blade root is successfully reduced by 96% along the blade axis and 86% radially.

1 Introduction

Offshore wind energy capacity has significantly increased in recent years. At the same time, the average individual capacity of installed OWTs has increased from 3 to 8.2 MW per turbine in 10 years time (Ramírez et al., 2022), and is expected to continue increasing. The required accuracy for installation is in the range of centimetres (Verma et al., 2019), while the vessel, crane, blades, and OWT assembly are all under the influence of environmental disturbances. Of these disturbances, the influence of wind during single-blade installation with a jack-up vessel is the most significant (Ren et al., 2018). A problem with the increasing turbine sizes is the greater sensitivity of larger blades to wind (de Leeuw, 2019). Larger turbines are expected to enter the market in the near future. However, there are still insufficient solutions for the increased influence of wind on the blade installation. A possible solution involves the use of a HMC between the crane and the load, providing high-precision compensation across multiple DOF for the blade motion at the hook. Several AMs for hook mounted compensation have been identified. However, these have not been modelled dynamically and their effectiveness for the desired application is unknown. The aim of this study is therefore to analyse and assess the compensation effectiveness of these AMs. From this analysis, a choice is made on AMs that are applied in a HMC concept. The main research question for the project reads: How can the highest compensation effectiveness be achieved using hook mounted actuation methods for offshore single-blade installation? The project contributes to a more extensive knowledge and understanding of the applicability of the individual AMs, and the use of local stabilization in the shape of a HMC for single-blade installation in general.

2 Single-blade Installation System

An overview of the SBIS during blade alignment is shown in fig. 1. The blade is picked up using a blade yoke (in yellow) at it's Center of Gravity (COG) ($\boldsymbol{p_{cog}}$) and suspended from a 3200 Mt Leg Encircling Cranes (LEC) crane on a jack-up vessel and aligned, but not connected to, the pre-installed turbine hub. The vessel is assumed to be rigidly connected to the seafloor. The influences of waves on the vessel are not taken into account, and no feedback from the blade or crane movement to the ship is considered, as the mass and inertia of the blade is significantly smaller than that of the ship (Ren et al., 2018). Tower flexibility and dynamics, such as excitation of the fore-aft natural frequency by wave loading

Table 1: Denotation of the positions and velocities in their corresponding frames

Frame	Origin	Position in frame	Orientation $\backslash\mathcal{N}$	Translational vel.	Rotational velocity
$\mathcal{G}$	$\mathbf{o}_g$	$\boldsymbol{p} = [x, y, z]^\top$	–	$\boldsymbol{v} = [\dot{x}, \dot{y}, \dot{z}]^\top$	–
$\mathcal{H}$	$\mathbf{o}_h$	$\boldsymbol{p}^h = [x^h, y^h, z^h]^\top$	$\boldsymbol{\theta}_h = [\alpha_h, \beta_h, \gamma_h]^\top$	$\boldsymbol{v}_h = [u_h, v_h, w_h]^\top$	$\boldsymbol{\omega}_h = [p_h, q_h, r_h]^\top$
$\mathcal{B}$	$\mathbf{o}_b$	$\boldsymbol{p}^b = [x^b, y^b, z^b]^\top$	$\boldsymbol{\theta}_b = [\alpha, \beta, \gamma]^\top$	$\boldsymbol{v}_b = [u, v, w]^\top$	$\boldsymbol{\omega}_b = [p, q, r]$

(Verma et al., 2019) are neglected.

The OWT used in the study is the International Energy Agency (IEA) 15-MW reference turbine, developed by the National Renewable Energy Laboratory (NREL). NREL reference turbines are specifically designed for research purposes and widely used in literature. This makes it a suitable choice for comparison and benchmarking.

The LEC is equipped with a tugger line system, visible in green in the system overview. The tugger lines are placed under pretension, pulling the load towards the boom, and kept at constant length by the winches. In the reference case, a static pretension of 40 kN is used. A traverse system ensures a horizontal orientation of the tugger lines.

The crane is also equipped with the Huisman Universal Quick Connector (UQC) system, which enables a rigid connection between the Lower Block (LB) (green block in fig. 1) and blade yoke. The UQC also includes a drive mechanism, called the power swivel, which can be used to rotate the suspended load around the z^h-axis relative to the LB. The moment around the z^h-axis is transferred through a slip coupling, limiting the maximum moment that can be transferred to $m_{slip} = r_{slip}\mu M_{tot} g\sqrt{2}$.

A global, hook-fixed and blade-fixed coordinate system are defined. All follow the right-hand rule. The orientation of the coordinate systems is shown in fig. 1.

- The origin of the global axis system, denoted by $\mathbf{o}_g$, is positioned at the intersection between the mean sea level (MSL) surface and the rotational axis of the crane (slewing axis). The three global axes are denoted x, y and z. The z-axis point upwards and the y-axis is aligned with the jack-up vessel's heading. The x-axis is oriented according to the right-hand rule. The crane is oriented such that the projection of the boom on the XY plane aligns with the x-axis. The orientations about the x-, y-, and z-axes are roll (α), pitch (β), and yaw (γ), respectively.

- The origin of the hook-fixed coordinate system $\mathbf{o}_h$ is located at the LB COG, which is assumed to be located in the centre of the LB. At $t = 0$, the axis orientation align with the global axis system.

- The blade and blade yoke are modelled as a single body. The origin of the blade-fixed coordinate system $\mathbf{o}_b$ is located at the blade COG, at the centre of the yoke, positioned directly under the LB along the z_h -axis at $t = 0$. At $t = 0$, the z^b -axis is pointed upwards parallel to the global z-axis, regardless of the blade rotation around the y^b-axis (blade pitch) within the blade yoke. The y^b-axis is aligned with the blade centreline.

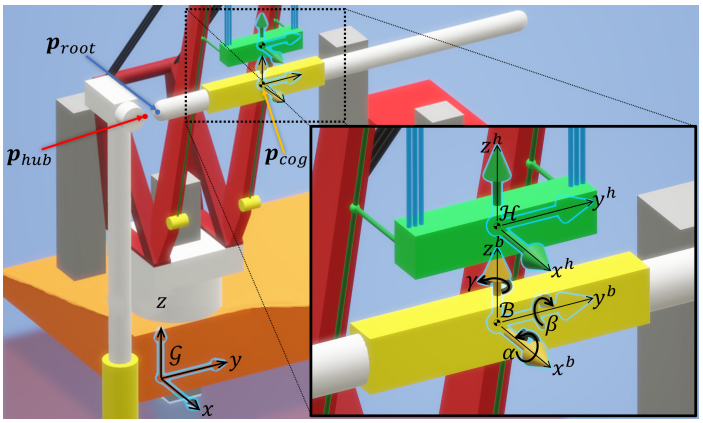

Figure 1: System overview, showing the orientation of the global, hook-fixed and blade-fixed coordinate system

3 Actuation Methods

The operation of each AMs is limited to a specific mechanical DOF. Each AM is only expected to be effective for this actuated DOF. As a result, it is likely not possible to control the blade root position in x, y and z using a single AM. Nevertheless, it is desired to directly compare the AMs within the DOF where they provide a solution. To achieve this, during the assessment of the individual AMs, the SBIS is described within the plane in which the AM operates, abstracted from the other DOF. This plane is called the operational plane. Table 2 provides an overview of the actuated DOF, operational plane, and the type of actuator used within each of the AMs. Here T_n^b stand for translation, and R_n^b for rotation in direction n within the blade-fixed coordinate system.

Table 2: Actuation Methods overview

Actuation method	Operational plane	Actuated DOF	Actuator type
XY table	XY	T_x^b, T_y^b	Hydraulic Cylinder
UQC	XY	R_z^b	Motor-Gearbox
Vanes	XY	R_z^b	Motor-Gearbox
Gyroscopes	YZ	R_x^b	Motor-Gearbox
COG shifting	YZ	R_x^b	Hydraulic Cylinder

The six AMs all use the Huisman UQC to establish a rigid connection between the LB and blade (yoke). The first AM is the XY table (AM1), which uses hydraulic cylinders to translate the blade relative to the LB. A counterweight CW with a mass equal to the combined blade and blade yoke is moved in equal but opposite direction. This way, the COG of the suspended load does not move, and reaction loads on the rest of the SBIS are minimized. The operation is described in the XY plane (yaw-plane).

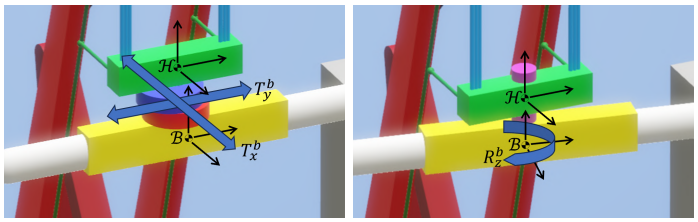

(a) AM1: XY table with CW

(b) AM2: UQC power swivel

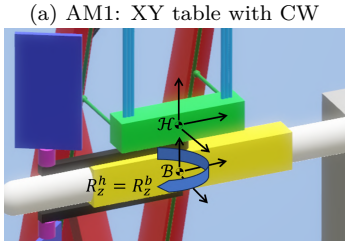

(c) AM3: Wind vanes

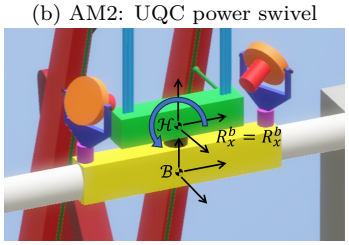

(d) AM4: Gyroscopes

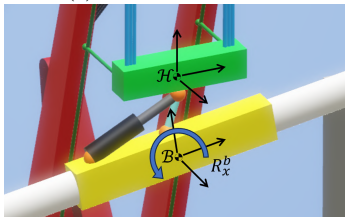

(e) AM5A: COG shifting

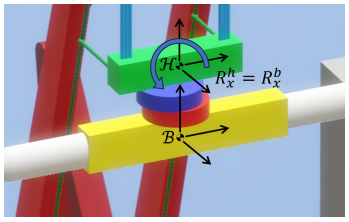

(f) AM5B: COG shifting with CW

Figure 2: AMs implemented in the SBIS (not to scale)

Two AMs operate around the z-axis, namely the UQC power swivel (AM2) and wind vanes (AM3). Figures 2b and 2c show the AMs within the SBIS. For AM3, two rotatable wind vanes are attached to the blade yoke. The vane's aerodynamic drag result in a moment around the z-axis. By rotating the vane, the drag can be adjusted, providing control over the resulting moment. Dual counter-rotating vanes are used to minimize undesired loading due to the generated lift. The operation of both AMs is described in the XY plane.

The gyroscopes (AM4) and COG shifting (AM5) actuate around the x-axis. Both are described in the YZ plane (roll-plane). For AM4, two counter-rotating gyroscopes are attached to the blade yoke, as shown in fig. 2d. Their spin axis is aligned with the y^h-axis. For this configuration, the gyroscopes generate a moment around the x-axis when rotated around their precession axis, aligned with the z^h-axis. Other contributions cancel out (Brown & Peck, 2009). By shifting the suspended loads COG in y-direction for AM5, the load is rotated around the x-axis until the COG is again below the main hoist pickup point. Two variants are considered, shown in figs. 2e and 2f, where either the blade itself (5A) or a CW is shifted, at the cost of added weight (5B).

4 Linear Analysis

To assess the behaviour of the SBIS for each AM, time domain simulations are conducted later. For this, the AMs need a controller. The SBIS is the combination of the crane, LB, blade (yoke) and AM. Each AM has its own working principle, affecting the dynamics of the SBIS, necessitating separate controllers for every AM. All controllersuse the blade root position as system output, denoted by $\boldsymbol{p}_{root}$ in fig. 1, and the mounting location on the hub as reference, denoted by $\boldsymbol{p}_{hub}$. A general control diagram is shown in fig. 4. Here, $[\boldsymbol{r}]$ is the reference root position, $[\boldsymbol{y}]$ is the system output and $[\boldsymbol{e}]$ is the error between $[\boldsymbol{r}]$ and $[\boldsymbol{y}]$. Finally, $[\boldsymbol{u}_1]$ is the control input to the SBIS, and $[\boldsymbol{d}]$ is the wind disturbance acting on the blade.

The hydraulic cylinders and electric motors used in the AMs contain internal control to regulate piston stroke and motor position or speed. The simplified internal dynamics are described by first-order transfer functions eq. (1).

$$\frac{d\,(s)}{d^{ref}\,(s)} = \frac{1}{\tau s + 1}, \qquad \frac{\theta_m\,(s)}{\theta_m^{ref}\,(s)} = \frac{1}{\tau s + 1} \tag{1}$$

The SBIS for each actuation method is reduced to a single mechanical DOF. Based on this description, a linear single DOF mass-spring-damper system (MSDS) of the SBIS is constructed for each AM, which is translated into a state-space representation. The linear analytical models enable frequency domain analysis, used to formulate a PID controller for each AM. The process steps are explained below:

1. Decomposition: The continuous SBIS is split into separate rigid bodies and described using representative masses, springs, and dampers. As only one mechanical DOF is considered, each rigid body i with mass M_i has a single generalized coordinate x_i, which represent the body's displacement from its equilibrium position. Figure 3 shows a simplified schematic of the SBIS and decomposition of the system. The system is decomposed into three bodies. The first represents the combined blade and blade yoke with mass M_{b^*}, the second representing the LB with mass M_{lb}, and finally a body for the crane with mass M_c, which represents the equivalent mass of the boom felt at the crane tip given by eq. (2). Here, I_{hinge} is the inertia of the boom around the crane hinge.

$$M_c = \frac{I_{hinge}}{(H_c - H_p)^2} \tag{2}$$

The coupling between the bodies is represented by springs and dampers. The pendulum restoring force between the crane tip and suspended load is represented by a spring with stiffness k_l, given by eq. (3). Here, g is the gravitational acceleration and M_{tot} is the total mass of the load suspended under the main hoist cable with length L_{mh}.

$$k_l = \frac{M_{tot} g}{L_{mh}} \tag{3}$$

Tugger lines run along the crane boom and provide an additional connection between the LB and crane boom. The axial stiffness of the tugger lines is denoted by k_t. The boom is modelled as a rigid lever. For small displacements, eq. (4) relates the displacement of the crane boom tip (x_c), and the tugger mount along the boom x_t.

$$x_t = \frac{L_1}{L_1 + L_2} x_c = \phi_t x_c \tag{4}$$

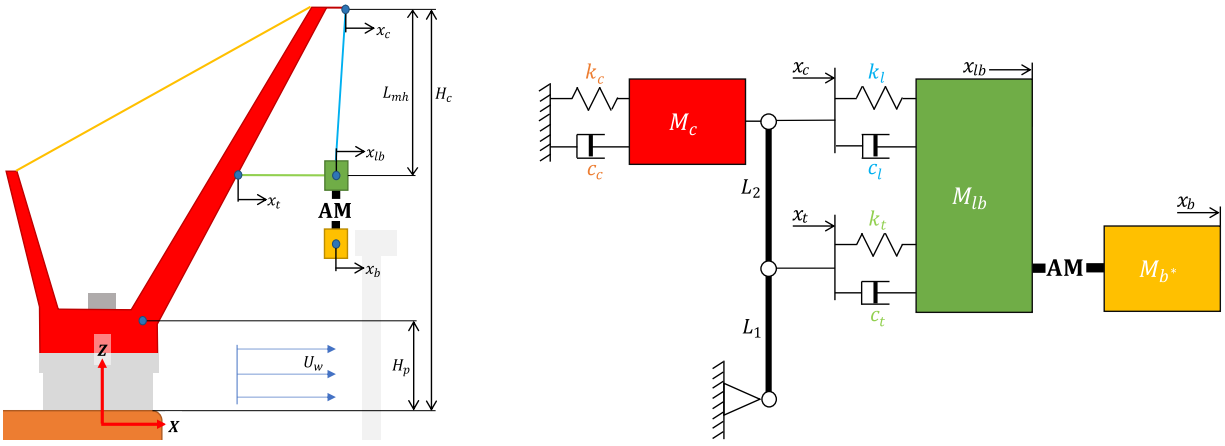

(a) Simplified schematic of SBIS in the XZ-plane (b) MSDS describing the same system in x-direction

Figure 3: Simplified schematic and representative MSDS of the SBIS

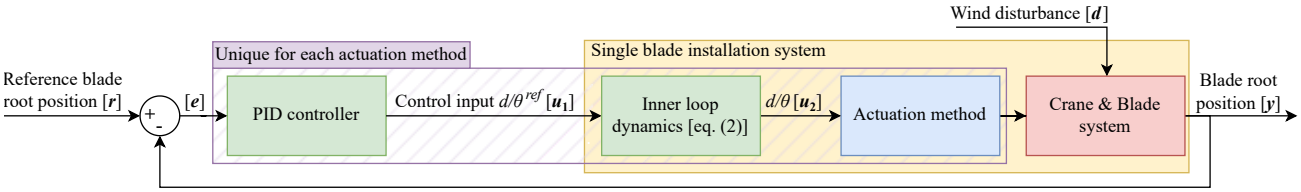

Figure 4: General control diagram for the SBIS with AM and linear controller.

2. Obtaining Equations of motion (EOM): The Lagrangian of the MSDS is given by eq. (5), and is a function of all the body kinetic energy terms (T) and spring potential energy terms (V), expressed within the generalized coordinates x_i and its derivative $\dot{x}_i$. The displacement of spring/damper j, given by d_j, is expressed in the generalized coordinates of the bodies between which it is located. For instance, the displacement of the spring representing the pendulum restoring force is given by $d_l = x_c - x_{lb}$. Rayleigh's dissipation function is given by eq. (6), which accounts for the dissipation of energy through damping. The EOM describing the system are found by evaluating the Euler-Lagrange equation provided in eq. (7) for each generalized coordinate.

$$L(x_i, \dot{x}_i, t) = T - V = \sum_{i=1}^{n} \frac{1}{2} M_i \dot{x}_i^2 - \sum_{j=1}^{m} \frac{1}{2} k_j d_j^2 \tag{5}$$

$$D(\dot{x}_i, t) = D = \sum_{j=1}^{m} \frac{1}{2} c_j \dot{d}_j^2 \tag{6}$$

$$\frac{d}{dt}\left(\frac{\delta L}{\delta \dot{x}_i}\right) - \frac{\delta L}{\delta x_i} + \frac{\delta D}{\delta \dot{x}_i} = 0 \tag{7}$$

3. State space representation: From the EOM, a state-space representation is derived. This mathematical representation of the physical system allows for analysis of the SBIS in the frequency domain. The state space system is given by eq. (8). Here $\boldsymbol{x}(t)$ is the state-vector, which contains the state and derivate of all the system's generalized coordinates. $\boldsymbol{u}(t)$ is the input vector, which contains the control input [$\boldsymbol{u}$] during control design. $\boldsymbol{y}(t)$ is the output vector containing the outputs of the system, which is the generalized coordinate corresponding with the blade root position, donated by x_b. $\boldsymbol{A}, \boldsymbol{B}, \boldsymbol{C}, \boldsymbol{D}$ are the state matrix, input matrix, output matrix and feed-through matrix, respectively.

$$\dot{\boldsymbol{x}}(t) = \boldsymbol{A}\boldsymbol{x}(t) + \boldsymbol{B}\boldsymbol{u}(t) \tag{8}$$

$$\boldsymbol{y}(t) = \boldsymbol{C}\boldsymbol{x}(t) + \boldsymbol{D}\boldsymbol{u}(t) \tag{9}$$

4. Controller design: A PID controller is proposed based on the open loop system response [$\boldsymbol{e}$] $\rightarrow$ [$\boldsymbol{y}$] (fig. 4). A minimal gain margin of 6 dB and a 60 degree phase margin are used as design requirements. The closed-loop bandwidth depends on the working principle of the AM and system parameters. Sensor noise and delay are not considered.

5 Assessment

The individual AMs, described within their respective operational planes, are simulated in the time domain. Nonlinear 3DOF (single plane & rotation) numerical models are constructed for each AMs, describing 15 MW OWT blade installation using the SBIS. The PID controllers developed using the 1DOF analytical models are implemented in the 3DOF models. The modelling and simulation itself is performed in a Matlab/Simulink environment. To assess the compensation effectiveness and actuator input for each AM, assessment criteria are defined.

During alignment, the guide pin, at $\boldsymbol{p}_{root}$, should be as close to the centre of the mating hole located at $\boldsymbol{p}_{hub}$. The offset between the two point projected on a plane in global XZ is called the radial root position error, and is formulated as eq. (10). The XZ projection plane is shown in fig. 5.

The second assessment criterion is this axial error between the blade root ($\boldsymbol{p}_{root}$) and the hub, $\boldsymbol{p}_{hub}$, in the global y-direction, quantified by eq. (11).

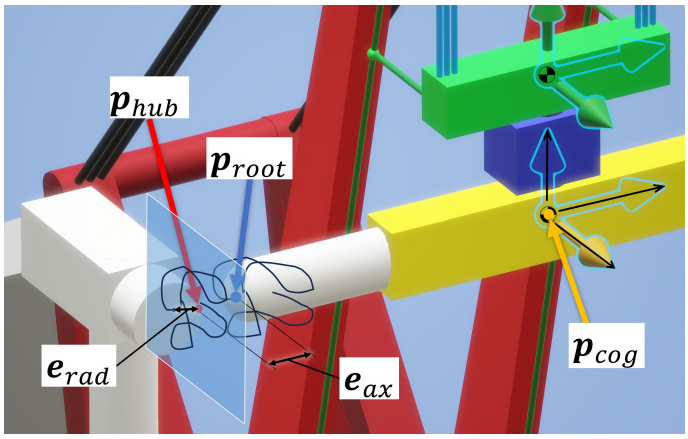

Figure 5: Projection of blade root motion on the XZ-plane

The third criterion is the relative velocity between the blade root and hub, defined by eq. (12). Verma et al. (2019) studied the effect of an impact between the guide pin and hub. It is found that unrepairable damage to the root laminate can occur at impact velocities above 0.6 m/s.

Proper alignment between the blade and hub is crucial, as misalignment can lead to improper mating and potential operational issues. The final criterion is defined as the blade's angle relative to the global y-axis, given by eq. (13).

$$\boldsymbol{e}_{rad} = \left\| \boldsymbol{p}_{root,xz} - \boldsymbol{p}_{hub,xz} \right\| \tag{10}$$

$$\boldsymbol{e}_{ax} = \left\| \boldsymbol{p}_{root,y} - \boldsymbol{p}_{hub,y} \right\| \tag{11}$$

$$\boldsymbol{e}_{v} = \left\| \dot{\boldsymbol{p}}_{root} - \dot{\boldsymbol{p}}_{hub} \right\| = \left\| \dot{\boldsymbol{p}}_{root} \right\| \tag{12}$$

$$\boldsymbol{e}_{\angle} = \arccos \frac{\boldsymbol{a} \cdot \boldsymbol{b}}{|\boldsymbol{a}|\,|\boldsymbol{b}|} \tag{13}$$

$$\boldsymbol{a} = \frac{\boldsymbol{p}_{root} - \boldsymbol{p}_{cog}}{\left\| \boldsymbol{p}_{root} - \boldsymbol{p}_{cog} \right\|} \qquad \boldsymbol{b} = [0, -1, 0] \tag{14}$$

Finally, the maximum actuator effort and mean power consumption are used as assessment criteria. The power consumption is given by eq. (15), where the force F and torque T are the actuator effort applied by the actuator, while v and ω are the actuator translational or rotational velocity, respectively. The actuator effort indicates the required size and capacity of the actuators, while power consumption given an indication of how long the tool can run on a battery.

$$P = Fv = T\omega \tag{15}$$

The MarIn toolbox wind model (Ren et al., 2018) is used to calculate aerodynamic loading on the 15 MW turbine blade, based on a TurbSim wind box (Jonkman, 2014). The Normal Turbulence Model (NTM) (eq. (16)) formulated in the International Electrotechnical Commission (IEC) 61400-1 standard is used to describe the turbulent airflow. The NTM provides a standard deviation of the wind turbulence (International Electrotechnical Commission, 2005), where I_{ref} is constant depending on the Turbulance Intensity (TI) category. The standard defines three categories (A, B, and C), where A results in the highest TI.

As per the IEC standard, the spectral decompensation of the turbulent airflow is described by the Kaimal spectral model (Jonkman, 2014), given by eq. (18). Here, σ_u is the standard deviation from the NTM, U_w is the mean wind speed and L_u the length scale defined in IEC 61400-1. For the reference case, an airflow aligned with positive x-direction, perpendicular to the blade orientation, is assumed. This direction results in the highest blade loading and is considered a critical position.

$$\sigma_u = I_{ref}(0.75U_w + 5.6) \tag{16}$$

$$TI = \frac{\sigma_u}{U_w} \tag{17}$$

$$S(f) = \sigma_u^2 \frac{4L_u/U_w}{(1 + 6fL_u/U_w)^{\frac{5}{3}}} \tag{18}$$

The results for the assessment criteria are presented in table 3. Additional outputs are presented, which are not used in the assessment, but offer more insights into operation and performance. These are the required hydraulic cylinder stroke length ($\Delta d = d_{max} - d_{min}$) and a rough estimate of the total suspended load for each AM.

6 Proposed HMC

These results are used to make a selection of AMs to use in a HMC concept. The XY table shows good compensation effectiveness, while low effectiveness is observed for both the power swivel and wind vanes. The gyroscope's generated moment is given by eq. (19), and depends on the current precession angle θ_{gy}. Beyond an angle of 90°, further precession no longer provides a moment over the desired axis. Due to this limitation, the gyroscopes cannot cope with the constant wind-induced moments and saturate within 40 s. For COG shifting, a negative correlation between the achieved radial and axial error is observed. A high effectiveness in the radial direction can be achieved, at the cost of a large pendulum amplitude, resulting in substantial axial errors. By reducing the control gain (AM5B,slow), the pendulating amplitude is significantly reduced, albeit at the expense of radial compensation effectiveness.

$$M_{gy} = \dot{\theta}_{gy} H_s \cos\theta_{gy} \tag{19}$$

For the final HMC concept, the XY table is employed for compensation in the x- and y-directions, while the gyroscope handles compensation in the z-direction. To avoid gyroscope saturation, the COG shifting method with CW is included, capable of generating a constant moment through shifting of the CW. Both the XY table and COG shifting utilize a CW translated in the y-direction. An efficient approach would be to merge these CWs. However, the COG shifting method demands a substantial stroke. Simulation runs show that a significant cylinder stroke in the y-direction can lead to stability issues for compensation in the x-direction. This prevents combination of the two CWs into a single CW, in combination with the existing PID controllers.

Table 3: Overview of simulation results for the AMs in XY plane

	AM1	AM2	AM3	AM4	AM5A	AM5B	AM5B,slow	Unit
Max. Radial error ($\boldsymbol{e}_{rad}$)	72	918	342	47	83	62	171	[mm]
Max. Axial Error ($\boldsymbol{e}_{ax}$)	0.67	18	70	7.9	3309	570	95	[mm]
Max. Blade root vel. ($\boldsymbol{e}_{v}$)	0.05	0.37	0.20	0.080	0.52	0.31	0.060	[m/s]
Max. Blade angle ($\boldsymbol{e}_{\angle}$)	1.4	1.8	0.66	0.11	0.20	0.12	0.34	[deg]
Mean Power consumption (P)	1.7	0.018	0.051	1.7	1.1	0.61	0.022	[kW]
Max. Actuator Effort (F/T)	40 [kN]	397 [kNm]	3.9 [kNm]	0.59 [kNm]	55 [kN]	33 [kN]	4.5 [kN]	-
Req. Stroke length (Δd)	1.06	-	-	-	2.3	2.2	1.3	[m]
Total suspended mass (M_{tot})	473	261	296	355	304	448	448	[t]

The HMC controller is a combination of three parallel PID controllers. A control diagram is provided in fig. 4 The XY table and gyroscope controllers, developed using the 1DOF models, are implemented without alteration. Both utilize a separate portion of the error signal and can operate in parallel. The COG shifting controller, is adjusted. Instead of blade root error, it considers the gyroscope's offset from the neutral position as input, requiring an extra system output: the gyroscope precession angle.

To evaluate the effectiveness of the HMC, the concept is applied in a 6DOF simulator. The simulator is again built in Matlab/Simulink and uses the MarIn wind model. Two systems are simulated: a baseline consisting of the SBIS without any actuation methods, and a model of the SBIS with the HMC. The simulation results are shown in fig. 3 and table 4

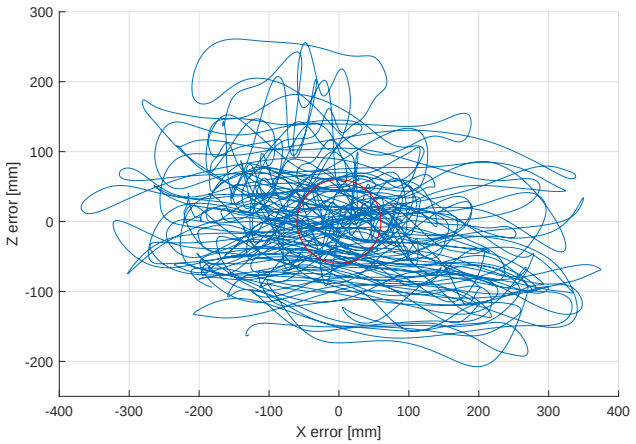

(a) Baseline

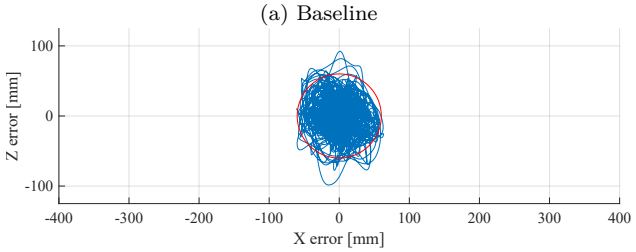

(b) SBIS with HMC

Figure 3: Radial blade root motion over a 10-minute period

Table 4: Compensation effectiveness of proposed HMC

	Baseline	HMC	Unit	Reduction
Max. Radial error	691	99.9	[mm]	85.5%
Max. Axial error	228	8.73	[mm]	96.2%
Max. Root vel.	0.244	0.0981	[m/s]	59.8%
Blade angle	1.43	0.788	[deg]	44.9%

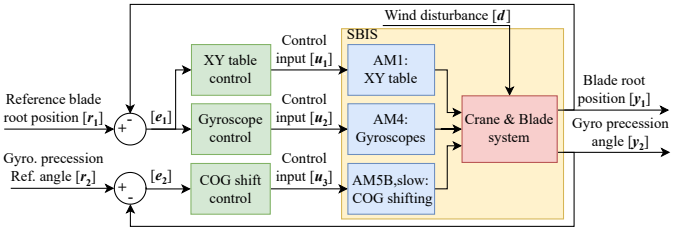

Figure 4: Diagram of combined linear HMC controller

7 Parameter study

In addition to comparing the SBIS with and without the HMC for the reference case, a sensitivity analysis is conducted by varying various system parameters. The resulting maximum radial and axial blade root position error are shown in fig. 2. The key findings for are summarized below:

Mean wind speed: As expected, higher wind speeds lead to increased blade motion and higher power consumption. Results suggest that installation of 15 MW OWT blades is viable up to around 12 m/s wind speed, with a maximum radial error close to the required accuracy of 60 to 80 mm.

Turbulence intensity: The result show sensitivity to turbulence intensity. turbulence class C demonstrates a 25% reduction in blade motion compared to class A.

Wind direction: The reference case, with wind aligned along the x-axis, is most critical. Rotation by $\pm 90°$ yields minimal blade motion. However, the resulting error should be interpreted cautiously due to the cross-flow assumption made in the MarIn wind model (Ren et al., 2018). The effective incoming wind speed is given by the cosine of the angle. This relation is also seen back in the results. Beyond 120°, tugger pretension is lost, leading to a loss of stability.

Static blade pitch: By changing the static blade pitch angle $\beta_\circ$, the loading on the blade changes significantly, both in overall magnitude, and the distribution of the wind-induced moment over the x- and z-axis. The proposed HMC lacks the capability to directly compensate around the z-axis, which favours blade angles where the wind-induced moment around this axis is minimal. This is the case for static pitch angle around -5 and -180 degrees. Due to the HMC's inability to handle large moments about the z-axis, a slight pitch angle increase from 20 to 25 degrees results in a massive increase in blade root error, due to large yaw-motions when tugger pretension is lost. On the other hand, the performance is increased by using a static pitch angle around -180 degrees, effectively minimizing aerodynamic loading.

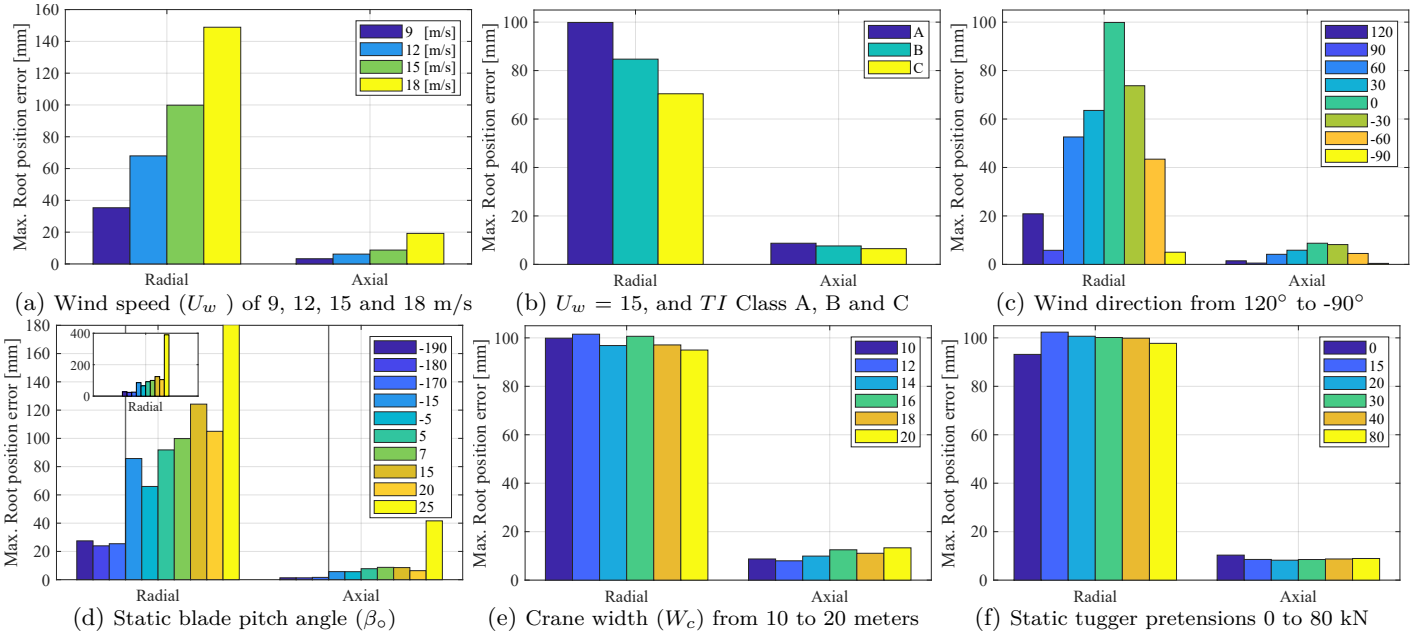

(a) Wind speed (U_w) of 9, 12, 15 and 18 m/s (b) U_w = 15, and TI Class A, B and C (c) Wind direction from 120° to -90°

(d) Static blade pitch angle ($\beta_\circ$) (e) Crane width (W_c) from 10 to 20 meters (f) Static tugger pretensions 0 to 80 kN

Figure 2: Simulation results of SBIS with HMC for various parameter variations

Tugger line angle: Introducing an angle to the tugger lines in the XY plane by increasing the crane width, creates additional coupling between x and y. Varying the tugger line angle from 0 to 27 degrees reveals a very slight increase in the axial error for larger angles, while stability is maintained.
Tugger line pretension: Tugger pretension is varied from 0 to 80 kN. As long as there is pretension, increased pretension yields a slight reduction in radial error and increase in axial error. Both effects are minute, though.

8 Conclusion

This study aims to provide an understanding of both the applicability of all the AMs, and the effectiveness of local load stabilization using a HMC for single-blade installation.

Six AMs are included in the assessment. Three of these AMs are used in the combined HMC concept. The chosen AMs are an XY table, used to control blade root position in the x- and y-directions, gyroscopes used for controlling blade root position in the z-direction, and COG shifting with CW to prevent gyroscope saturation. The HMC uses the PID controllers developed based on the linear 1DOF representation, operating in parallel to control the blade root position. The behaviour of the SBIS with the HMC is compared to a baseline without any AM within a 6DOF simulator, to verify the performance of the HMC and its controller. The blade root motion is successfully reduced by 96% along the blade axis and 86% radially. As expected, the remaining blade root error after compensation is sensitive to the mean wind speed, turbulence intensity, and angle of the incoming wind. The HMC shows robustness to variations in tugger line angle and pretension. The static blade pitch angle inside the yoke is an important system parameter, affecting the magnitude and distribution of the wind-induced moment on the blade. Static blade pitch angles around -180 result in optimal HMC performance, as for these configurations, the wind induced moment around the Z-axis is minimal. This is significant, as the HMC concept does not include an AM that allows for direct control over blade rotation around the z-axis. Instead, the XY table compensates for the blade rotation by translating the entire blade at the COG, resulting in a large required cylinder stroke length.

Two AMs were assessed that actuate the blade around the z-axis, both showing poor performance. Further exploration of AMs that can directly control the blade rotation around z could lead to improvement of the HMC concept. Additional improvement can be made in optimization of counterweights and gyroscopes sizes, potentially reducing weight and improving system performance. Further suggestions for future work include; exploring the compensating for the now neglected hub motion using the HMC, examining the stability of the HMC once the blade is mated to the hub, and the impact of sensor noise and delay on the HMC's performance.

References

Brown, D., & Peck, M. (2009). Energetics of control moment gyroscopes as joint actuators. *Journal of guidance, control, and dynamics*, *32*(6), 1871–1883.

de Leeuw, K. (2019). Single lift blade alignment for large offshore wind turbines. https://repository.tudelft.nl/islandora/object/uuid:c006c829-ab8b-4acc-ac79-f1c9f6f15abd

International Electrotechnical Commission. (2005). Iec61400-1: 2005 wind turbines–part 1: Design requirements. *24*, 2020. https://webstore.iec.ch/publication/5426

Jonkman, B. (2014). Turbsim user's guide v2. *Natl. Renew. Energy Lab.*

Ramírez, L., Fraile, D., Brindley, G., Walsh, C., & Van de Velde, L. (2022). Offshore wind in europe: Key trends and statistics 2020.

Ren, Z., Jiang, Z., Skjetne, R., & Gao, Z. (2018). Development and application of a simulator for offshore wind turbine blades installation. *Ocean Engineering*, *166*, 380–395. https://doi.org/10.1016/j.oceaneng.2018.05.011

Verma, A. S., Jiang, Z., Vedvik, N. P., Gao, Z., & Ren, Z. (2019). Impact assessment of a wind turbine blade root during an offshore mating process. *Engineering Structures*, *180*, 205–222. https://doi.org/10.1016/j.engstruct.2018.11.012

B

Actuator dynamics

In this appendix, the derivation of the time constant used to describe the behaviour of the internal control loops provided in figure B.1 for the motor-gearbox systems is provided. As stated before, the time constant depends on system properties, most importantly the gearbox and motor stiffness and the inertia of the load. For all three actuation methods that use a motor-gearbox, the same motor and gearbox properties are assumed, based on the available system information of the UQC power swivel. These system properties are again summarized in table B.1.

Figure B.2 provides a block diagram with a mass-spring-damper representation of the motor-gearbox connected to a load. The load itself varies for the three actuation methods and are also given in table B.1. The motor supplies a force on the gearbox, which results in displacement of the gearbox. This displacement is transferred through the load through the gearbox itself, which has certain stiffness and damping. A state-space representation for the motor-gearbox subsystem is provided in equation (B.1).

$$\dot{\boldsymbol{x}} = \begin{bmatrix} \dot{x}_{gb} \\ \ddot{x}_{gb} \\ \dot{x}_{load} \\ \ddot{x}_{load} \end{bmatrix} = A\boldsymbol{x} + B\boldsymbol{u} = A \begin{bmatrix} x_{gb} \\ \dot{x}_{gb} \\ x_{load} \\ \dot{x}_{load} \end{bmatrix} + B \begin{bmatrix} F_m \end{bmatrix}$$

$$= \begin{bmatrix} 0 & 1 & 0 & 0 \\ \frac{-k_{gb}}{M_{gb}} & \frac{-c_{gb}}{M_{gb}} & \frac{k_{gb}}{M_{gb}} & \frac{c_{gb}}{M_{gb}} \\ 0 & 0 & 0 & 1 \\ \frac{-k_{gb}}{M_{load}} & \frac{-c_{gb}}{M_{load}} & \frac{k_{gb}}{M_{load}} & \frac{c_{gb}}{M_{load}} \end{bmatrix} \begin{bmatrix} x_{gb} \\ \dot{x}_{gb} \\ x_{load} \\ \dot{x}_{load} \end{bmatrix} + \begin{bmatrix} 0 \\ \frac{1}{M_{gb}} \\ 0 \\ 0 \end{bmatrix} \begin{bmatrix} F_m \end{bmatrix} \quad \text{(B.1)}$$

The motor speed and position controllers designed in this appendix for the inner loop are not directly used in the final models, as the simplified dynamics described in section 3.3 are implemented instead. The controllers are used to estimate the behaviour of the inner control loop. This way, an appropriate value can be chosen for the time constant that is used to describe the behaviour of the simplified system within the linear models.

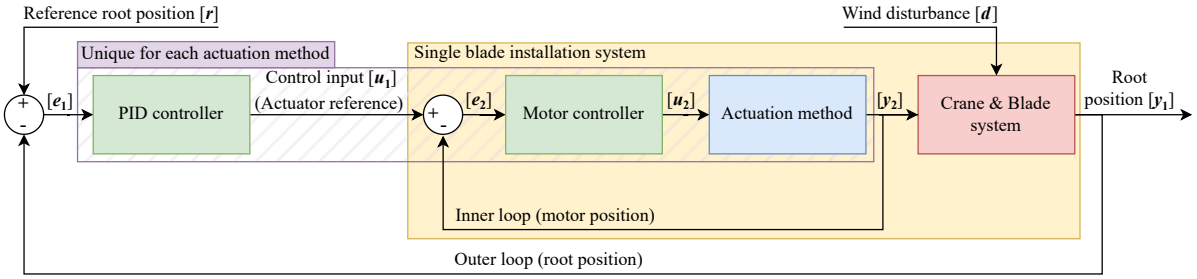

Figure B.1: Control diagram showing the inner actuator control loop

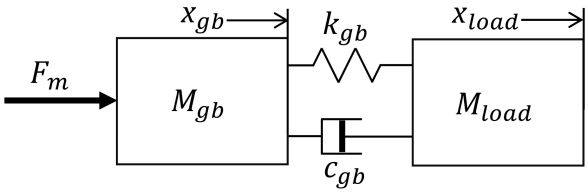

Figure B.2: Mass-spring-damper system for the motor-gearbox system

Table B.1: UQC power swivel drive system parameters

Symbol	Value	Unit	Description
k_m	144e3	Nm/rad	Motor torsional stiffness
J_m	0.178	kg·m^2	Motor rotational inertia
N	123.5	-	Gear ratio
T_{nom}	150e3	Nm	Nominal output torque
I_{gy}	16.8e3	kg·m^2	Gyroscope rotational inertia
I_v	10.2e3	kg·m^2	Vane rotational inertia
I_{b^*}	4.68e6	kg·m^2	Blade(yoke) rotational inertia

B.1. Gyroscopes internal controller

The control diagram for the internal controller of the gyroscope is provided in figure B.3. The control input from the outer controller [u$_1$] is a reference motor velocity $\dot{\theta}_{gb}$. The inner controller uses the error between this reference signal and the measured motor velocity as an input signal [e$_2$].

To tune the controller of the motor speed loop, a rule of thumbs is used, provided by Huisman for the tuning of motor speed and position controllers. The rule is given in equation (B.3). Here ω_{des} is the desired bandwidth of the controller, or the frequency at which the magnitude of the Bode plot crosses the 0 dB line, J_m is the motor inertia.

$$PID = K_p \left(1 + \frac{1}{T_i}\frac{1}{s} + T_d \cdot s\right) \tag{B.2}$$

$$K_p = 2\pi \cdot \omega_{des} \cdot J_m \tag{B.3}$$

$$T_i = 5 \cdot 2\pi \cdot \omega_{des} T_d = 0 \tag{B.4}$$

This rule of thumb scales the P action in equation (B.2) such that the desired bandwidth is reached. The integration time constant T_i is chosen such that the integration is 5 times slower than the desired bandwidth to ensure enough phase margin is present. The desired bandwidth is chosen to be 6 Hz. The resulting controller parameter and performance is provided in table B.2. An open loop and closed loop Bode response of the inner loop is provided in figure B.4. Finally, a step response of the closed inner loop is provided in figure B.5. The step response provides a value for the time constant that is applied in the final model.

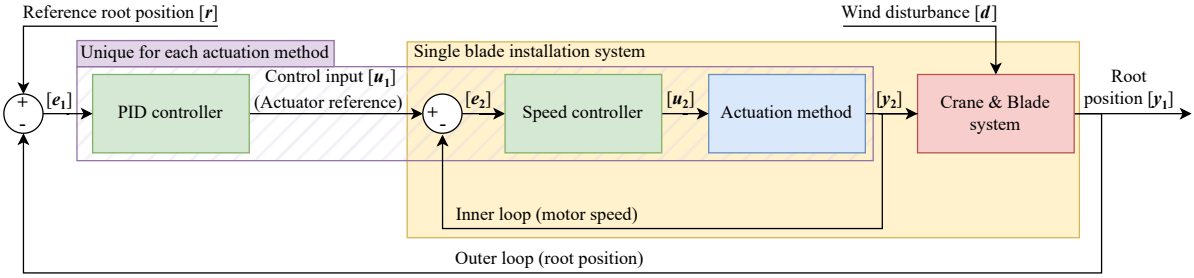

Figure B.3: Control diagram for motor velocity internal control loop

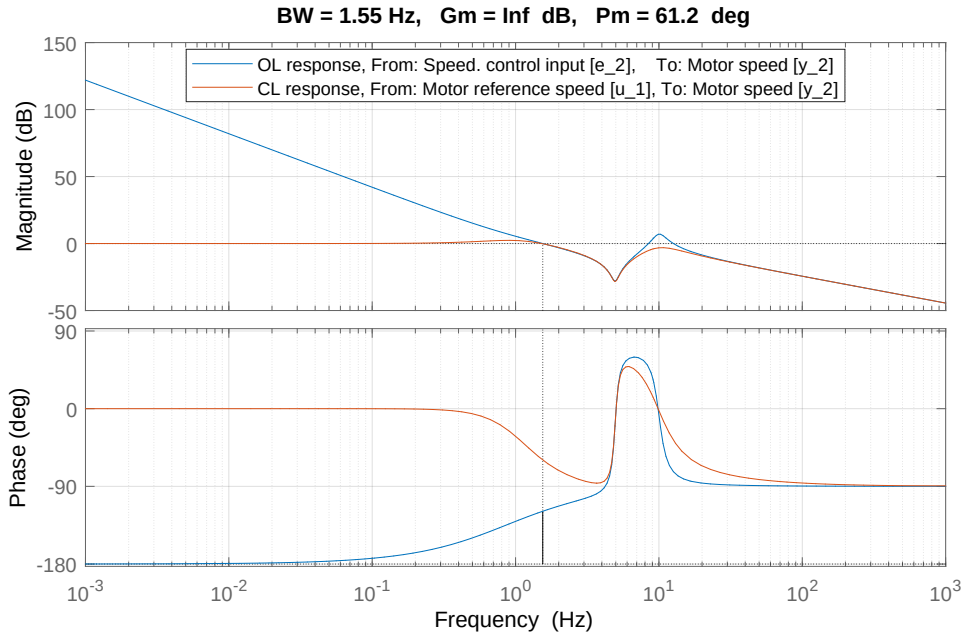

Figure B.4: Gyroscope inner loop OL and CL frequency response

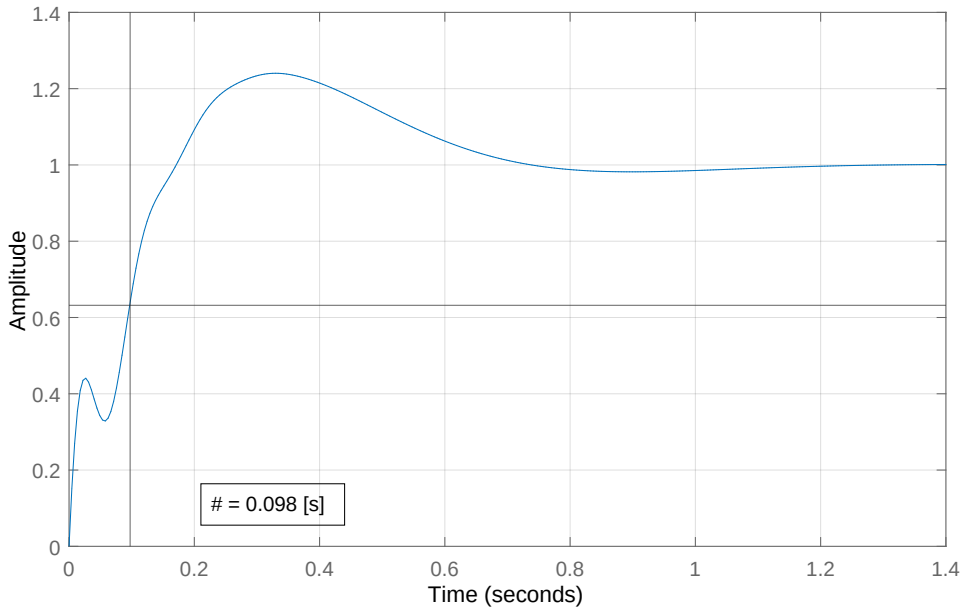

Figure B.5: Gyroscope inner loop step response

Table B.2: Control parameters and performance for the gyroscope inner loop speed controller

Parameter	Value	unit
K_p	2.05e+05	-
T_i	0.186	s
Phase Margin	61	deg
Gain Margin	∞	dB
Bandwidth	1.55	Hz
Time constant	0.098	s

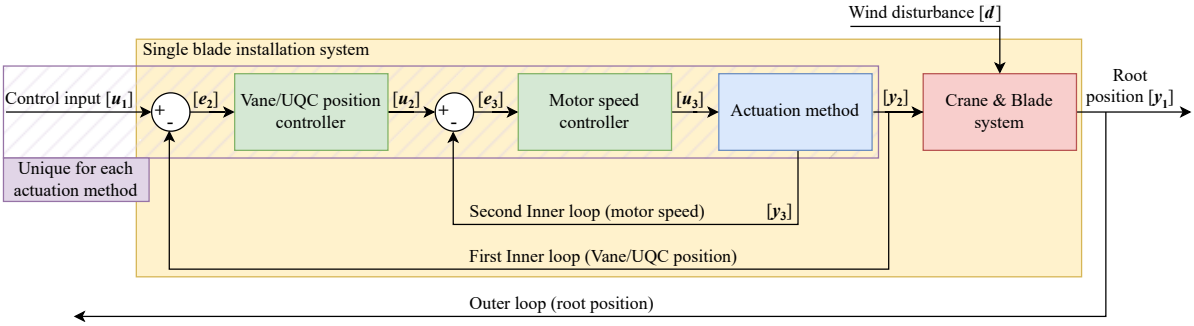

Figure B.6: Control diagram for motor position internal control loop

Table B.3: Control parameters and performance for the UQC power swivel (AM2) and wind vanes (AM3) inner loop motor speed and position controllers

Parameter	AM2	AM3	unit
K_p	2.05e+06	2.05e+06	-
T_i	0.0133	0.0133	s
Phase Margin	68	80	deg
Gain Margin	∞	∞	dB
Bandwidth	0.0925	62.3	Hz
$K_{p,pos}$	0.0245	2.4	-
Phase Margin	90	90	deg
Gain Margin	6	6.1	dB
Bandwidth	0.004	0.384	Hz
Time constant	39.6	0.896	s

B.2. UQC power swivel & Vanes internal controller

A control diagram for the internal controller of the UQC power swivel (AM2) and wind vanes (AM3) is provided in figure B.6. In this case, the outer controller (not included in the diagram) provides a reference position θ_{gb} as a control input [u1]. In order to control the motor position, an extra position control loop is added to the motor control loop. The first inner loop uses the error between the reference signal [u_1] and the measured motor position as an input signal [e_2]. The second inner loop uses the error between this reference signal [u_2] and the measured motor velocity [y_3] as an input signal [e_2].

The same rule of thumb in equation (B.3) is used to tune the inner motor speed loop. The outer position controller is simply a gain, P_{pos}, which is used to position the open loop response curve ([e_2] $\rightarrow$ [y_2]) to a gain margin of 6 dB. The resulting controller parameters and performance is provided in table B.3. An open loop and closed loop Bode response of the second inner loop (speed loop) is provided in figure B.7 and figure B.10 for the UQC power swivel and wind vanes, respectively.

Finally, An open loop and closed loop Bode response of the first inner loop (position loop) is provided in figure B.8 and figure B.11. Finally, the step response of the closed inner loop is provided in figure B.9 and figure B.12 for the UQC power swivel and wind vanes, respectively. These step responses provide the value for the time constant that is applied in the final model.

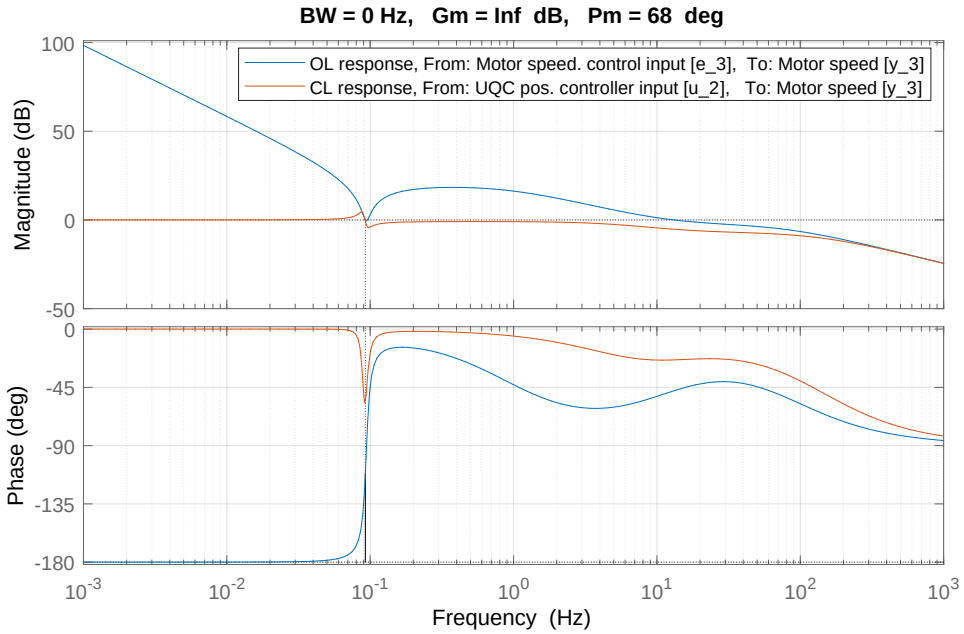

Figure B.7: Power swivel second inner loop (speed loop) OL and CL frequency response

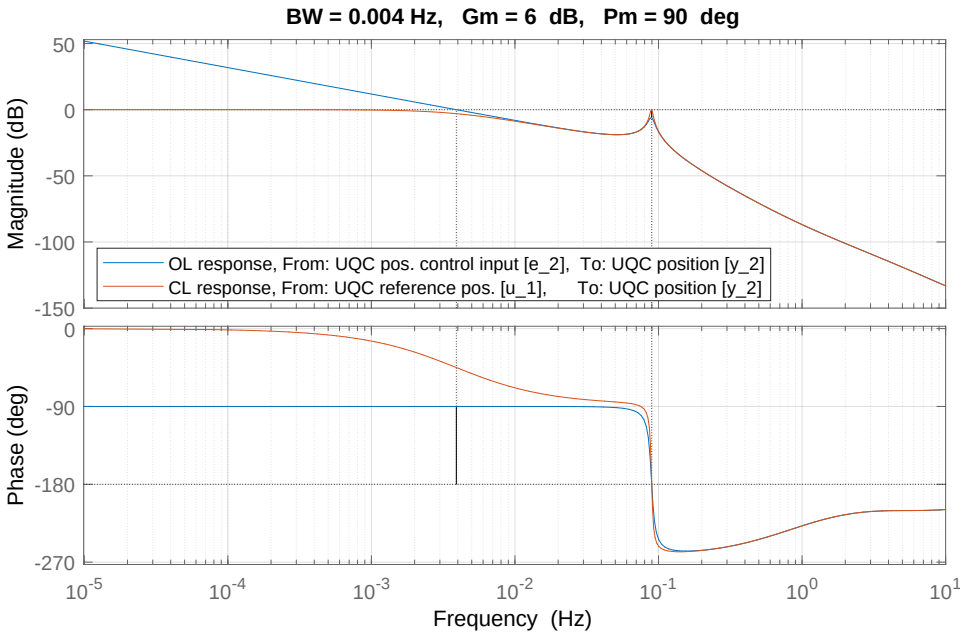

Figure B.8: Power swivel first inner loop (position loop) OL and CL frequency response

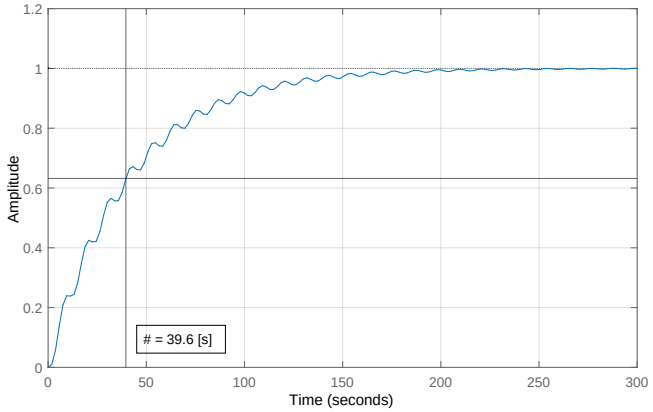

Figure B.9: Power swivel first inner loop step response

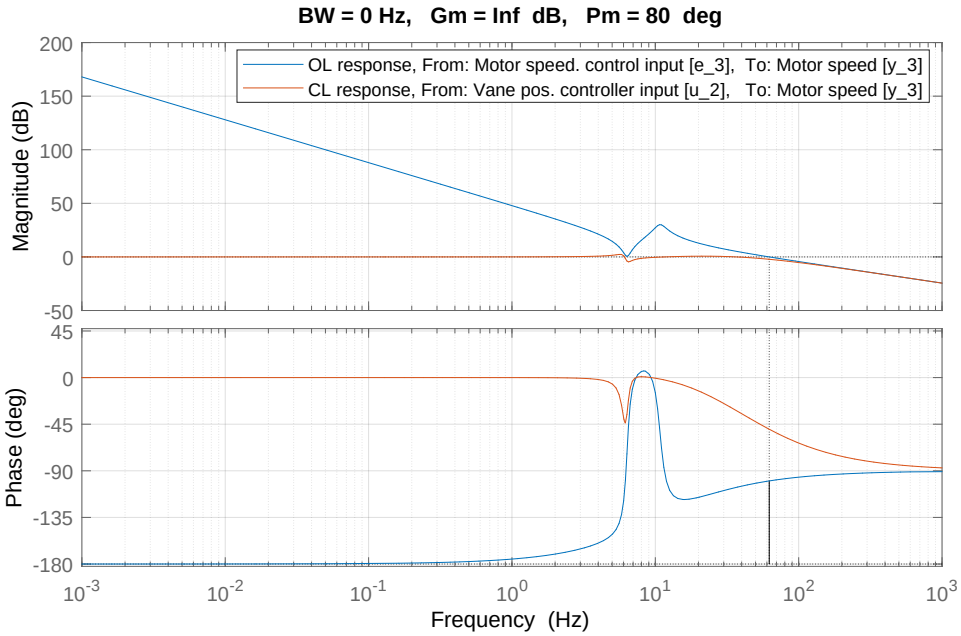

Figure B.10: Vane second inner loop (speed loop) OL and CL frequency response

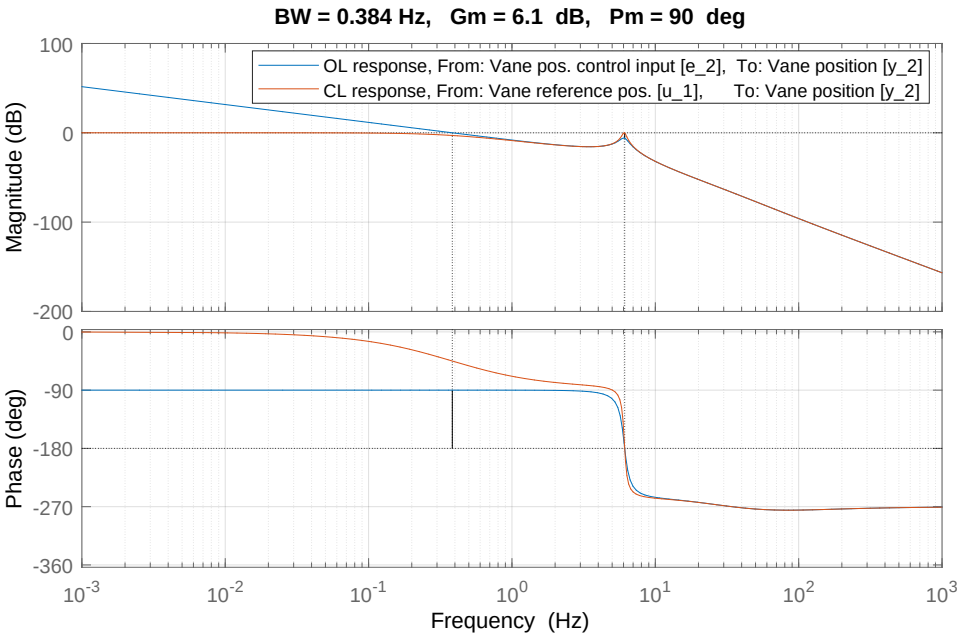

Figure B.11: Vane first inner loop (position loop) OL and CL frequency response

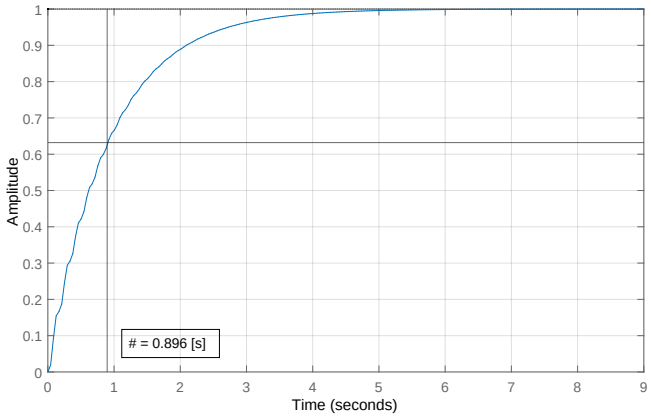

Figure B.12: Vane first inner loop step response

C

State space models

In this appendix, the state space representations are provided for the equations of motion provided in chapter 3.

C.1. XY table

$$\dot{\boldsymbol{x}} = \begin{bmatrix} \dot{x}_b \\ \ddot{x}_b \\ \dot{x}_{cw} \\ \ddot{x}_{cw} \\ \dot{x}_{lb} \\ \ddot{x}_{lb} \\ \dot{x}_c \\ \ddot{x}_c \end{bmatrix} = \boldsymbol{A}\boldsymbol{x} + \boldsymbol{B}\boldsymbol{u} = \boldsymbol{A} \begin{bmatrix} x_b \\ \dot{x}_b \\ x_{cw} \\ \dot{x}_{cw} \\ x_{lb} \\ \dot{x}_{lb} \\ x_c \\ \dot{x}_c \end{bmatrix} + \boldsymbol{B} \begin{bmatrix} d_1 \\ d_2 \\ F_w \end{bmatrix}$$

$$= \begin{bmatrix} 0 & 1 & 0 & 0 & 0 & 0 & 0 & 0 \\ \frac{-k_h}{M_{b^*}} & \frac{-c_h}{M_{b^*}} & 0 & 0 & \frac{k_h}{M_{b^*}} & \frac{c_h}{M_{b^*}} & 0 & 0 \\ 0 & 0 & 0 & 1 & 0 & 0 & 0 & 0 \\ 0 & 0 & \frac{-k_h}{M_{cw}} & \frac{-c_h}{M_{cw}} & \frac{k_h}{M_{cw}} & \frac{c_h}{M_{cw}} & 0 & 0 \\ 0 & 0 & 0 & 0 & 0 & 1 & 0 & 0 \\ \frac{k_h}{M_{lb}} & \frac{c_h}{M_{lb}} & \frac{k_h}{M_{lb}} & \frac{c_h}{M_{lb}} & \frac{-2k_h-k_t-k_l}{M_{lb}} & \frac{-2c_h-c_t-c_l}{M_{lb}} & \frac{\phi_t k_t+k_l}{M_{lb}} & \frac{\phi_t c_t+c_l}{M_{lb}} \\ 0 & 0 & 0 & 0 & 0 & 0 & 0 & 1 \\ 0 & 0 & 0 & 0 & \frac{k_t+k_l}{M_c} & \frac{c_t+c_l}{M_c} & \frac{-\phi_t k_t-k_l-k_c}{M_c} & \frac{-\phi_t c_t-c_l-c_c}{M_c} \end{bmatrix} \begin{bmatrix} x_b \\ \dot{x}_b \\ x_{cw} \\ \dot{x}_{cw} \\ x_{lb} \\ \dot{x}_{lb} \\ x_c \\ \dot{x}_c \end{bmatrix}$$

$$+ \begin{bmatrix} 0 & 0 & 0 \\ \frac{k_h}{M_{b^*}} & 0 & \frac{1}{M_{b^*}} \\ 0 & 0 & 0 \\ 0 & \frac{-k_h}{M_{cw}} & 0 \\ 0 & 0 & 0 \\ \frac{-k_h}{M_{lb}} & \frac{k_h}{M_{lb}} & 0 \\ 0 & 0 & 0 \\ 0 & 0 & 0 \end{bmatrix} \begin{bmatrix} d_1 \\ d_2 \\ F_w \end{bmatrix} \tag{C.1}$$

$$\boldsymbol{y} = \boldsymbol{C}\boldsymbol{x} = \begin{bmatrix} 1 & 0 & 0 & 0 & 0 & 0 & 0 & 0 \end{bmatrix} \boldsymbol{x} \tag{C.2}$$

As part of the XY table's working principle, a mass equal to the combined blade and blade yoke is moved in equal, but opposite direction from the blade (yoke). In theory, the COG doesn't move, and inertial loading is fed back to the rest of the system is minimized. Therefore, the input signals to the two cylinders should be chosen in a way to enable this. In the models, it is assumed that the counterweight is chosen to match the exact mass of the blade and yoke. In this case, both cylinders should have an equal control input ($d_2 = -d_1 = d$). This simplifies the B matrix to the B matrix provided by equation (C.3).

$$\boldsymbol{Bu} = \begin{bmatrix} 0 & 0 & 0 \\ \frac{k_h}{M_{b^*}} & 0 & \frac{1}{M_{b^*}} \\ 0 & 0 & 0 \\ 0 & \frac{-k_h}{M_{cw}} & 0 \\ 0 & 0 & 0 \\ \frac{-k_h}{M_{lb}} & \frac{k_h}{M_{lb}} & 0 \\ 0 & 0 & 0 \\ 0 & 0 & 0 \end{bmatrix} \begin{bmatrix} d \\ d \\ F_w \end{bmatrix} = \begin{bmatrix} 0 \\ d\frac{k_h}{M_{b^*}} + F_w\frac{1}{M_{b^*}} \\ 0 \\ d\frac{-k_h}{M_{cw}} \\ 0 \\ d\frac{-k_h}{M_{lb}} + d\frac{k_h}{M_{lb}} \\ 0 \\ 0 \end{bmatrix} \rightarrow \begin{bmatrix} 0 & 0 \\ \frac{k_h}{M_{b^*}} & \frac{1}{M_{b^*}} \\ 0 & 0 \\ \frac{-k_h}{M_{cw}} & 0 \\ 0 & 0 \\ 0 & 0 \\ 0 & 0 \\ 0 & 0 \end{bmatrix} \begin{bmatrix} d \\ F_w \end{bmatrix} \tag{C.3}$$

C.2. Power swivel

$$\dot{\boldsymbol{x}} = \begin{bmatrix} \dot{x}_b \\ \ddot{x}_b \\ \dot{x}_{lb} \\ \ddot{x}_{lb} \\ \dot{x}_c \\ \ddot{x}_c \end{bmatrix} = \boldsymbol{Ax} + \boldsymbol{Bu} = \boldsymbol{A} \begin{bmatrix} x_b \\ \dot{x}_b \\ x_{lb} \\ \dot{x}_{lb} \\ x_c \\ \dot{x}_c \end{bmatrix} + \boldsymbol{B} \begin{bmatrix} \theta_m \\ F_w \end{bmatrix}$$

$$= \begin{bmatrix} 0 & 1 & 0 & 0 & 0 & 0 \\ \frac{-k_{gb}}{M_{b^*}+M_{gb}} & \frac{-c_{gb}}{M_{b^*}+M_{gb}} & \frac{k_{gb}}{M_{b^*}+M_{gb}} & \frac{c_{gb}}{M_{b^*}+M_{gb}} & 0 & 0 \\ 0 & 0 & 0 & 1 & 0 & 0 \\ \frac{k_{gb}}{M_{lb}} & \frac{c_{gb}}{M_{lb}} & \frac{-k_{gb}-k_t-k_l}{M_{lb}} & \frac{-c_{gb}-c_t-c_l}{M_{lb}} & \frac{\phi_t k_t+k_l}{M_{lb}} & \frac{\phi_t c_t+c_l}{M_{lb}} \\ 0 & 0 & 0 & 0 & 0 & 1 \\ 0 & 0 & \frac{k_t+k_l}{M_c} & \frac{c_t+c_l}{M_c} & \frac{-\phi_t k_t-k_l-k_c}{M_c} & \frac{-\phi_t c_t-c_l-c_c}{M_c} \end{bmatrix} \begin{bmatrix} x_b \\ \dot{x}_b \\ x_{lb} \\ \dot{x}_{lb} \\ x_c \\ \dot{x}_c \end{bmatrix}$$

$$+ \begin{bmatrix} 0 & 0 \\ \frac{k_{gb}}{M_{b^*}+M_{gb}} & \frac{1}{M_{b^*}+M_{gb}} \\ 0 & 0 \\ \frac{-k_{gb}}{M_{lb}} & 0 \\ 0 & 0 \\ 0 & 0 \end{bmatrix} \begin{bmatrix} \theta_m \\ F_w \end{bmatrix} \tag{C.4}$$

$$\boldsymbol{y} = \boldsymbol{Cx} = \begin{bmatrix} 1 & 0 & 0 & 0 & 0 & 0 \end{bmatrix} \boldsymbol{x} \tag{C.5}$$

C.3. Wind vanes

$$\dot{\boldsymbol{x}} = \begin{bmatrix} \dot{x}_b \\ \ddot{x}_b \\ \dot{x}_c \\ \ddot{x}_c \\ \dot{x}_v \\ \ddot{x}_v \end{bmatrix} = \boldsymbol{A}\boldsymbol{x} + \boldsymbol{B}\boldsymbol{u} = \boldsymbol{A} \begin{bmatrix} x_b \\ \dot{x}_b \\ x_c \\ \dot{x}_c \\ x_v \\ \dot{x}_v \end{bmatrix} + \boldsymbol{B} \begin{bmatrix} \theta_m \\ F_w \end{bmatrix}$$

$$= \begin{bmatrix} 0 & 1 & 0 & 0 & 0 & 0 \\ \frac{-k_t-k_l}{M_{b^*}+M_{lb}} & \frac{-c_t-c_l}{M_{b^*}+M_{lb}} & \frac{\phi_t k_t+k_l}{(M_{b^*}+M_{lb})} & \frac{\phi_t c_t+c_l}{(M_{b^*}+M_{lb})} & \frac{K_v}{M_{b^*}+M_{lb}} & 0 \\ 0 & 0 & 0 & 1 & 0 & 0 \\ \frac{k_t+k_l}{M_c} & \frac{c_t+c_l}{M_c} & \frac{-\phi_t k_t-k_l-k_c}{M_c} & \frac{-\phi_t c_t-c_l-c_c}{M_c} & 0 & 0 \\ 0 & 0 & 0 & 0 & 0 & 1 \\ 0 & 0 & 0 & 0 & \frac{-k_{gb}}{M_{gb}+M_v} & \frac{-c_{gb}}{M_{gb}+M_v} \end{bmatrix} \begin{bmatrix} x_b \\ \dot{x}_b \\ x_c \\ \dot{x}_c \\ x_v \\ \dot{x}_v \end{bmatrix}$$

$$+ \begin{bmatrix} 0 & 0 \\ 0 & \frac{1}{M_{b^*}+M_{lb}} \\ 0 & 0 \\ 0 & 0 \\ 0 & 0 \\ \frac{k_{gb}}{M_{gb}+M_v} & 0 \end{bmatrix} \begin{bmatrix} \theta_m \\ F_w \end{bmatrix} \tag{C.6}$$

$$\boldsymbol{y} = \boldsymbol{C}\boldsymbol{x} = \begin{bmatrix} 1 & 0 & 0 & 0 & 0 & 0 \end{bmatrix} \boldsymbol{x} \tag{C.7}$$

C.4. Gyroscopes

$$\dot{\boldsymbol{x}} = \begin{bmatrix} \dot{x}_b \\ \ddot{x}_b \\ \dot{x}_c \\ \ddot{x}_c \\ \dot{x}_{gy} \\ \ddot{x}_{gy} \end{bmatrix} = \boldsymbol{A}\boldsymbol{x} + \boldsymbol{B}\boldsymbol{u} = \boldsymbol{A} \begin{bmatrix} x_b \\ \dot{x}_b \\ x_c \\ \dot{x}_c \\ x_{gy} \\ \dot{x}_{gy} \end{bmatrix} + \boldsymbol{B} \begin{bmatrix} \dot{\theta}_m \\ F_w \end{bmatrix}$$

$$= \begin{bmatrix} 0 & 1 & 0 & 0 & 0 & 0 \\ \frac{-k_l-k_g}{M_{b^*}+M_{gb}} & \frac{-c_l}{M_{b^*}+M_{gb}} & \frac{k_l}{M_{b^*}+M_{gb}} & \frac{c_l}{M_{b^*}+M_{gb}} & 0 & \frac{K_{gy}}{M_{b^*}+M_{gb}} \\ 0 & 0 & 0 & 1 & 0 & 0 \\ \frac{k_l}{M_c} & \frac{c_l}{M_c} & \frac{-k_l-k_c}{M_c} & \frac{-c_l-c_c}{M_c} & 0 & 0 \\ 0 & 0 & 0 & 0 & 0 & 1 \\ 0 & 0 & 0 & 0 & \frac{-k_{gb}}{M_{gb}+M_{gy}} & \frac{-c_{gb}}{M_{gb}+M_{gy}} \end{bmatrix} \begin{bmatrix} x_b \\ \dot{x}_b \\ x_c \\ \dot{x}_c \\ x_{gy} \\ \dot{x}_{gy} \end{bmatrix}$$

$$+ \begin{bmatrix} 0 & 0 \\ 0 & \frac{1}{M_{b^*}+M_{gb}} \\ 0 & 0 \\ 0 & 0 \\ 0 & 0 \\ \frac{c_{gb}}{M_{gb}+M_{gy}} & 0 \end{bmatrix} \begin{bmatrix} \dot{\theta}_m \\ F_w \end{bmatrix} \tag{C.8}$$

$$\boldsymbol{y} = \boldsymbol{C}\boldsymbol{x} = \begin{bmatrix} 1 & 0 & 0 & 0 & 0 & 0 \end{bmatrix} \boldsymbol{x} \tag{C.9}$$

C.5. COG shifting

$$\dot{\boldsymbol{x}} = \begin{bmatrix} \dot{x}_b \\ \ddot{x}_b \\ \dot{x}_c \\ \ddot{x}_c \\ \dot{x}_h \\ \ddot{x}_h \\ \dot{x}_l b \\ \ddot{x}_l b \\ \dot{x}_b m \\ \ddot{x}_b m \end{bmatrix} = \boldsymbol{A}\boldsymbol{x} + \boldsymbol{B}\boldsymbol{u} = \boldsymbol{A} \begin{bmatrix} x_b \\ \dot{x}_b \\ x_c \\ \dot{x}_c \\ x_h \\ \dot{x}_h \\ x_l b \\ \dot{x}_{lb} \\ x_b m \\ \dot{x}_{bm} \end{bmatrix} + \boldsymbol{B} \begin{bmatrix} d \\ F_w \end{bmatrix}$$

$$= \begin{bmatrix} 0 & 1 & 0 & 0 & 0 & 0 & 0 & 0 & 0 & 0 \\ \frac{-k_l - k_g}{I_{b^*} + I_{lb}} & \frac{-c_l}{I_{b^*} + I_{lb}} & \frac{k_l}{I_{b^*} + I_{lb}} & \frac{c_l}{I_{b^*} + I_{lb}} & \frac{-k_h L_{cog} - g \cdot M_{b^*}}{I_{b^*} + I_{lb}} & \frac{-c_h L_{cog} + g \cdot M_{b^*}}{I_{b^*} + I_{lb}} & \frac{k_h L_{cog}}{I_{b^*} + I_{lb}} & \frac{c_h L_{cog}}{I_{b^*} + I_{lb}} & 0 & 0 \\ 0 & 0 & 0 & 1 & 0 & 0 & 0 & 0 & 0 & 0 \\ \frac{k_l}{I_c} & \frac{c_l}{I_c} & \frac{-k_l - k_c}{I_c} & \frac{-c_l - c_c}{I_c} & 0 & 0 & 0 & 0 & 0 & 0 \\ 0 & 0 & 0 & 0 & 0 & 1 & 0 & 0 & 0 & 0 \\ 0 & 0 & 0 & 0 & \frac{-k_h + \frac{g \cdot M_{b^*}}{L_{cog}}}{M_{b^*}} & \frac{-k_h - \frac{g \cdot M_{b^*}}{L_{cog}}}{M_{b^*}} & \frac{k_h}{M_{b^*}} & \frac{c_h}{M_{b^*}} & 0 & 0 \\ 0 & 0 & 0 & 0 & 0 & 0 & 0 & 1 & 0 & 0 \\ 0 & 0 & 0 & 0 & \frac{k_h}{M_{lb}} & \frac{c_h}{M_{lb}} & \frac{-k_h - k_p}{M_{lb}} & \frac{-c_h - c_p}{M_{lb}} & \frac{k_p}{M_{lb}} & \frac{c_p}{M_{lb}} \\ 0 & 0 & 0 & 0 & 0 & 0 & 0 & 0 & 0 & 1 \\ 0 & 0 & 0 & 0 & 0 & 0 & \frac{k_p}{M_{bm}} & \frac{c_p}{M_{bm}} & \frac{-k_{bm} - k_p}{M_{bm}} & \frac{-c_{bm} - c_p}{M_{bm}} \end{bmatrix} \begin{bmatrix} x_b \\ \dot{x}_b \\ x_c \\ \dot{x}_c \\ x_h \\ \dot{x}_h \\ x_l b \\ \dot{x}_l b \\ x_b m \\ \dot{x}_b m \end{bmatrix}$$

$$+ \begin{bmatrix} 0 & 0 \\ \frac{k_h L_{cog}}{I_{b^*} + I_{lb}} & \frac{1}{I_{b^*} + I_{lb}} \\ 0 & 0 \\ 0 & 0 \\ 0 & 0 \\ \frac{k_h}{M_{b^*}} & 0 \\ 0 & 0 \\ \frac{-k_h}{M_{lb}} & 0 \\ 0 & 0 \\ 0 & 0 \end{bmatrix} \begin{bmatrix} d \\ F_w \end{bmatrix} \quad \text{(C.10)}$$

$$\boldsymbol{y} = \boldsymbol{C}\boldsymbol{x} = \begin{bmatrix} 1 & 0 & 0 & 0 & 0 & 0 & 0 & 0 & 0 & 0 \end{bmatrix} \boldsymbol{x} \quad \text{(C.11)}$$

C.6. Parameter values

Table C.1: Values used in the mass-spring-damper systems and equivalent state-space models

	Baseline	XY table	Power swivel	Wind vanes	Gyroscopes	COG shifting
M_c	286e3	286e3	9.06e6	9.06e6	1.06e9	286e3
M_b	114e3	114e3	4.68e7	6.21e7	5.53e7	114e3
M_{lb}	147e3	234e3	1.30e6	-	-	191e3
M_{cw}	-	125e3	-	-	-	-
M_v	-	-	-	1.56e4	-	-
M_{gy}	-	-	-	-	1.64e4	-
I_c	-	-	-	-	-	1.06e9
$I_{b*} + I_{lb}$	-	-	-	-	-	4.94e7
k_c	19.5e6	19.5e6	1.65e8	1.65e8	1.01e10	1.01e10
k_l	6.55e4	1.37e5	1.67e6	1.89e6	3.56e8	4.02e8
k_t	4.66e5	4.74e5	2.34e7	2.34e7	-	-
k_h	-	1.51e7	-	-	-	1.51e7
k_{gb}	-	-	1.63e7	1.63e7	1.63e7	-
k_g	-	-	-	-	9.96e6	1.06e7
k_{bm}	-	-	-	-	-	2.72e6
k_p	-	-	-	-	-	8.81e4
c_c	2.67e5	2.67e5	1.55e6	1.55e6	1.31e8	1.31e8
c_l	5.23e3	1.02e4	3.58e5	4.34e5	1.40e7	1.41e7
c_t	1.40e4	1.89e4	1.34e6	1.52e6	-	-
c_h	-	3.93e5	-	-	-	3.93e5
c_{gb}	-	-	2.76e6	3.57e4	5.16e4	-
c_{bm}	-	-	-	-	-	3.53e4
c_p	-	-	-	-	-	6.55e3

D
Verification

To study the basic behaviour of the numerical models, verification runs were performed on the 3DOF and 6DOF baseline models. Two verification cases are defined, for which the resulting behaviour of the system is discussed in appendices D.1.1 and D.2.1 for the 3DOF and 6DOF numerical models, respectively.

VC1: The suspended blade is subjected to an acceleration in y^b and x^b-direction. First, at t=10, an acceleration of 1 m/s^2 is applied in y^b at the blade COG for 2.5 seconds. Later, at t=100, a moment of 1 m/s^2 in x^b-direction is applied on the blade COG for another 2.5 seconds.

VC2: To verify the operation of the wind model and the response of the system, the system is subjected to a uniform airflow with a constant velocity of 15 m/s applied from t=50 onwards.

D.1. 3DOF numerical models

D.1.1. Time domain simulations

The verification runs are performed on the XY and YZ baseline models, presented in section 4.3. For the XY model, the system is first considered without tugger lines, as the resulting behaviour is easy to grasp. The run is then repeated with tugger lines. No pretension is applied to the tuggers during the verification runs.

Figure D.1a presents the motion of the blade at the COG for VC1 without tugger lines. As expected, the acceleration results in a pendulum motion of the suspended load under the crane. The pendulum motion of the load also results in a motion of the crane at the tip. However, this displacement is very small, due to the relatively high crane stiffness. The small amount of pendulum damping results in a decrease in swing amplitude over time. When the acceleration in x^b is applied, the blade is already swinging in y direction. As a result, there is a very small offset between the position of the blade COG and the lower block COG, due to the finite stiffness of the UQC connection between the two bodies. The result is a very small misalignment of the blade and hook fixed coordinate systems. When the acceleration is applied at the origin of the blade fixed coordinate system, the small offset generates a small moment on the lower block. This can be seen as the minor yaw rotation present after the acceleration in x^b is applied.

Although this contribution is very small, the behaviour does demonstrate an important coupling between the translational and rotational DOF. This coupling is especially significant for the XY table. When there is misalignment present between the position of the blade fixed and hook fixed coordinate system within the XY plane, and a force is exerted perpendicular to the existing offset, the force result in a translation acceleration AND an acceleration around the yaw axis. A schematic of the described dynamics is provided in figure 5.2.

In figure D.1b the blade movement is shown for the system with tugger lines. The additional tugger lines results in an additional coupling between the blade's x and y motion. As the blade swing in the y-direction, the distance between the tugger mounting on the crane and block increases slightly. As a result, the tugger lines pull the blade towards the crane. The difference between the previous case and this case with tugger lines is more obvious when an acceleration in x^b is applied. Due to the tugger lines, the load is no longer capable of freely swinging in positive x. The movement in the x-direction is significantly reduced by the tugger lines. Also, the stiffness of the system is higher in this direction due

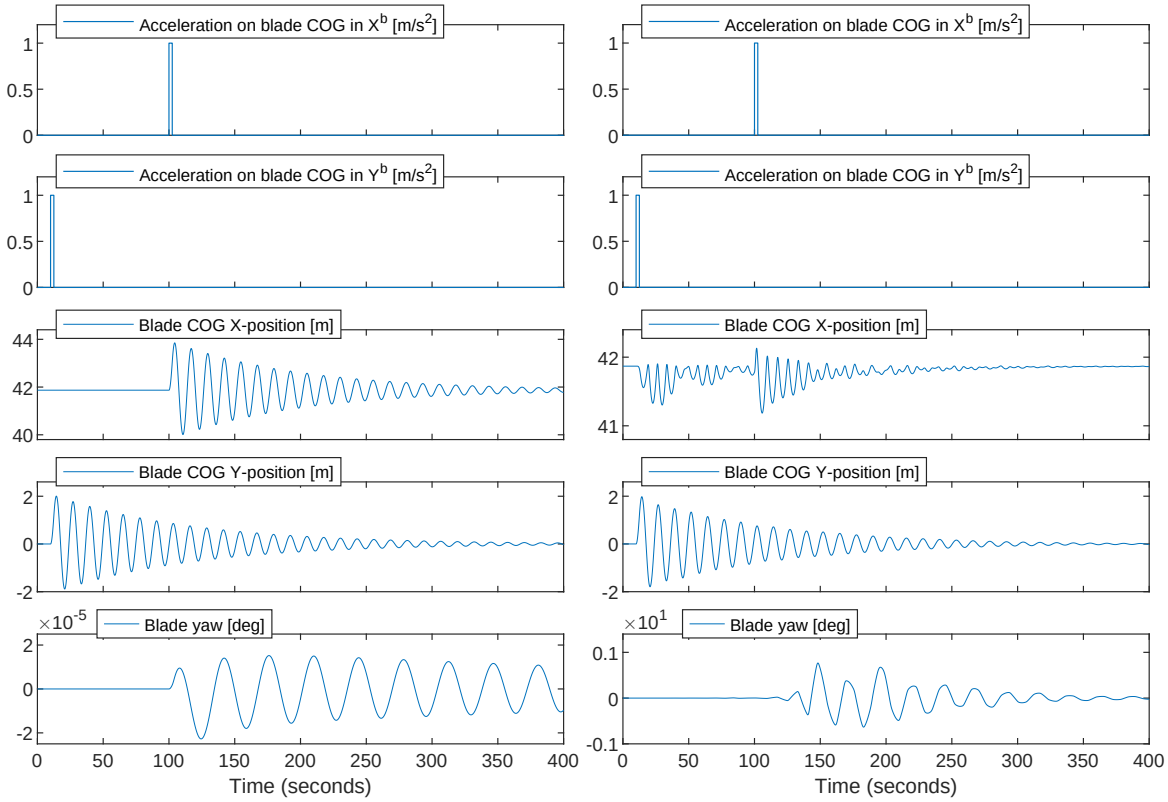

(a) XY Baseline SBIS without tuggers

(b) XY Baseline SBIS with tuggers

Figure D.1: Blade motion for verification case 1 (VC1), acceleration in y^b and x^b at t=10 and t=100s, respectively

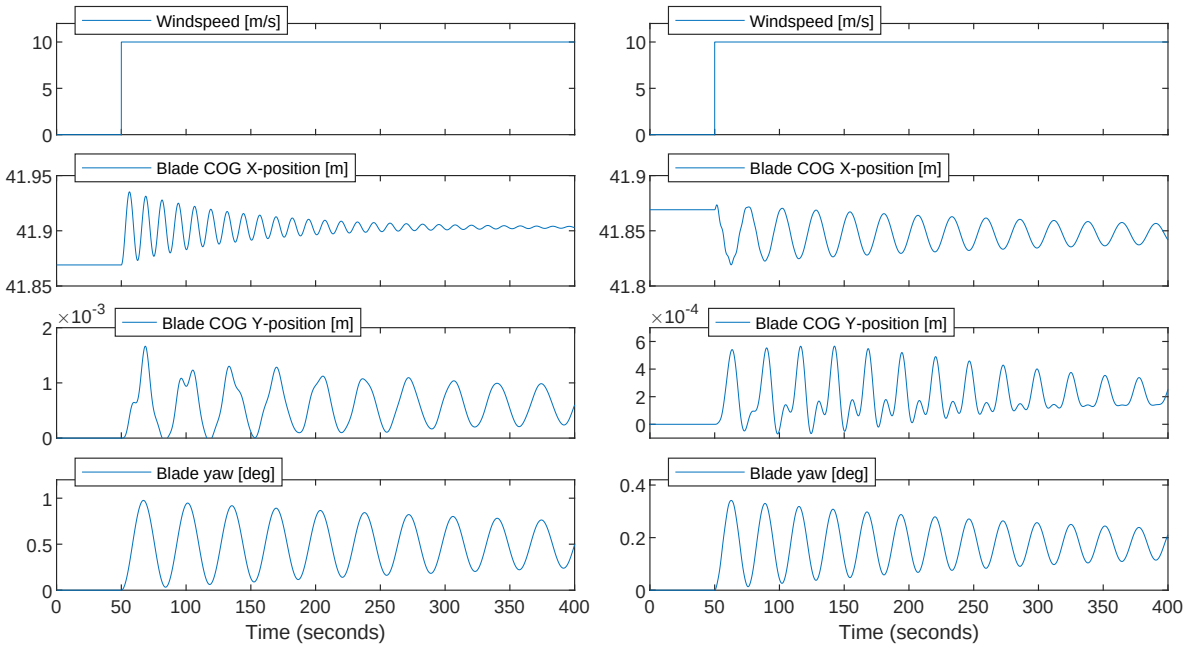

(a) XY Baseline SBIS without tuggers

(b) XY Baseline SBIS with tuggers

Figure D.2: Blade motion for verification case 2 (VC2), introduction of a uniform airflow at t=50.

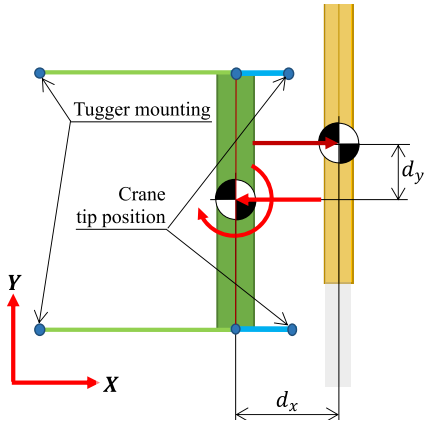

Figure D.3: Coupling between loads in XY and yaw

to the additional tugger lines, which is visible in the results as the higher frequency pendulation in x. Again, the motion decays due to the damping in the tugger lines and pendulum. Finally, a coupling can be seen between the pendulation of the suspended load and rotation of the blade around the z-axis after the acceleration in x^b has been applied to the system. This is due to the slightly asymmetrical loading of the two tugger lines on the blade due to the swinging of the load in the y-direction.

In figure D.2a, the blade COG motion is shown for VC2 without tugger lines. At t=50 a uniform flow is introduced to the system. The uniform flow creates aerodynamic load on the blade. The wind direction is aligned with the positive x-axis. The wind load has a component in x-direction due to the drag. The lift of the blade acts in the z-direction, and is not reflected in this model. Because the drag is not equal on both sides of the blade, the wind load also produces a moment around the blade COG. This results in yaw motion. The rotation of the suspended load creates an uneven load on the two hoist cables, which leads to a restoring moment. The rotation results in a small component of the drag in y. This causes the movement of the blade root COG in y-direction. Within the blade motion in y-direction, a second sinusoidal contribution can be observed. The frequency corresponds to the pendulation of the load in the y-direction after the blade COG is initially displacement by the drag component in y-direction.

Something noticeable about the resulting blade motion for VC2 with tuggers in figure D.2b, is the changed behaviour of the blade motion in the x-direction. The tuggers constrain the movement of the blade and make it harder for the blade to yaw. Because the tuggers are tensile springs, and not pretension is applied, the tugger only exerts a force when under tension. Due to the wind induced moment around z, the blade will rotate around one of the tugger connections. This behaviour is outlined in figure D.4a. The wind exerts a moment around the z-axis, causing the blade to rotate in yaw. The rotation causes the COG to move towards the crane. The results show how the frequency of the blade COG movement agrees with blade yaw. Again in the y-direction, the two contributions of pendulum motion and wind drag are separately visible.

Figures D.5a and D.5b show the blade movement for VC1 and VC2, respectively. The model in YZ does not contain tugger lines, as the contribution of the tugger lines in this plane has been neglected. The acceleration on the blade COG result in a pendulum motion. The initial amplitude, frequency, and damping agrees with the XY model as expected. The coupling between y- and z-motion is clearly visible. When the blade swings out, the blade is lifted as it were, as the cable length remains approximately equal. A roll motion of the blade is observed during the pendulum motion. This is due to the offset between the location where the main hoist attaches tot the suspended load, and the COG of the blade. This offset is visible in figure D.4b. This same offset is also responsible for the momentary but forceful roll movement of the blade when acceleration is applied to the blade. Due to the moment arm, the acceleration causes a rotation on top of the translation. However, due to the relatively high damping of the hoist cables along their length, this movement is quickly damped out. The higher damping of the hoist also causes the oscillation of the blade's COG z-position to damp out faster than in the y-direction. As expected, the aerodynamic load provides a moment and lift force. Due to blade rotation, a result of the small component of lift in the y-direction is also visible.

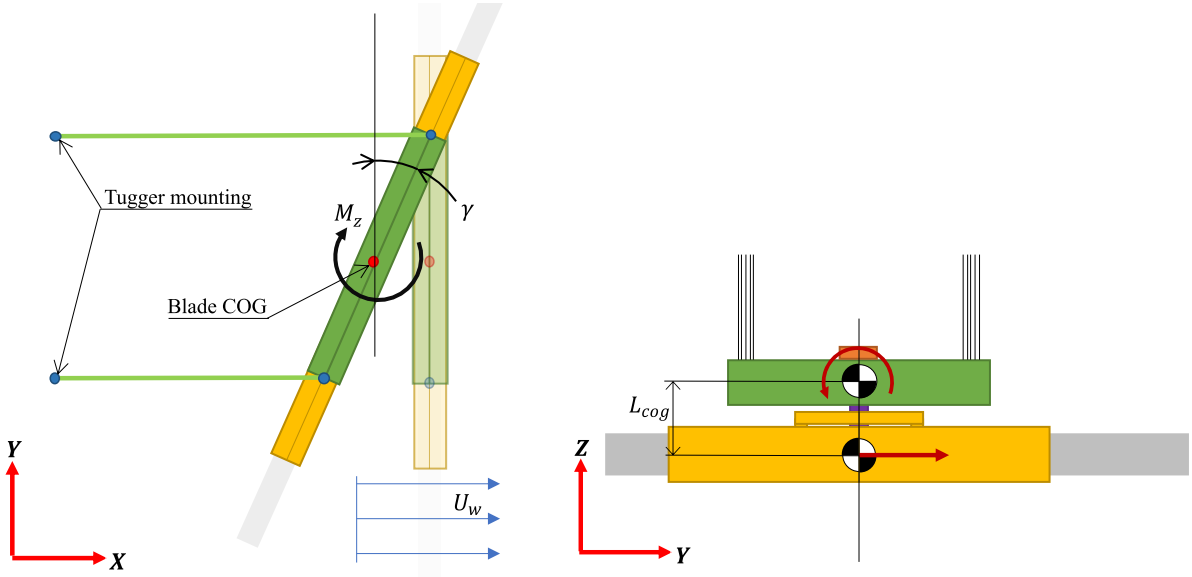

(a) COG movement due to blade rotation with tugger lines

(b) Roll due to acceleration at blade COG

Figure D.4: Examples of coupling between different DOF in the 3DOF numerical model

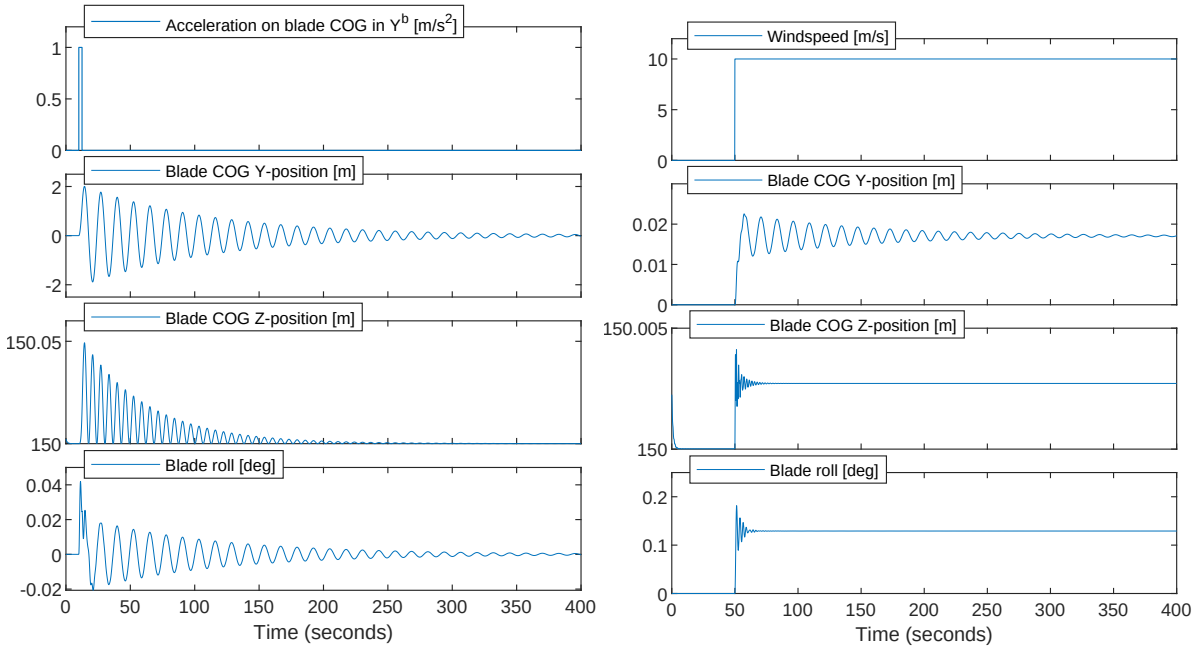

(a) Verification case 1 (VC1), acceleration in y^b at t=10.

(b) Verification case 2 (VC2), introduction of a uniform airflow at t=50.

Figure D.5: Blade motion for verifications runs on the YZ Baseline SBIS

D.1.2. Frequency domain comparison

Below, the open loop response for the linearized system is plotted for the 5 actuation methods, along with the open loop response of the linear models from chapter 3. The response of the linearized numerical models generally agrees with that of the simplified linear models. Some deviations can be observed in certain responses due to non-linear effects that were not considered in the simplified linear models.

The additional coupling between the DOF described in appendix D.1.1 and shown in Figure D.3 is not immediately visible in the open loop response for the XY table, as the model is linearized at t=0, where the hook and blade fixed coordinate systems are aligned. To demonstrate how the non-linear coupling effect the system, the 3DOF numerical model is linearized again, while the y-cylinder is given a certain offset d_y. Figure D.7 shows the open loop responses for a cylinder offset of 0.1, 0.25 and 0.5 meter. The coupling is clearly visible, and results in a negative phase peak, which increases for a larger cylinder offset. Due to this dynamic, the system can become unstable for high XY table cylinder strokes.

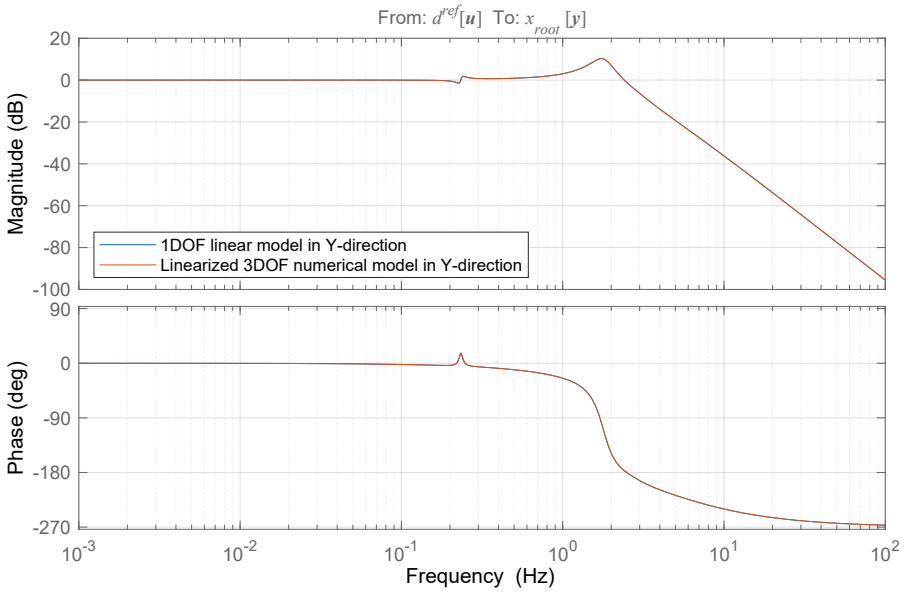

Figure D.6: Comparison between linear 1DOF and linearized 3DOF numerical model for SBIS with XY table

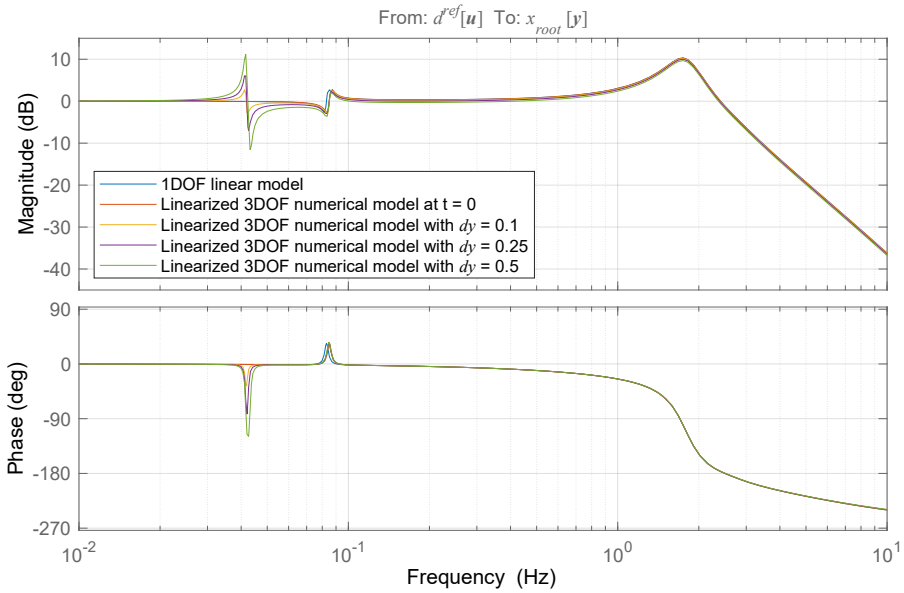

Figure D.7: Comparison between linearized 3DOF numerical models for SBIS with XY table with various cylinder offsets

Figure D.8 and figure D.9 show the comparison in the open loop response between the linear single DOF models, and the linearized 3DOF models for the power swivel (AM2) and wind vanes (AM3). For these models, there are no significant differences in the behaviour described by the linear and nonlinear models. Additionally, there are no strong effects of the additional coupling between the degrees of freedom for these actuation methods, as was the case for the XY table. This is partly because the blade-fixed and hook-fixed coordinate systems do not move relative to each other for these actuation methods.

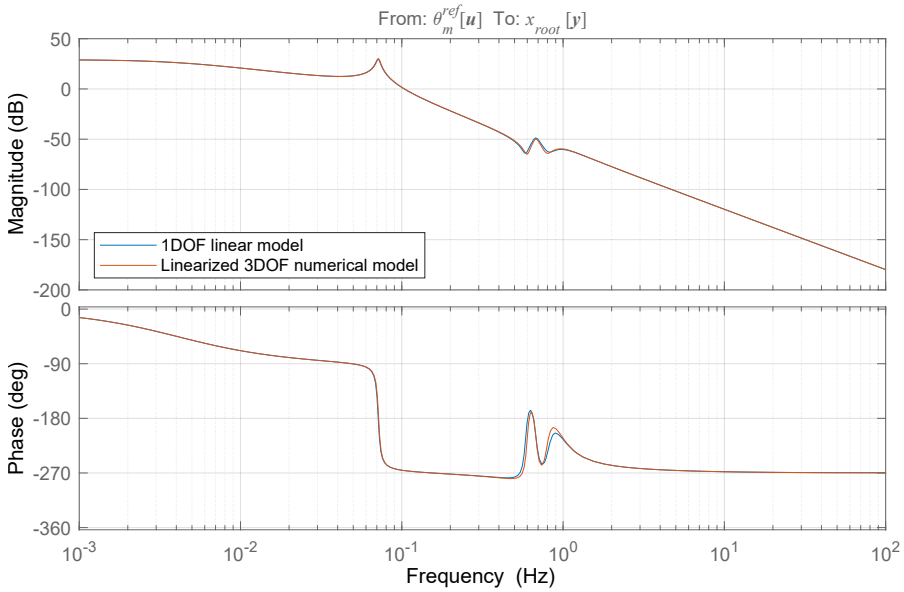

Figure D.8: Comparison between linear 1DOF and linearized 3DOF numerical model for SBIS with UQC power swivel

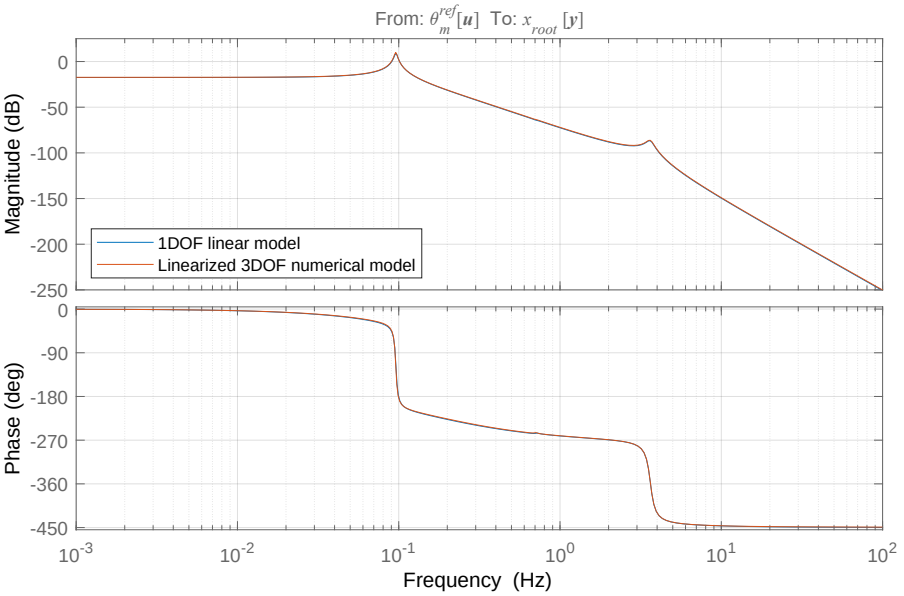

Figure D.9: Comparison between linear 1DOF and linearized 3DOF numerical model for SBIS with wind vanes

Figure D.10 and figure D.11 show the comparison of the open-loop response between the linear single DOF models and the linearized 3DOF models in the YZ plane. For the gyroscopes, similar to the power swivel and the wind vanes, there are no significant differences between the two models. However, for the COG shifting method, a larger difference can be observed in the response. This is likely the result of the simplified coupling formulas used to connect the translational and rotational models together.

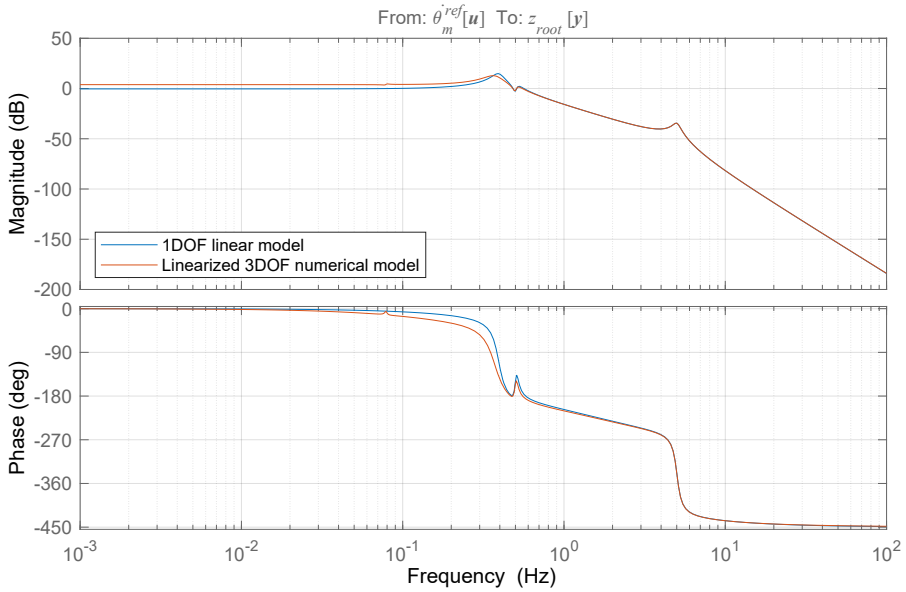

Figure D.10: Comparison between linear 1DOF and linearized 3DOF numerical model for SBIS with gyroscopes

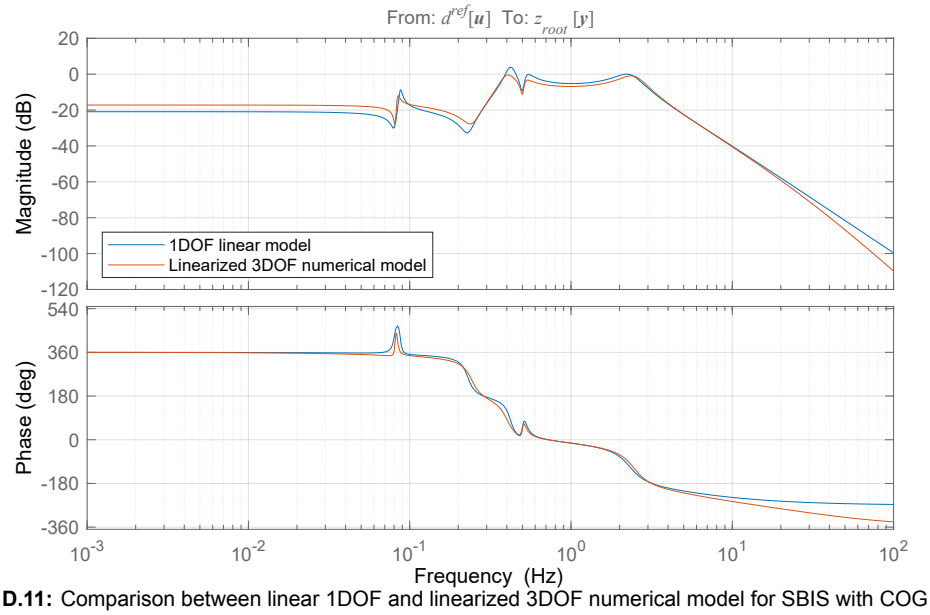

Figure D.11: Comparison between linear 1DOF and linearized 3DOF numerical model for SBIS with COG shifting

D.2. 6DOF simulator model

D.2.1. Time domain simulations

As with the 3DOF numerical models, the two verification cases are simulated for the baseline simulator model. The system response for VC1 without a tugger line is shown in figure D.13a. The same dynamics observed in the 3DOF XY and YZ models are again observed for the 6DOF model. The pendulum motion in both the x- and y-directions is coupled with the motion of the blade COG in the z-direction. Additionally, a roll and pitch movement of the blade can be seen during the pendulum movements. This is again due to the offset between the COG of the blade and the attachment of the main hoist on the lower block, represented by L_{cog}. The momentary but powerful roll and pitch motion of the blade resulting due to the acceleration acting on the blade COG is also visible.

In figure D.13b, the addition of tuggers results in a significant reduction in blade motion in the x-direction. Compared to the 3DOF XY model, more damping is observed in this case. This additional damping is a result of the additional coupling between DOFs. In appendix D.1.1, an important coupling between the translational plane and yaw was already observed. When there is a misalignment between the blade-fixed and hook-fixed coordinate systems, translational loads also result in a yaw moment. The same coupling occurs for the other rotational DOFs in the 6DOF model. This is clearly seen in figure D.13a, where the coupling between the pendulum motion of the blade in the x-direction and the resulting pitch motion is evident. Figure D.12 provides a schematic representation of the suspended load, depicted for the XY table actuation method. Since there is always an offset in the z^h-direction between the blade-fixed and hook-fixed coordinate systems, coupling always occurs. During swinging of the load in the x-direction, energy is transferred to the main hoist cables through this coupling, where it can be dissipated more quickly due to the higher damping in the main hoist cables.

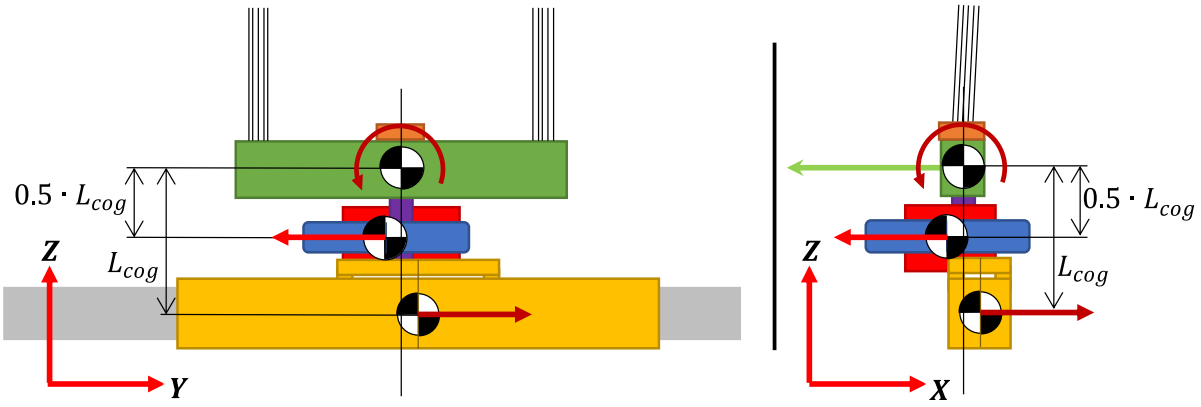

Figure D.12: Additional coupling between DOFs in the simulator model

The 6DOF model VC2 was also tested. The results with and without a tugger are shown in figures D.14a and D.14b. Here too, the additional coupling between the 6DOF is apparent. In the case with a tugger, a strong coupling is observed between the COG x motion and yaw, as shown in figure 5.16. A new dynamic that was not visible before is the wind-induced blade pitching motion, resulting from the pitch moment induced on the blade by wind loading. Figure D.14b once again, shows the coupling between the blade COG x motion and blade pitch due to the L_{cog} offset.

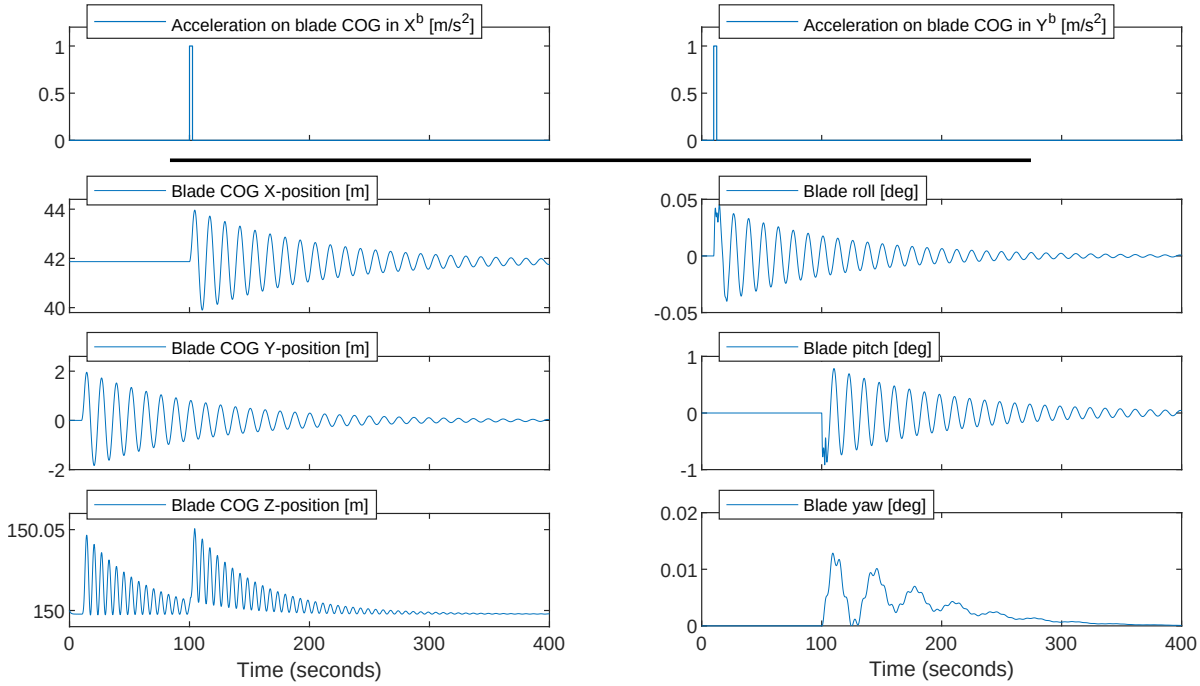

(a) Baseline model of SBIS with HMC, without tuggers

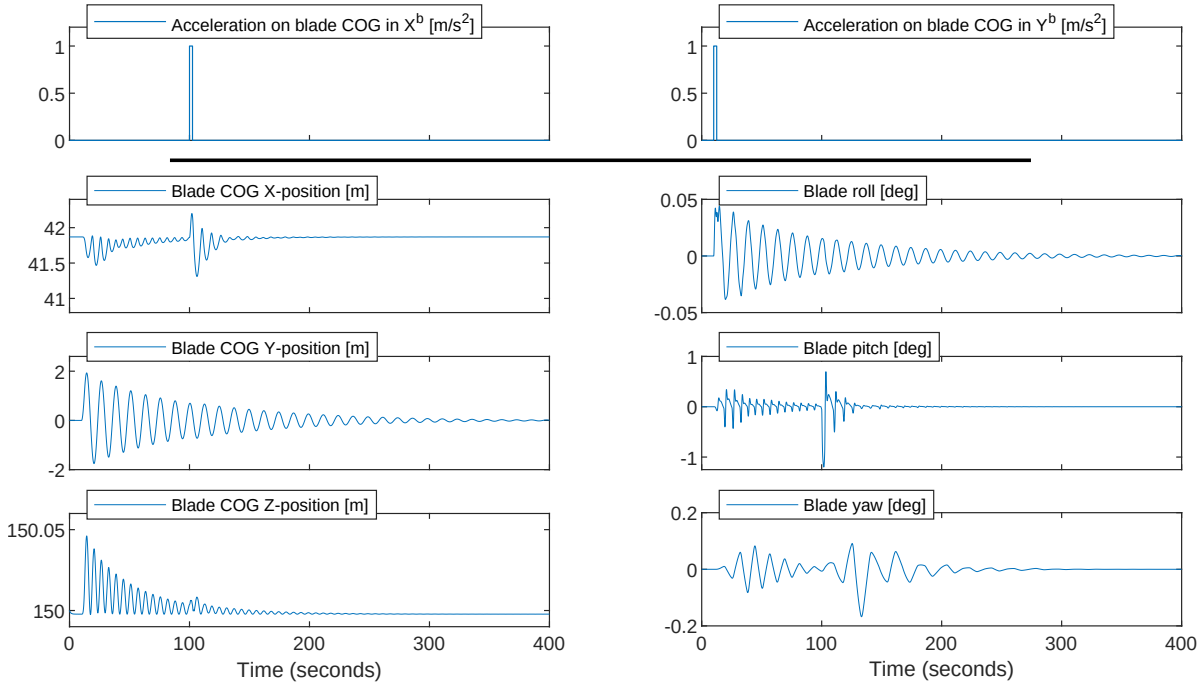

(b) Baseline model of SBIS with HMC, with tuggers

Figure D.13: Blade motion for acceleration in y^b and x^b direction at blade COG.

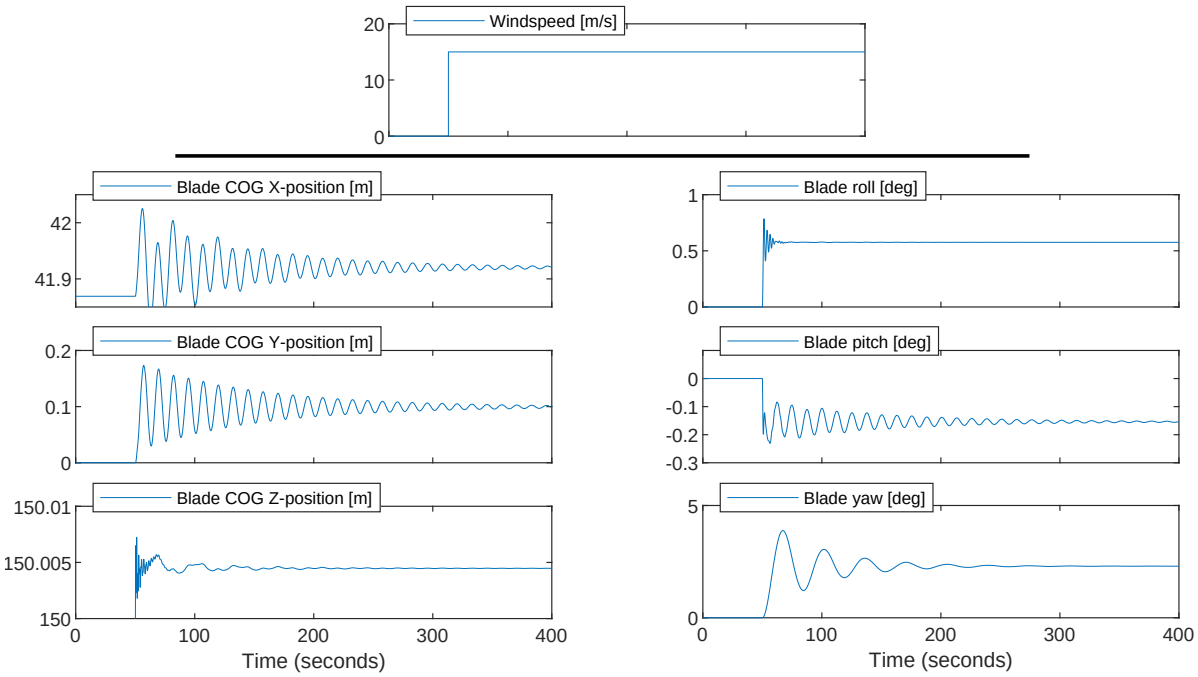

(a) Baseline model of SBIS with HMC, without tuggers

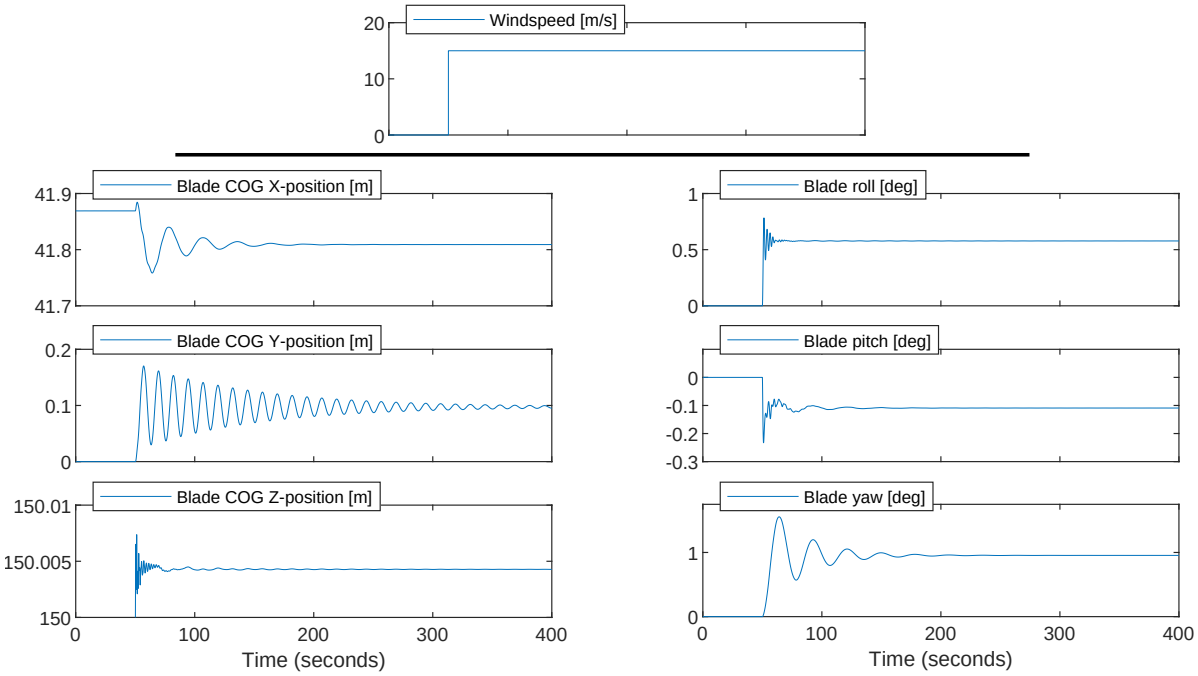

(b) Baseline model of SBIS with HMC, with tuggers

Figure D.14: Blade motion after the introduction of a uniform airflow at t=50.

D.2.2. Frequency domain comparison

As was done for the 3DOF numerical models, the open loop response of the linearized simulator model is compared to that of the single DOF linear models to study the open loop frequency response. Linearization is performed in the Simulink model linearizer app. The HMC is a combination of three actuation methods, and the controller is a combination of three linear controllers as well. As there is coupling between the DOF, the parallel systems do affect each other, which makes is impossible to compare their individual response simultaneously. To capture the dynamics of the SBIS with a single actuation method, without the effect of the controllers, the control loops of the other actuation methods are disconnected. Otherwise, the dynamics of the other controller would be visible in the response due to the coupling between the DOF.

XY table

During linearization of the 6DOF simulator model for studying the XY table, both the gyroscope and the COG shifting controller are disconnected from the model. This is shown in the control diagram in figure D.17. The XY table controller is excluded from the open loop response by definition. Figures D.15 and D.17 shown the open loop response from $u_{1,y}$ to $y_{1,y}$ and $u_{1,x}$ to $y_{1,x}$ respectively. To study the effect of the DOF coupling as a result of L_{cog} discussed before and shown figure D.12, the offset L_{cog} is varied over three linearization.

For the open loop response in y-direction, no significant difference is observed for the linearized 6DOF simulator model with the reference value for L_{cog}. However, for a significant increase in L_{cog}, the additional coupling is clearly visible in the open loop response.

For the response in x-direction in figure D.17, the additional coupling due to the L_{cog} offset is very significant. Compensation using the XY table in the x-direction results in a reaction moment around the combined hook and blade pitch axis. This rotation directly results in a displacement of the blade in the x-direction, due to the offset between the combined COG pitch axis and the blade axis. On top of this, the rotation also results in feedback to the system through the hoist cables, and more significantly the tugger lines. This feedback to the tugger lines due to the pitching moment results in the additional phase peaks in the open loop response, which can affect controller performance. For larger values of L_{cog}, the effect is exaggerated. To reduce the effect, the offset L_{cog} should be minimized. In the HMC, the counterweight is assumed to be located between the blade and lower block COG, as shown in figure D.12, as this is the case for the current XY table concept. However, placing the counterweight closer to the blade might be beneficial, as this reduces the pitching moment generated during compensation in x-direction using the XY table. Alternatively, it could be desirable to mount the tugger lines as close to the combined hook and blade pitch axis as possible. When the combined blade and lower block rotates around this combined pitch axis, this will not result in feedback to the tugger lines.

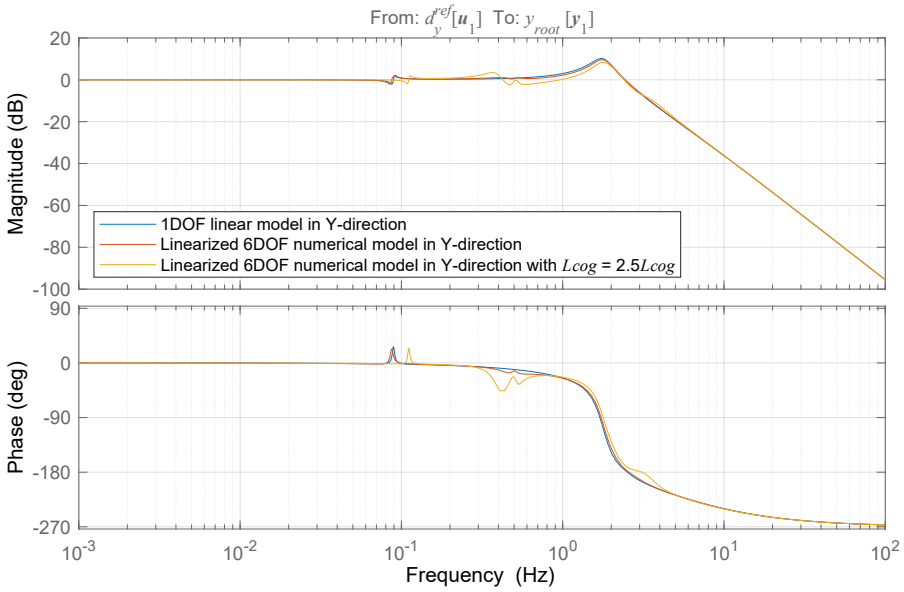

Figure D.15: Comparison between linear 1DOF and linearized 6DOF simulator model

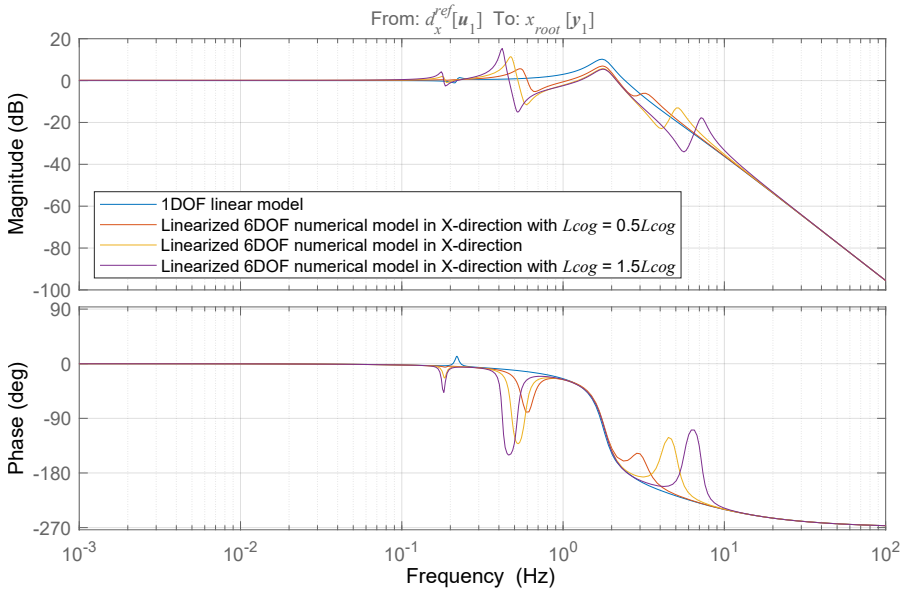

Figure D.16: Comparison between linear 1DOF and linearized 6DOF simulator model

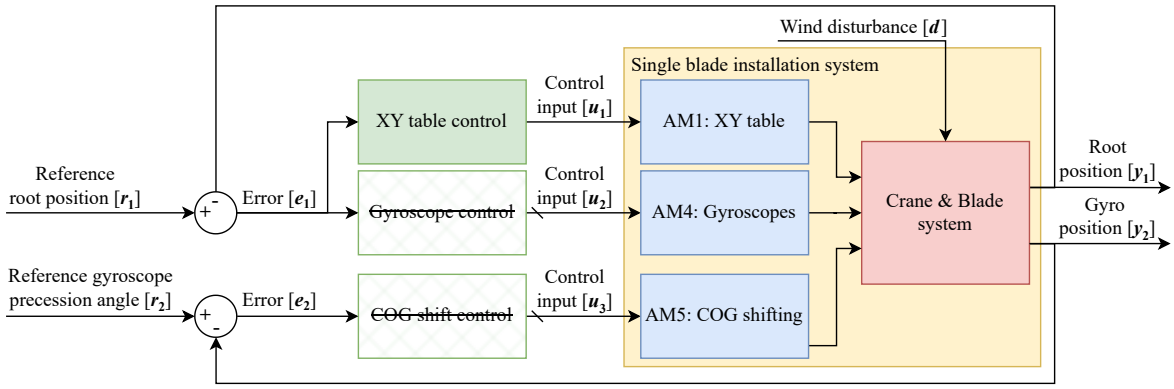

Figure D.17: Comparison between linear 1DOF and linearized 6DOF simulator model

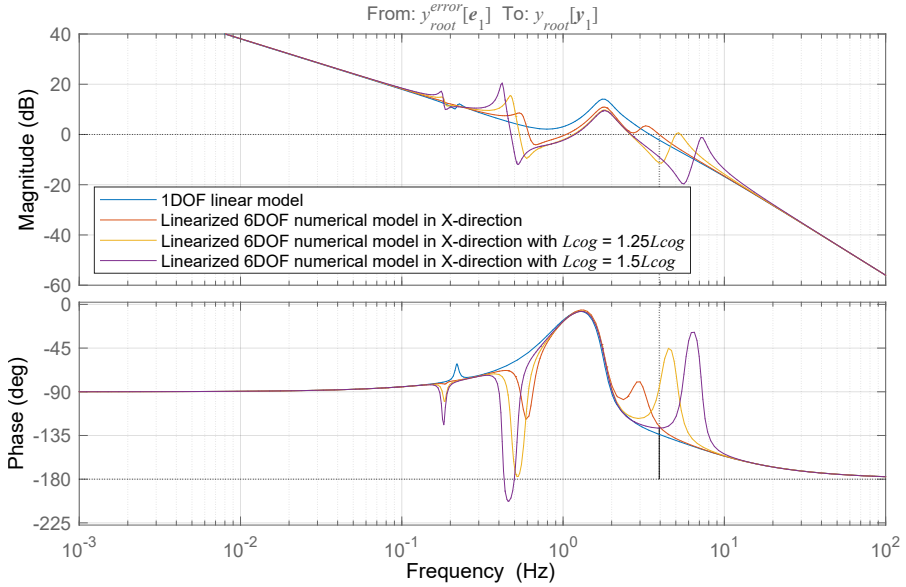

Figure D.18: Comparison between linear 1DOF and linearized 6DOF simulator model

COG shifting

To compare the COG shifting dynamics with the 1DOF model, the gyroscope and XY table controller are decoupled. The Bode graph shows the open-loop response from [u_3] to [$y_{1,z}$]. The control input is applied to the XY table yoke's y cylinder to enable comparison with the 1DOF model. The response of the linearized 6DOF numerical model and the 1DOF linear models closely match. The linearized response of the COG shifting method is also shown for two alternative values of L_{cog}. As expected, this distance has an effect on the system's response. A significant dip in gain can be observed around 0.1Hz, corresponding to the pendulum frequency of the suspended load under the main hoist. For larger values of L_{cog}, the coupling between the actuated DOF and undesired DOFs is greater, as expected.

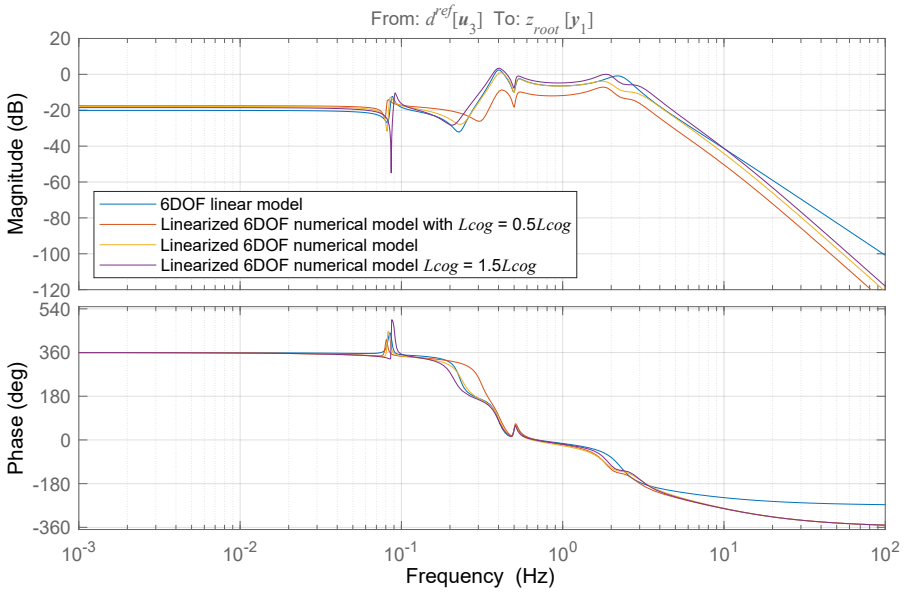

Figure D.19: Comparison between linear 1DOF and linearized 6DOF simulator model

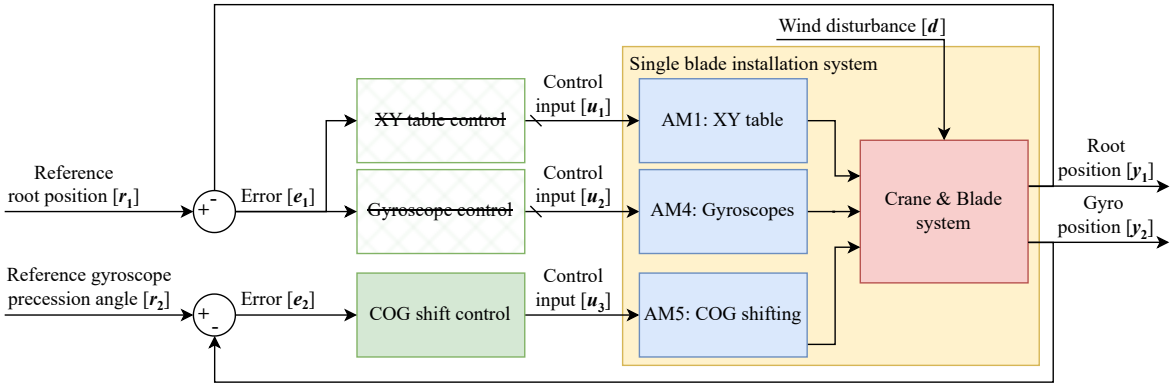

Figure D.20: Comparison between linear 1DOF and linearized 6DOF simulator model

Gyroscopes

Below in figure D.22, the open-loop response for the gyroscopes is shown. From the responses, it can be seen that the additional DOF coupling does not have a significant effect on the gyroscopes. This is as expected, since the gyroscopes provide minimal feedback to the system. For larger values of L_{cog}, small effects can be observed, but these remain limited compared to the COG shifting and especially the XY table actuation methods.

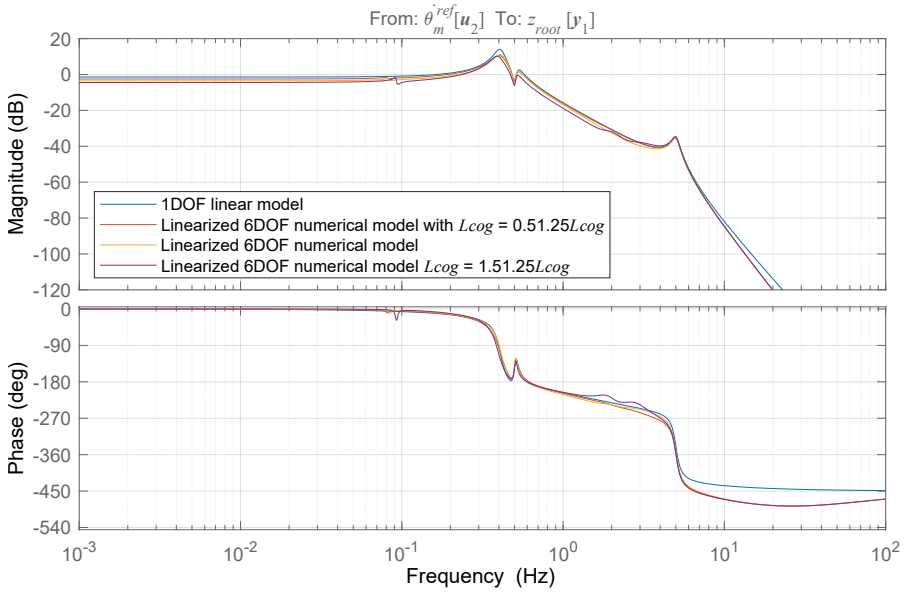

Figure D.21: Comparison between linear 1DOF and linearized 6DOF simulator model

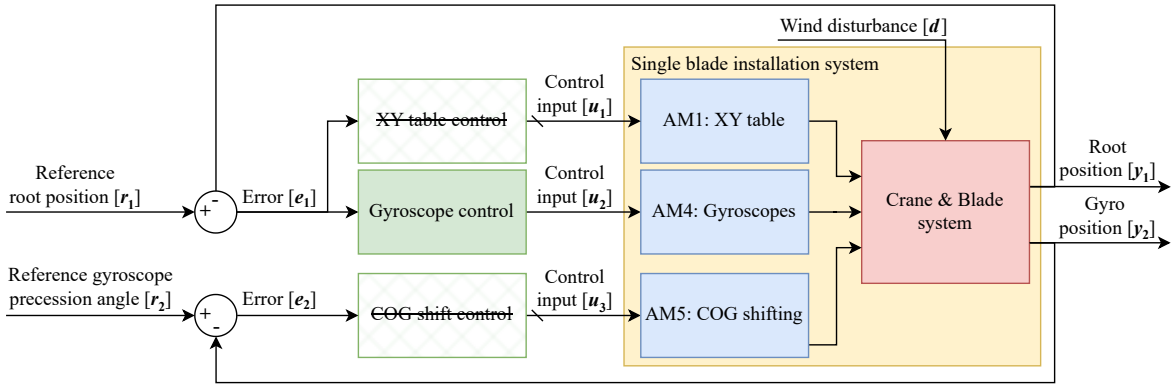

Figure D.22: Comparison between linear 1DOF and linearized 6DOF simulator model

E

Parameters

E.1. Basic parameters for the SBIS

Description	Symbol	Value	Unit
Air density	p_{air}	1.225	kg/m^3
Gravitational acceleration	g	9.81	m/s^2
Width between tugger mounting (on crane)	W_c	10	m
Lower block width	W_{lb}	10	m
Offset between LB COG and blade yoke COG in z^b at t=0	L_{cog}	9.45	m
Turbine hub height above MSL	H_{hub}	150	m
Crane height above hinge	H_c	168.34	m
Crane pedestal height (above deck)	H_p	32.5	m
Jack-up deck height (above MSL)	H_{deck}	25	m
Gyroscope angular momentum	H_s	5.92e6	N.m.s
Gearbox rotational inertia	J_{gb}	5.4e3	kg.m^2
Gyroscope rotational inertia (around precession axis)	I_{gy}	1.10e4	kg.m^2
Vane rotational inertia	I_v	1.21e4	kg.m^2
Gearbox stiffness	k_{gb}	1.63e7	N/m
Hydraulic cylinder stiffness	k_h	1.506e7	N/m
Main hoist stiffness (along length)	k_{mh}	8.05e6	N/m
Tugger line stiffness (along length)	k_t	4.737e5	N/m
UQC connection stiffness	k_{uqc}	5e8	N/m
Gearbox damping	c_{gb}	2.76e6	N.s/m
Servo gearbox damping gyroscope	$c_{gb_{gy}}$	5.16e4	N.s/m
Servo Gearbox damping vanes	c_{gb_v}	3.56e4	N.s/m
Hydraulic cylinder damping	c_h	3.93e5	N.s/m
Main hoist damping (along length)	c_{mh}	2.23e5	N.s/m
Tugger line damping (along length)	c_t	2.22e4	N.s/m
UQC connection damping	c_{uqc}	5.00e8	N.s/m

E.2. Actuation methods

AM	Baseline	AM1	AM2	AM3	AM4	AM5	AM5.B	HMC	Unit
M_b	114	114	114	149	203	114	114	114	ton
M_h	147	234	147	147	147	191	234	323	ton
M_{cw}	0	125	0	0	0	0	125	125	ton
$M_{cw.2}$	0	0	0	0	0	0	0	100	ton
I_{b_x} (×1e7)	4.68	4.68	4.68	6.08	5.41	4.68	4.68	4.68	kg.m^2
I_{b_y} (×1e5)	5.18	5.18	5.18	5.18	5.18	5.18	5.18	5.18	kg.m^2
I_{b_z} (×1e7)	4.68	4.68	4.68	6.07	5.40	4.68	4.68	4.68	kg.m^2
I_{h_x} (×1e6)	1.27	2.55	1.27	1.27	1.27	2.55	2.55	9.71	kg.m^2
I_{h_y} (×1e6)	0.126	1.40	0.126	0.126	0.126	1.40	1.40	1.33	kg.m^2
I_{h_z} (×1e6)	1.3	2.02	1.3	1.3	1.3	2.02	2.02	9.20	kg.m^2
L_{mh}	38.34	33.89	38.34	38.34	38.34	33.89	33.89	33.89	m

E.3. 6DOF numerical model

$$
\begin{aligned}
M_c &= \text{diag}\{3.65e5,\quad 2.86e5,\quad 5.88e6,\quad 1.06e9,\quad 6.92e7,\quad 9.10e6\}\\
K_c &= \text{diag}\{2.00e7,\quad 3.00e6,\quad 5.70e7,\quad 1.01e10,\quad 3.70e9,\quad 1.65e8\}\cdot\\
D_c &= \text{diag}\{2.70e5,\quad 4.00e4,\quad 1.83e6,\quad 1.31e8,\quad 2.02e7,\quad 1.55e6\}\cdot\\
K_{qc} &= \text{diag}\{k_{uqc},\quad k_{uqc},\quad k_{uqc},\quad k_{uqc},\quad k_{uqc},\quad k_{uqc}\}\\
D_{qc} &= \text{diag}\{c_{uqc},\quad c_{uqc},\quad c_{uqc},\quad c_{uqc},\quad c_{uqc},\quad c_{uqc}\}\\
K_h &= \text{diag}\{k_h,\quad k_h,\quad k_{uqc},\quad k_{uqc},\quad k_{uqc},\quad k_{uqc}\}\\
D_h &= \text{diag}\{c_h,\quad c_h,\quad c_{uqc},\quad c_{uqc},\quad c_{uqc},\quad c_{uqc}\}
\end{aligned}
$$

Description	x^i	y^i	z^i	i
COG counterweight initial position	41.87	0.00	157.09	g
XY counterweight initial position	41.87	0.00	154.73	g
Lower block initial position	41.87	0.00	159.45	g
Blade (yoke) initial position	41.87	0.00	150.00	g
Crane tip (center) initial position	41.87	0.00	193.34	g
Blade root target position	41.87	-28.62	150.00	g
Blade COG initial position	41.87	0.00	150.00	g
Main hoist mounting on craneboom	41.87	$\pm$ 5.00	193.34	g
Main hoist mounting on lower block	41.87	$\pm$ 5.00	161.45	g
Tuggerline mounting on lower block	41.87	$\pm$ 5.00	159.45	g
Tuggerline mounting on craneboom	33.42	$\pm$ 5.00	159.45	g
Main hoist mounting on craneboom	0.00	$\pm$ 5.00	0.00	h
Main hoist mounting on lower block	0.00	$\pm$ 5.00	2.00	h
Tuggerline mounting on lower block	0.00	$\pm$ 5.00	0.00	h
Blade root position	-0.19	0.00	-0.03	b
Blade tip position	-0.19	117.18	-0.03	b

F

Miscellaneous

F.1. XY table schematic in operational plane

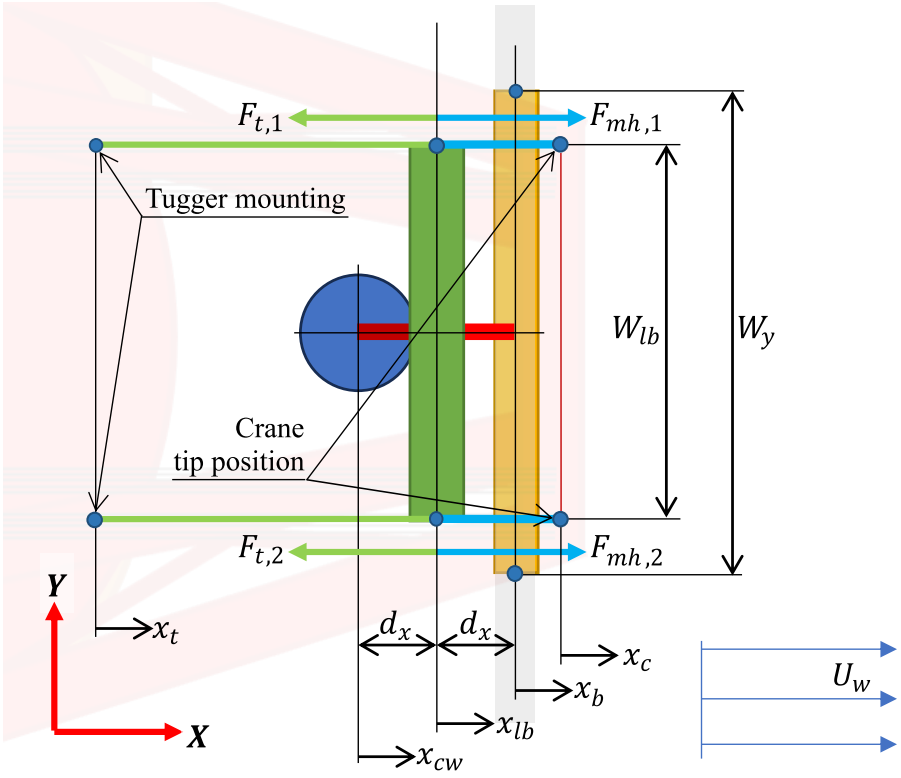

Figure F.1: Schematic overview of the SBIS with XY table within the operational plane

F.2. Kaimal spectrum

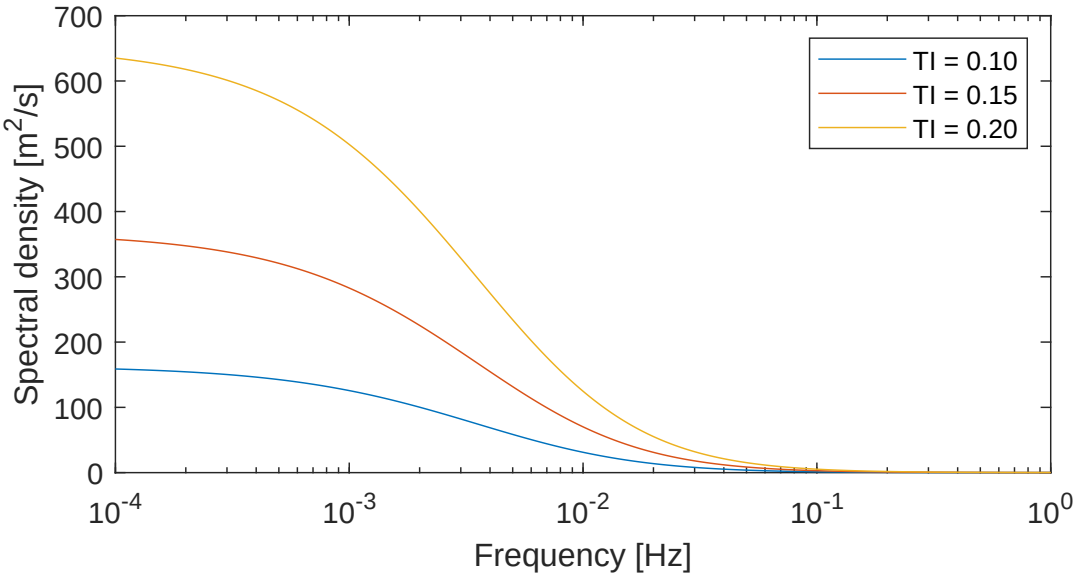

Figure F.2: Kaimal spectral density distribution for U_w = 12 m/s, TI = 0.1, 0.15 and TI = 0.2

F.3. COG shifting with counterweight

In the figure below, the open-loop responses of the COG shifting actuation method and the COG shifting method with a counterweight are compared. Since these two methods operate in a slightly different manner, their responses are not identical. Firstly, it can be observed that the pendulum frequency associated with the pendulum motion of the suspended load on the main hoist is different. This is caused by the increased mass of the suspended load due to the contribution of the extra counterweight.

In the case where the counterweight is moved instead of the blade itself, the third natural frequency, which corresponds to the cylinder eigenfrequency coupled to rotation around the x axis, is visible at a different location in the open-loop response. This is due to the difference in the relative z offset between the lower block and the actuated mass. For the COG actuation method, this distance is given by L_{cog}, while for the situation with a counterweight, it is given as $L_{cog}/2$ (see figure D.12). As a result, the corresponding eigenfrequency is at a higher frequency, which means the corresponding phase jump moves along to a higher frequency for the situation with a counterweight. Therefore, it is possible to use the same controller for this actuation method as for the case without a counterweight.

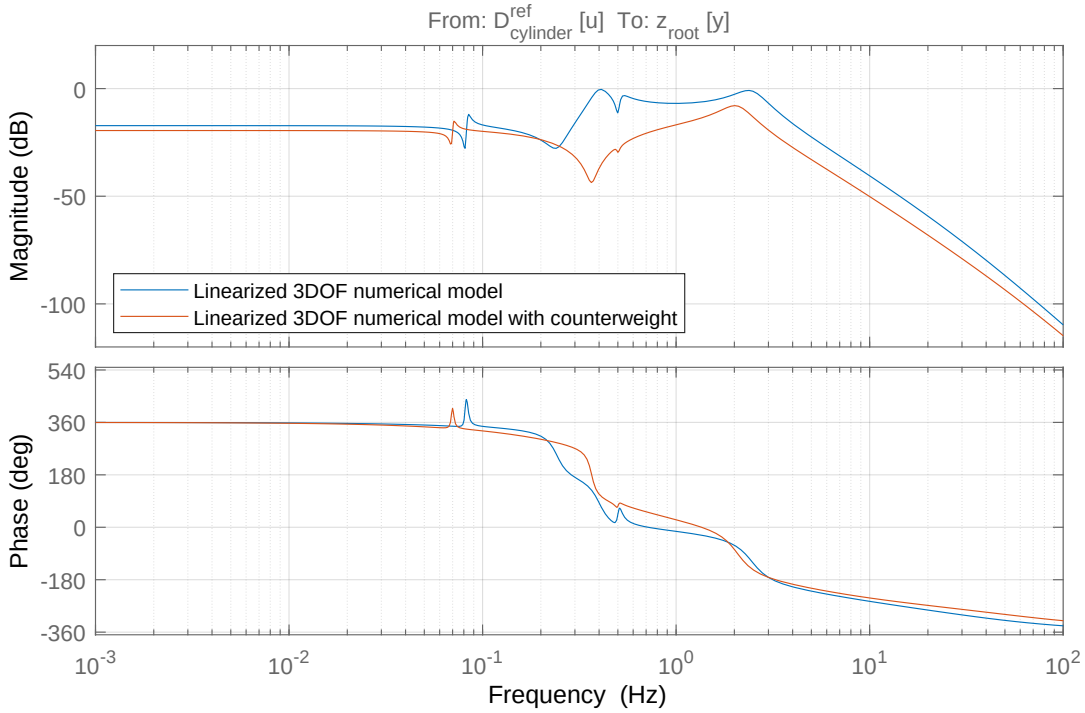

Figure F.3: Comparison between open loop responses for COG shifting with and without counterweight.

F.4. XY table actuation effort per cylinder

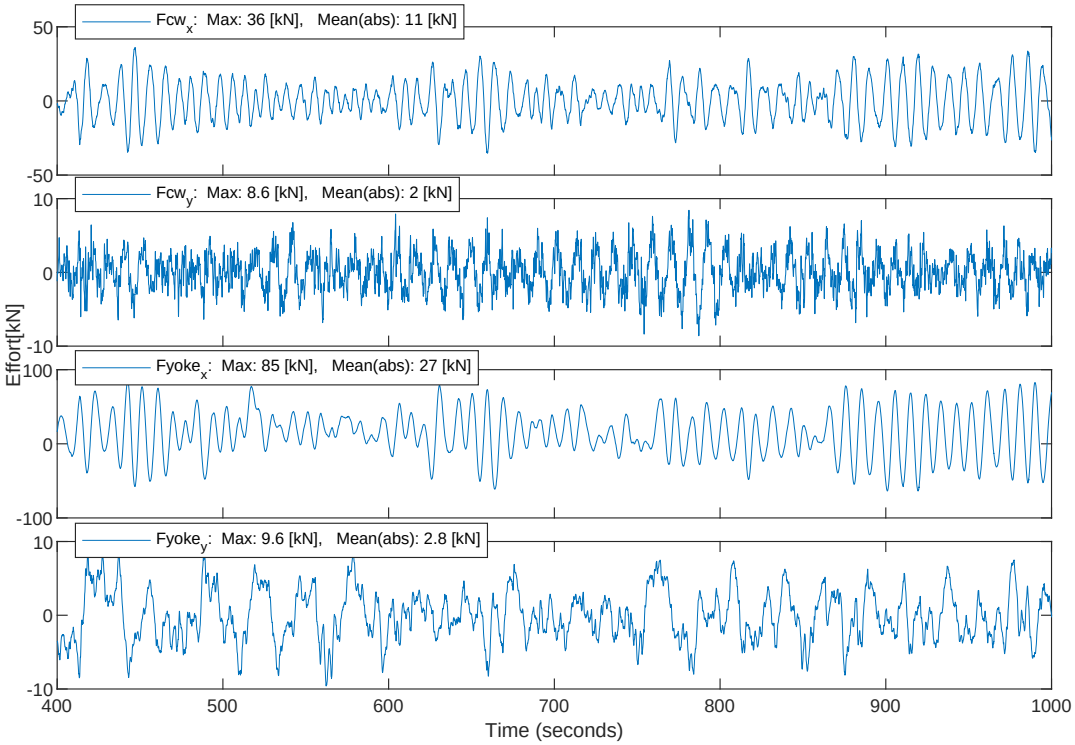

Figure F.4: 6DOF simulator results for the SBIS with HMC, U_w = 15, TI = 0.18.

G

TurbSim Input

```
TurbSim Input File. Valid for TurbSim v1.50, 25-Sep-2009

---------Runtime Options-----------------------------------
48              RandSeed1       - First random seed  (-2147483648 to 2147483647)
RANLUX              RandSeed2       - Second random seed (-2147483648 to 2147483647) for intrinsic pRNG, or an alternative pRNG: "RanLux" or "RNSNLW"
False               WrBHHTP         - Output hub-height turbulence parameters in binary form? (Generates RootName.bin)
False               WrFHHTP         - Output hub-height turbulence parameters in formatted form?  (Generates RootName.dat)
False               WrADHH          - Output hub-height time-series data in AeroDyn form?  (Generates RootName.hh)
False               WrADFF          - Output full-field time-series data in TurbSim/AeroDyn form? (Generates Rootname.bts)
True                WrBLFF          - Output full-field time-series data in BLADED/AeroDyn form?  (Generates RootName.wnd)
False               WrADTWR         - Output tower time-series data? (Generates RootName.twr)
True               WrFMTFF          - Output full-field time-series data in formatted (readable) form?  (Generates RootName.u, RootName.v, RootName.w)
False               WrACT           - Output coherent turbulence time steps in AeroDyn form? (Generates RootName.cts)
True                Clockwise       - Clockwise rotation looking downwind? (used only for full-field binary files - not necessary for AeroDyn)
 0                  ScaleIEC        - Scale IEC turbulence models to exact target standard deviation? [0=no additional scaling; 1=use hub scale uniformly; 2=use individual scales]

--------Turbine/Model Specifications-----------------------
9                  NumGrid_Z       - Vertical grid-point matrix dimension
33                 NumGrid_Y       - Horizontal grid-point matrix dimension
0.27777777777777777777                 TimeStep        - Time step [seconds]
600                AnalysisTime    - Length of analysis time series [seconds] (program will add time if necessary: AnalysisTime = MAX(AnalysisTime, UsableTime+GridWidth/MeanHHWS) )
1000                 UsableTime      - Usable length of output time series [seconds] (program will add GridWidth/MeanHHWS seconds)
150.00             HubHt           - Hub height [m] (should be > 0.5*GridHeight)
40                 GridHeight      - Grid height [m]
160                GridWidth       - Grid width [m] (should be >= 2*(RotorRadius+ShaftLength))
0                  VFlowAng        - Vertical mean flow (uptilt) angle [degrees]
0                  HFlowAng        - Horizontal mean flow (skew) angle [degrees]

--------Meteorological Boundary Conditions-------------------
"IECKAI"           TurbModel       - Turbulence model ("IECKAI"=Kaimal, "IECVKM"=von Karman, "GP_LLJ", "NWTCUP", "SMOOTH", "WF_UPW", "WF_07D", "WF_14D", or "NONE")
3                   IECstandard     - Number of IEC 61400-x standard (x=1,2, or 3 with optional 61400-1 edition number (i.e. "1-Ed2") )
A                IECturbc        - IEC turbulence characteristic ("A", "B", "C" or the turbulence intensity in percent) ("KHTEST" option with NWTCUP model, not used for other models)
"NTM"              IEC_WindType    - IEC turbulence type ("NTM"=normal, "xETM"=extreme turbulence, "xEWM1"=extreme 1-year wind, "xEWM50"=extreme 50-year wind, where x=wind turbine class 1, 2, or 3)
default            ETMc            - IEC Extreme Turbulence Model "c" parameter [m/s]
default            WindProfileType - Wind profile type ("JET","LOG"=logarithmic,"PL"=power law,"IEC"=PL on rotor disk,LOG elsewhere, or "default")
```

```
150             RefHt           - Height of the reference wind speed [m]
18                URef            - Mean (total) wind speed at the reference height [m/s] (or "default" for JET wind profile)
default             ZJetMax         - Jet height [m] (used only for JET wind profile, valid 70-490 m)
default             PLExp           - Power law exponent [-] (or "default")
default             Z0              - Surface roughness length [m] (or "default")

--------Non-IEC Meteorological Boundary Conditions------------
default             Latitude        - Site latitude [degrees] (or "default")
0.05                RICH_NO         - Gradient Richardson number
default             UStar           - Friction or shear velocity [m/s] (or "default")
default             ZI              - Mixing layer depth [m] (or "default")
default             PC_UW           - Hub mean u'w' Reynolds stress (or "default")
default             PC_UV           - Hub mean u'v' Reynolds stress (or "default")
default             PC_VW           - Hub mean v'w' Reynolds stress (or "default")
default             IncDec1         - u-component coherence parameters (e.g. "10.0  0.3e-3" in quotes) (or "default")
default             IncDec2         - v-component coherence parameters (e.g. "10.0  0.3e-3" in quotes) (or "default")
default             IncDec3         - w-component coherence parameters (e.g. "10.0  0.3e-3" in quotes) (or "default")
default             CohExp          - Coherence exponent (or "default")

--------Coherent Turbulence Scaling Parameters-------------------
"M:\coh_events\eventdata"  CTEventPath     - Name of the path where event data files are located
"Random"            CTEventFile     - Type of event files ("LES", "DNS", or "RANDOM")
true                Randomize       - Randomize the disturbance scale and locations? (true/false)
 1.0                DistScl         - Disturbance scale (ratio of wave height to rotor disk). (Ignored when Randomize = true.)
 0.5                CTLy            - Fractional location of tower centerline from right (looking downwind) to left side of the dataset. (Ignored when Randomize = true.)
 0.5                CTLz            - Fractional location of hub height from the bottom of the dataset. (Ignored when Randomize = true.)
30.0                CTStartTime     - Minimum start time for coherent structures in RootName.cts [seconds]

================================================
NOTE: Do not add or remove any lines in this file!
================================================
```